



**LEHIGH**  
U N I V E R S I T Y

Library &  
Technology  
Services

The Preserve: Lehigh Library Digital Collections

# Niobium Oxide Catalysts: Synthesis, Characterization, And Catalysis.

## Citation

Jehng, Jih-Mirn. *Niobium Oxide Catalysts: Synthesis, Characterization, And Catalysis*. 1990, <https://preserve.lehigh.edu/lehigh-scholarship/graduate-publications-theses-dissertations/theses-dissertations/nio-bium-oxide>.

Find more at <https://preserve.lehigh.edu/>

*This document is brought to you for free and open access by Lehigh Preserve. It has been accepted for inclusion by an authorized administrator of Lehigh Preserve. For more information, please contact [preserve@lehigh.edu](mailto:preserve@lehigh.edu).*

## INFORMATION TO USERS

**The most advanced technology has been used to photograph and reproduce this manuscript from the microfilm master. UMI films the text directly from the original or copy submitted. Thus, some thesis and dissertation copies are in typewriter face, while others may be from any type of computer printer.**

**The quality of this reproduction is dependent upon the quality of the copy submitted. Broken or indistinct print, colored or poor quality illustrations and photographs, print bleedthrough, substandard margins, and improper alignment can adversely affect reproduction.**

In the unlikely event that the author did not send UMI a complete manuscript and there are missing pages, these will be noted. Also, if unauthorized copyright material had to be removed, a note will indicate the deletion.

Oversize materials (e.g., maps, drawings, charts) are reproduced by sectioning the original, beginning at the upper left-hand corner and continuing from left to right in equal sections with small overlaps. Each original is also photographed in one exposure and is included in reduced form at the back of the book.

Photographs included in the original manuscript have been reproduced xerographically in this copy. Higher quality 6" x 9" black and white photographic prints are available for any photographs or illustrations appearing in this copy for an additional charge. Contact UMI directly to order.

U·M·I

University Microfilms International  
A Bell & Howell Information Company  
300 North Zeeb Road, Ann Arbor, MI 48106-1346 USA  
313/761-4700 800/521-0600



**Order Number 9109573**

**Niobium oxide catalysts: Synthesis, characterization, and  
catalysis**

**Jehng, Jih-Mirn, Ph.D.**

**Lehigh University, 1990**

**Copyright ©1990 by Jehng, Jih-Mirn. All rights reserved.**

**U·M·I**  
300 N. Zeeb Rd.  
Ann Arbor, MI 48106



# **NIOBIUM OXIDE CATALYSTS: SYNTHESIS, CHARACTERIZATION, AND CATALYSIS**

by  
**JIH-MIRN JEHNG**

**A Dissertation  
Presented to the Graduate Committee  
of Lehigh University  
in Candidacy for the Degree of  
Doctor of Philosophy**

**in**

**Department of Chemical Engineering**

**Lehigh University, Bethlehem, PA  
1990**

**Copyright © Jih-Mirn Jehng 1990  
All Right Reserved**

**CERTIFICATE OF APPROVAL**

Approved and recommended for acceptance as a dissertation  
in partial fulfillment of the requirements for the degree  
of Doctor of Philosophy

*Israel E. Wachs*

**Dr. Israel E. Wachs**  
Advisor and Committee Chairman

**Special Committee Directing  
The Doctoral Work of  
Jih-Mrin Jehng**

*James T. Hsu*

**Dr. James T. Hsu**

*Andrew Klein*

**Dr. Andrew Klein**

*Larry Murrell*

**Dr. Larry L. Murrell**

*Sept. 5, 1990*  
**(Date)**

## TABLE OF CONTENTS

	Page
<b>ACKNOWLEDGMENTS</b>	vi
<b>LIST OF TABLES</b>	vii
<b>LIST OF FIGURES</b>	x
<b>ABSTRACT</b>	1
 <b>CHAPTER</b>	
<b>1. A. A REVIEW OF NIOBIUM OXIDE CATALYSIS</b>	<b>2</b>
1.1. Introduction	3
1.2. Bulk Layered Niobium Oxides	5
1.3. Surface Niobium Oxide Phases	6
1.4. Hydrated Niobium Oxide	8
1.5. Niobium Oxide Support	10
1.6. Niobium Mixed Oxides	11
1.7. Conclusions	14
B. THE SCOPE OF THE RESEARCH STUDY	16
 <b>2. STRUCTURAL CHEMISTRY AND RAMAN SPECTRA OF NIOBIUM OXIDES</b>	<b>37</b>
Summary	38
2.1. Introduction	39
2.2. Experimental	42
2.2.1. Materials	42
2.2.2. BET Surface Area Measurement	42
2.2.3. Raman Spectroscopy	43
2.3. Results	44
2.3.1. Octahedrally-Coordinated Niobium Oxide Compounds	44
- Slightly Distorted Niobium oxides	44
- Highly Distorted Niobium Oxides	45
- Layered Oxides	45
- Bulk Niobium Oxide ( $Nb_2O_5$ )	47
2.3.2. Tetrahedrally-Coordinated Niobium Oxide compound	49
2.4. Discussions	49
2.5. Conclusions	65
 <b>3. NIOBIUM OXIDE SOLUTION CHEMISTRY</b>	<b>78</b>
Summary	79
3.1. Introduction	80
3.2. Experimental	83

3.2-1.Materials and Preparations	83
3.2-2.Raman Spectroscopy	84
<b>3.3. Results</b>	<b>85</b>
3.3.1.Niobium Oxide in Alkaline Solutions	85
3.3.2.Niobium Oxide in Acidic oxalate Solutions	86
- Niobium Oxalate Solubility	86
- Solution pH	86
- Oxalic Acid Concentrations	87
- Nb Concentrations	88
- H <sup>+</sup> Concentrations	89
3.4. Discussions	90
3.5. Conclusions	101
 <b>4. MOLECULAR STRUCTURES OF SUPPORTED NIOBIUM OXIDE CATALYSTS UNDER AMBIENT CONDITIONS</b>	 111
Summary	112
4.1. Introduction	113
4.2. Experimental	115
4.2.1.Materials and Preparations	115
4.2.2.BET Surface Area Measurement	117
4.2.3.Raman Spectroscopy	117
4.2.4.X-Ray Photoelectron Spectroscopy (XPS)	118
4.3. Results	118
4.3.1.BET Surface Area Measurements	118
4.3.2.X-Ray Photoelectron Spectroscopy	119
4.3.3.Raman Spectroscopy	120
4.3.3-1. Nb <sub>2</sub> O <sub>5</sub> /MgO	120
4.3.3-2. Nb <sub>2</sub> O <sub>5</sub> /Al <sub>2</sub> O <sub>3</sub>	121
4.3.3-3. Nb <sub>2</sub> O <sub>5</sub> /TiO <sub>2</sub>	122
4.3.3-4. Nb <sub>2</sub> O <sub>5</sub> /ZrO <sub>2</sub>	123
4.3.3-5. Nb <sub>2</sub> O <sub>5</sub> /SiO <sub>2</sub>	124
4.4. Discussions	125
4.5. Conclusions	134
 <b>5. MOLECULAR STRUCTURES OF SUPPORTED NIOBIUM OXIDE CATALYSTS UNDER IN SITU CONDITIONS</b>	 153
Summary	154
5.1. Introduction	155
5.2. Experimental	158
5.2.1.Materials and Preparations	158
5.2.2.In Situ Raman Spectroscopy	159
5.3. Results	161
5.3.1.Nb <sub>2</sub> O <sub>5</sub> /SiO <sub>2</sub>	161
5.3.2.Nb <sub>2</sub> O <sub>5</sub> /TiO <sub>2</sub>	161
5.3.3.Nb <sub>2</sub> O <sub>5</sub> /ZrO <sub>2</sub>	162
5.3.4.Nb <sub>2</sub> O <sub>5</sub> /Al <sub>2</sub> O <sub>3</sub>	163
5.3.5.Nb <sub>2</sub> O <sub>5</sub> /MgO	164
5.4. Discussions	164
5.5. Conclusions	175

<b>6. SURFACE ACIDITY AND REACTIVITY OF SUPPORTED NIOBIUM OXIDE CATALYSTS</b>	<b>190</b>
Summary	191
6.1. Introduction	192
6.2. Experimental	195
6.2.1. Materials	195
6.2.2. Acidity Studies	196
6.2.3. Catalysis Studies	197
6.3. Results	199
6.3.1. Surface Acidities of Bulk Niobium Oxide and Supported Niobium Oxide Catalysts	199
- Bulk Niobium Oxide	199
- Supported Niobium Oxide Catalysts	200
6.3.2. Reactivity of Bulk Niobium Oxide and Supported Niobium Oxide Catalysts	201
- Bulk Niobium Oxide	201
- Supported Niobium Oxide Catalysts	202
6.4. Discussions	204
- Molecular Structures of Supported Niobium Oxide Catalysts	204
- Molecular Structure-Acidity Relationships	207
- Molecular Structure-Reactivity Relationships	211
6.5. Conclusions	214
<b>7. CONCLUSIONS</b>	<b>228</b>
<b>REFERENCES</b>	<b>232</b>
<b>CURRICULUM VITAE</b>	<b>250</b>

## ACKNOWLEDGMENTS

I am indebted to my advisor, Professor Israel E. Wachs of Chemical Engineering, for his numerous guidance and counsel leading me into an interesting field of heterogeneous catalysis. The other members of the dissertation committee, Dr. Larry L. Murrell, and Professors Andrew Klein and James T. Hsu of Chemical Engineering are acknowledged for their valuable comments and suggestions on this work. I am also grateful to Dr. Frank D. Hardcastle for introducing the theories and experiments of laser Raman spectroscopy.

Many individuals contributed to the preparation of this work. I would like to thank Mr. Goutam Deo for his assistance in catalysis studies, Mr. Michael Vuurman for setting up and aiding in in-situ Raman studies, and Dr. Andrzej M. Turek for performing pyridine adsorption IR studies. I would also like to thank Dr. Paul McCaslin at Unocal Inc. for performing XPS measurements on various samples. I am grateful to Dr. Allen Jacobson at Exxon research center for providing the most important layered niobium oxide reference compounds and Professor Satohiro Yoshida at Kyoto University in Japan for providing  $\text{YbNbO}_4$  reference compound. Financial support for this work by Niobium Products Company, Inc. is gratefully acknowledged.

Finally, I wish to thank my wife, Hsueh-Lin Hsu, for giving me a lovely son, Jonathan, and her encouragement and support during this long-range study.

## LIST OF TABLES

	<b>Page</b>
<b>Table 1.1: Photocatalysis of aqueous methanol solutions over layered niobium oxides</b>	<b>19</b>
<b>Table 1.2: The molecular size of alcohols effects on the H<sub>2</sub> evolution rate over layered niobium oxide</b>	<b>20</b>
<b>Table 1.3: Ethanol dehydrogenation depends on the nature of oxide supports</b>	<b>21</b>
<b>Table 1.4: Surface niobium oxide phase stabilizes oxide supports at elevated temperatures</b>	<b>22</b>
<b>Table 1.5: Surface niobium oxide phase forms strong Brønsted acid sites on oxide supports</b>	<b>23</b>
<b>Table 1.6: Catalytic applications of niobium oxide supported on silica</b>	<b>24</b>
<b>Table 1.7: Catalytic applications of niobium oxide supported on alumina</b>	<b>25</b>
<b>Table 1.8: Catalytic applications of niobium oxide supported on titania</b>	<b>26</b>
<b>Table 1.9: Alkylation of benzene with methanol over H<sub>3</sub>PO<sub>4</sub>-treated niobium oxides</b>	<b>27</b>
<b>Table 1.10: Hydrolysis of phenyloxiran over Nb<sub>2</sub>O<sub>5</sub>.H<sub>2</sub>O in liquid solutions</b>	<b>28</b>
<b>Table 1.11: Hydrogenation of carbon monoxide to synthetic fuels over supported ruthenium catalysts</b>	<b>29</b>

<b>Table 1.12:Hydrogenation of carbon monoxide to synthetic fuels over supported rhodium catalysts</b>	<b>30</b>
<b>Table 1.13:Dehydration of isopropanol to proene over supported MoO<sub>3</sub>/Nb<sub>2</sub>O<sub>5</sub> catalysts</b>	<b>31</b>
<b>Table 1.14:Dehydration of isopropanol to proene over supported V<sub>2</sub>O<sub>5</sub>/Nb<sub>2</sub>O<sub>5</sub> catalysts</b>	<b>32</b>
<b>Table 1.15:The conversion of isobutylene to methacrolein over niobium mixed oxide catalysts</b>	<b>33</b>
<b>Table 1.16:Oxidative dehydrogenation of ethane to ethylene over niobium mixed oxide catalysts</b>	<b>34</b>
<b>Table 1.17:Oxidation of o-xylene to phthalic anhydride over niobium mixed oxide catalysts</b>	<b>35</b>
<b>Table 1.18:NO<sub>x</sub> reduction with NH<sub>3</sub> to N<sub>2</sub> over niobium mixed oxide catalysts</b>	<b>36</b>
<b>Table 2.1: The relationships between niobium oxide structures and Raman frequencies</b>	<b>66</b>
<b>Table 3.1: The aqueous potassium niobate species and Raman bands relationships at a pH range from 14.5 to 0.55</b>	<b>103</b>
<b>Table 4.1: The influence of calcination temperature on the surface areas of supported niobium oxide catalysts</b>	<b>137</b>
<b>Table 4.2: Raman bands of supported niobium oxide catalysts under ambient conditions (hydrated state)</b>	<b>138</b>

<b>Table 5.1: Raman bands of supported niobium oxide catalysts under in situ conditions (dehydrated state)</b>	<b>177</b>
<b>Table 5.2: A molecular structure model for the dehydrated surface niobium oxide species</b>	<b>178</b>
<b>Table 6.1: Surface acid sites present in bulk niobium oxide as a function of temperature treatment</b>	<b>216</b>
<b>Table 6.2: The reactivity and selectivity of methanol oxidation reaction over bulk <math>\text{Nb}_2\text{O}_5</math></b>	<b>218</b>
<b>Table 6.3: The reactivity of methanol oxidation reaction over supported niobium oxide catalysts</b>	<b>219</b>
<b>Table 6.4: The selectivity of methanol oxidation reaction over supported niobium oxide catalysts</b>	<b>220</b>
<b>Table 6.5: The activation energy of methanol oxidation over supported niobium oxide catalysts as a function of <math>\text{Nb}_2\text{O}_5</math> loading</b>	<b>221</b>

## LIST OF FIGURES

	<b>Page</b>
<b>Figure 2.1:Raman spectra of the BNbO<sub>3</sub> (B= Li, Na, K) compounds</b>	<b>67</b>
<b>Figure 2.2:Raman spectra of the highly distorted niobium oxide compounds</b>	<b>68</b>
<b>Figure 2.3:Raman spectra of the KCa<sub>2</sub>Na<sub>n-3</sub>Nb<sub>n</sub>O<sub>3n+1</sub> (n=3,4,5) layered oxide compounds</b>	<b>69</b>
<b>Figure 2.4:Raman spectra of the HCa<sub>2</sub>Nb<sub>3</sub>O<sub>10</sub> (hydrated/dehydrated) layered oxide compound</b>	<b>70</b>
<b>Figure 2.5:In situ Raman spectra of the HCa<sub>2</sub>Nb<sub>3</sub>O<sub>10</sub> layered oxide compound</b>	<b>71</b>
<b>Figure 2.6:The surface area of bulk niobium oxide as a function of calcination temperature</b>	<b>72</b>
<b>Figure 2.7:Raman spectra of bulk niobium oxide as a function of calcination temperatures</b>	<b>73</b>
<b>Figure 2.8:In situ Raman spectra of Nb<sub>2</sub>O<sub>5</sub>.nH<sub>2</sub>O (120°C)</b>	<b>74</b>
<b>Figure 2.9:In situ Raman spectra of Nb<sub>2</sub>O<sub>5</sub> (500°C)</b>	<b>75</b>
<b>Figure 2.10:Raman spectrum of the YbNbO<sub>4</sub> compound</b>	<b>76</b>
<b>Figure 2.11:The Raman band intensity ratios for the KCa<sub>2</sub>Na<sub>n-3</sub>Nb<sub>n</sub>O<sub>3n+1</sub> (n=3,4,5) layered oxide compounds</b>	<b>77</b>
<b>Figure 3.1:Raman spectrum of K<sub>8</sub>Nb<sub>6</sub>O<sub>19</sub>.XH<sub>2</sub>O in 10M KOH aqueous solution as a function of pH</b>	<b>104</b>

<b>Figure 3.2:The solubility of niobium oxalate in aqueous oxalic acid solutions</b>	<b>105</b>
<b>Figure 3.3:Raman spectra of niobium oxalate in aqueous solutions as a function of the solution pH</b>	<b>106</b>
<b>Figure 3.4:Raman spectra of the aqueous oxalic acid solutions</b>	<b>107</b>
<b>Figure 3.5:Raman spectra of niobium oxalate in aqueous solutions as a function of the <math>C_2O_4^{2-}</math> concentration</b>	<b>108</b>
<b>Figure 3.6:Raman spectra of niobium oxalate in aqueous solutions as a function of the Nb concentration</b>	<b>109</b>
<b>Figure 3.7:Raman spectra of niobium oxalate in aqueous solutions as a function of the <math>H^+</math> concentration</b>	<b>110</b>
<b>Figure 4.1:The surface areas of the supported niobium oxide catalysts as a function of <math>Nb_2O_5</math> loading</b>	<b>139</b>
<b>Figure 4.2:The X-ray photoelectron spectroscopy analysis of supported niobium oxide catalysts</b>	<b>140</b>
<b>Figure 4.3:The Raman spectra of MgO supported niobium oxide (calcined at 500°C) as a function of <math>Nb_2O_5</math> loading</b>	<b>141</b>
<b>Figure 4.4:The Raman spectra of 5 wt% <math>Nb_2O_5/MgO</math> as a function of calcination temperature</b>	<b>142</b>

**Figure 4.5:**The Raman spectra of aqueously prepared  $\text{Al}_2\text{O}_3$  supported niobium oxide (calcined at 500°C) as a function of  $\text{Nb}_2\text{O}_5$  loading 143

**Figure 4.6:**The Raman spectra of nonaqueously prepared  $\text{Al}_2\text{O}_3$  supported niobium oxide (calcined at 500°C) as a function of  $\text{Nb}_2\text{O}_5$  loading 144

**Figure 4.7:**The Raman spectra of 5 wt%  $\text{Nb}_2\text{O}_5/\text{Al}_2\text{O}_3$  as a function of calcination temperature 145

**Figure 4.8:**The Raman spectra of  $\text{TiO}_2$  supported niobium oxide (calcined at 450°C) as a function of  $\text{Nb}_2\text{O}_5$  loading 146

**Figure 4.9:**The Raman spectra of 5 wt%  $\text{Nb}_2\text{O}_5/\text{TiO}_2$  as a function of calcination temperature 147

**Figure 4.10:**The Raman spectra of  $\text{ZrO}_2$  supported niobium oxide (calcined at 450°C) as a function of  $\text{Nb}_2\text{O}_5$  loading 148

**Figure 4.11:**The Raman spectra of 3 wt%  $\text{Nb}_2\text{O}_5/\text{ZrO}_2$  as a function of calcination temperature 149

**Figure 4.12:**The Raman spectra of  $\text{SiO}_2$  supported niobium oxide (calcined at 500°C) as a function of  $\text{Nb}_2\text{O}_5$  loading 150

**Figure 4.13:**The Raman spectra of  $\text{SiO}_2$  supported niobium oxide (calcined at 600°C) as a function of  $\text{Nb}_2\text{O}_5$  loading 151

**Figure 4.14:**The Raman spectra of 4 wt%  $\text{Nb}_2\text{O}_5/\text{SiO}_2$  as a function of calcination temperature 152

<b>Figure 5.1:In situ Raman spectra of 2 wt% Nb<sub>2</sub>O<sub>5</sub>/SiO<sub>2</sub></b>	<b>179</b>
<b>Figure 5.2:In situ Raman spectra of 4 wt% Nb<sub>2</sub>O<sub>5</sub>/SiO<sub>2</sub></b>	<b>180</b>
<b>Figure 5.3:In situ Raman spectra of 1 wt% Nb<sub>2</sub>O<sub>5</sub>/TiO<sub>2</sub></b>	<b>181</b>
<b>Figure 5.4:In situ Raman spectra of 7 wt% Nb<sub>2</sub>O<sub>5</sub>/TiO<sub>2</sub></b>	<b>182</b>
<b>Figure 5.5:In situ Raman spectra of 1 wt% Nb<sub>2</sub>O<sub>5</sub>/ZrO<sub>2</sub></b>	<b>183</b>
<b>Figure 5.6:In situ Raman spectra of 5 wt% Nb<sub>2</sub>O<sub>5</sub>/ZrO<sub>2</sub></b>	<b>184</b>
<b>Figure 5.7:In situ Raman spectra of 5 wt% Nb<sub>2</sub>O<sub>5</sub>/Al<sub>2</sub>O<sub>3</sub></b>	<b>185</b>
<b>Figure 5.8:In situ Raman spectra of 19 wt% Nb<sub>2</sub>O<sub>5</sub>/Al<sub>2</sub>O<sub>3</sub></b>	<b>186</b>
<b>Figure 5.9:In situ Raman spectra of the Nb<sub>2</sub>O<sub>5</sub>/Al<sub>2</sub>O<sub>3</sub> system as a function of Nb<sub>2</sub>O<sub>5</sub> loading</b>	<b>187</b>
<b>Figure 5.10:In situ Raman spectra of 5 wt% Nb<sub>2</sub>O<sub>5</sub>/MgO</b>	<b>188</b>
<b>Figure 5.11:In situ Raman spectra of 10 wt% Nb<sub>2</sub>O<sub>5</sub>/MgO</b>	<b>189</b>
<b>Figure 6.1:The Lewis acid surface sites present in the supported niobium oxide catalysts</b>	<b>222</b>
<b>Figure 6.2:The Brønsted acid surface sites present in the supported niobium oxide catalysts</b>	<b>223</b>
<b>Figure 6.3:The reactivity of the SiO<sub>2</sub> supported niobium oxide catalysts as a function of Nb<sub>2</sub>O<sub>5</sub> loading</b>	<b>224</b>

<b>Figure 6.4:The selectivity of the <math>\text{SiO}_2</math> supported niobium oxide catalysts as a function of <math>\text{Nb}_2\text{O}_5</math> loading</b>	<b>225</b>
<b>Figure 6.5:Arrhenius plot of bulk <math>\text{Nb}_2\text{O}_5</math> for methanol oxidation</b>	<b>226</b>
<b>Figure 6.6:Arrhenius plot of supported niobium oxide catalysts for methanol oxidation</b>	<b>227</b>

## ABSTRACT

The molecular structure-reactivity relationships for supported niobium oxide catalysts were achieved by combining Raman spectroscopy structural studies with chemical probes that measured the acidity and reactivity of the surface niobium oxide sites. Supported niobium oxide catalysts form a two-dimensional overlayer on oxide supports, and the monolayer coverage of these systems is reached at  $\sim 19\%$   $\text{Nb}_2\text{O}_5/\text{Al}_2\text{O}_3$ ,  $\sim 7\%$   $\text{Nb}_2\text{O}_5/\text{TiO}_2$ ,  $\sim 5\%$   $\text{Nb}_2\text{O}_5/\text{ZrO}_2$ , and  $\sim 2\%$   $\text{Nb}_2\text{O}_5/\text{SiO}_2$ , but not for the  $\text{Nb}_2\text{O}_5/\text{MgO}$  system due to the incorporation of  $\text{Nb}^{+5}$  into the  $\text{MgO}$  support. Molecular structures of the surface niobium oxide species under ambient conditions are controlled by the surface pH of the system. Upon dehydration process, only one dehydrated surface niobium oxide species corresponding to the highly distorted  $\text{NbO}_6$  octahedral structure at  $\sim 980 \text{ cm}^{-1}$  is present on silica. The highly distorted  $\text{NbO}_6$  octahedra responsible for Raman bands at  $\sim 985$  and  $\sim 935 \text{ cm}^{-1}$  are also observed on titania and zirconia at monolayer coverage. Below half monolayer coverage on alumina, two dehydrated surface niobium oxide species possessing highly and moderately distorted  $\text{NbO}_6$  octahedra with  $\text{Nb}=\text{O}$  Raman bands at  $\sim 980$  and  $\sim 883 \text{ cm}^{-1}$ , respectively, are present. Upon approaching monolayer coverage on alumina, additional Raman bands at  $\sim 935$  and  $\sim 647 \text{ cm}^{-1}$  characteristic of highly and slightly distorted  $\text{NbO}_6$  octahedra are present and are suggestive of a layered niobium oxide structure. Multiple niobium oxide species are present in the  $\text{Nb}_2\text{O}_5/\text{MgO}$  system due to the strong acid-base interactions of  $\text{Nb}_2\text{O}_5$  with the  $\text{Mg}^{2+}$  and the  $\text{Ca}^{2+}$  surface cations. The highly distorted  $\text{NbO}_6$  octahedra possess  $\text{Nb}=\text{O}$  bonds and are associated with Lewis acid sites. The surface layered niobium oxide species are associated with Brønsted acid sites. The Lewis acid sites are present on all the supported niobium oxide systems, but the Brønsted acid sites are limited to the  $\text{Nb}_2\text{O}_5/\text{Al}_2\text{O}_3$  and  $\text{Nb}_2\text{O}_5/\text{SiO}_2$  systems. The surface niobium oxide Lewis acid sites are significantly more active when coordinated to the  $\text{Al}_2\text{O}_3$  and  $\text{SiO}_2$  surfaces than to the  $\text{TiO}_2$ ,  $\text{ZrO}_2$ , and  $\text{MgO}$  surfaces. Furthermore, the surface niobium oxide sites on silica behaves as redox sites and the surface niobium oxide on alumina are acid sites during partial oxidation reactions.

# **CHAPTER 1**

## **A REVIEW OF NIOBIUM OXIDE CATALYSTS**

### 1.1. INTRODUCTION

In the past two decades, niobium-based materials have been found to be effective catalysts for many catalytic reactions: pollution abatement, selective oxidation, hydrocarbon conversion, hydrotreating, hydrogenation/dehydrogenation, carbon monoxide hydrogenation for synthetic fuels and chemicals, polymerization, hydration/dehydration and photochemistry/electrochemistry [1]. In the 1970's, niobium-based catalysts were primarily investigated for their performance in the area of selective oxidation reactions (partial oxidation, ammoxidation, and oxidative dehydrogenation). In the 1980's, the use of niobium-based catalysts became more versatile, and their catalytic applications received more attention in the areas of hydrocarbon conversion reactions (cracking, alkylation, metathesis, isomerization, and reforming) and carbon monoxide hydrogenation to synthetic fuels and chemicals. In the latter part of 1980's, niobium-based catalysts were further developed and utilized for the catalytic reactions of dehydration/hydration, esterification, and photocatalysis. The previous studies have pointed out that the development of new niobium oxide materials is essential to advancing the catalytic applications of niobium oxides.

One of the most interesting developments in niobium-

based catalytic materials is that niobium oxide can form bulk layered structures [2-4] as well as two-dimensional surface niobium oxide phases on high surface area oxide supports such as  $\text{Al}_2\text{O}_3$ ,  $\text{TiO}_2$ , and  $\text{SiO}_2$  [5-12]. The layered niobium oxide materials doped with 0.1 wt% Pt or Ni exhibit an unusually high and stable activity for photocatalysis of  $\text{H}_2\text{O}$  into  $\text{H}_2$  and  $\text{O}_2$  [2,3]. The two-dimensional surface niobium oxide phases have a pronounced effect on the physical and chemical properties of the oxide supports. The thermal stability of the  $\text{Al}_2\text{O}_3$  and  $\text{TiO}_2$  supports is increased by the presence of the surface niobium oxide overlayers [12]. Furthermore, the surface niobium oxide phase on the  $\text{Al}_2\text{O}_3$  support was also found to possess strong Brønsted acidity which results in a high hydrocarbon cracking activity at elevated temperatures [5].

The  $\text{Nb}_2\text{O}_5/\text{TiO}_2$  catalysts were reported to possess considerable activity for the reduction of  $\text{NO}$  with  $\text{NH}_3$  from stationary emissions [13]. Silica supported niobium oxide catalysts were found to be active and selective for ethanol dehydrogenation [9], propene metathesis [6], and propene photocatalysis [14]. In addition, the synthesis of methyl methacrylate from methyl propionate and formaldehyde was also catalyzed by the  $\text{Nb}_2\text{O}_5/\text{SiO}_2$  system [15-16]. Thus, bulk layered structures and two-dimensional niobium oxide phases, on different oxide supports, have shown extensive

catalytic applications.

The present review is limited to niobium oxide materials because most of the recent studies have concentrated on the catalytic properties of niobium oxide, and is classified into 1) bulk layered niobium oxides, 2) surface niobium oxide phases, 3) hydrated niobium oxide, 4) niobium oxide support, and 5) niobium mixed oxides.

## 1.2. BULK LAYERED NIOBIUM OXIDES

Layered niobium oxides,  $M[Ca_2Nb_nO_{3n+1}]$  ( $M= K, Rb, \text{ and } Cs$ ;  $n= 3 \text{ or } 4$ ), can undergo an alkali exchange reactions with the protons present in aqueous acidic solutions due to their high ionic conductivity. The ion-exchanged layered niobium oxides,  $H[Ca_2Nb_nO_{3n+1}]$  ( $n= 3 \text{ and } 4$ ), were found to exhibit an unusually high activity for the photocatalysis of aqueous methanol solutions to  $H_2$  and  $O_2$  [2,3]. The  $H_2$  evolution rates over the layered niobium oxides in aqueous methanol solutions (with or without ion-exchange) are shown in Table 1.1, and the  $H^+$ -exchanged  $KCa_2Nb_3O_{10}$  doped with 0.1 wt% Pt possesses the highest  $H_2$  evolution rate. The  $H_2$  evolution rates in the aqueous solutions was also found to decrease with increasing size of the alcohol molecule due to the limited intercalation space as shown in Table 1.2.

Thus, the layered niobium oxides possess interesting catalytic properties.

### 1.3. SURFACE NIOBIUM OXIDE PHASES

In the past few years, supported niobium oxide catalysts, on oxide supports such as  $\text{Al}_2\text{O}_3$ ,  $\text{TiO}_2$ ,  $\text{SiO}_2$ , and PVG (Porous Vycor Glass), have received much attention as the potential new niobium-based catalytic materials [5-12,17,18]. Deposition of niobium oxide on high surface area oxide supports yields high surface area niobium oxide catalysts that possess important physical and chemical properties. The molecular states of the dispersed surface niobium oxide phases contrast sharply to bulk  $\text{Nb}_2\text{O}_5$ , and are reflected in the unique molecular structures and catalytic properties of the surface niobium oxide phases.

The catalytic properties for ethanol dehydrogenation over the supported niobium oxide on  $\text{Al}_2\text{O}_3$  and  $\text{SiO}_2$ , as well as bulk  $\text{Nb}_2\text{O}_5$ , are shown in Table 1.3 [7]. The surface niobium oxide phases exhibit very high activity and selectivity for ethanol dehydrogenation compared to bulk  $\text{Nb}_2\text{O}_5$ , and the specific oxide support has a pronounced effect on the catalytic properties of the supported niobium oxide catalysts. The surface niobium oxide phases also

impart thermal stability to oxide supports,  $\text{Al}_2\text{O}_3$  and  $\text{TiO}_2$ , at elevated temperatures by retarding the loss of surface area and phase transformations as shown in Table 1.4. This stabilizing effect extends the useful temperature range of catalytic materials and decreases catalyst deactivation. The surface niobium oxide phase also forms strong Brønsted acid sites on these oxide supports as shown in Table 1.5 [19-22]. The Brønsted acidity is necessary for many catalytic reactions such as hydrocarbon conversion and pollution abatement. Thus, the thermal stability, Brønsted acidity and high surface area of the surface niobium oxide phases have led to many catalytic applications for these novel catalytic materials.

A new application of supported niobium oxide catalysts is the redox properties found for  $\text{Nb}_2\text{O}_5/\text{SiO}_2$  and  $\text{Nb}_2\text{O}_5/\text{PVG}$  catalysts during photocatalytic oxidative dehydrogenation of alcohols (2-propanol) and olefins (ethylene and propylene) [14,17]. The surface niobium oxide phases on silica and PVG are catalytically active only when the surface niobium oxide phases are irradiated with ultraviolet light in the presence of alcohols and olefins. The UV-VIS absorption measurements showed that the surface niobium oxide phases were reduced by the alcohols and olefins during irradiation to form  $\text{Nb}^{+4}$ , and were reoxidized by gaseous oxygen. Thus, the surface niobium

oxide phases on silica and PVG possess redox properties for photocatalysis.

Another significant new application of supported niobium oxide catalysts is the promotional effect of niobium oxide upon  $V_2O_5/TiO_2$  catalysts for selective reduction of  $NO_x$  with  $NH_3$  [23]. The addition of niobium oxide to  $V_2O_5/TiO_2$  catalysts significantly increases the catalytic activity and allows the reaction to be performed at lower temperatures. The low reaction temperatures are important for emission control of stationary sources which usually operate at temperatures less than 300°C. The surface niobium oxide phases also suppress the oxidation of  $SO_2$  to  $SO_3$ , a highly undesirable side reaction, over the  $V_2O_5/TiO_2$  catalysts. In addition, the surface niobium oxide phases on titania stabilize these catalysts during high temperature treatments to reactivate the catalyst. The catalytic applications of supported niobium oxide catalysts are summarized in Table 1.6-8.

#### 1.4. HYDRATED NIOBIUM OXIDE

Hydrated niobium oxide,  $Nb_2O_5 \cdot nH_2O$ , is a new type of strong solid acid exhibiting high catalytic activity and selectivity for hydration of olefins, dehydration of

alcohols, esterification of carboxylic acids with alcohols, and condensation of butylaldehyde [24-29]. Hydrated niobium oxide catalyzes the hydration of ethylene to ethanol with 97% selectivity, high activity and long catalyst life. The esterification of ethyl alcohol with acetic acid occurs over hydrated niobium oxide with 100% selectivity. The dehydration of butylaldehyde to 2-ethylhexenal over hydrated niobium oxide is achieved with 92.5% conversion and 95.5% selectivity without the catalyst contaminating the product and effluent, as usually occurs.

Acidity measurements have shown that considerable strong Brønsted acid sites are present on hydrated niobium oxide when it is treated at 120-300°C. The acidity and catalytic activity decreases dramatically at high temperature treatments (>400°C) due to loss in surface area, removal of water, and crystallization of the hydrated niobium oxide structure. However, the addition of phosphoric acid to the hydrated niobium oxide surface retards the loss in surface area during high temperature treatments (400-600°C) and enhances the surface acidity. The  $H_3PO_4$ -treated niobium oxide catalysts exhibit high activity for the alkylation of benzene with methanol as shown in Table 1.9 [30]. The catalytic activity depends on the  $H_3PO_4$  concentration, and 1 mol/dm<sup>3</sup>  $H_3PO_4$  on the hydrated niobium oxide surface possesses the highest activity for

alkylation of  $C_6H_6$  to  $C_6H_5CH_3$ .

Recently, hydrated niobium oxide,  $Nb_2O_5 \cdot nH_2O$ , was also found to be an effective catalyst for the hydrolysis, isomerization, and solvolysis of phenyloxirane in liquid solutions [31]. The hydrolysis of phenyloxirane in liquid solutions over some solid acid catalysts is presented in Table 1.10, and  $Nb_2O_5 \cdot nH_2O$  exhibits a higher activity and selectivity towards 1-phenyl-1,2-ethanediol than the other solid acid catalysts due to its high surface hydrophilicity [31].

## 1.5. NIOBIUM OXIDE SUPPORT

Recent catalytic studies have revealed that niobium oxide is a highly effective oxide support material for supported metallic catalysts used in carbon monoxide hydrogenation to synthetic fuels and chemicals [32]. Niobium oxide has been recently used as support for metals such as Ru, Rh, and Ni [32-34] and exhibit higher olefin selectivity during carbon monoxide hydrogenation compared to conventional oxide supports such as alumina and silica. The influence of the oxide support upon supported ruthenium catalysts during the hydrogenation of carbon monoxide to synthetic fuels is presented in Table 1.11 [33].

Supporting ruthenium on niobia decreases the formation of methane and by-products, and increases the yield of olefins. The influence of the oxide support on the supported rhodium catalysts during the hydrogenation of carbon monoxide to synthetic fuels is also presented in Table 1.12 [32]. The niobia supported rhodium catalysts exhibit very high activity and selectivity towards olefin production compared to the analogous alumina supported systems.

Metal oxides can also be supported on niobium oxide. The niobium oxide support promotes the catalytic properties of the supported vanadium and molybdenum oxide catalysts during the dehydration of isopropanol to propene (see Table 1.13 and 1.14). The niobia supported molybdenum oxide catalysts exhibit higher isopropanol dehydration activity and propene selectivity than bulk  $\text{MoO}_3$  [35]. Similarly, the niobia supported vanadium oxide catalysts exhibit a 60-230 increase in activity relative to bulk  $\text{V}_2\text{O}_5$  for the dehydration of isopropanol to propene [36].

## 1.6. NIOBIUM MIXED OXIDES

Niobium oxide reacts with most metal oxides to form new niobium mixed oxide phases. The molecular structures of these niobium mixed oxide phases depend on the relative

composition of the mixed oxides and the calcination temperature. Niobium mixed oxides have a pronounced impact on the resulting niobium oxide catalytic properties especially in the area of selective oxidation reactions. The presence of niobium oxide as a catalyst component usually shows an improvement in both the catalytic activity and selectivity. Some of the most widely used niobium mixed oxide catalysts are found in selective oxidation and pollution abatement reactions and are presented as follows:

- $\text{Nb}_2\text{O}_5$ - $\text{MoO}_3$  mixed oxides with a niobium to molybdenum atomic ratio between 0.5 and 2 exhibit high selectivities to acrylic and methacrylic acids for acrolein oxidation [37]. The selective oxidation of isobutylene to methacrolein over the mixed oxides  $\text{Mo}_{12}\text{Bi}_9\text{O}_x$ ,  $\text{Mo}_{12}\text{Nb}_3\text{O}_x$ , and  $\text{Mo}_{12}\text{Bi}_9\text{Nb}_3\text{O}_x$  are shown in Table 1.15 [38]. Catalysis studies indicate that the bismuth molybdate-niobate systems results in much higher isobutylene conversion (96%) and methacrolein selectivity (74%). Similar improvements for these niobium mixed oxide catalysts were also found for the selective oxidation of propylene to acrolein, propylene ammoxidation to acrylonitrile, and butene oxidative dehydrogenation to 1,3-butadiene.

- The oxidative dehydrogenation of ethane to ethylene is also improved by adding niobium oxide to mixed molybdenum and vanadium oxide materials as shown in Table 1.16 [39]. The addition of niobium oxide to the  $\text{MoO}_3\text{-V}_2\text{O}_5$  mixed oxides enhances the selectivity for the oxidation of ethane to ethylene to 100% and significantly lowers the reaction temperature ( $286^\circ\text{C}$ ) required to achieve 10% conversion.
- Niobium oxide was also found to promote vanadium pentoxide catalysts for the oxidation of o-xylene to phthalic anhydride as shown in Table 1.17 [40], and the catalytic activity was found to depend on the  $\text{Nb}_2\text{O}_5$  concentration. A 3:2 ratio of the  $\text{Nb}_2\text{O}_5\text{/V}_2\text{O}_5$  mixed oxide catalyst exhibits the highest activity for the oxidation of o-xylene to phthalic anhydride.
- Niobium oxide has recently been found to be an effective promoter for the reduction of  $\text{NO}_x$  with  $\text{NH}_3$  to  $\text{N}_2$  and  $\text{H}_2\text{O}$  over iron oxide catalysts [41]. The presence of niobium oxide in the  $\text{FeO}_x$  catalyst

remarkably enhanced the catalytic activity for  $\text{NO}_x$  reduction from 40% conversion to 90% conversion at reaction temperatures between 300 and 400°C as shown in Table 1.18. The catalytic activity for the reduction of  $\text{NO}_x$  with  $\text{NH}_3$  to  $\text{N}_2$  and  $\text{H}_2\text{O}$  over a  $\text{TiO}_2$  catalyst is also considerably enhanced by adding  $\text{Nb}_2\text{O}_5$  [20].

## 1.7. CONCLUSIONS

The literature review of niobium oxide catalysts reveals that niobium-based materials are effective catalysts for many catalytic reactions: pollution abatement, selective oxidation, hydrocarbon conversion, dehydrogenation, carbon monoxide hydrogenation for synthetic fuels and chemicals, hydration/dehydration, and photochemistry. The niobium oxide catalytic materials are present as bulk layered niobium oxides, surface niobium oxide phases, hydrated niobium oxide, oxide support, or mixed oxide. Recent research activities are focusing on the development of new niobium-based catalysts such as surface niobium oxide phases and layered niobium oxide compounds. The surface niobium oxide phase has a pronounced effect on the physical and chemical properties of oxide supports (i.e., acidity and thermal stability),

and these important characteristics are being utilized in many catalytic applications. However, the molecular states of the surface niobium oxide phases on oxide supports as well as the relationships between the molecular structures of the surface niobium oxide phases and the corresponding catalytic properties are not presently understood and are essential for the molecular design of improved niobium-based catalysts.

## THE SCOPE OF THE RESEARCH STUDY

- **The Structural Chemistry and Raman Spectra of Niobium Oxides**

Raman spectroscopy is a very powerful technique for investigating the structure of metal oxide materials since it is extremely sensitive to the metal-oxygen bond lengths and metal oxide structures. A series of reference niobium oxide compounds with known structures will be systematically studied by Raman spectroscopy. The niobium oxide structures-Raman spectra relationships will be established from these studies.

- **Niobium Oxide Solution Chemistry**

Aqueous niobium oxide species which exist in both basic and acidic oxalic acid solutions will be investigated by Raman spectroscopy. The molecular structures of the aqueous niobium oxide ionic species will be determined as a function of the solution pH.

- **Supported Niobium Oxide Catalysts**

Supported niobium oxide catalysts (on oxide supports such as  $MgO$ ,  $Al_2O_3$ ,  $TiO_2$ ,  $ZrO_2$ , and  $SiO_2$ ) will be synthesized using niobium oxalate and niobium ethoxide precursors. The nature of the surface niobium oxide phases, under ambient and in situ conditions, on the different oxide supports will be determined by comparing the Raman spectra of the supported niobium oxide catalysts with those of the niobium oxide reference compounds. In addition, the samples will be further characterized by X-ray diffraction (XRD), X-ray photoelectron spectroscopy (XPS), and Fourier-transform infrared spectroscopy (FTIR) of pyridine adsorption in order to determine the monolayer content and surface acidity of these supported niobium oxide catalysts.

- **Catalysis Studies**

The reactivity of the supported niobium oxide catalysts will be probed by the sensitive methanol oxidation reaction. The methanol oxidation reaction has two different pathways which depend on the nature of the active sites present on the catalyst surface. Surface redox sites produce  $HCHO$  and  $HCOOCH_3$ , and surface acid sites produce only  $CH_3OCH_3$ . Comparison of the reactivity

data with the corresponding molecular characterization information should allow the establishment of molecular structure-reactivity relationships for supported niobium oxide catalysts. Knowledge of the molecular structure-reactivity relationships should assist in the molecular design of supported niobium oxide catalysts for specific applications.

**Table 1.1: Photocatalysis of aqueous methanol solutions over layered niobium oxides**

<u>Catalyst</u>	<u><math>H_2</math> evolution rate (<math>\mu\text{mol}\cdot\text{h}^{-1}</math>)</u>		
	<u>Original</u>	<u><math>H^+</math>-exchanged</u>	<u><math>H^+</math>-exchanged + 0.1 wt% Pt</u>
$K_4Nb_6O_{17}^*$	130	750	740
$KCa_2Nb_3O_{10}$	14	5900	19000
$RbCa_2Nb_3O_{10}$	3	3100	17000
$CsCa_2Nb_3O_{10}$	2	970	8300
$KCa_2NaNb_4O_{13}$	5	790	18000

\* not layered structure

**Catalyst: 1g, Hg lamp (450W)**  
**Aqueous methanol solution: 50ml  $CH_3OH$  and 300ml  $H_2O$**

**Table 1.2: The molecular size of alcohols effects on the H<sub>2</sub> evolution rate over layered niobium oxides**

<u>Alcohol</u>	<u>H<sub>2</sub> evolution rate (μmol·h<sup>-1</sup>)</u>		
	<u>KCa<sub>2</sub>Nb<sub>3</sub>O<sub>10</sub></u>	<u>H<sup>+</sup>-exchanged</u>	<u>H<sup>+</sup>-exchanged + 0.1 wt% Pt</u>
Methanol	6.9	920	4700
Ethanol	7.0	73	380
2-propanol	3.7	48	220
1-propanol	2.5	27	43
1-butanol	2.5	19	30

**Table 1.3: Ethanol dehydrogenation depends on the nature of oxide supports**

<u>Catalyst</u>	<u>Reaction Temp.</u>	<u>Initial rate</u>	<u>% Selectivity</u>		
			<u>Acetaldehyde</u>	<u>Ethene</u>	<u>Diethyl ether</u>
<b>5.5% <math>\text{Nb}_2\text{O}_5/\text{SiO}_2</math></b>	523K	1.25	96.1	2.8	1.1
	548K	1.66	93.2	6.1	0.7
	573K	3.17	84.4	13.7	1.9
<b>6.3% <math>\text{Nb}_2\text{O}_5/\text{Al}_2\text{O}_3</math></b>	523K	4.03	4.6	5.7	89.7
	548K	5.33	4.1	19.6	76.3
	573K	11.78	3.4	26.9	69.7
<b><math>\text{Nb}_2\text{O}_5</math></b>	523K	2.05E-5	68.3	16.2	15.5
	573K	8.43E-5	32.2	40.7	27.2

Initial rate unit: mol min<sup>-1</sup> g<sub>Nb</sub><sup>-1</sup>

\* M. Nishimura, K. Asakura, and Y. Iwasawa, J. Chem. Soc. Chem. Commun., 1986

Table 1.4: Surface niobium oxide phase stabilizes oxide supports at elevated temperatures

Treatment	TiO <sub>2</sub> * (Degussa P-25)	8% Nb <sub>2</sub> O <sub>5</sub> /TiO <sub>2</sub> * (Degussa P-25)
500°C-2 hrs. in Air	56 m <sup>2</sup> /g (Anatase/Rutile)	56 m <sup>2</sup> /g (Anatase/Rutile)
700°C-2 hrs. in Air	31 m <sup>2</sup> /g (Anatase/Rutile)	46 m <sup>2</sup> /g (Anatase/Rutile)
850°C-2 hrs. in Air	12 m <sup>2</sup> /g (Rutile)	20 m <sup>2</sup> /g (Anatase/Rutile)
Treatment	Al <sub>2</sub> O <sub>3</sub> ** (Degussa $\gamma$ -Aluminum Oxide C)	2.9% Nb <sub>2</sub> O <sub>5</sub> /Al <sub>2</sub> O <sub>3</sub> ** (Degussa $\gamma$ -Aluminum Oxide C)
500°C-16 hrs. in Air	99 m <sup>2</sup> /g	97 m <sup>2</sup> /g
1100°C-16 hrs. in He/O <sub>2</sub> /H <sub>2</sub> O	7 m <sup>2</sup> /g	71 m <sup>2</sup> /g

\* J. M. Jehng, F. D. Hardcastle, and I. E. Wachs, Solid State Ionics 32, 33, 904, 1989

\*\* L. L. Murrell and D. C. Grenoble, U. S. Patent 4,415,480, 1983

**Table 1.5: Surface niobium oxide phase froms strong Bronsted acid sites on oxide supports**

Method of Bronsted Acidity Determination	Oxide Materials	
	TiO <sub>2</sub> *	10% Nb <sub>2</sub> O <sub>5</sub> /TiO <sub>2</sub> *
Isomerization of Cyclo-propane to Propene	5% Coversion	20% Coversion
	Al <sub>2</sub> O <sub>3</sub> (Degussa $\gamma$ -Alumina Oxide C)	2.9% Nb <sub>2</sub> O <sub>5</sub> /Al <sub>2</sub> O <sub>3</sub>
Modified Benesi Method	3 $\mu$ Moles/g (S.A.C.**)	50 $\mu$ Moles/g (S.A.C.**)
Light Gas Oil Cracking (Relative Activity)	1***	76***

\*S. Okzaki and T. Okuyama, Bull. Chem. Soc. Jpn., 56, 2159 (1983)

\*\*L. L. Murrell and D. C. Grenoble, U.S. Patent 4,415,480 (1983)

\*\*\*L. L. Murrell and D. C. Grenoble, and C. J. Kim, U.S. Patent 4,233,139 (1980)

**Table 1.6: Catalytic applications of niobium oxide supported on silica**

- Olefin metathesis
- Olefin Dimerization
- Olefin Isomerization
- Alcohol dehydrogenation
- Acetylene trimerization to benzene
- Methyl methacrylate from condensation of HCHO and methyl propionate
- Photocatalysis of alcohol and olefin

**Table 1.7: Catalytic applications of niobium oxide supported on alumina**

- Light gas oil cracking
- Hydrocarbon isomerization
- Alcohol dehydration
- Acetylene trimerization to benzene

**Table 1.8: Catalytic applications of niobium oxide supported on titania**

- $\text{H}_2\text{S}$  and CO to  $\text{CH}_3\text{SH}$  and  $\text{CH}_3\text{SCH}_3$
- Selective reduction of  $\text{NO}_x$  to  $\text{N}_2$  and  $\text{H}_2\text{O}$
- Alcohol dehydrogenation

**Table 1.9: Alkylation of benzene with methanol over  $H_3PO_4$ -treated niobium oxides**

<u>Catalyst</u>	<u>Conversion of <math>C_6H_6</math> to <math>C_6H_5CH_3</math> for 50mg catalyst (mol%·m<sup>-2</sup>)</u>
$Nb_2O_5$	0.3
0.5M $H_3PO_4/Nb_2O_5$	2.3
1.0M $H_3PO_4/Nb_2O_5$	2.5
2.0M $H_3PO_4/Nb_2O_5$	2.1
5.0M $H_3PO_4/Nb_2O_5$	0.35

Table 1.10: Hydrolysis of phenyloxiran over  $\text{Nb}_2\text{O}_5 \cdot n\text{H}_2\text{O}$  in liquid solutions

<u>Catalyst</u>	<u>Conversion (%)</u>	<u>Selectivity (%)</u>	
		PA	PE
$\text{Nb}_2\text{O}_5 \cdot n\text{H}_2\text{O}$	100	11.4	88.6
$\text{SiO}_2\text{-Al}_2\text{O}_3$ ( $\text{Al}_2\text{O}_3\text{-}13.5$ wt%)	96.1	34.8	61.2
$\text{SiO}_2\text{-Al}_2\text{O}_3$ ( $\text{Al}_2\text{O}_3\text{-}28.5$ wt%)	92.0	36.4	55.7
Zeolite ( $\text{SiO}_2/\text{Al}_2\text{O}_3\text{-}2100$ )	36.3	33.8	2.5

PA: Phenylacetaldehyde

PE: 1-Phenyl-1,2-ethanediol

**Table 1.11: Hydrogenation of carbon monoxide to synthetic fuels over supported ruthenium catalysts**

<u>Catalyst</u>	<u>Temp. (°C)</u>	<u>CO Conversion (%)</u>	<u>Selectivity (%) CH<sub>4</sub> &gt; C<sub>2</sub></u>
Ru	226	3.5	96
1% Ru/SiO <sub>2</sub>	223	4.1	87
1% Ru/Al <sub>2</sub> O <sub>3</sub>	228	8.8	66
1% Ru/Nb <sub>2</sub> O <sub>5</sub>	244	5.7	41
			59

**Table 1.12: Hydrogenation of carbon monoxide to synthetic fuels over supported rhodium catalysts**

<u>Catalyst</u>	<u>Temp. (°C)</u>	<u>CO Conversion (%)</u>	<u>Selectivity (%)</u>			
			<u>C<sub>1</sub></u>	<u>C<sub>2</sub></u>	<u>C<sub>3-C<sub>5</sub></sub></u>	<u>CO<sub>2</sub></u>
2.3% Rh/Nb <sub>2</sub> O <sub>5</sub>	220	75.9	71.8	6.8	19.7	1.7
2.3% Rh/Al <sub>2</sub> O <sub>3</sub>	220	1.4	89.2	7.6	-	3.2

**Table 1.13: Dehydration of isopropanol to propene over supported  $\text{MoO}_3/\text{Nb}_2\text{O}_5$  catalysts**

<u>Catalyst</u>	<u>Conversion (%)</u>	<u>Selectivity (%)</u>	
		<u>Acetone</u>	<u>Propene</u>
$\text{MoO}_3$	0.5	46	54
3 wt% $\text{Mo}/\text{Nb}_2\text{O}_5$	4	49	51
5 wt% $\text{Mo}/\text{Nb}_2\text{O}_5$	10	30	70
8 wt% $\text{Mo}/\text{Nb}_2\text{O}_5$	9	21	79
$\text{Nb}_2\text{O}_5$	very low	nondetectable	

Table 1.14: Dehydration of isopropanol to propene over supported  $V_2O_5/Nb_2O_5$  catalysts

<u>Catalyst</u>	<u>Activity</u> molecules $\cdot mg(V_2O_5)^{-1} \cdot s^{-1}$
$V_2O_5$	$1 \times 10^{17}$
0.14 wt% $V_2O_5/Nb_2O_5$	$2.3 \times 10^{19}$
0.59 wt% $V_2O_5/Nb_2O_5$	$8 \times 10^{18}$
0.95 wt% $V_2O_5/Nb_2O_5$	$6 \times 10^{18}$

**Table 1.15: The conversion of isobutylene to methacrolein over niobium mixed oxide catalysts**

<u>Mixed oxide catalyst</u>	<u>Isobutylene conversion</u>	<u>Methacrolein selectivity</u>	<u>CO and CO<sub>2</sub> selectivity</u>
Mo <sub>12</sub> Bi <sub>9</sub> O <sub>x</sub>	71.5	69.9	24.8
Mo <sub>12</sub> Nb <sub>3</sub> O <sub>x</sub>	82.6	65.8	29.1
Mo <sub>12</sub> Bi <sub>9</sub> Nb <sub>3</sub> O <sub>x</sub>	96.1	74.4	22.7

**Table 1.16: Oxidative dehydrogenation of ethane to ethylene over niobium mixed oxide catalysts**

<u>Mixed oxide catalyst</u>	<u>Temperature (°C) for 10% conversion</u>	<u>Ethylene selectivity</u>
$\text{Mo}_{1.0}$	500	88
$\text{Mo}_{0.92}\text{V}_{0.08}$	562	59
$\text{Mo}_{0.8}\text{V}_{0.2}$	540	100
$\text{Mo}_{0.8}\text{Nb}_{0.2}$	634	74
$\text{Mo}_{0.73}\text{V}_{0.18}\text{Nb}_{0.09}$	286	100

**Table 1.17: Oxidation of o-xylene to phthalic anhydride over niobium mixed oxide catalysts**

<u>Mixed oxide catalyst</u>	<u>Activity (mol·g<sup>-1</sup>·min<sup>-1</sup> × 10<sup>5</sup>)</u>
$V_2O_5$	2.2
20 $Nb_2O_5$ -80 $V_2O_5$	5.7
40 $Nb_2O_5$ -60 $V_2O_5$	8.2
60 $Nb_2O_5$ -40 $V_2O_5$	11.8
80 $Nb_2O_5$ -20 $V_2O_5$	7.0

**Table 1.18: NO<sub>x</sub> reduction with NH<sub>3</sub> to N<sub>2</sub> over niobium mixed oxide catalysts**

<u>Mixed oxide catalyst</u>	<u>NO<sub>x</sub> conversion at 300 °C (%)</u>	<u>NO<sub>x</sub> conversion at 400 °C (%)</u>
FeO <sub>x</sub>	40	15
5 Nb <sub>2</sub> O <sub>5</sub> -95 FeO <sub>x</sub>	87	78
20 Nb <sub>2</sub> O <sub>5</sub> -80 FeO <sub>x</sub>	90	95
50 Nb <sub>2</sub> O <sub>5</sub> -50 FeO <sub>x</sub>	85	92
80 Nb <sub>2</sub> O <sub>5</sub> -20 FeO <sub>x</sub>	62	90
95 Nb <sub>2</sub> O <sub>5</sub> -5 FeO <sub>x</sub>	45	78
Nb <sub>2</sub> O <sub>5</sub>	12	42

## **CHAPTER 2**

# **STRUCTURAL CHEMISTRY AND RAMAN SPECTRA OF NIOBIUM OXIDES**

## SUMMARY

A series of niobium oxide reference compounds were investigated by Raman spectroscopy in order to determine the relationship between niobium oxide structures and their corresponding Raman spectra. The assignments of the Raman bands were based on the known niobium oxide structures. The Raman studies indicate that the Raman frequencies strongly depend on the symmetry of the niobium oxide structures. For the slightly distorted octahedral  $\text{NbO}_6$  structures ( $\text{KNbO}_3$ ,  $\text{NaNbO}_3$ , and  $\text{LiNbO}_3$ ), the major Raman frequencies appear in the  $500\text{-}700\text{ cm}^{-1}$  region. For the highly distorted octahedral  $\text{NbO}_6$  structures ( $\text{K}_8\text{Nb}_6\text{O}_{19}$ ,  $\text{AlNbO}_4$ , and  $\text{Nb}(\text{HC}_2\text{O}_4)_5$ ), the major Raman frequencies shift from the  $500\text{-}700$  to the  $850\text{-}1000\text{ cm}^{-1}$  region. The distortions in the niobium oxide compounds are caused by the tilting of two adjacent  $\text{NbO}_6$  octahedra and the off-center displacement of the Nb atom. Both slightly distorted and highly distorted octahedral  $\text{NbO}_6$  sites coexist in  $\text{H-Nb}_2\text{O}_5$  and the  $\text{KCa}_2\text{Na}_{n-3}\text{Nb}_n\text{O}_{3n+1}$ ,  $n=3$  to 5, layered compounds. Most of the niobium oxide compounds possess an octahedrally-coordinated  $\text{NbO}_6$  structure with different extents of distortion, and only a few rare earth  $\text{ANbO}_4$  ( $\text{A} = \text{Y}$ ,  $\text{Yb}$ ,  $\text{Sm}$ , and  $\text{La}$ ) compounds possess a tetrahedrally-coordinated  $\text{NbO}_4$  structure. For the tetrahedral  $\text{NbO}_4$  structure of  $\text{YbNbO}_4$  the major Raman frequency appears at  $\sim 813\text{ cm}^{-1}$ . In situ Raman studies assisted in the discrimination between bulk and surface functionalities in the niobium oxide reference compounds possessing high surface areas ( $\text{Nb}_2\text{O}_5\text{.nH}_2\text{O}$  and  $\text{HCa}_2\text{Nb}_3\text{O}_{10}$ ).

## 2.1. INTRODUCTION

Niobium oxide,  $\text{Nb}_2\text{O}_5$ , has been reported to exist in different polymorphic forms [42-45], and the phase transformations of niobium oxide strongly depend on the heat treatment. Upon heat treatments between 300-1000°C, amorphous niobium oxide increases in degree of crystallinity and forms more stable  $\text{Nb}_2\text{O}_5$  phases. Amorphous niobium oxide,  $\text{Nb}_2\text{O}_5 \cdot n\text{H}_2\text{O}$ , possesses distorted  $\text{NbO}_6$  octahedra,  $\text{NbO}_7$  pentahedra, and  $\text{NbO}_8$  hexahedra as structural units [46]. The TT- $\text{Nb}_2\text{O}_5$  phase, 300-500°C, possesses a pseudohexagonal unit cell, with a constitutional defect of an oxygen atom per unit cell, and forms tetragonal and pentagonal bipyramids [42] with 6 or 7 oxygen atoms coordinated to the Nb atom. The T- $\text{Nb}_2\text{O}_5$  phase, 700-800°C, possesses an orthorhombic unit cell, and forms distorted tetragonal or pentagonal bipyramids with 6 or 7 oxygen atoms coordinated to the Nb atom. One out of seventeen Nb atoms occupies the interstitial sites between two unit cells and is surrounded by 8 oxygen atoms [47]. These polyhedra are joined by corner or edge-sharing in the ab-plane and by corner-sharing along the c-axis. The H- $\text{Nb}_2\text{O}_5$  phase, above 1000°C, is the most thermodynamically stable form of the  $\text{Nb}_2\text{O}_5$  polymorphs. The structure of H- $\text{Nb}_2\text{O}_5$  contains two different sizes of  $\text{ReO}_3$ -type blocks:

3x4 and 3x5 blocks composed of corner or edge-shared NbO<sub>6</sub> octahedra. Only 1/28 Nb sites are tetrahedra [48]. Thus, the coordination number of the Nb atom decreases from 8 oxygen atoms to 6 oxygen atoms during the heat treatments.

The niobium oxide structure can be modified by cation substitution into the crystalline lattice to form different kinds of niobium oxide compounds: perovskite structure [49-51], layered structure [52-54], and Nb<sub>6</sub>O<sub>19-8</sub> clusters [55-57]. These modifications enhance the physical and chemical properties of niobium oxide. The perovskite niobium oxide compounds are used in various fields of materials science such as glasses [58,59] and ceramics [60,61], and the layered niobium oxide compounds undergo intercalation reactions with organic amines [4]. Nb<sub>2</sub>O<sub>5</sub> also reacts with oxalic acid to form niobium oxalate complexes which can exist in aqueous solution [62]. The above niobium oxide compounds possess an octahedrally-coordinated NbO<sub>6</sub> structure with different extents of distortion. The tetrahedrally-coordinated NbO<sub>4</sub> structure is not a typical structure for niobium oxide because the Nb<sup>5+</sup> atom is too large to fit into an oxygen-anion tetrahedron. Only a few rare earth ANbO<sub>4</sub> (A= Y, Yb, Sm, and La) compounds have been found to possess tetrahedral coordination [14,63,64].

Raman spectroscopy is very sensitive to the structure

and bond order of metal oxides, especially in the region of metal-oxygen stretching modes, because many of the Raman frequencies depend on the bond order in the structure [44]. A higher metal-oxygen bond order, corresponding to a shorter bond distance, shifts the Raman band to higher wavenumbers. In this study, various niobium oxide reference compounds are characterized by Raman spectroscopy and divided into two main categories: the octahedrally-coordinated and the tetrahedrally-coordinated niobium oxide compounds. The octahedrally-coordinated niobium oxide compounds consist of slightly distorted niobium oxides, highly distorted niobium oxide structures, layered structures, and pure niobium oxide. Tetrahedrally-coordinated  $ANbO_4$  ( $A = Y, Yb, Sm$ , and  $La$ ) compounds have been reported by Blasse [63], Rooksby et al. [64], and Yoshida et al. [14] to possess a slightly distorted scheelite structure with  $NbO_4$  units, and only  $YNbO_4$  has previously been characterized by Raman spectroscopy. In the present study  $YbNbO_4$  was used as the niobium oxide reference compound containing a tetrahedrally-coordinated  $NbO_4$  structure. The niobium oxide structure-Raman spectroscopy relationships developed for the reference compounds will subsequently be used to assign the molecular structures of the surface niobium oxide phases in supported niobium oxide catalysts.

## 2.2. EXPERIMENTAL

### 2.2.1. Materials

Hydrated niobium pentoxide,  $\text{Nb}_2\text{O}_5 \cdot n\text{H}_2\text{O}$ , was provided by Niobium Products Company (Pittsburgh, PA) with a minimum purity of 99.0%. The major impurities after calcining at 800°C are 0.02% Ta and 0.01% Cl. Niobium oxalate was also provided by Niobium Products Company with the chemical analysis of 20.5%  $\text{Nb}_2\text{O}_5$ , 790 ppm Fe, 680 ppm Si, and 0.1% insoluble solid.

The  $\text{BNbO}_3$  (B=Li, Na, and K) compounds were obtained from Johnson Matthey Chemicals Company with a purity greater than 99.99%. Potassium niobate,  $\text{K}_8\text{Nb}_6\text{O}_{19}$ , was obtained from Pfaltz and Bauer, Inc.. The  $\text{KCa}_2\text{Na}_{n-3}\text{Nb}_n\text{O}_{3n+1}$  ( $n=3, 4$ , and  $5$ ) compounds were provided by A. Jacobson of Exxon Research and Engineering Company, and the detailed synthesis procedures of these layered oxides were described by Jacobson et al. [54]. The hydrated  $\text{HCa}_2\text{Nb}_3\text{O}_{10}$  layered oxide was also provided by A. Jacobson. The dehydrated  $\text{HCa}_2\text{Nb}_3\text{O}_{10}$  layered oxide was prepared by drying the hydrated  $\text{HCa}_2\text{Nb}_3\text{O}_{10}$  layered oxide at 120°C for 16 hours.

### 2.2.2. BET Surface Area Measurement

The BET surface areas of bulk niobium oxide samples were obtained with a Quantsorb surface area analyzer

(Quantachrome corporation, Model OS-9) using a 3:7 ratio of N<sub>2</sub>/He mixture as a probe gas. Typically, 0.200-0.300 gram of sample was used for the measurement and the sample was outgassed at 250°C prior to N<sub>2</sub> adsorption.

### 2.2.3. Raman Spectroscopy

Raman spectra were obtained with a Spex triplemate spectrometer (Model 1877) couple to an EG&G intensified photodiode array detector which were cooled thermoelectrically to -35°C, and interfaced with an EG&G OMA III Optical Multichannel Analyzer (Model 1463). The samples were excited by the 514.5 nm line of the Ar<sup>+</sup> laser with a 10 mw power. The laser beam was focused on the sample illuminator, where the sample typically spins at about 2000 rpm to avoid local heating, and was reflected into the spectrometer by a 90° angle with the incident light. The scattered Raman light was collected by the spectrometer at room temperature, and analyzed with an OMA III software package. The overall spectral resolution of the spectra was determined to be about 2 cm<sup>-1</sup>. The detailed schematic diagram of the Raman spectrometer is described elsewhere [65].

An in situ quartz cell was designed in order to investigate the Raman changes upon dehydration of the

niobium oxide samples above room temperature. The sample holder was made from a quartz glass, and the sample disc was held by a stationary slot in the sample holder. The sample was heated by a cylindrical heating coil surrounding the quartz cell, and the temperature was measured with an internal thermocouple. The cell was capable of operating up to 600°C. Reaction-gas mixtures were introduced into the cell from a manifold at a rate of 50 to 500 cm<sup>3</sup>/min with a delivery pressure of 150-200 torr.

## 2.3. RESULTS

### 2.3.1. Octahedrally-Coordinated Niobium Oxide Compounds

#### Slightly distorted niobium oxides

The Raman spectra of the BNbO<sub>3</sub> (B=Li, Na, and K) reference compounds are shown in Fig. 2.1. The major Raman band of these reference compounds appears in the 620-630 cm<sup>-1</sup> region and a shoulder appears in the 520-580 cm<sup>-1</sup> region. The LiNbO<sub>3</sub> compound possesses additional Raman bands at ~870, ~430, ~375, and ~325 cm<sup>-1</sup>. However, the intensity of these Raman bands is significantly decreased for the NaNbO<sub>3</sub> compound and are essentially absent for the KNbO<sub>3</sub> compound. For the KNbO<sub>3</sub> compound, an additional Raman band is observed at ~840 cm<sup>-1</sup>. Multiple and strong

Raman bands in the low wavenumber region, between 100-300  $\text{cm}^{-1}$ , are also observed for these reference compounds.

#### Highly distorted niobium oxides

The Raman spectra of the  $\text{K}_8\text{Nb}_6\text{O}_{19}$ ,  $\text{AlNbO}_4$ , and  $\text{Nb}(\text{HC}_2\text{O}_4)_5$  reference compounds are shown in Fig. 2.2. In the high wavenumber region (800-1000  $\text{cm}^{-1}$ ),  $\text{K}_8\text{Nb}_6\text{O}_{19}$  possesses Raman bands at  $\sim 900$ ,  $\sim 880$ , and  $\sim 840$   $\text{cm}^{-1}$ ,  $\text{AlNbO}_4$  possesses a Raman band at  $\sim 930$   $\text{cm}^{-1}$ , and  $\text{Nb}(\text{HC}_2\text{O}_4)_5$  possesses a Raman band at  $\sim 960$   $\text{cm}^{-1}$ . In the intermediate wavenumber region (400-800  $\text{cm}^{-1}$ ), the major Raman band of these niobium oxide compounds appears at  $\sim 540$   $\text{cm}^{-1}$  ( $\text{K}_8\text{Nb}_6\text{O}_{19}$ ),  $\sim 420$   $\text{cm}^{-1}$  ( $\text{AlNbO}_4$ ), and  $\sim 570$   $\text{cm}^{-1}$  ( $\text{Nb}(\text{HC}_2\text{O}_4)_5$ ). Additional Raman bands at  $\sim 580$ ,  $\sim 730$ , and  $\sim 780$   $\text{cm}^{-1}$  are observed for  $\text{AlNbO}_4$ . In the low wavenumber region (100-300  $\text{cm}^{-1}$ ),  $\text{K}_8\text{Nb}_6\text{O}_{19}$  and  $\text{Nb}(\text{HC}_2\text{O}_4)_5$  have Raman bands at  $\sim 230$  and  $\sim 290$   $\text{cm}^{-1}$  and  $\text{AlNbO}_4$  has Raman bands at  $\sim 275$ ,  $\sim 240$ ,  $\sim 210$ , and  $\sim 180$   $\text{cm}^{-1}$ .

#### Layered oxides

The Raman spectra of the  $\text{KCa}_2\text{Na}_{n-3}\text{Nb}_n\text{O}_{3n+1}$  ( $n=3$ , 4, and 5) layered oxide reference compounds are presented in Fig. 2.3. The major Raman band of these layered oxides appears at  $\sim 930$   $\text{cm}^{-1}$ . Additional Raman bands at  $\sim 760$ ,  $\sim 575$ , and

300-500  $\text{cm}^{-1}$  are also present for the  $\text{KCa}_2\text{Nb}_3\text{O}_{10}$  compound. A shift of the Raman band from  $\sim 760 \text{ cm}^{-1}$  to  $\sim 825 \text{ cm}^{-1}$  is observed upon increasing the number of layers from 3 to 4, and this band further shifts to  $\sim 840 \text{ cm}^{-1}$  as the number of layers is increased to 5. The Raman bands at  $\sim 450$  and  $\sim 375 \text{ cm}^{-1}$  disappear for the compounds possessing 3 and 4 layers.

The hydrated and dehydrated states of the  $\text{HCa}_2\text{Nb}_3\text{O}_{10}$  layered oxide were investigated by Raman spectroscopy, and the results are shown in Fig. 2.4. The  $\sim 930 \text{ cm}^{-1}$  Raman band for the  $\text{KCa}_2\text{Nb}_3\text{O}_{10}$  compound, Fig. 2.3, shifts to  $\sim 965 \text{ cm}^{-1}$  for the hydrated  $\text{HCa}_2\text{Nb}_3\text{O}_{10}$  compound. The Raman spectrum of the hydrated  $\text{HCa}_2\text{Nb}_3\text{O}_{10}$  layered oxide is very similar to the spectrum of the dehydrated  $\text{HCa}_2\text{Nb}_3\text{O}_{10}$  layered oxide. However, the strong Raman band at  $\sim 965 \text{ cm}^{-1}$  significantly broadens, the weak Raman band at  $\sim 840 \text{ cm}^{-1}$  disappears, and the Raman band at  $\sim 320 \text{ cm}^{-1}$  forms doublets upon dehydration of the  $\text{HCa}_2\text{Nb}_3\text{O}_{10}$  layered oxide. The dehydrated state of the  $\text{HCa}_2\text{Nb}_3\text{O}_{10}$  layered oxide was further investigated by in situ Raman spectroscopy under flowing dry air, see Fig. 2.5, and reveals that the broad Raman band at  $\sim 965 \text{ cm}^{-1}$  is actually composed of two bands at  $\sim 980$  and  $\sim 960 \text{ cm}^{-1}$  upon complete dehydration.

### Bulk niobium oxide (Nb<sub>2</sub>O<sub>5</sub>)

The surface area of bulk niobium oxide after different thermal treatments is presented in Fig. 2.6. The results show that the niobium oxide surface area dramatically decreases with increasing calcination temperature due to the formation of larger Nb<sub>2</sub>O<sub>5</sub> crystallites. The Raman spectra of bulk niobium oxide after thermal treatments from 120°C to 1000°C are shown in Fig. 2.7. For Nb<sub>2</sub>O<sub>5</sub>.nH<sub>2</sub>O dried at 120°C for 16 hours, a broad and weak Raman band is observed at ~900 cm<sup>-1</sup> as well as a broad and strong Raman band at ~650 cm<sup>-1</sup>. Upon heating the niobium oxide sample for 2 hours at 500°C in air, the broad Raman band at ~900 cm<sup>-1</sup> becomes even weaker and the strong Raman band at ~650 cm<sup>-1</sup> shifts to ~690 cm<sup>-1</sup>. The Nb<sub>2</sub>O<sub>5</sub> (500°C) Raman bands in the low wavenumber region (200-300 cm<sup>-1</sup>) become more intense and better resolved than those of Nb<sub>2</sub>O<sub>5</sub>.nH<sub>2</sub>O (120°C) in this region. The Raman features of the Nb<sub>2</sub>O<sub>5</sub> sample treated at 800°C for 2 hours are similar to those of the Nb<sub>2</sub>O<sub>5</sub> (500°C) sample. However, additional weak Raman bands in the 400-500 cm<sup>-1</sup> region are observed in the Nb<sub>2</sub>O<sub>5</sub> (800°C) sample. For the Nb<sub>2</sub>O<sub>5</sub> sample treated at 1000°C for 2 hours, the Raman results indicate that a phase transformation of the Nb<sub>2</sub>O<sub>5</sub> sample has occurred and additional Raman bands are observed in the spectrum

(particularly in the high wavenumber region between 900-1000  $\text{cm}^{-1}$ ).

In situ Raman studies of the high surface area  $\text{Nb}_2\text{O}_5 \cdot n\text{H}_2\text{O}$  ( $120^\circ\text{C}$ ) sample were also undertaken in order to discriminate between bulk and surface functionalities [65], and the spectra in the  $700$ - $1100$   $\text{cm}^{-1}$  region are presented in Fig. 2.8. For the untreated  $\text{Nb}_2\text{O}_5 \cdot n\text{H}_2\text{O}$  ( $120^\circ\text{C}$ ), a broad Raman band is observed in the  $800$ - $900$   $\text{cm}^{-1}$  region. For the  $\text{Nb}_2\text{O}_5 \cdot n\text{H}_2\text{O}$  ( $120^\circ\text{C}$ ) treated at  $200^\circ\text{C}$  for 1 hour, the Raman features remain broad and are somewhat similar to the untreated  $\text{Nb}_2\text{O}_5 \cdot n\text{H}_2\text{O}$  ( $120^\circ\text{C}$ ). Two new Raman bands, however, are observed at  $\sim 930$  and  $\sim 980$   $\text{cm}^{-1}$  after thermal treatment at  $400^\circ\text{C}$  for 1 hour. These two Raman bands are still present after cooling to  $50^\circ\text{C}$ . However, these two Raman bands disappear after the sample is rehydrated by exposure to ambient water vapor overnight. The major niobium oxide Raman band remained at  $\sim 650$   $\text{cm}^{-1}$  during this thermal treatment and indicates that the  $\text{Nb}_2\text{O}_5 \cdot n\text{H}_2\text{O}$  sample did not undergo phase transformations. In situ Raman studies of  $\text{Nb}_2\text{O}_5$  ( $500^\circ\text{C}$ ) are also presented in Fig. 2.9, but no significant changes in the Raman features are observed during the thermal treatment.

### 2.3.2. Tetrahedrally-Coordinated Niobium Oxide Compound

The Raman spectrum of  $\text{YbNbO}_4$  is shown in Fig. 2.10. Raman studies reveal that  $\text{YbNbO}_4$  possessing Raman bands at  $\sim 813$ ,  $\sim 331$ ,  $\sim 717$ , and  $\sim 435 \text{ cm}^{-1}$ . Raman bands at  $\sim 992$ ,  $\sim 678$ ,  $\sim 630$ , and  $\sim 237 \text{ cm}^{-1}$  indicate that  $\text{YbNbO}_4$  also possesses a structure similar to  $\text{H-Nb}_2\text{O}_5$  (see Fig. 2.7). The Raman bands below  $200 \text{ cm}^{-1}$  are due to lattice vibrations.

## 2.4. DISCUSSIONS

Raman spectroscopy has been found to be very useful for studying the structure of different niobium oxide compounds because the Raman band is sensitive to the niobium oxide symmetry and bond order [44]. A higher niobium-oxygen bond order, corresponding to a shorter bond distance, shifts the Raman band to higher wavenumbers. Every niobium oxide compound in this study has a unique Raman spectrum which is related to the symmetry and bond order of its structure. The Raman band assignments are based on the corresponding Nb-O bond order and known structure. The tetrahedral  $\text{NbO}_4^{-3}$  species does not exist in aqueous solutions because of the high electronegativity and small radius of the oxygen atom [66]. In addition, the

tetrahedral  $\text{NbO}_4$  structure is rarely found in niobium oxide compounds because the  $\text{Nb}^{5+}$  atom is usually too large to fit into an oxygen-anion tetrahedron [63]. The niobium oxide compounds containing the exceptional  $\text{NbO}_4$  tetrahedra possess a slightly distorted scheelite structure [63]. It appears that the  $\text{Nb}^{5+}$  atom is too small to form a regular octahedral  $\text{NbO}_6$  structure [67] and the oxygens in a regular octahedral  $\text{NbO}_6$  structure do not obey Pauling's electrostatic valence rule [68]. Consequently, the niobium oxide compounds predominantly contain  $\text{NbO}_6$  octahedra with different extents of distortion due to corner or edge-shared  $\text{NbO}_6$  polyhedra.

The  $\text{BNbO}_3$  ( $\text{B} = \text{Na}$  and  $\text{K}$ ) compounds belong to the perovskite structure family. The Nb atom lies at each corner of a cubic cell and the oxygen atom lies at the center of each cubic edge. Each Nb atom is surrounded by six oxygen atoms to form a  $\text{NbO}_6$  octahedra and two adjacent  $\text{NbO}_6$  octahedra are connected by a shared corner. The cation ( $\text{Na}$  or  $\text{K}$ ) lies in the center of the cubic cell. In an ideal perovskite structure all  $\text{NbO}_6$  octahedra would be perfectly regular with six equal Nb-O bond distances, parallel or antiparallel to one another. However, such an ideal perovskite structure does not exist in the  $\text{BNbO}_3$  ( $\text{B} = \text{Na}$  and  $\text{K}$ ) compounds because of the tilting of the  $\text{NbO}_6$

octahedra as well as the displacements of the Nb atoms from the center which is induced by the cation (Na or K) and the unbalanced interatomic forces present in the perovskite structures [49].

The perovskite  $BNbO_3$  (B= Na and K) compounds possess a major Raman band at  $620-630\text{ cm}^{-1}$  and a shoulder in the  $520-580\text{ cm}^{-1}$  region (Fig. 2.1). These bands correspond to slightly different Nb-O bond distances and are assigned to the symmetric stretching mode of the  $NbO_6$  octahedra of these perovskite compounds. The  $LiNbO_3$  compound contains a hexagonal close packing structure in which the regular  $NbO_6$  octahedra connected by shared corners with a  $30^\circ$  tilting angle between two adjacent  $NbO_6$  octahedra and a  $0.26\text{ \AA}$  off-center displacement of the Nb atom [49]. The  $LiNbO_3$  compound possesses similar Raman features as the perovskite  $BNbO_3$  (B= Na and K) compounds in the  $500-700\text{ cm}^{-1}$  region. For the  $LiNbO_3$  (hexagonal close packing) Raman spectrum, the additional Raman band at  $\sim 870\text{ cm}^{-1}$  is assigned to the symmetric stretching mode of the Nb-O-Nb linkage, and the associated bending modes of the Nb-O-Nb linkage appear at  $\sim 430$  and  $\sim 375\text{ cm}^{-1}$ . For the  $NaNbO_3$  (perovskite) compound, however, the intensity of the Raman bands at  $\sim 870$ ,  $\sim 430$ , and  $\sim 375\text{ cm}^{-1}$  significantly decrease. This is probably due to the lower tilt angle,  $18^\circ$ , between the adjacent  $NbO_6$

octahedra [50]. Furthermore, the disappearance of these Raman bands in the  $\text{KNbO}_3$  (perovskite) Raman spectrum suggests that no tilting occurs between the adjacent  $\text{NbO}_6$  octahedra in this structure and is consistent with Katz et al.'s results [51]. A new Raman band is observed at  $\sim 840 \text{ cm}^{-1}$  for  $\text{KNbO}_3$  which is characteristic of the symmetric stretching mode of the Nb-O-Nb co-linear bond present in the structure. The distortions of the  $\text{BNbO}_3$  (B=Li, Na, and K) compounds depend on the size of the A cations. For the larger size cation such as K the cation is coordinated to 12 oxygens, and free space is unavailable for the  $\text{NbO}_6$  octahedra to tilt relative to one another. Consequently, the  $\text{NbO}_6$  octahedra maintain the parallel orientation. However, the smaller size Li cation only has 6-coordinated oxygens and forms an octahedral  $\text{LiO}_6$  structure. The orientations of the  $\text{NbO}_6$  and  $\text{LiO}_6$  octahedra induce the tilts between the two adjacent  $\text{NbO}_6$  octahedra [49].

It is known that niobium oxide can exist as  $\text{Nb}_6\text{O}_{19}^{-8}$  clusters in alkaline aqueous solutions and Nb complexes in acidic aqueous solutions as well as precipitates from such solutions. The  $\text{Nb}_6\text{O}_{19}^{-8}$  unit is a well-characterized structure which consists of three different types of Nb-O bonds at each niobium center (see Fig. 2.2): a short Nb=O

terminal double bond, a longer Nb=O-Nb bridging bond, and a very long and weak Nb---O bond connected to the center of the cage-like octahedral structure [55-57]. From the known structure of  $K_8Nb_6O_{19}$ , the main frequencies of the  $K_8Nb_6O_{19}$  Raman spectrum in Fig. 2.2 can be assigned: Nb=O terminal stretching mode ( $\sim 900$ ,  $\sim 880$ , and  $\sim 840$   $\text{cm}^{-1}$ ), edge-shared octahedral  $NbO_6$  stretching mode ( $\sim 730$ ,  $\sim 540$ , and  $\sim 460$   $\text{cm}^{-1}$ ), Nb---O stretching mode ( $\sim 290$   $\text{cm}^{-1}$ ), and Nb=O-Nb bending mode ( $\sim 230$   $\text{cm}^{-1}$ ). The multiple terminal stretching modes present in the high wavenumber region are due to unequal Nb=O bond lengths that are present in the  $K_8Nb_6O_{19}$  structure.

The niobium oxalate structure consists of a  $[NbO(OH)(C_2O_4)_2H_2O]$  or  $[NbO(C_2O_4)_3]$  unit and water molecules connected by hydrogen bonds [69-72]. The presence of different niobium oxalate units is dependent on the preparation methods. The  $[NbO(OH)(C_2O_4)_2H_2O]$  unit has a pentagonal bipyramidal structure with a short Nb=O terminal double bond and a long Nb-OH<sub>2</sub> bond nearly perpendicular to the pentagonal equatorial plane which consists of two bidentate oxalato ligands and a hydroxyl group. The  $[NbO(C_2O_4)_3]$  unit also has a pentagonal bipyramidal structure with a short Nb=O terminal double bond and three bidentate oxalato ligands coordinated to the pentagonal

equatorial plane. The sharp and strong Raman band at  $\sim 960$   $\text{cm}^{-1}$  in the niobium oxalate Raman spectrum is assigned to the  $\text{Nb}=\text{O}$  terminal double bond, and the Raman band at  $\sim 290$   $\text{cm}^{-1}$  is assigned to the long and weak  $\text{Nb}-\text{OH}_2$  bond. The Raman band at  $\sim 570$   $\text{cm}^{-1}$  arises from the bidentate oxalato ligands coordinated to the niobium atom which is characteristic of the breathing mode of the  $\text{Nb}-\text{O}_2-\text{C}_2$  bridging bond.

The structure of  $\text{AlNbO}_4$  consists of highly distorted octahedral  $\text{NbO}_6$  and  $\text{AlO}_6$ , two  $\text{NbO}_6$  units and two  $\text{AlO}_6$  units, sharing edges together to form a unit cell and linked to the adjacent unit cell by sharing two corners [73]. The  $\text{Nb}-\text{O}$  bond which links to the adjacent unit cell by sharing two corners possesses the shortest bond length, and Raman band at  $\sim 930$   $\text{cm}^{-1}$  is characteristic of the symmetric stretching mode of this shortest  $\text{Nb}=\text{O}$  terminal double bond. Raman bands in the  $400-800$   $\text{cm}^{-1}$  wavenumber region are assigned to the symmetric and antisymmetric stretching mode of the  $\text{Nb}-\text{O}-\text{Nb}$  linkage, and the associated bending modes appear in the low wavenumber region ( $200-300$   $\text{cm}^{-1}$ ). Thus, the  $\text{K}_8\text{Nb}_6\text{O}_{19}$ ,  $\text{AlNbO}_4$ , and  $\text{Nb}(\text{HC}_2\text{O}_4)_5$  compounds possess a highly distorted octahedral  $\text{NbO}_6$  structure with Raman bands appearing in the high wavenumber region,  $850-1000$   $\text{cm}^{-1}$ , which are characteristic of the symmetric stretching mode

of the Nb=O terminal double bond.

The structure of the  $K[Ca_2Na_{n-3}Nb_nO_{3n+1}]$  ( $n=3,4,5$ ) layered oxides contains corner-shared  $NbO_6$  octahedra with a large cation occupying 12-coordinated sites in the center of each cube as found in the perovskite structure [53]. The thickness of each perovskite layer is determined by the number of corner-shared  $NbO_6$  octahedra connected along the direction perpendicular to the layers ( $n=3,4,5$ ). The  $KCa_2Nb_3O_{10}$  structure has been determined by Dion et al. [51] to possess two types of  $NbO_6$  sites connected to the cations (K and Ca): one is the capping sites between two adjacent layers and the other is the internal sites in the layer.

Raman studies also detect the two types of  $NbO_6$  sites present in the layered oxide compounds: a highly distorted octahedral structure, Raman band at  $\sim 930$   $cm^{-1}$ , and a slightly distorted octahedral structure, Raman band at  $\sim 580$   $cm^{-1}$ . The relative concentrations of the two  $NbO_6$  octahedra in the layered oxide compounds can be determined by taking the ratio of these Raman bands (the integrated Raman intensity of the bands at  $\sim 930$  and  $\sim 580$   $cm^{-1}$ ). The Raman  $I(\sim 930\text{ cm}^{-1})/I(\sim 580\text{ cm}^{-1})$  ratios for the different layered compounds are shown in Fig. 2.11 and decrease with increasing number of niobium oxide layers. For example,

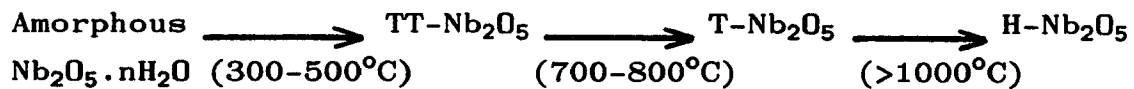
the Raman measurements of the layered oxide  $KCa_2Nb_3O_{10}$ ,  $n=3$ , has a  $I(\sim 930 \text{ cm}^{-1})/I(\sim 580 \text{ cm}^{-1})=2$  which reflects the ratio of the highly distorted octahedral sites to the slightly distorted octahedral sites. This is consistent with the layered oxide structure described by Dion et al. [52]. Upon increasing the number of the niobium oxide layers, the  $I(\sim 930 \text{ cm}^{-1})/I(\sim 580 \text{ cm}^{-1})$  ratio further decreases to 1 for  $K(Ca_2Na)Nb_4O_{13}$ ,  $n=4$ , and 0.8 for  $K(Ca_2Na_2)Nb_5O_{16}$ ,  $n=5$ , as expected from the known structures [53]. The quantitative agreement between the Raman ratios and the actual ratios in these layered structures reveals that the Raman cross sections of the slightly distorted and highly distorted  $NbO_6$  octahedra are essentially the same. The Raman  $I(\sim 800 \text{ cm}^{-1})/I(\sim 580 \text{ cm}^{-1})$  ratios in Fig. 2.11, however, do not change with increasing number of niobium oxide layers. This indicates that the Raman band at  $\sim 800 \text{ cm}^{-1}$  is associated with the slightly distorted  $NbO_6$  site band at  $\sim 580 \text{ cm}^{-1}$ , and corresponds to different Nb-O bond lengths. Increasing the number of niobium oxide layers also shifts the band from  $\sim 760$  to  $\sim 840 \text{ cm}^{-1}$  and eliminates the Raman bands at  $\sim 450$  and  $\sim 375 \text{ cm}^{-1}$ . These Raman features reflect the different extents of distortions that exist in the layered oxide compounds, and are probably due to the different sizes between the Ca and Na cations.

Many of these layered oxide compounds can also undergo an alkali ion exchange reaction with the protons present in aqueous acidic solutions due to their high ionic conductivity. The potassium cation in the layered oxide  $\text{KCa}_2\text{Nb}_3\text{O}_{10}$  exchanges with the hydrogen proton in an aqueous acidic solution to form the layered oxide  $\text{HCa}_2\text{Nb}_3\text{O}_{10}$ . The layered oxide  $\text{HCa}_2\text{Nb}_3\text{O}_{10}$  possesses a tetragonal unit cell with an interlayer separation  $14.38\text{\AA}$ , which is contracted relative to the values of  $14.73\text{\AA}$  observed for the layered oxide  $\text{KCa}_2\text{Nb}_3\text{O}_{10}$  [54]. When hydrogen replaces potassium, the interlayer hydrogen stabilizes the terminal oxygen atoms by forming a terminal -OH group interacting with a terminal oxygen in the adjacent layer. The stoichiometry corresponds to one proton for every pair of terminal oxygens from the adjacent layers. The hydrated  $\text{HCa}_2\text{Nb}_3\text{O}_{10}$  compound has a composition  $\text{HCa}_2\text{Nb}_3\text{O}_{10} \cdot 1.5\text{H}_2\text{O}$  with an interlayer separation  $16.23\text{\AA}$ . The interlayer hydrogen bonding between the two adjacent terminal oxygens creates some free volume in the  $\text{HCa}_2\text{Nb}_3\text{O}_{10}$  structure to accommodate 1.5 water molecules [54].

The Raman spectra of the hydrated and dehydrated states of the layered oxide  $\text{HCa}_2\text{Nb}_3\text{O}_{10}$  indicate that the  $\text{Nb}=\text{O}$  terminal double bond is affected by the absorbed water since the Raman band at  $\sim 965 \text{ cm}^{-1}$  significantly broadens

upon dehydration, and the Nb=O bending mode at  $\sim 320\text{ cm}^{-1}$  splits into two bands at  $\sim 325$  and  $310\text{ cm}^{-1}$  (see Fig. 2.4). The Raman band at  $\sim 840\text{ cm}^{-1}$  is assigned to the Nb=O antisymmetric stretching mode which is better resolved in the hydrated state. The *in situ* Raman studies of the layered oxide  $\text{HCa}_2\text{Nb}_3\text{O}_{10}$  further indicate that the Nb=O terminal double bond at  $\sim 965\text{ cm}^{-1}$  broadens and splits into two bands at  $\sim 960$  and  $\sim 980\text{ cm}^{-1}$  upon dehydration (see Fig. 2.5). Thus, the *in situ* Raman studies demonstrate that the water molecules in the layered oxide  $\text{HCa}_2\text{Nb}_3\text{O}_{10}$  structure associate with all the interlayer terminal oxygens to form Nb=O---H bonds. The results are in agreement with the structural studies of Jacobson et al. [54]. The *in situ* Raman studies of the layered oxide  $\text{HCa}_2\text{Nb}_3\text{O}_{10}$  also reveal that hydrogen bonding via water molecule addition results in a decrease in the Nb=O bond order and its corresponding vibrational frequency.

Bulk  $\text{Nb}_2\text{O}_5$  undergoes the following phase transformations during heat treatments [74-76]:



The amorphous  $\text{Nb}_2\text{O}_5 \cdot n\text{H}_2\text{O}$  contains slightly distorted  $\text{NbO}_6$ ,  $\text{NbO}_7$ , and  $\text{NbO}_8$  polyhedra [42]. The strong and broad Raman

band at  $\sim 650$   $\text{cm}^{-1}$  is assigned to the symmetric stretching mode of the niobia polyhedra. The broad Raman feature reflects the distribution of the  $\text{NbO}_6$ ,  $\text{NbO}_7$ , and  $\text{NbO}_8$  sites in the structure of the amorphous  $\text{Nb}_2\text{O}_5 \cdot n\text{H}_2\text{O}$ . The weak and broad Raman band at  $\sim 900$   $\text{cm}^{-1}$  is assigned to the symmetric stretching mode of the  $\text{Nb=O}$  surface sites because of the response of this band to surface dehydration during the in situ Raman studies (see following paragraph). Heat treatment at  $500^\circ\text{C}$  for 2 hours leads to crystallization into the TT- $\text{Nb}_2\text{O}_5$  phase. The corresponding shift of the Raman band from  $\sim 650$   $\text{cm}^{-1}$  to  $\sim 690$   $\text{cm}^{-1}$  is due to the increasing bond order of the niobia polyhedra, and the sharpening of Raman band at  $\sim 690$   $\text{cm}^{-1}$  is due to the more ordered structure present in the TT- $\text{Nb}_2\text{O}_5$  phase. The TT- $\text{Nb}_2\text{O}_5$  phase contains octahedral and pentagonal bipyramid structures, and the weak Raman band at  $\sim 900$   $\text{cm}^{-1}$  is due to the small concentration of  $\text{Nb=O}$  surface sites after the thermal treatment. Additional Raman bands in the low wavenumber region,  $200$ - $300$   $\text{cm}^{-1}$ , are also observed in the TT- $\text{Nb}_2\text{O}_5$  spectrum which are characteristic of the bending modes of the  $\text{Nb-O-Nb}$  linkages. Raman features of the T- $\text{Nb}_2\text{O}_5$  ( $800^\circ\text{C}$ ) phase are similar to those of the TT- $\text{Nb}_2\text{O}_5$  ( $500^\circ$ ) phase (see Fig. 2.7). This indicates that the T- $\text{Nb}_2\text{O}_5$  ( $800^\circ\text{C}$ ) phase possesses a structure similar to the TT- $\text{Nb}_2\text{O}_5$  ( $500^\circ\text{C}$ ) phase, and is consistent with Weissman et

al.'s conclusions that the TT- $\text{Nb}_2\text{O}_5$  and T- $\text{Nb}_2\text{O}_5$  phases possess nearly identical structures [45].

The H- $\text{Nb}_2\text{O}_5$  phase contains 3x4 and 3x5 blocks of corner or edge-shared octahedral  $\text{NbO}_6$  as well as one tetrahedral site per 28 Nb sites. Bhide et al. [77] have assigned the Raman band in the high wavenumber region, 900-1200  $\text{cm}^{-1}$ , to the Nb=O terminal bond. Therefore, Raman bands at  $\sim 997$  and  $\sim 900$   $\text{cm}^{-1}$  for the H- $\text{Nb}_2\text{O}_5$  phase in Fig. 2.7 are characteristic of the symmetric and antisymmetric stretching modes of the Nb=O terminal bond. The corner-shared octahedral  $\text{NbO}_6$  in the H- $\text{Nb}_2\text{O}_5$  phase also form a Nb-O-Nb co-linear bond with a corresponding Raman band appearing at  $\sim 840$   $\text{cm}^{-1}$ . Raman bands in the 500-800  $\text{cm}^{-1}$  region are characteristic of the stretching modes of the slightly distorted octahedral  $\text{NbO}_6$  structures. At the low temperature treatments ( $<800^\circ\text{C}$ ), the structure of niobium oxide possesses the slightly distorted octahedral niobia polyhedra. The structure of the niobium oxide treated at high temperatures, greater than  $1000^\circ\text{C}$ , possesses a highly distorted octahedral  $\text{NbO}_6$  structure in addition to the slightly distorted octahedral  $\text{NbO}_6$  structure. Thus, the phase transformations of niobium oxide are strongly dependent on the heat treatments and this is reflected in the Raman spectra.

In situ Raman studies of amorphous  $\text{Nb}_2\text{O}_5 \cdot \text{nH}_2\text{O}$  provide additional discrimination between bulk and surface functionalities in this high surface area oxide because moisture can only coordinate to surface functionalities [78]. During in situ Raman experiment the samples are heated to desorb the adsorbed moisture, and those Raman features that respond to the dehydration treatment are identified as surface functionalities. This process is reversed by reabsorbing water vapor on the surface functionalities. The in situ Raman studies of  $\text{Nb}_2\text{O}_5 \cdot \text{nH}_2\text{O}$  (see Fig. 2.8) demonstrate that the broad and weak Raman bands in the  $800\text{-}900 \text{ cm}^{-1}$  region shift to higher frequencies due to thermal desorption of the adsorbed moisture. After dehydration of  $\text{Nb}_2\text{O}_5 \cdot \text{nH}_2\text{O}$  at  $400^\circ\text{C}$  in air for 1 hour, two new Raman bands are observed at  $\sim 930$  and  $\sim 980 \text{ cm}^{-1}$  which are characteristic of two different  $\text{Nb}=\text{O}$  surface sites. No phase transformations occurred during this thermal treatment since the Raman features of bulk niobium oxide remained the same. Bulk  $\text{Nb}_2\text{O}_5$  ( $500^\circ\text{C}$ ) was also investigated by in situ Raman spectroscopy (see Fig. 2.9). The results indicate that the concentration of the  $\text{Nb}=\text{O}$  terminal sites of  $\text{Nb}_2\text{O}_5$  ( $500^\circ\text{C}$ ) is too small to be observed due to the much lower surface area. Thus, the amorphous  $\text{Nb}_2\text{O}_5 \cdot \text{nH}_2\text{O}$  material possesses terminal  $\text{Nb}=\text{O}$  sites on the surface, and the number of terminal  $\text{Nb}=\text{O}$  sites can

be eliminated by high temperature calcinations which dramatically decreased the surface area. The *in situ* Raman studies confirm the presence of the terminal Nb=O surface sites on amorphous  $\text{Nb}_2\text{O}_5 \cdot n\text{H}_2\text{O}$  and the assignment of the Raman band at  $\sim 900 \text{ cm}^{-1}$  to the terminal Nb=O surface sites.

The rare earth  $\text{ANbO}_4$  (A= Y, Sm, and La) compounds have been investigated by Blasse [63] and Rooksby et al. [64], and they determined that these compounds possess  $\text{NbO}_4$  tetrahedra that appear to be isomorphous with the scheelite  $\text{CaWO}_4$  structure. Blasse [63] studied the  $\text{YNbO}_4$  compound by Raman spectroscopy, and predicted the vibrational modes of a regular  $\text{NbO}_4$  tetrahedra with no interactions and distortions to occur at  $816 \text{ cm}^{-1}(\nu_1)$ ,  $650 \text{ cm}^{-1}(\nu_3)$ ,  $420 \text{ cm}^{-1}(\nu_4)$ , and  $340 \text{ cm}^{-1}(\nu_2)$ . Yoshida et al. [14] investigated the  $\text{YbNbO}_4$  compound by XANES and EXAFS techniques, and determined that the  $\text{YbNbO}_4$  compound possesses a  $\text{NbO}_4$  tetrahedra. The  $\text{ANbO}_4$  (A= Y, Yb, Sm, and La) compounds were further studied by Kinzhibalo et al. [79] and Trunov et al. [80], who determined that these compounds possess a fergusonite structure at room temperature. In the fergusonite structure, the coordination number of the Nb atom contains four oxygen atoms with distances of  $1.83\text{--}1.93\text{\AA}$  and two further oxygen atoms with distances of  $2.40\text{--}2.52\text{\AA}$  as a result of the

connection between two adjacent tetrahedra. The transition from the octahedral fergusonite to the tetrahedral scheelite depends on temperature. An increase in temperature results in bonds breaking between the niobium atom and the two further oxygen atoms, and the Nb atom coordination becomes tetrahedral.

For the  $ANbO_4$  ( $A = Y, Yb, Sm$ , and  $La$ ) compounds, the transition temperature from the octahedral fergusonite to the tetrahedral scheelite depends on the ionic radius of the rare earth metal. The rare earth metal possessing a small ionic radius has a high phase transition temperature because of the relatively short bond distances between the niobium atom and the two further oxygen atoms. Thus, the rare earth  $ANbO_4$  ( $A = Y, Yb, Sm$ , and  $La$ ) compounds possess  $NbO_6$  octahedra at room temperature, and transition from a  $NbO_6$  octahedra to a  $NbO_4$  tetrahedra occurs at high temperature. For example, the phase transitions of the  $YNbO_4$  and the  $YbNbO_4$  compounds occur above  $825^\circ C$  [80]. Blasse [63] did not address the  $YNbO_4$  structures as a function of temperature. The multiple Raman bands appearing in the  $400-800\text{ cm}^{-1}$  region for the  $YNbO_4$  compound reported by Blasse [63] are probably due to the simultaneous presence of  $NbO_4$  tetrahedra and  $NbO_6$  octahedra in the structure.

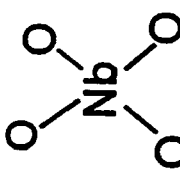
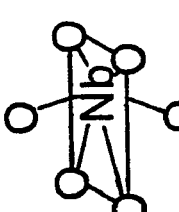
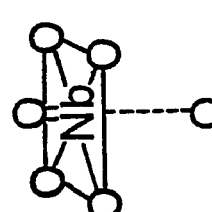
Raman studies of the annealed  $\text{YbNbO}_4$  compound reveal bands at  $\sim 813$ ,  $\sim 717$ ,  $\sim 435$ , and  $\sim 331 \text{ cm}^{-1}$ . The Raman bands appearing at  $\sim 813$  and  $\sim 331 \text{ cm}^{-1}$  are due to the Nb-O symmetric modes of the  $\text{NbO}_4$  tetrahedral structure and Raman bands appearing at  $\sim 717$  and  $\sim 435 \text{ cm}^{-1}$  are due to the Nb-O antisymmetric modes of the  $\text{NbO}_4$  tetrahedral structure. This is consistent with Blasse's results that the vibrational modes of a regular  $\text{NbO}_4$  tetrahedra, with no interactions and distortions, should occur at  $816 \text{ cm}^{-1}(\nu_1)$ ,  $650 \text{ cm}^{-1}(\nu_3)$ ,  $420 \text{ cm}^{-1}(\nu_4)$ , and  $340 \text{ cm}^{-1}(\nu_2)$  [63]. Additional weak Raman bands appearing at  $\sim 992$ ,  $\sim 678$ ,  $\sim 630$ , and  $\sim 237 \text{ cm}^{-1}$  indicate that the  $\text{YbNbO}_4$  compound also contains an impurity of  $\text{H-Nb}_2\text{O}_5$  due to a small excess of niobium oxide in the sample. Thus, tetrahedrally-coordinated niobium oxide reference compounds possess their major Raman bands in the  $790\text{--}830 \text{ cm}^{-1}$  region.

In summary, most of the niobium oxide compounds contain an octahedral  $\text{NbO}_6$  structure with different extents of distortions present in the structures. Niobium oxide compounds containing a tetrahedral  $\text{NbO}_4$  structure are extremely rare. The major Raman frequencies of the niobium oxide compounds with the corresponding structure symmetry are classified in Table 1.

## 2.5. CONCLUSIONS

The relationships between niobium oxide structures and their corresponding Raman spectra were systematically studied for various types of niobium oxide compounds. The Raman frequencies strongly depend on the bond order of the niobium oxide structure. A higher niobium-oxygen bond order, corresponding to a shorter bond distance, shifts the Raman frequency to higher wavenumbers. Most of the niobium oxide compounds possess an octahedrally-coordinated  $\text{NbO}_6$  structure, slightly or highly distorted. Only a few niobium oxide compounds (such as  $\text{YNbO}_4$ ,  $\text{YbNbO}_4$ ,  $\text{LaNbO}_4$ , and  $\text{SmNbO}_4$ ) can possess a tetrahedrally-coordinated  $\text{NbO}_4$  structure which is similar to the scheelite-like structure. For the tetrahedral  $\text{NbO}_4$  structure, the major Raman frequency appears in the  $790\text{-}830\text{ cm}^{-1}$  region. For the slightly distorted octahedral  $\text{NbO}_6$  structure, the major Raman frequencies appear in the  $500\text{-}700\text{ cm}^{-1}$  wavenumber region. For the highly distorted octahedral  $\text{NbO}_6$  structure, the Raman frequency shifts from the  $500\text{-}700$  to  $850\text{-}1000\text{ cm}^{-1}$  region. Both slightly distorted and highly distorted octahedral  $\text{NbO}_6$  sites coexist in  $\text{H-Nb}_2\text{O}_5$  and the  $\text{KCa}_2\text{Na}_{n-3}\text{Nb}_n\text{O}_{3n+1}$ ,  $n=3$  to 5, layered compounds. The distortions in the niobium oxide compounds are caused by the corner or edge-shared  $\text{NbO}_6$  polyhedra.

**Table 2.1: The relationships between niobium oxide structures and Raman frequencies**

Symmetry	Raman Bands	Compounds
	790-830 $\text{cm}^{-1}$	$\text{YNbO}_4$ $\text{YbNbO}_4$
	500-700 $\text{cm}^{-1}$	$\text{Nb}_2\text{O}_5$ (amorphous, $\text{TT}$ , $\text{T}$ , and $\text{H}$ ) $\text{LiNbO}_3$ $\text{NaNbO}_3$ $\text{KNbO}_3$ Layered oxides
	850-1000 $\text{cm}^{-1}$	$\text{Nb}_2\text{O}_5$ (amorphous and $\text{H}$ ) $\text{AlNbO}_4$ $\text{K}_8\text{Nb}_6\text{O}_{19}$ $\text{Nb}(\text{HC}_2\text{O}_4)_5$ Layered oxides

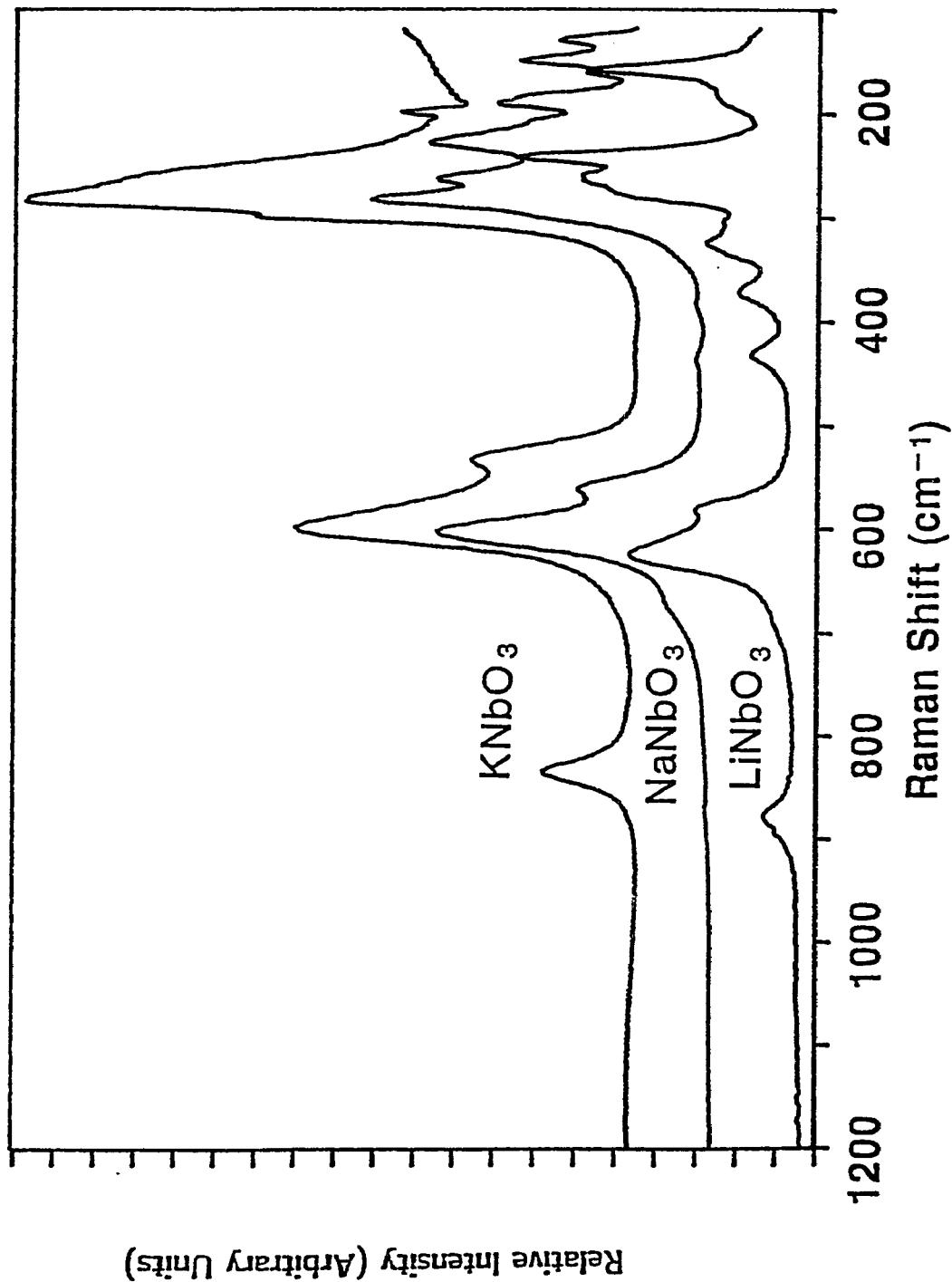


Fig. 2.1: Raman spectra of the  $\text{BNbO}_3$  ( $\text{B}=\text{Li, Na, K}$ ) perovskite compounds

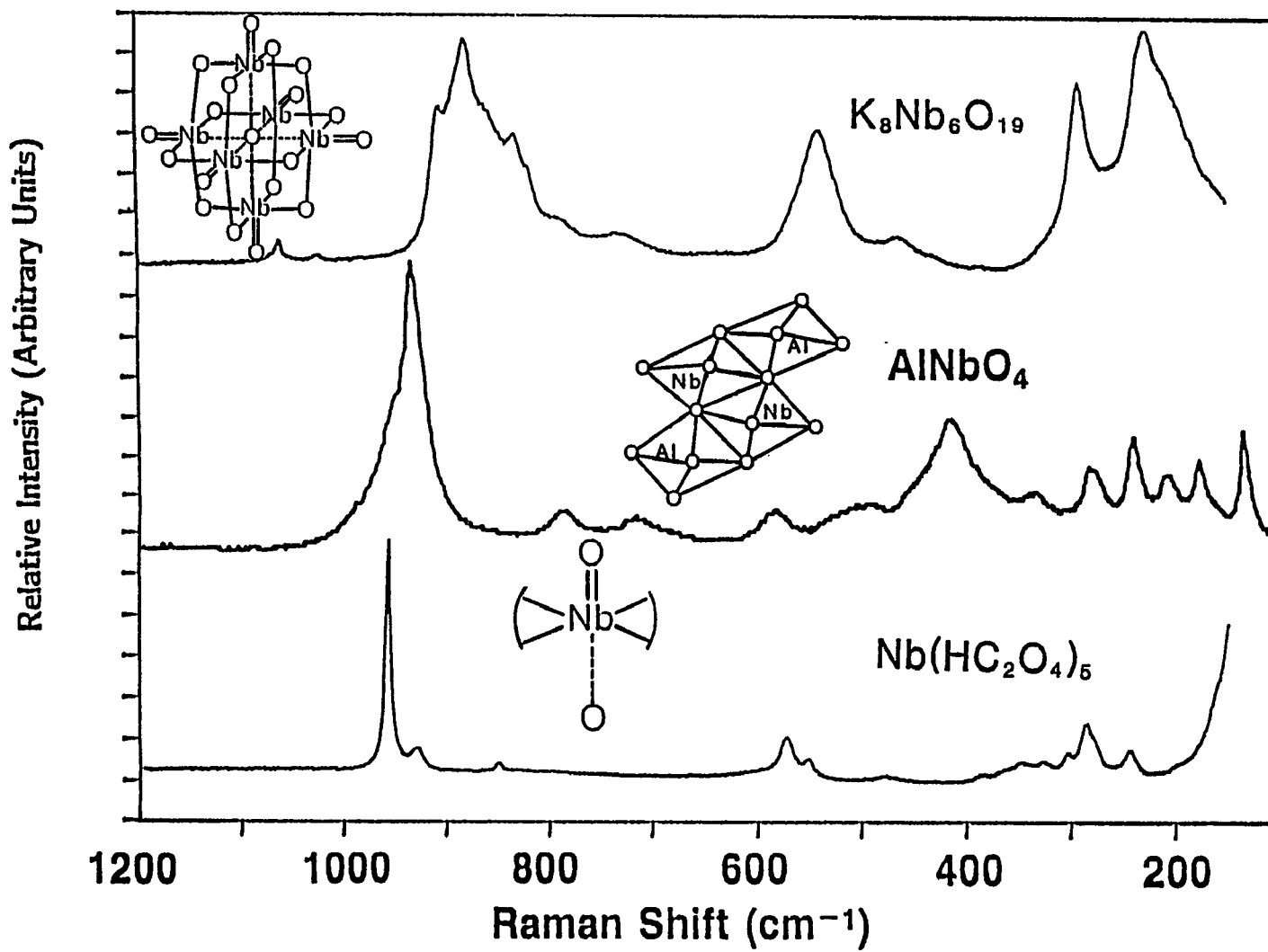


Fig. 2.2: Raman spectra of the highly distorted niobium oxide compounds

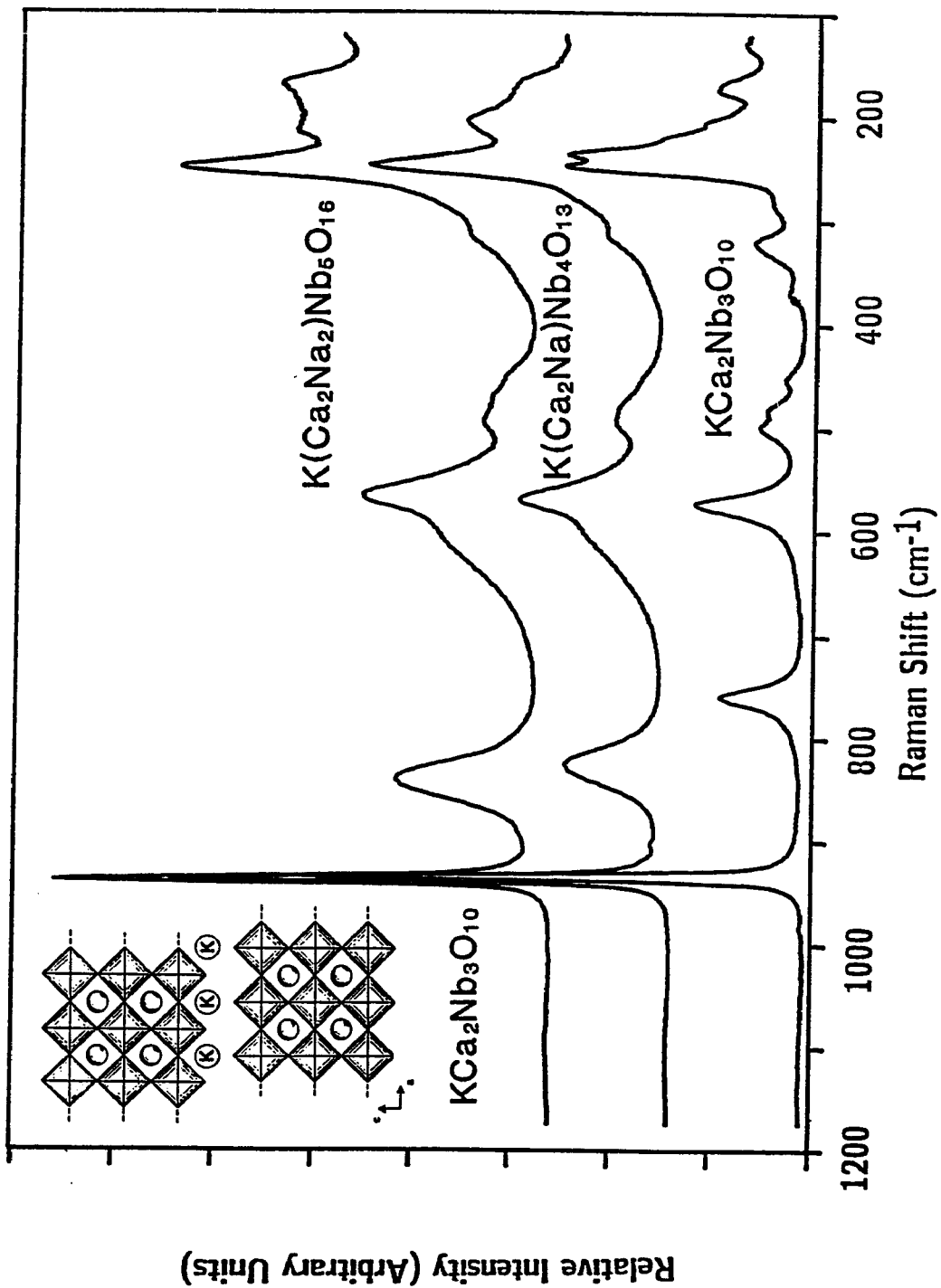


Fig. 2.3: Raman spectra of the  $KCa_2Na_{n-3}Nb_nO_{3n+1}$  ( $n=3,4,5$ ) layered oxide compounds

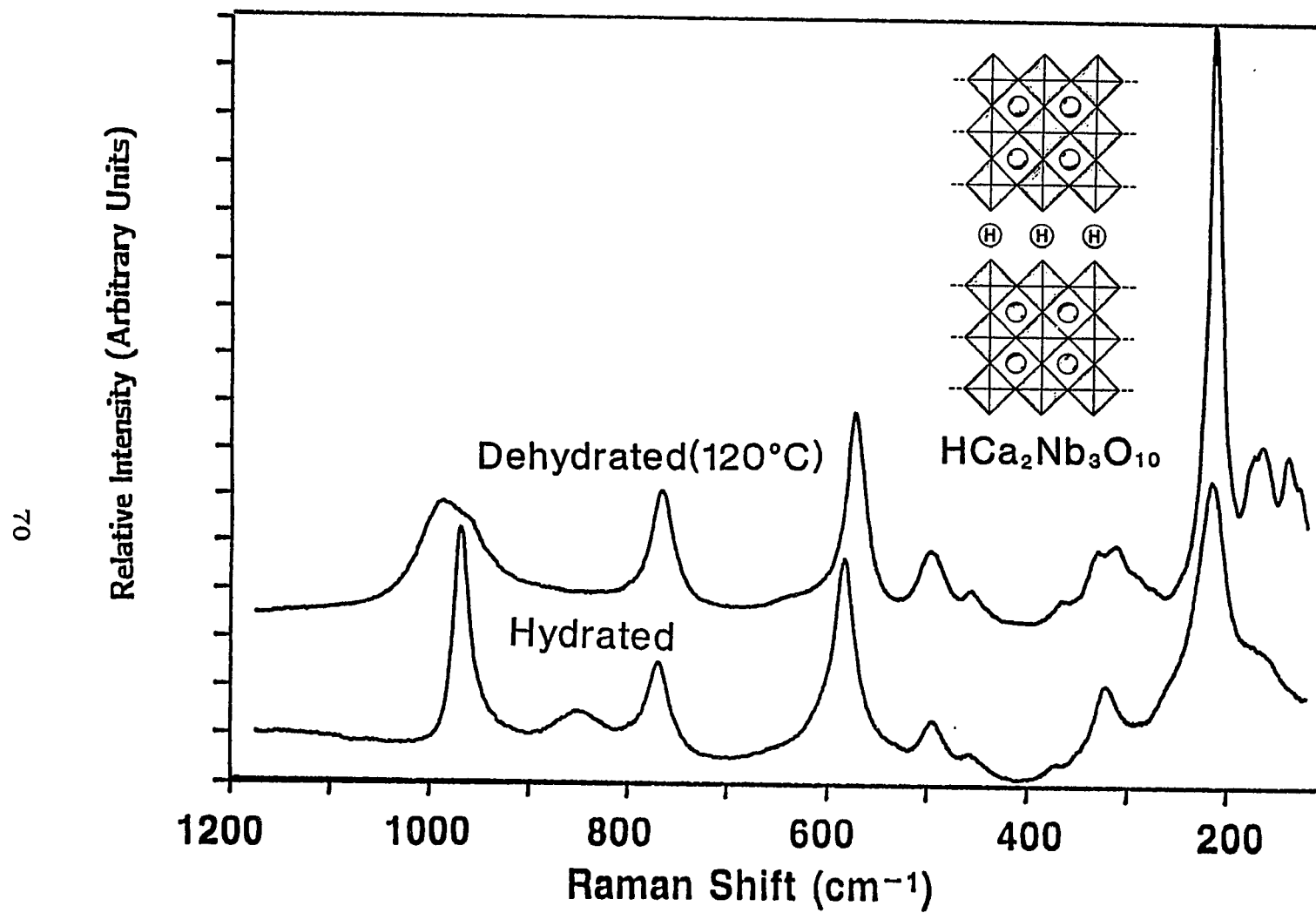


Fig. 2.4: Raman spectra of the  $\text{HCa}_2\text{Nb}_3\text{O}_{10}$  (hydrated/dehydrated) layered oxide compounds

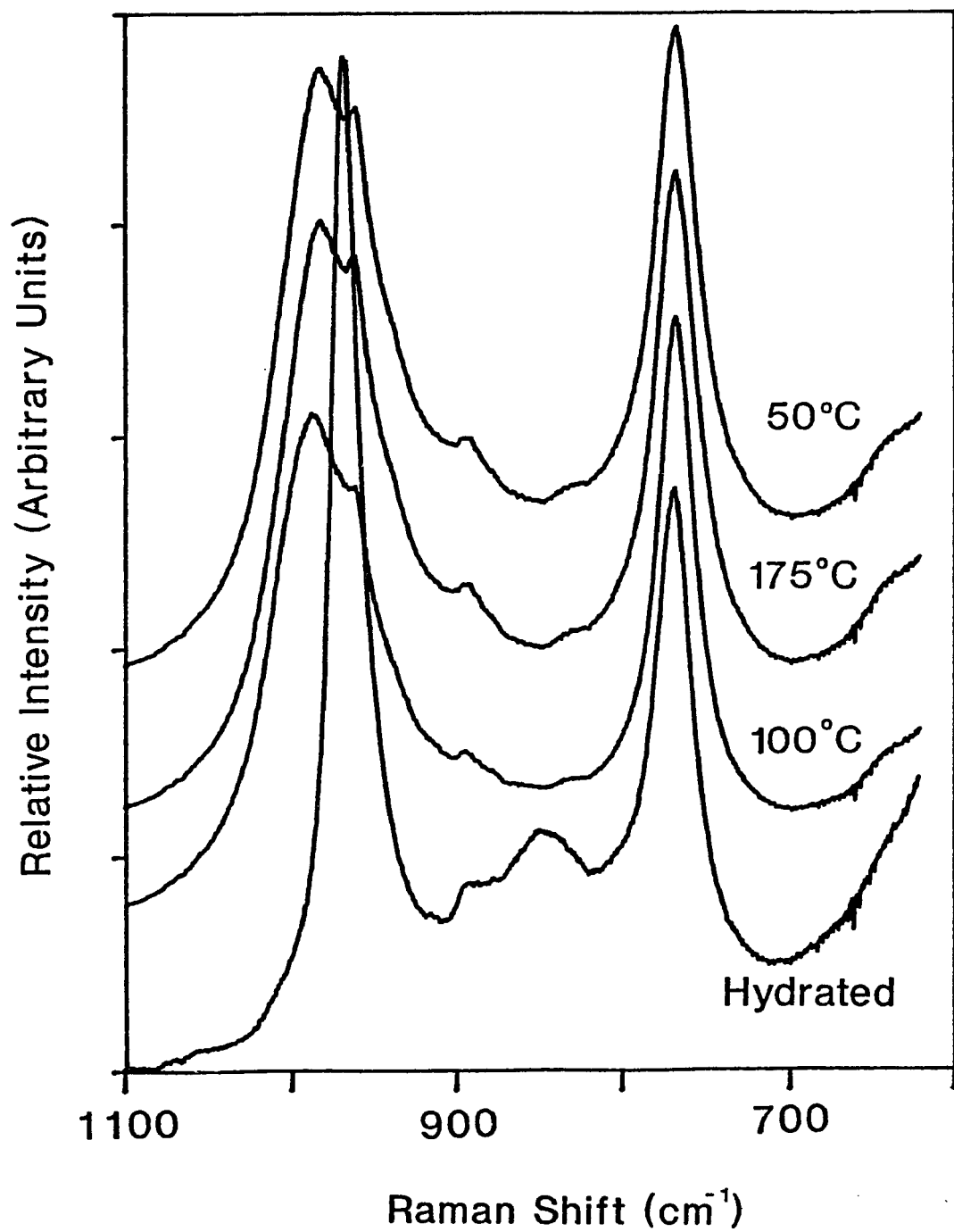


Fig. 2.5: In situ Raman spectra of the  $\text{HCa}_2\text{Nb}_3\text{O}_{10}$  layered oxide compound

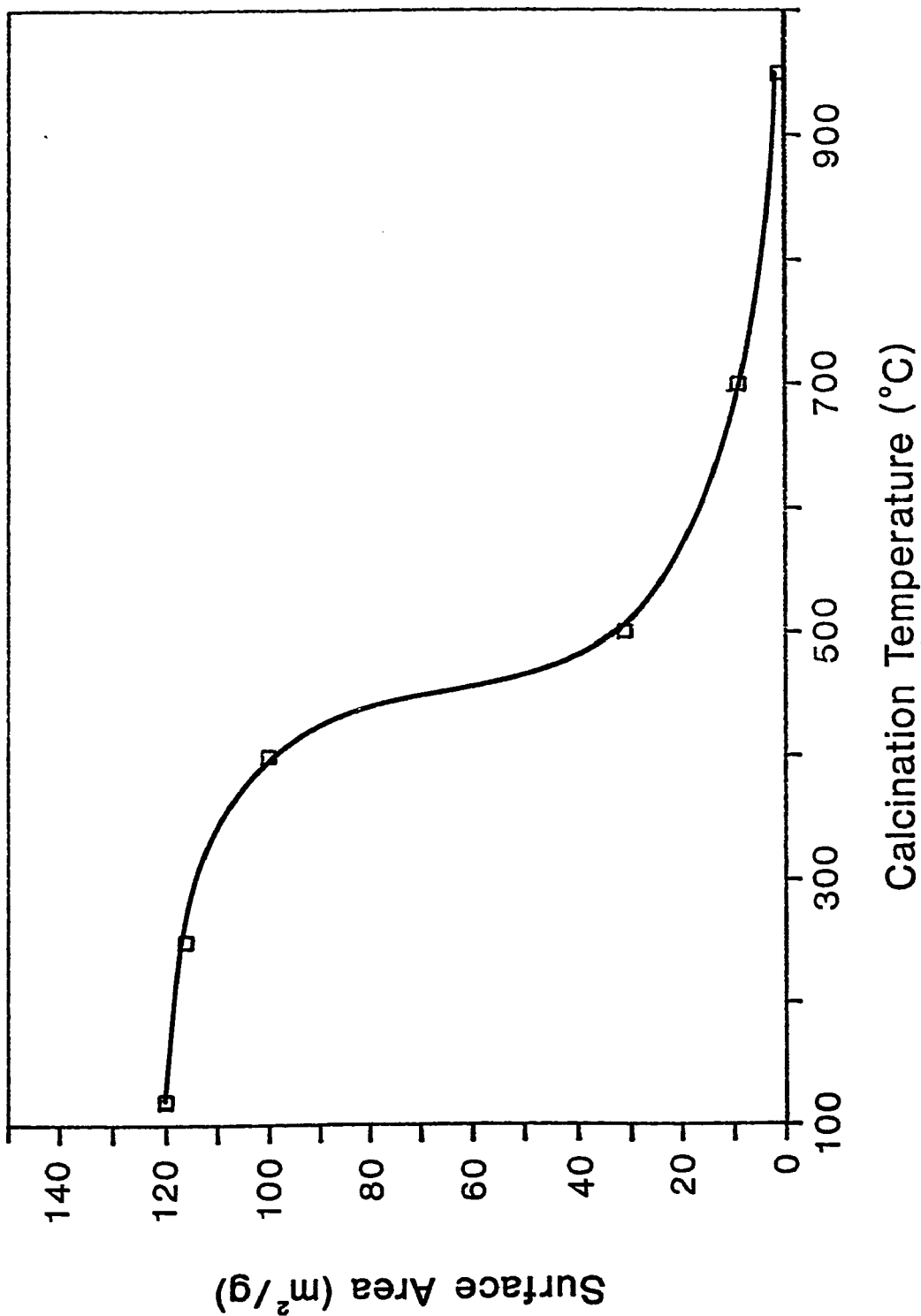


Fig. 2.6: The surface area of bulk niobium oxide as a function of calcination temperature

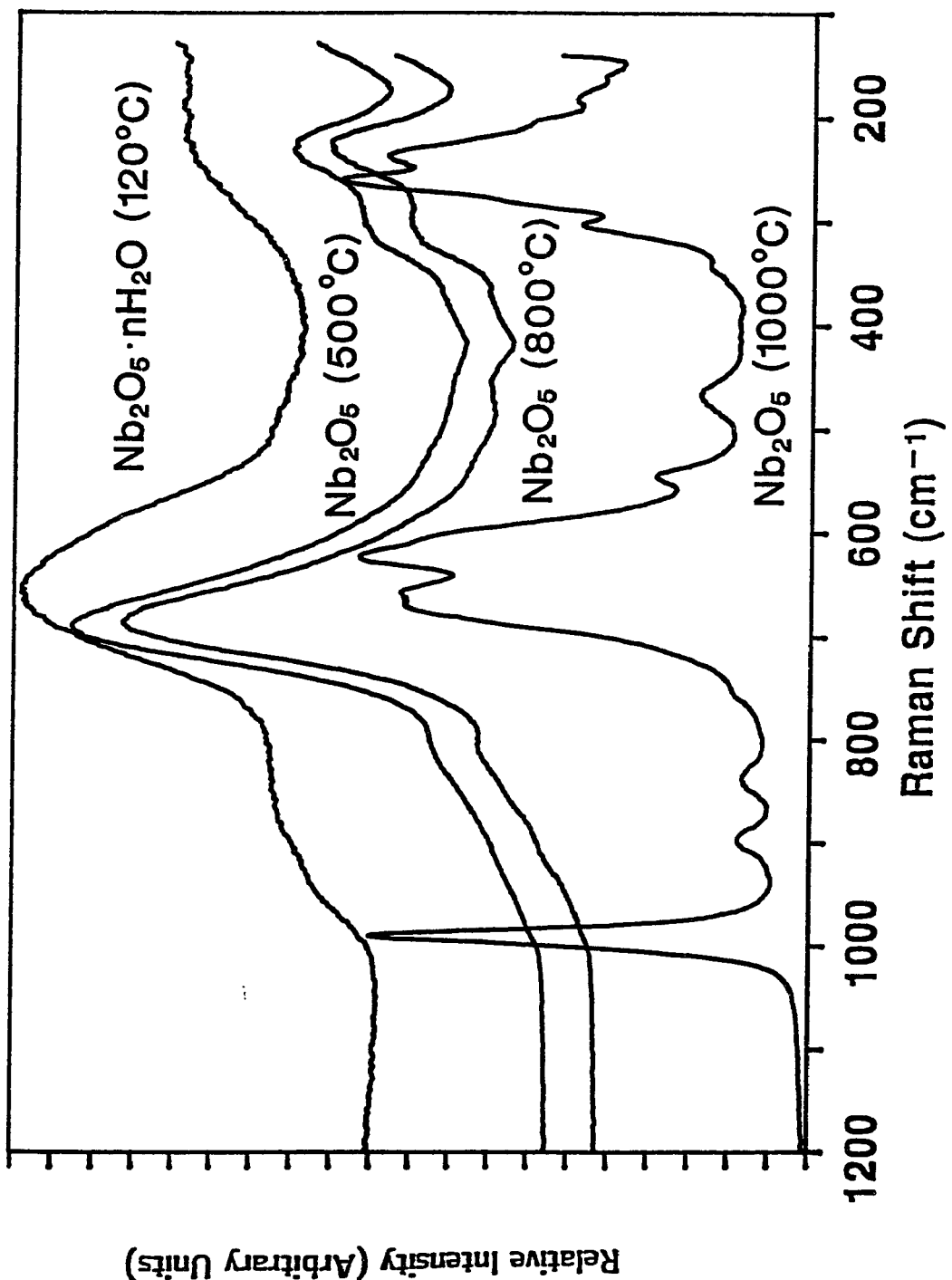


Fig. 2.7: Raman spectra of bulk niobium oxide as a function of calcination temperatures

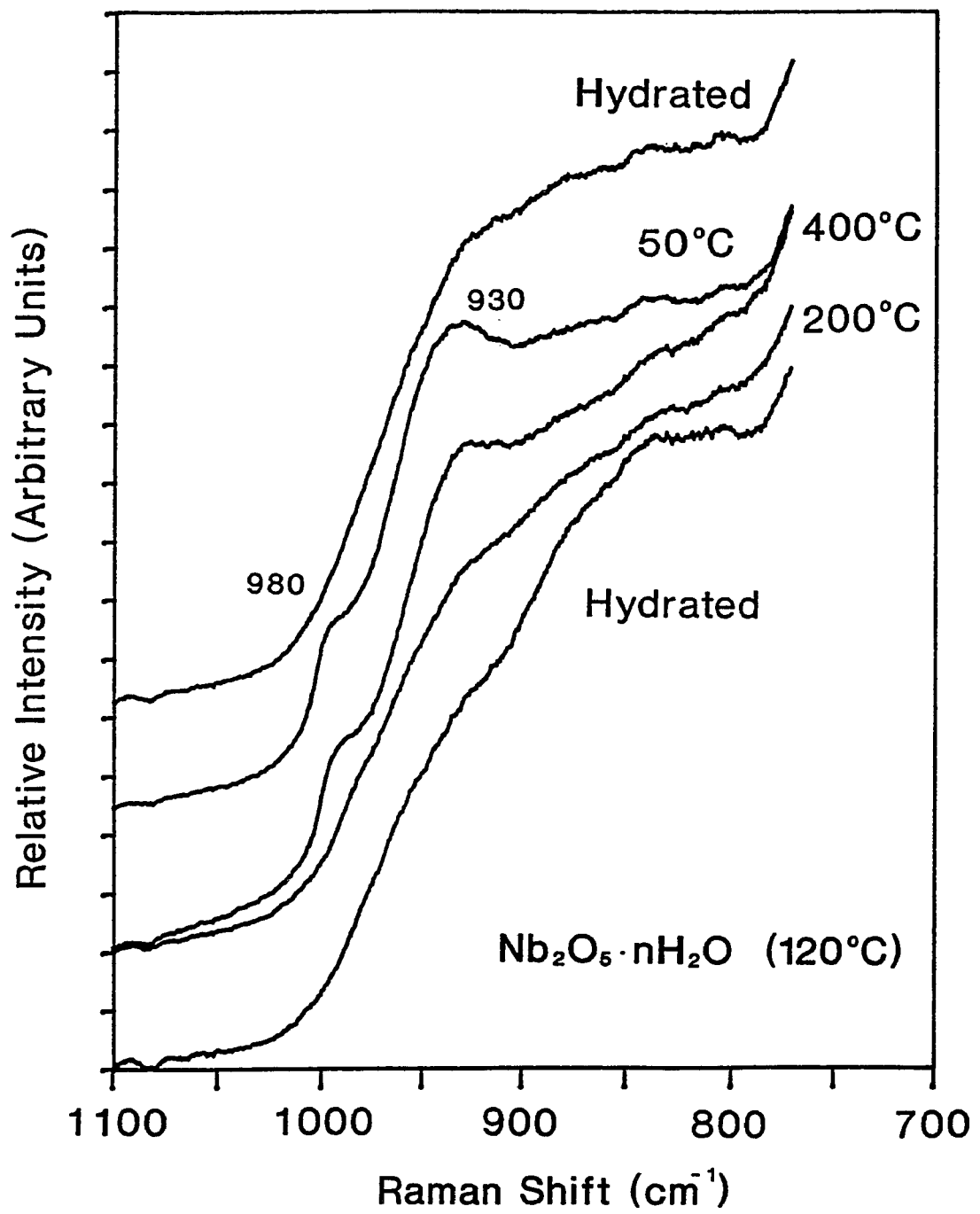


Fig. 2.8: In situ Raman Spectra of  $\text{Nb}_2\text{O}_5 \cdot \text{nH}_2\text{O}$  (120°C)

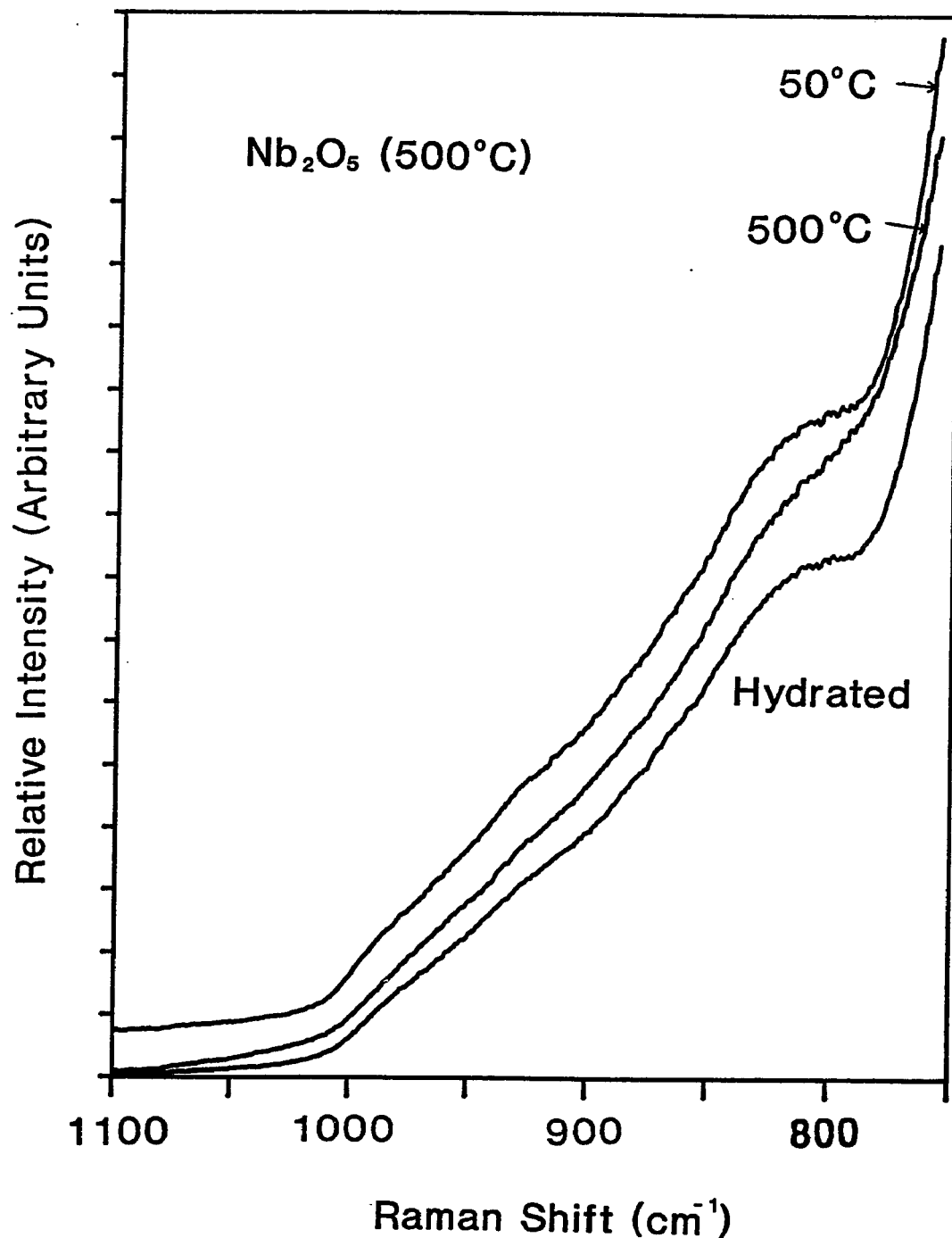


Fig. 2.9: In situ Raman spectra of  $\text{Nb}_2\text{O}_5$  (500°C)

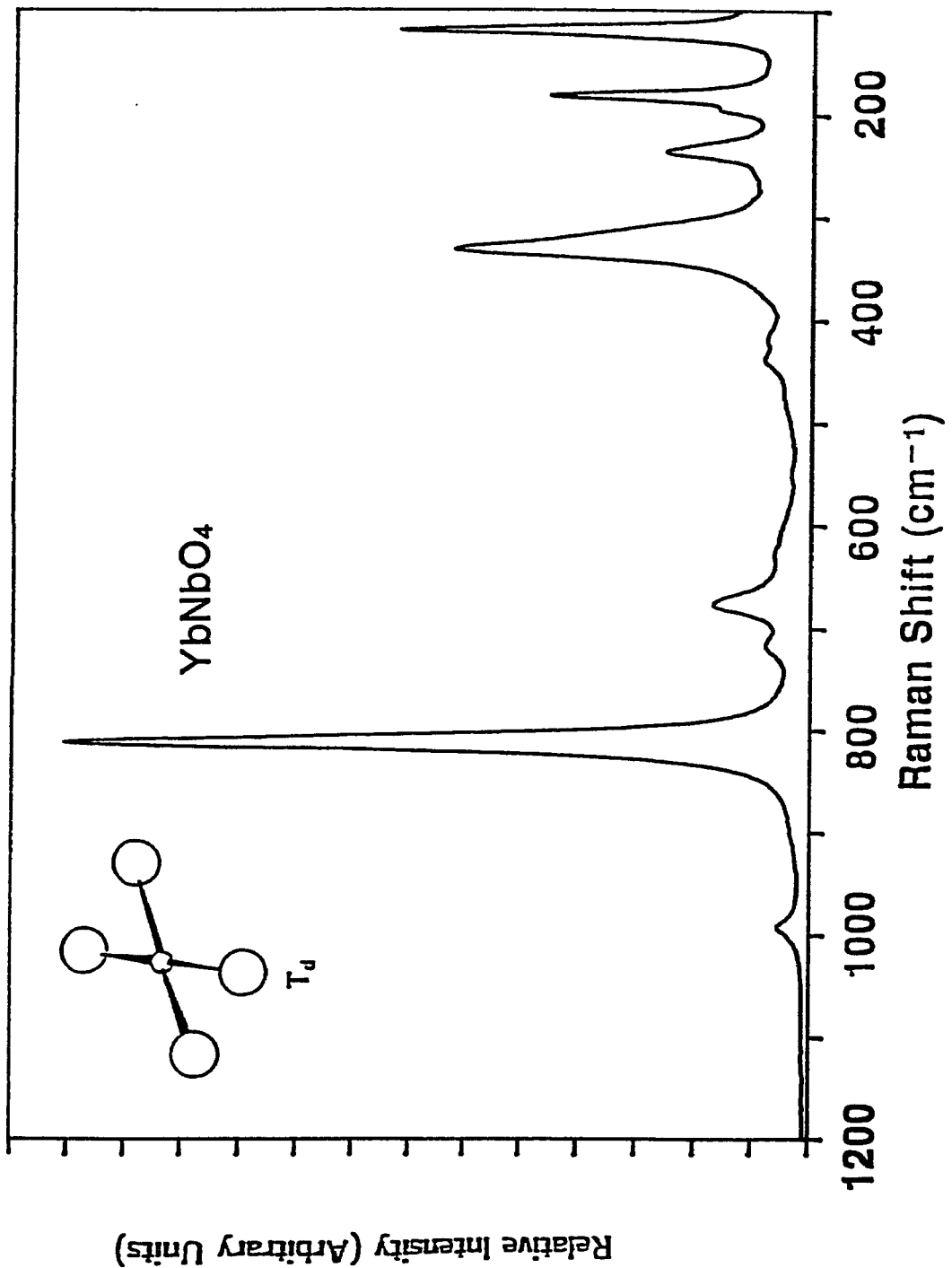


Fig. 2.10: Raman spectrum of the  $\text{YbNbO}_4$  compound

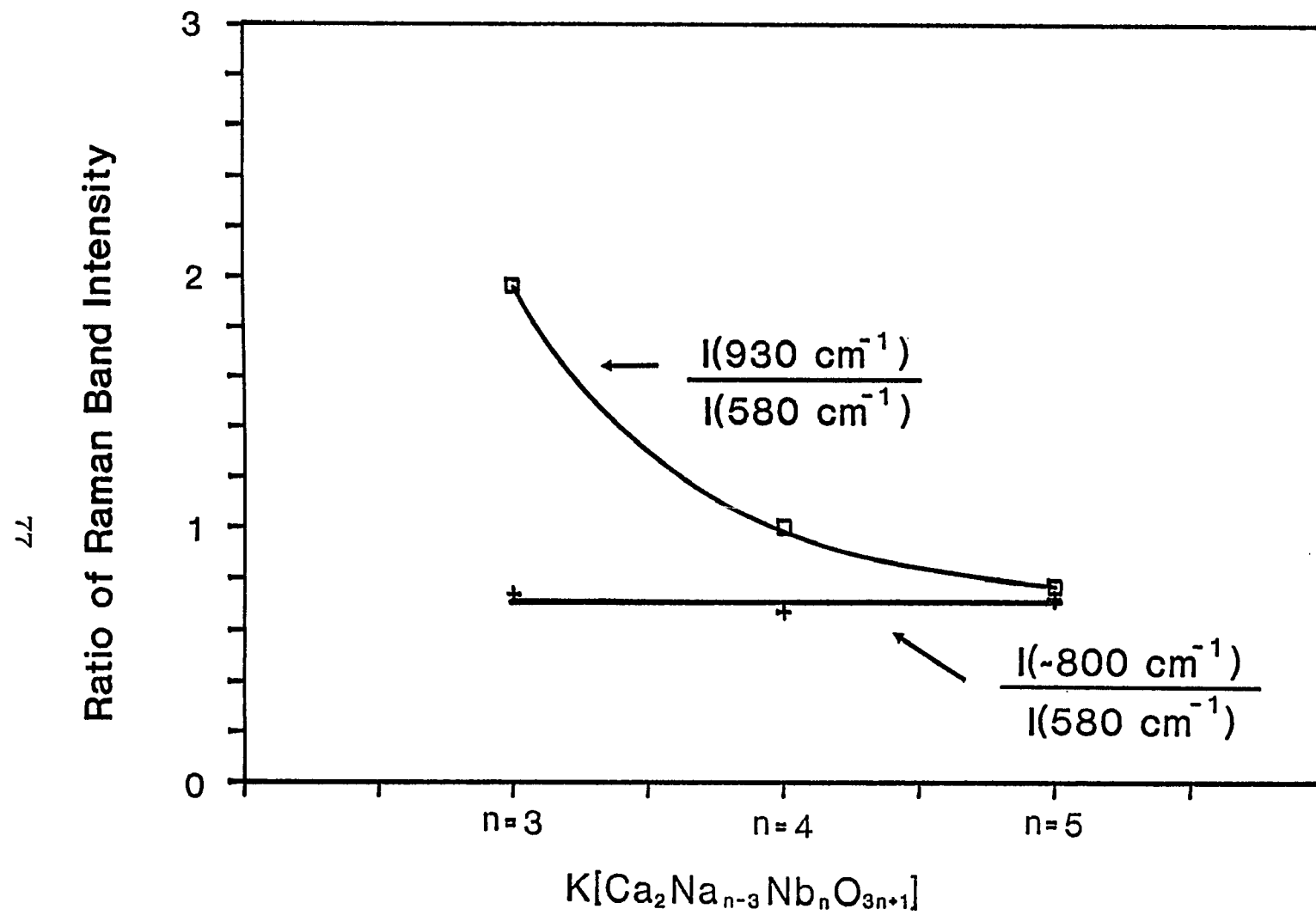


Fig. 2.11: The Raman band intensity ratios for the  $KCa_2Na_{n-3}Nb_nO_{3n+1}$  ( $n=3,4,5,$ ) layered oxide compounds

## **CHAPTER 3**

### **NIOBIUM OXIDE SOLUTION CHEMISTRY**

## SUMMARY

The solution chemistry of niobium oxide, in both alkaline and acidic oxalate solutions, was investigated by Raman spectroscopy in order to determine the molecular structures of the various aqueous niobium oxide species. The aqueous potassium niobate species were studied as a function of pH from 14.5 to 0.55. Different types of niobium oxide ionic species such as  $H_xNb_6O_{19}^{-(8-x)}$  ( $x=0-3$ ),  $Nb_{12}O_{36}^{-12}$ , and  $Nb_2O_5 \cdot nH_2O$  exist in aqueous solutions, and the solution pH as well as niobium oxide concentration determine the different niobium oxide ionic species. The aqueous niobium oxide ionic species are unstable at a pH below 6.5, and hydrolyze and polymerize to form  $Nb_2O_5 \cdot nH_2O$  precipitate. In acidic solutions containing oxalic acid two niobium oxalate ionic species are present,  $[NbO(C_2O_4)_2(H_2O)_2]$  and  $[NbO(C_2O_4)_3]$ , and the equilibrium between these two niobium oxalate ionic species is dependent on the solution pH, oxalic acid concentration, Nb concentration, and  $H^+$  concentration. The niobium oxalate ionic species are stable in the pH range from 0.5 to 3.0, and also form the  $Nb_2O_5 \cdot nH_2O$  precipitate at a pH above 3.0. The present study demonstrated the ability of Raman spectroscopy to directly determine the solution chemistry and molecular structures of niobium oxide species in aqueous solutions.

### 3.1. INTRODUCTION

The aqueous solution chemistry of the oxides of vanadium, molybdenum, and tungsten has been studied by modern x-ray crystallographic and nuclear magnetic resonance spectroscopic techniques in order to determine the relationships between structure, bonding, and reactivity [81,82]. The molecular structures of these metal oxides in aqueous solutions depend on the solution pH and metal oxide concentration [82,83]. In general, the small ionic species  $\text{VO}_4^{-3}$ ,  $\text{MoO}_4^{-2}$ , and  $\text{WO}_4^{-2}$  are present in aqueous solutions at the most basic environment and dilute concentrations. The small metal ionic species start to hydrolyze and polymerize to form larger ionic species ( $\text{V}_{10}\text{O}_{28}^{-6}$ ,  $\text{Mo}_7\text{O}_{24}^{-6}$ , and  $\text{W}_{12}\text{O}_{39}^{-6}$ ) at moderate acidities and metal oxide concentrations [83]. The nature of the niobium oxide species in aqueous solutions has not received as much attention as the corresponding oxides of vanadium, molybdenum, and tungsten because of the difficulty in preparing pure, stable niobium ionic species in aqueous solutions and the inability to obtain good  $^{93}\text{Nb}$  NMR data. No magnetic resonances have yet been observed for  $^{93}\text{Nb}$  in the solid state as well as solutions due to the excessive linewidths which result from the large quadrupole coupling constant [81].

The  $\text{Nb}^{5+}$  complexes can exist in both alkaline and acidic solutions due to the amphoteric character of niobium oxide. These complexes also exhibit an unusually pronounced tendency to hydrolyze due to their low stability in aqueous solutions and high affinity for oxygen ligands. Consequently, niobium oxide aqueous solutions tend to polymerize into a colloidal state. The alkali-metal niobates in aqueous solutions contain the hexaniobate ionic species,  $[\text{H}_x\text{Nb}_6\text{O}_{19}]^{(8-x)-}$  ( $X=0-3$ ), at a solution pH greater than 7. Raman spectroscopy [57,58] and  $^{170}\text{O}$  nuclear magnetic resonance [84] studies suggest that the hexaniobate ionic species consists of three types of Nb-O bonds: 6 Nb=O terminal bonds, 12 Nb-O-Nb bridging bonds, and 1  $\text{Nb}_6\text{O}$  sixfold bridging bond. The hexaniobate ionic species,  $\text{Nb}_6\text{O}_{19}^{-8}$ , starts to degrade into tetrameric,  $\text{Nb}_4\text{O}_{16}^{-12}$ , and monomeric,  $\text{NbO}_2(\text{OH})_4^{-3}$ , species in very basic solutions (pH  $\sim 14$ ) [85,86]. The alkali-metal niobates in aqueous solutions form a hydrated  $\text{Nb}_2\text{O}_5$  precipitate at a solution pH below 7.9 [87]. Thus, the presence of various niobate ionic species in aqueous solutions primarily depends on the solution pH and the coordination number of the Nb atom appears to be 6 for the soluble niobium oxide ionic species. The tetrahedral  $\text{NbO}_4^{-3}$  species does not exist in aqueous solutions due to the high electronegativity of niobium and the relatively small size

of the oxygen ligands [88].

Acidic solutions of niobium oxide are prepared by reacting the hydrated niobium oxide with an oxalic acid aqueous solution. The presence of oxalic acid stabilizes the niobium oxide in aqueous solutions by forming niobium oxalate ionic species such as  $\text{NbO}(\text{C}_2\text{O}_4)_3^{-3}$ ,  $\text{NbO}(\text{C}_2\text{O}_4)_2(\text{H}_2\text{O})_2^{-1}$ , and  $\text{NbO}(\text{C}_2\text{O}_4)(\text{OH})_2(\text{H}_2\text{O})_2^{-1}$  [87,89]. For the niobium oxalate species in aqueous solutions,  $\text{NbO}(\text{C}_2\text{O}_4)_3^{-3}$  and  $\text{NbO}(\text{C}_2\text{O}_4)_2(\text{H}_2\text{O})_2^{-1}$ , the coordination number of the Nb atom appears to be 7 [88]. The hydrolysis and polymerization mechanisms of the niobium oxide ionic species in aqueous solutions have been proposed in the literatures [87,90-92]. However, no studies have been performed to determine the chemistry and structure of the niobium oxalate ionic species in acidic aqueous solutions.

Raman spectroscopy is a very powerful technique for determining the molecular structures of metal oxides not only in the solid state, but also in aqueous solutions because of the weak Raman scattering of water. It can discriminate between different types of metal-oxygen bonds such as  $\text{Nb}=\text{O}$  ( $850-1000 \text{ cm}^{-1}$ ),  $\text{Nb}-\text{O}$  ( $500-700 \text{ cm}^{-1}$ ), and  $\text{Nb}-\text{O}-\text{Nb}$  ( $200-300 \text{ cm}^{-1}$ ). In the present study, aqueous potassium niobate solutions were investigated by Raman spectroscopy to determine the molecular structures of the niobium oxide

ionic species in alkaline solutions, particularly in the pH range from 0.55 to 6.50 where very little data is available. The chemistry and structure of niobium oxalate in acidic solutions were also studied by Raman spectroscopy as a function of the solution pH, the oxalic acid concentration, the niobium concentration, and the  $H^+$  concentration. The aqueous solution chemistry of niobium oxide needs to be better understood in order to determine the molecular structures of the surface niobium oxide phases on oxide supports under ambient conditions where the surfaces are hydrated.

### 3.2. Experimental

#### 3.2.1. Materials and Preparations

Potassium niobate,  $K_8Nb_6O_{19} \cdot XH_2O$ , was obtained from Pfaltz & Bauer, Inc. (Waterbury, CT). Niobium oxalate,  $Nb(HC_2O_4)_5$ , was provided by Niobium Products Company (Pittsburgh, PA) with the chemical analysis of 20.5%  $Nb_2O_5$ , 790 ppm Fe, 680 ppm Si, and 0.1% insoluble solid. Oxalic acid, potassium chloride, potassium hydroxide, nitric acid, and hydrochloric acid were obtained from Fisher Scientific Company (Fair Lawn, NJ) with a minimum purity of 99.9%. Ammonium hydroxide,  $NH_4OH$ , was purchased from J. T. Baker

Chemical Company (Phillisburg, NJ).

The alkaline solutions were prepared as follows: 0.5 gram of potassium niobate was dissolved in a 10M KOH aqueous solution and the pH of solution was varied from 14.5 to 0.5 by adding hydrochloric acid. The pH of the resulting solution was measured with a Beckman Φ 34 pH meter (Model 123141) and a Beckman combination electrode (Model 39838). The pH of the initial aqueous potassium niobate solution was found to be 14.5. The acidic solutions were prepared as follows: three grams of niobium oxalate was dissolved into a 1.2M oxalic acid aqueous solution, and the pH of the solution was varied from 0.50 to 5.00 by the addition of ammonium hydroxide into the solution.

### 3.2.2. Raman Spectroscopy

Raman spectroscopy measurements were obtained with a Spex triplemate spectrometer (model 1877) couple to an EG&G intensified photodiode array detector, cooled thermoelectrically to -35°C, and interfaced with an EG&G OMA III Optical Multichannel Analyzer (model 1463). The liquid sample was placed into a 0.8-1.10x90 mm capillary tube (Kimax-51), and excited by the 514.5 nm line of the Ar<sup>+</sup> laser with 100 mw of power. The laser beam was focused

on the sample illuminator, where the capillary tube was held by a V-shape cell mount in the liquid sample holder. The indirect scattered laser beam and the Raman scattering were reflected into the spectrometer by a 90° angle with the incident light. The scattered Raman light was collected by the spectrometer at room temperature, and analyzed with an OMA III software package. The overall spectral resolution of the spectra was determined to be better than 2  $\text{cm}^{-1}$ .

### 3.3. RESULTS

#### 3.3.1. Niobium Oxide in Alkaline Solutions

The Raman spectra of aqueous potassium niobate solutions in the pH range of 14.5 to 0.55 are shown in Fig. 3.1. At high pH (~14.5), the potassium niobate solution possesses Raman bands at ~1060, ~865, ~815, ~520, ~290, and ~230  $\text{cm}^{-1}$ . Upon decreasing the pH to 11.50, by the addition of hydrochloric acid into the solution, the major Raman band at ~865  $\text{cm}^{-1}$  shifts to ~880  $\text{cm}^{-1}$ , the Raman band at ~290  $\text{cm}^{-1}$  decreases in intensity, and an additional Raman band appears at ~380  $\text{cm}^{-1}$ . Further decreasing the solution pH to 6.5 causes the Raman band at ~880  $\text{cm}^{-1}$  to shift to ~901  $\text{cm}^{-1}$ , the Raman bands at ~520 and ~290  $\text{cm}^{-1}$

to completely disappear, and an additional Raman band at  $\sim 480\text{ cm}^{-1}$  to appear. At low pH (<3.65), the Raman band at  $\sim 630\text{ cm}^{-1}$  becomes dominant and the Raman band at  $\sim 901\text{ cm}^{-1}$  becomes broad and weak. The aqueous potassium niobate solution prepared at a pH of 0.55 was further evacuated at  $120^\circ\text{C}$  to remove the excess water, and the resulting precipitate possesses Raman bands at  $\sim 900$ ,  $\sim 650$ , and  $\sim 250\text{ cm}^{-1}$  which are similar to  $\text{Nb}_2\text{O}_5\cdot\text{nH}_2\text{O}$  [93].

### 3.3.2. Niobium Oxide in Acidic Oxalate Solutions

#### Niobium oxalate solubility

Niobium oxalate has a low solubility in aqueous solutions, but its solubility can be dramatically increased by the addition of oxalic acid. The solubility curve of niobium oxalate in aqueous solutions is shown in Fig. 3.2 as a function of the oxalic acid concentration. At high oxalic acid concentrations, however, the niobium oxalate and oxalic acid precipitate from solution.

#### Solution pH

A series of Raman spectra of niobium oxalate in aqueous oxalic acid solutions are shown in Fig. 3.3. The solution pH was varied from 0.50 to 5.00 by the addition of ammonium hydroxide to the aqueous solutions. At low pH

(0.50), the niobium oxalate aqueous solution possesses Raman bands at  $\sim 940$  and  $\sim 920$   $\text{cm}^{-1}$  in the high wavenumber region (900-1000  $\text{cm}^{-1}$ ) which are characteristic of Nb=O terminal stretching modes [89]. After the addition of ammonium hydroxide to increase the solution pH to 3.00, the Raman bands at  $\sim 940$  and  $\sim 920$   $\text{cm}^{-1}$  shift to  $\sim 932$  and  $\sim 914$   $\text{cm}^{-1}$ , respectively, and their relative intensity changes. In the intermediate wavenumber region (500-800  $\text{cm}^{-1}$ ), Raman bands are present at  $\sim 570$ ,  $\sim 545$ , and  $\sim 522$   $\text{cm}^{-1}$ . In the low wavenumber region (200-400  $\text{cm}^{-1}$ ), the relative intensity of the  $\sim 305$  and  $\sim 275$   $\text{cm}^{-1}$  Raman bands also changes with increasing solution pH. The Raman bands at  $\sim 845$  and  $\sim 460$   $\text{cm}^{-1}$  are due to the vibrational modes of the free  $\text{C}_2\text{O}_4^{2-}$  ionic species in aqueous solutions (see Fig. 3.4). At high pH (>5.00), two additional Raman bands appear at  $\sim 675$  and  $\sim 230$   $\text{cm}^{-1}$  which are characteristic of hydrated niobium oxide [93].

#### Oxalic acid concentrations

The Raman spectra of niobium oxalate in aqueous solutions possessing different oxalic acid concentrations are shown in Fig. 3.5. The Raman bands at  $\sim 940$  and  $\sim 920$   $\text{cm}^{-1}$  are characteristic of Nb=O terminal stretching modes, and their relative intensity changes with increasing  $\text{C}_2\text{O}_4^{2-}$

concentration. The intensity of the  $C_2O_4^{2-}$  Raman bands at  $\sim 845$  and  $\sim 460$   $cm^{-1}$  increases with increasing  $C_2O_4^{2-}$  concentration as expected (see Fig. 3.4). In the intermediate region ( $500-800$   $cm^{-1}$ ), weak Raman bands appear at  $\sim 795$ ,  $\sim 569$ ,  $\sim 545$ , and  $\sim 517$   $cm^{-1}$ , and the intensity of  $\sim 517$   $cm^{-1}$  Raman band increases with increasing  $C_2O_4^{2-}$  concentration. In the low wavenumber region ( $200-400$   $cm^{-1}$ ), Raman bands are present at  $\sim 365$ ,  $\sim 325$ ,  $\sim 305$ , and  $\sim 275$   $cm^{-1}$ , and their relative intensity also changes with increasing  $C_2O_4^{2-}$  concentration.

#### Nb concentrations

The Raman spectra of niobium oxalate aqueous solutions with different Nb concentrations are shown in Fig. 3.6. At low Nb concentration (0.08M), Raman bands appear at  $\sim 932$  and  $\sim 918$   $cm^{-1}$  which are characteristic of Nb=O terminal stretching modes and the Raman bands at  $\sim 845$  and  $\sim 460$   $cm^{-1}$  are due to the free  $C_2O_4^{2-}$  ionic species. Upon increasing the Nb concentration in the aqueous solution, the Raman band at  $\sim 932$   $cm^{-1}$  shifts to  $\sim 943$   $cm^{-1}$ , and the relative intensity of two Nb=O terminal bands at  $\sim 940$  and  $\sim 918$   $cm^{-1}$  changes. In the intermediate region ( $500-800$   $cm^{-1}$ ), Raman bands appear at  $\sim 795$ ,  $\sim 569$ ,  $\sim 545$ , and  $\sim 517$   $cm^{-1}$ . In the low wavenumber region ( $200-400$   $cm^{-1}$ ), Raman bands are

present at  $\sim 365$ ,  $\sim 325$ ,  $\sim 305$ , and  $\sim 275$   $\text{cm}^{-1}$ , and their relative intensity also changes. At high Nb concentration ( $>0.7\text{M}$ ), an additional broad and weak Raman band appears at  $\sim 870$   $\text{cm}^{-1}$ .

### $\text{H}^+$ concentrations

The Raman spectra of niobium oxalate in aqueous solutions with different  $\text{H}^+$  concentrations are shown in Fig. 3.7. The  $\text{H}^+$  concentrations were determined by the addition of nitric acid into the aqueous solution. The Raman bands at  $\sim 1045$  and  $\sim 715$   $\text{cm}^{-1}$  are due to the free  $\text{NO}_3^{-1}$  ionic species [94], and the Raman bands at  $\sim 847$  and  $\sim 460$   $\text{cm}^{-1}$  are due to the free  $\text{C}_2\text{O}_4^{-2}$  ionic species. The relative intensity of the two  $\text{Nb=O}$  terminal bands at  $\sim 941$  and  $\sim 919$   $\text{cm}^{-1}$  changes with increasing  $\text{H}^+$  concentration. In the intermediate region ( $500$ - $800$   $\text{cm}^{-1}$ ), Raman bands appear at  $\sim 795$ ,  $\sim 569$ ,  $\sim 545$ , and  $\sim 517$   $\text{cm}^{-1}$ , and the intensity of the  $\sim 517$   $\text{cm}^{-1}$  Raman band decreases with increasing  $\text{H}^+$  concentration. In the low wavenumber region ( $200$ - $400$   $\text{cm}^{-1}$ ), Raman bands are present at  $\sim 365$ ,  $\sim 325$ ,  $\sim 305$ , and  $\sim 275$   $\text{cm}^{-1}$ , and their relative intensity also changes with increasing  $\text{H}^+$  concentration.

### 3.4. DISCUSSIONS

Raman studies of the aqueous potassium niobate solution at a pH of 14.5 (see Fig. 3.1) and the corresponding  $K_8Nb_6O_{19}$  crystalline solid [57] suggest that the  $Nb_6O_{19}^{-8}$  ionic species in the liquid state and the solid state possess a similar structure. The presence of  $Nb_6O_{19}^{-8}$  ionic species in the aqueous potassium niobate solution was also concluded from light-scattering [95], ultracentrifugation [96,97], and potentiometric measurements [98]. In the high wavenumber region (800-1200  $\text{cm}^{-1}$ ), a strong and sharp Raman band at  $\sim 865 \text{ cm}^{-1}$  for the aqueous  $Nb_6O_{19}^{-8}$  ionic species indicates that unequal Nb=O bond lengths do not exist in the aqueous  $Nb_6O_{19}^{-8}$  structure. The Raman band appearing at  $\sim 1060 \text{ cm}^{-1}$  is due to the vibrational mode of KOH [94]. In the intermediate wavenumber region (400-800  $\text{cm}^{-1}$ ), the Raman band appearing at  $\sim 810 \text{ cm}^{-1}$  is characteristic of the Nb=O antisymmetric stretching mode and the Raman bands at  $\sim 735$  and  $\sim 520 \text{ cm}^{-1}$  are characteristic of the Nb-O-Nb antisymmetric and symmetric stretching modes, respectively. In the low wavenumber region (200-400  $\text{cm}^{-1}$ ), Raman bands appearing at  $\sim 290$  and  $\sim 240 \text{ cm}^{-1}$  are due to the Nb---O (central oxygen) stretching mode and the Nb-O-Nb bending mode, respectively. The existence of the Raman band at  $\sim 290 \text{ cm}^{-1}$  indicates that

the  $\text{Nb}_6\text{O}_{19}^{-8}$  structure is still retained at a solution pH of 14.5.

Upon decreasing the solution pH to 11.5, the equilibria between  $\text{Nb}_6\text{O}_{19}^{-8}$ , hexaniobate ionic species, and  $\text{H}_x\text{Nb}_6\text{O}_{19}^{-(8-x)}$  ( $x=1-3$ ), protonated hexaniobate ionic species, exist in aqueous solutions [99]. The Raman band at  $\sim 865 \text{ cm}^{-1}$  shifts to  $\sim 880 \text{ cm}^{-1}$  due to an increase of the  $\text{Nb}=\text{O}$  bond order resulting from protonation of the  $\text{Nb}_6\text{O}_{19}^{-8}$  species with decreasing solution pH. This is consistent with Griffith et al.'s results that the  $\text{V}=\text{O}$  Raman band of the aqueous  $\text{V}_{10}\text{O}_{28}^{-6}$  species increases by about  $15 \text{ cm}^{-1}$  due to the increased distortion of the  $\text{V}_{10}\text{O}_{28}^{-6}$  structure with decreasing solution pH [100].

Further decreasing the solution pH to 6.5 causes the major Raman band to shift to  $\sim 901 \text{ cm}^{-1}$  due to the formation of a polymeric  $\text{Nb}_{12}\text{O}_{36}^{-12}$  species in the aqueous solution [99]. The Raman band at  $\sim 290 \text{ cm}^{-1}$  disappears for the aqueous potassium niobate solution at a pH of 6.5 indicating that the aqueous  $\text{H}_x\text{Nb}_6\text{O}_{19}^{-(8-x)}$  ( $x=0-3$ ) species are not present at a solution pH of 6.5 and below. An additional Raman band appears at  $\sim 480 \text{ cm}^{-1}$  which is assigned to the symmetric stretching of  $\text{Nb}-\text{O}-\text{Nb}$  bridging bonds in the polymeric  $\text{Nb}_{12}\text{O}_{36}^{-12}$  species. The Raman band at  $\sim 630 \text{ cm}^{-1}$  becomes dominant at a solution pH of 3.65 and

below due to the formation of a hydrated  $\text{Nb}_2\text{O}_5$  precipitate which is similar to  $\text{Nb}_2\text{O}_5 \cdot n\text{H}_2\text{O}$  [93]. The Raman band at  $\sim 901 \text{ cm}^{-1}$  also becomes broad and weak upon further decreasing the solution pH below 6.5 and indicates that hydrolysis and polymerization of the  $\text{Nb}=\text{O}$  bonds extensively occurs below a pH of 6.5. After evacuating the aqueous potassium niobate solution (pH 0.55) at  $120^\circ\text{C}$ , the hydrated  $\text{Nb}_2\text{O}_5$  precipitate possesses broad Raman bands at  $\sim 900$  (vw),  $\sim 650$  (s), and  $\sim 250 \text{ cm}^{-1}$  (m) characteristic of  $\text{Nb}_2\text{O}_5 \cdot n\text{H}_2\text{O}$ .

Thus, the aqueous potassium niobate species are stabilized in the pH range from 6.5 to 14.5, and start to form a hydrated  $\text{Nb}_2\text{O}_5$  precipitate at the pH  $\sim 6.5$  and below. The relationships between the aqueous potassium niobate species and the corresponding Raman bands over the entire pH range are shown in Table 3.1. At high pH ( $> 6.5$ ), the aqueous potassium niobate species possess their major Raman band in the  $850\text{--}1000 \text{ cm}^{-1}$  region due to the presence of  $\text{Nb}=\text{O}$  bonds. At low pH ( $< 6.5$ ), the major Raman band shifts from  $850\text{--}1000 \text{ cm}^{-1}$  to  $\sim 630 \text{ cm}^{-1}$  indicating that  $\text{Nb}-\text{O}$  bonds form in the structures due to hydrolysis and polymerization of the aqueous potassium niobate species. The solution chemistry of potassium niobate above a pH of 6.5 is in agreement with prior Raman studies which the presence of different niobate ionic species in aqueous solutions

depends on the solution pH and the  $\text{NbO}_2(\text{OH})_4^{-3}$  monomer only exists in very basic and dilute solutions [100].

Niobium oxide complexes can also dissolve in oxalic acid aqueous solutions and form stable niobium oxide ionic species containing 1, 2 or 3 oxalate groups [88,101,102]. The equilibria between these niobium oxide ionic species depend on the solution pH, the oxalic acid concentration, and the Nb concentration. The presence of oxalic acid in the aqueous solutions has a pronounced effect on the niobium oxalate solubility (see Fig. 3.2) because the oxalic acid concentration controls the formation of the stable aqueous niobium oxide ionic species. For oxalic acid concentrations smaller than 0.4M, the free oxalate ionic species break the Nb-O-Nb linkages and chelates to the Nb atom to form isolated niobium oxide ionic species with a 3:1 and 2:1 coordinated-oxalate/Nb ratio in the aqueous solutions. The chelating effect is more strong for the 3/1 complex than for the 2/1 complex due to the high electronegativity of the  $\text{C}_2\text{O}_4^{-2}$  ligands [103-105], and results in the increase of the niobium oxalate solubility in aqueous solutions. For oxalic acid concentrations between 0.4M and 1.4M, the niobium oxalate solubility curve starts to level off and reaches its saturation point. For oxalic acid concentrations greater than 1.4M, the niobium

oxalate solubility decreases to its initial low value because the total concentration of the  $C_2O_4^{2-}$  species (free and chelated) reaches its solubility limit.

The crystal structure of niobium oxalate complexes was determined from X-ray diffraction data to consist of either  $[NbO(OH)(C_2O_4)_2H_2O]$  or  $[NbO(C_2O_4)_3]$  units and water molecules connected by hydrogen bonds [70-73]. The  $[NbO(OH)(C_2O_4)_2H_2O]$  unit has a pentagonal bipyramidal structure with a short Nb=O terminal double bond and a long Nb-OH<sub>2</sub> bond nearly perpendicular to the pentagonal equatorial plane which consists of two bidentate oxalate ligands and a hydroxyl group. The  $[NbO(C_2O_4)_3]$  unit also has a pentagonal bipyramidal structure with a short Nb=O terminal double bond and three bidentate oxalate ligands coordinated to the pentagonal equatorial plane.

The  $Na[NbO(C_2O_4)_2H_2O] \cdot 4H_2O$ , the 2/1 complex, and  $Na_3[NbO(C_2O_4)_3] \cdot 4H_2O$ , the 3/1 complex, crystal structures were investigated by Muller et al. using Raman and IR spectroscopy [84]. The 2/1 and 3/1 complexes exhibit strong and sharp Raman bands at  $\sim 960$  and  $\sim 940$   $cm^{-1}$ , respectively, as well as a weak Raman band at  $\sim 930$   $cm^{-1}$ , which are characteristic of Nb=O bonds. For the 2/1 complex, the Raman bands at  $\sim 570$  and  $\sim 545$   $cm^{-1}$  arise from the two bidentate oxalate ligands coordinated to the Nb

atom and are characteristic of the stretching modes of the Nb-O<sub>2</sub>-C<sub>2</sub> bridging bonds. For the 3/1 complex, the Raman bands at ~575 and ~525 cm<sup>-1</sup> arise from the three bidentate oxalate ligands coordinated to the Nb atom and are characteristic of the stretching modes of the Nb-O<sub>2</sub>-C<sub>2</sub> bridging bonds. The 2/1 complex also possesses a Raman band at ~290 cm<sup>-1</sup> which is characteristic of the Nb-OH<sub>2</sub> stretching mode and, as expected, this Raman band is not observed for the 3/1 complex.

The Raman spectrum of the solid niobium oxalate complex, Nb(HC<sub>2</sub>O<sub>4</sub>)<sub>5</sub> [93], employed in this study possesses Raman bands at ~960, ~930, ~575, ~550, and ~285 cm<sup>-1</sup>. This suggests that the structure of the niobium oxalate complex possesses the same [NbO(C<sub>2</sub>O<sub>4</sub>)<sub>2</sub>H<sub>2</sub>O] unit as that of the Na[NbO(C<sub>2</sub>O<sub>4</sub>)<sub>2</sub>H<sub>2</sub>O].4H<sub>2</sub>O complex because of their similar Raman spectra. Upon dissolving the niobium oxalate complex in aqueous solution, two Nb=O terminal bonds appear in the aqueous Raman spectra (see Fig. 3.3) indicating that two niobium oxalate ionic species, [NbO(C<sub>2</sub>O<sub>4</sub>)<sub>2</sub>H<sub>2</sub>O] (Nb=O band at ~940 cm<sup>-1</sup>) and [NbO(C<sub>2</sub>O<sub>4</sub>)<sub>3</sub>] (Nb=O band at ~920 cm<sup>-1</sup>), coexist in the solution. The two aqueous niobium oxalate ionic species exhibit their Nb=O Raman bands about 20 cm<sup>-1</sup> lower than found in the solid state because hydrogen bonding in the aqueous environment decreases the Nb=O bond

order.

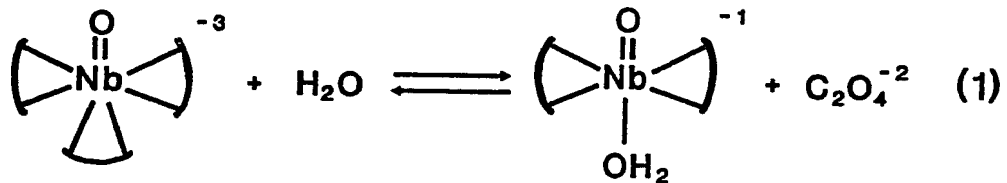
The Raman spectra also reveal that the relative intensity of two  $\text{Nb}=\text{O}$  bands,  $\sim 940$  and  $\sim 920 \text{ cm}^{-1}$ , changes with increasing pH (see Fig. 3.3) due to the shift of equilibrium point between these two aqueous niobium oxalate ionic species upon the addition of ammonium hydroxide into the solution. The hydrolysis of  $[\text{NbO}(\text{C}_2\text{O}_4)_3]$  ionic species occurs as one of the oxalate groups is replaced by OH groups, and forms the  $[\text{NbO}(\text{C}_2\text{O}_4)_2(\text{OH})_2]$  ionic specie. The change of relative intensity of two Raman bands,  $\sim 275$  and  $\sim 305 \text{ cm}^{-1}$ , which are assigned to the bending modes of the two  $\text{Nb}=\text{O}$  terminal bonds,  $\sim 940$  and  $\sim 920 \text{ cm}^{-1}$ , respectively, also suggests that the  $[\text{NbO}(\text{C}_2\text{O}_4)_3]$  ionic species tend to hydrolyze at higher solution pH. Similarly, the  $[\text{NbO}(\text{C}_2\text{O}_4)_2\text{H}_2\text{O}]$  ionic species tend to hydrolyze at higher solution pH.

Upon increasing the solution pH to 3.00 by further addition of ammonium hydroxide, a very weak Raman band appearing at  $\sim 900 \text{ cm}^{-1}$  increases its intensity and suggests the formation of an additional niobium ionic species in the aqueous solution. This is consistent with Muller et al.'s IR studies that a dimeric  $[\text{Nb}_2\text{O}_4(\text{OH})_2(\text{C}_2\text{O}_4)_2]$  ionic species is present and possesses IR bands at  $\sim 890$  and  $\sim 630 \text{ cm}^{-1}$  due to  $\text{Nb}=\text{O}$  and  $\text{Nb}-\text{O}-\text{Nb}$  bonds, respectively [89]. The

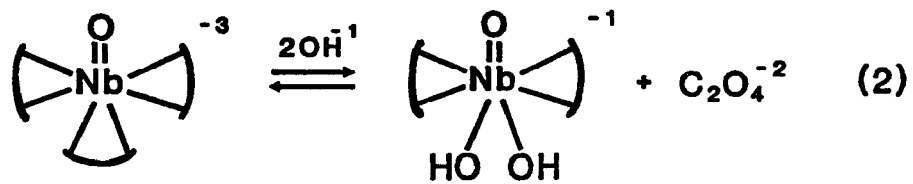
equilibria between these niobium oxalate ionic species are reached because of the absence of changes in the relative Raman intensity in the 900-1000  $\text{cm}^{-1}$  region. The increase of Raman intensity at  $\sim 520 \text{ cm}^{-1}$  with increasing pH is due to the formation of Nb-O-Nb bonds in the aqueous niobium oxalate species. This is also consistent with the conclusion that the dimeric  $[\text{Nb}_2\text{O}_4(\text{OH})_2(\text{C}_2\text{O}_4)_2]$  ionic species is present in the aqueous solution. At a pH greater than 3.00, the addition of ammonium hydroxide causes the dimeric  $[\text{Nb}_2\text{O}_4(\text{OH})_2(\text{C}_2\text{O}_4)_2]$  ionic species to hydrolyze and coagulate to a hydrated  $\text{Nb}_2\text{O}_5$  precipitate possessing Raman bands at  $\sim 675$  and  $\sim 230 \text{ cm}^{-1}$  which is similar to TT- $\text{Nb}_2\text{O}_5$  [93].

The aqueous solution chemistry of niobium oxalate is proposed as follows:

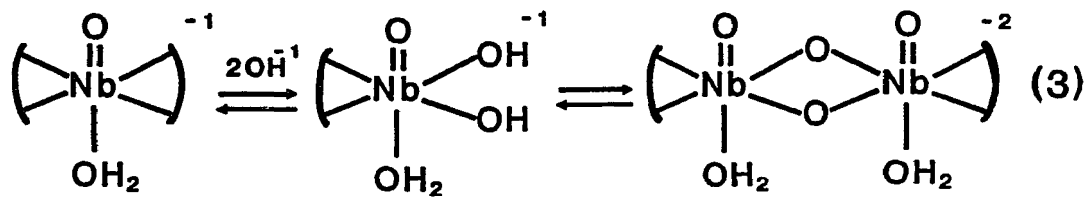
### Equilibrium



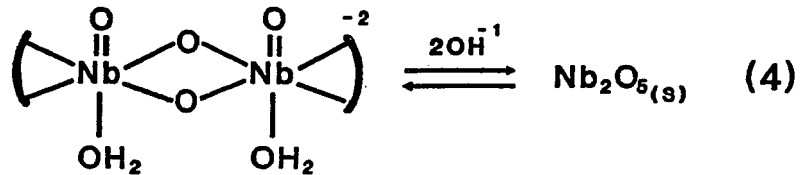
### Hydrolysis



### Hydrolysis



### Polymerization

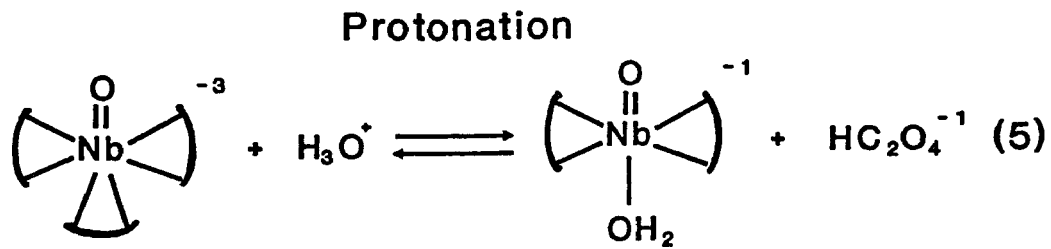


Eqn. 1 is the equilibrium between the  $[\text{NbO}(\text{C}_2\text{O}_4)_2\text{H}_2\text{O}]$  and  $[\text{NbO}(\text{C}_2\text{O}_4)_3]$  ionic species, Eqn. 2-3 are the hydrolysis of these two ionic species to form the dimeric  $[\text{Nb}_2\text{O}_4(\text{OH})_2(\text{C}_2\text{O}_4)_2]$  ionic species upon the addition of ammonium hydroxide, and Eqn. 4 is the polymerization of the dimeric  $[\text{Nb}_2\text{O}_4(\text{OH})_2(\text{C}_2\text{O}_4)_2]$  ionic species to form a hydrated  $\text{Nb}_2\text{O}_5$  precipitate upon the further addition of ammonium hydroxide.

The equilibrium between the  $[\text{NbO}(\text{C}_2\text{O}_4)_2\text{H}_2\text{O}]$  and  $[\text{NbO}(\text{C}_2\text{O}_4)_3]$  ionic species (see Eqn. 1) is determined by the  $\text{C}_2\text{O}_4^{2-}$  concentration in the aqueous niobium oxalate solutions. At low  $\text{C}_2\text{O}_4^{2-}$  concentrations ( $<0.1\text{M}$ ), the equilibrium is driven to the right hand side of the Eqn. 1, and the  $[\text{NbO}(\text{C}_2\text{O}_4)_2\text{H}_2\text{O}]$  ionic species, Raman band at  $\sim 940\text{ cm}^{-1}$  (see Fig. 3.5), is the dominant species in the aqueous niobium oxalate solutions. Upon increasing the  $\text{C}_2\text{O}_4^{2-}$  concentration, the equilibrium is driven in the other direction, and an increase in the  $[\text{NbO}(\text{C}_2\text{O}_4)_3]$  ionic species, Raman band at  $\sim 920\text{ cm}^{-1}$ , occurs in the aqueous niobium oxalate solutions. The relative intensity of the two niobium oxalate ionic species,  $[\text{NbO}(\text{C}_2\text{O}_4)_2\text{H}_2\text{O}]$  and  $[\text{NbO}(\text{C}_2\text{O}_4)_3]$  also changes with the Nb concentration (see Fig. 3.6). At low Nb concentration ( $<0.08\text{M}$ ), the two niobium oxalate ionic species possess about the same Raman

intensity in the aqueous niobium oxalate solutions. Upon increasing the Nb concentration, however, the intensity of the  $[\text{NbO}(\text{C}_2\text{O}_4)_2\text{H}_2\text{O}]$  ionic species starts to increase. The Nb concentration and the  $\text{C}_2\text{O}_4^{2-}$  concentration have an opposite effect on the equilibrium of the aqueous niobium oxalate ionic species.

The relative intensity of the two niobium oxalate ionic species,  $[\text{NbO}(\text{C}_2\text{O}_4)_2\text{H}_2\text{O}]$  and  $[\text{NbO}(\text{C}_2\text{O}_4)_3]$ , also changes with the  $\text{H}^+$  concentration in the aqueous solution (see Fig. 3.7). The  $[\text{NbO}(\text{C}_2\text{O}_4)_3]$  ionic species in aqueous niobium oxalate solutions reacts with the hydrogen proton to form the  $[\text{NbO}(\text{C}_2\text{O}_4)_2\text{H}_2\text{O}]$  ionic species as shown below [87] :



At high  $H^+$  concentration, the  $[NbO(C_2O_4)_2H_2O]$  ionic species becomes slightly more dominant in the aqueous niobium oxalate solutions.

The present study demonstrates the ability of Raman spectroscopy to directly monitor the niobium oxide species present in the aqueous solutions. Consequently, Raman spectroscopy allows the determination of the various niobium oxide molecular structures present in solution as well as the aqueous solution chemistry. This aspect of Raman spectroscopy was used to study the niobium oxide solution chemistry in both alkaline and acid aqueous solutions. In acidic oxalate solutions, the niobium oxalate solution chemistry was shown to depend on the solution pH, oxalic acid concentration, Nb concentration, and  $H^+$  concentration.

### 3.5. CONCLUSIONS

Niobium oxide complexes can exist both in alkaline solutions and in acidic oxalate solutions. In alkaline solutions, niobium oxide contains different types of niobium oxide ionic species such as  $H_xNb_6O_{19}^{-(8-x)}$  ( $x=0-3$ ), and  $Nb_{12}O_{36}^{-12}$  polymer. The presence of the different niobium oxide ionic species is dependent on the solution

pH. At high pH (~14.5), the hexaniobate ionic species,  $\text{Nb}_6\text{O}_{19}^{-8}$ , exists in aqueous solutions. In the pH range between 11.5 and 14.5, the equilibria between the  $\text{Nb}_6\text{O}_{19}^{-8}$  and  $\text{H}_x\text{Nb}_6\text{O}_{19}^{-(8-x)}$  ( $x=1,2,3$ ) hexaniobate ionic species exist in aqueous solutions. At low pH (<6.5), the hexaniobate ionic species starts to polymerize to form  $\text{Nb}_{12}\text{O}_{36}^{-12}$  species, and further forms a hydrated  $\text{Nb}_2\text{O}_5$  precipitate. In acidic oxalate solutions, niobium oxide contains two niobium oxalate ionic species,  $[\text{NbO}(\text{C}_2\text{O}_4)_2\text{H}_2\text{O}]$  and  $[\text{NbO}(\text{C}_2\text{O}_4)_3]$ , and the equilibria between these two niobium oxalate ionic species are dependent on the solution pH, oxalic acid concentration, Nb concentration, and  $\text{H}^+$  concentration. The niobium oxalate ionic species is stable in the pH range from 0.5 to 3.0, and forms hydrated  $\text{Nb}_2\text{O}_5$  precipitate at a pH greater than 3.0. The present study demonstrates the ability of Raman spectroscopy to directly determine the solution chemistry and molecular structures of niobium oxide species in aqueous solutions.

**Table 3.1: The aqueous potassium niobate species and Raman bands relationships at a pH range from 14.5 to 0.55**

<u>Solution pH</u>	<u>Species</u>	<u>Raman bands (cm<sup>-1</sup>)</u>
14.5	$\text{Nb}_6\text{O}_{19}^{-8}$	865(s), 815(w), 730 (w), 520(m), 290(s), 230(w)
11.5	$\text{H}_x\text{Nb}_6\text{O}_{19}^{-(8-x)}$ ( $x=1,2,3$ )	880(s), 820(w), 520(m), 420(w), 290(w)
6.5	$\text{Nb}_{12}\text{O}_{36}^{-12}$ $\text{Nb}_2\text{O}_5 \cdot n\text{H}_2\text{O}$	901(s), 480(m), 420(w) 880(vw), 630(w)
3.65	$\text{Nb}_{12}\text{O}_{36}^{-12}$ $\text{Nb}_2\text{O}_5 \cdot n\text{H}_2\text{O}$	901(w), 420(w) 880(w), 630(m), 280(w)
0.55	$\text{Nb}_2\text{O}_5 \cdot n\text{H}_2\text{O}$	880(w), 630(s), 420(w), 280(w)

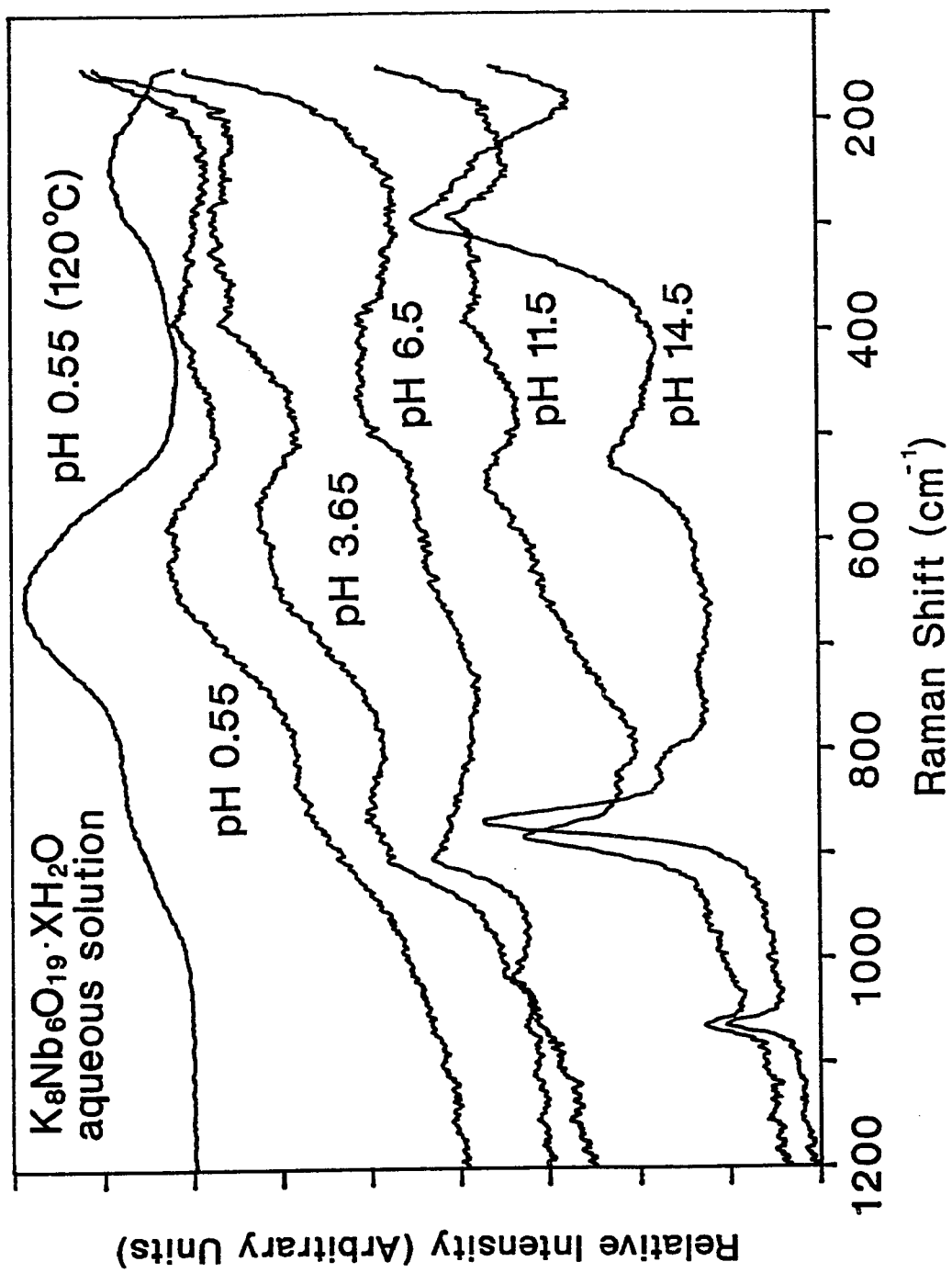


Fig. 3.1: Raman spectrum of potassium niobate in aqueous solutions as a function of the solution pH

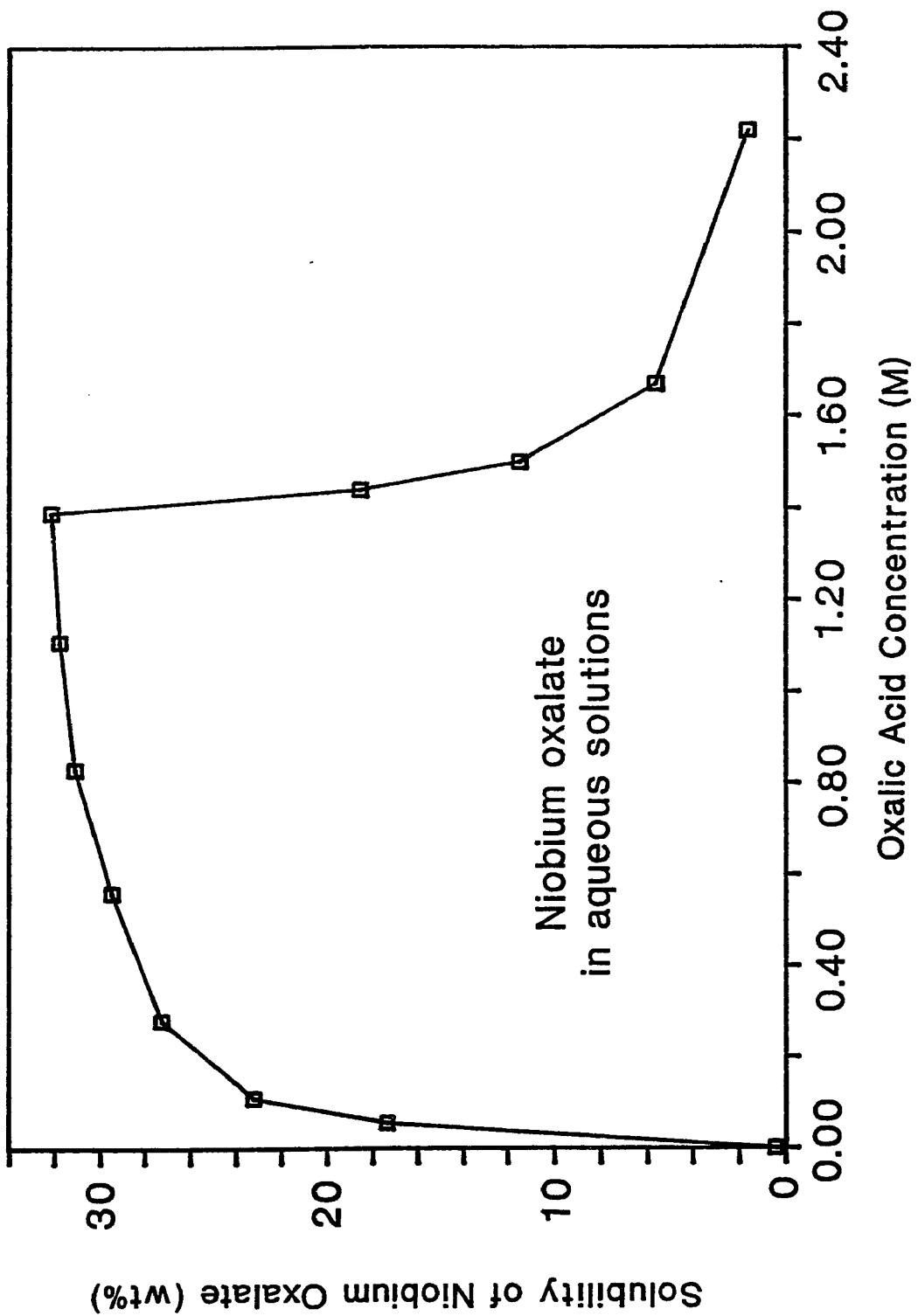


Fig. 3.2: The solubility of niobium oxalate in aqueous oxalic acid solutions

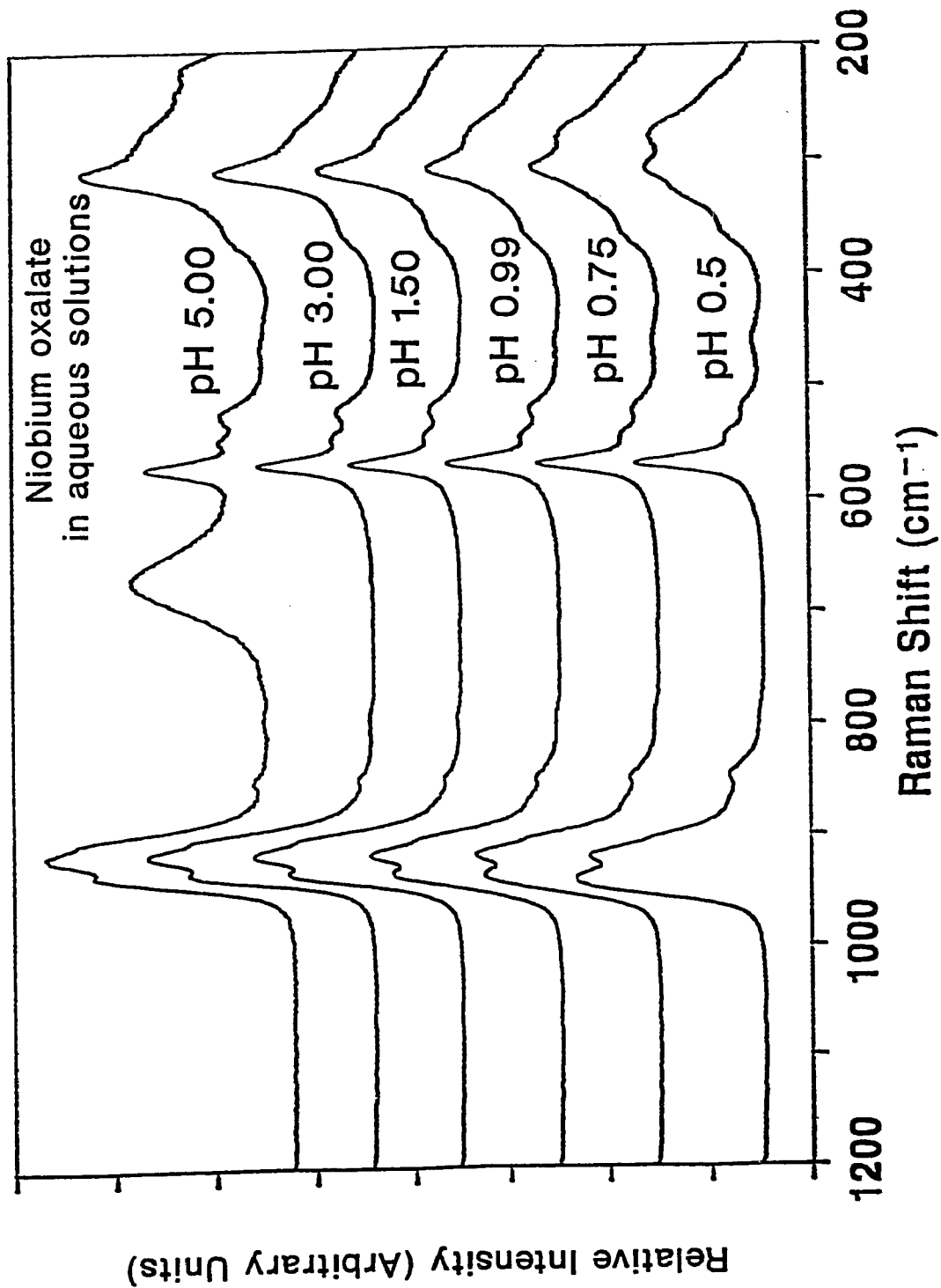


Fig. 3.3: Raman spectra of niobium oxalate in aqueous solutions as a function of the solution pH

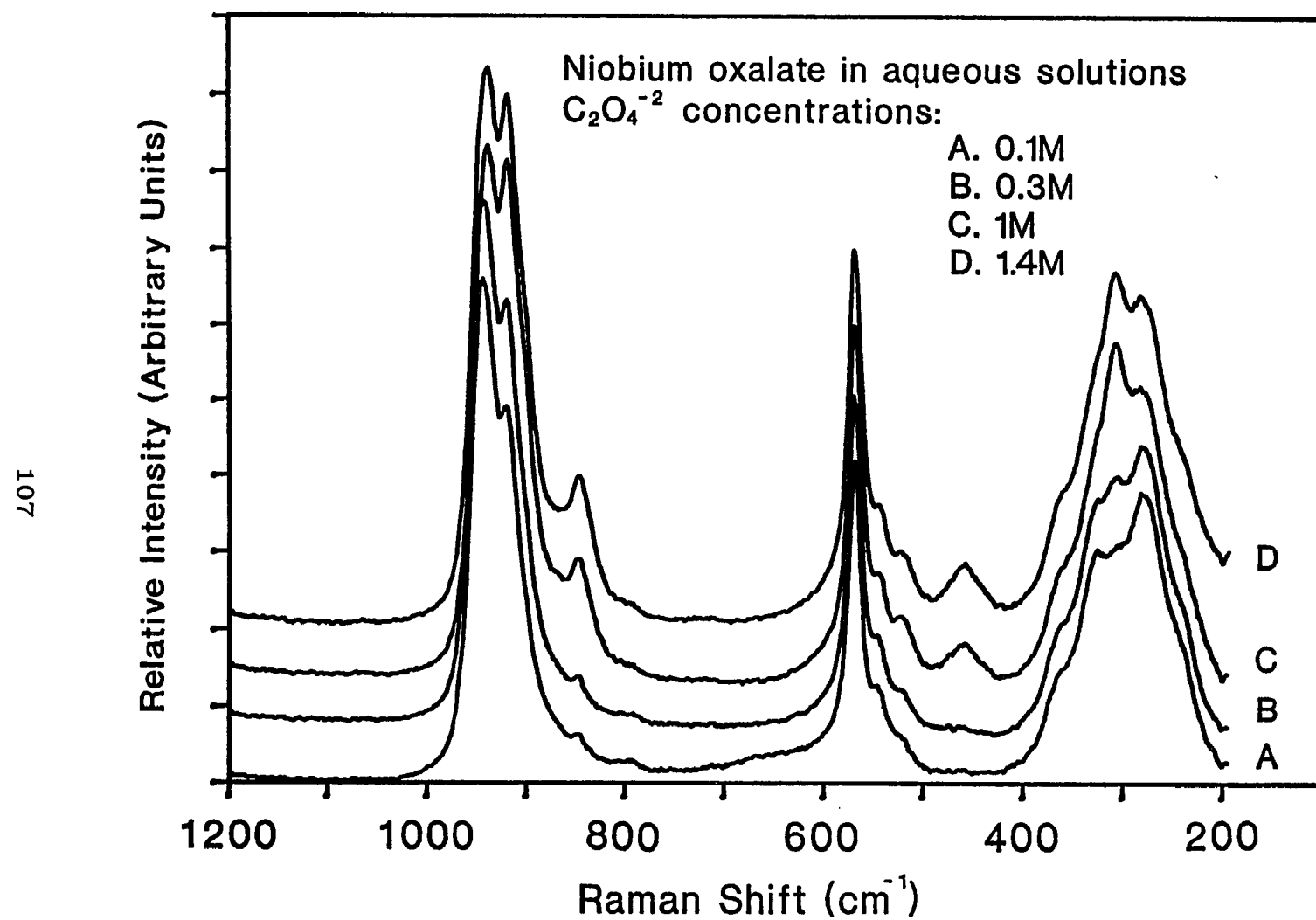


Fig. 3.4: Raman spectra of niobium oxalate in aqueous solutions as a function of the  $C_2O_4^{2-}$  concentration

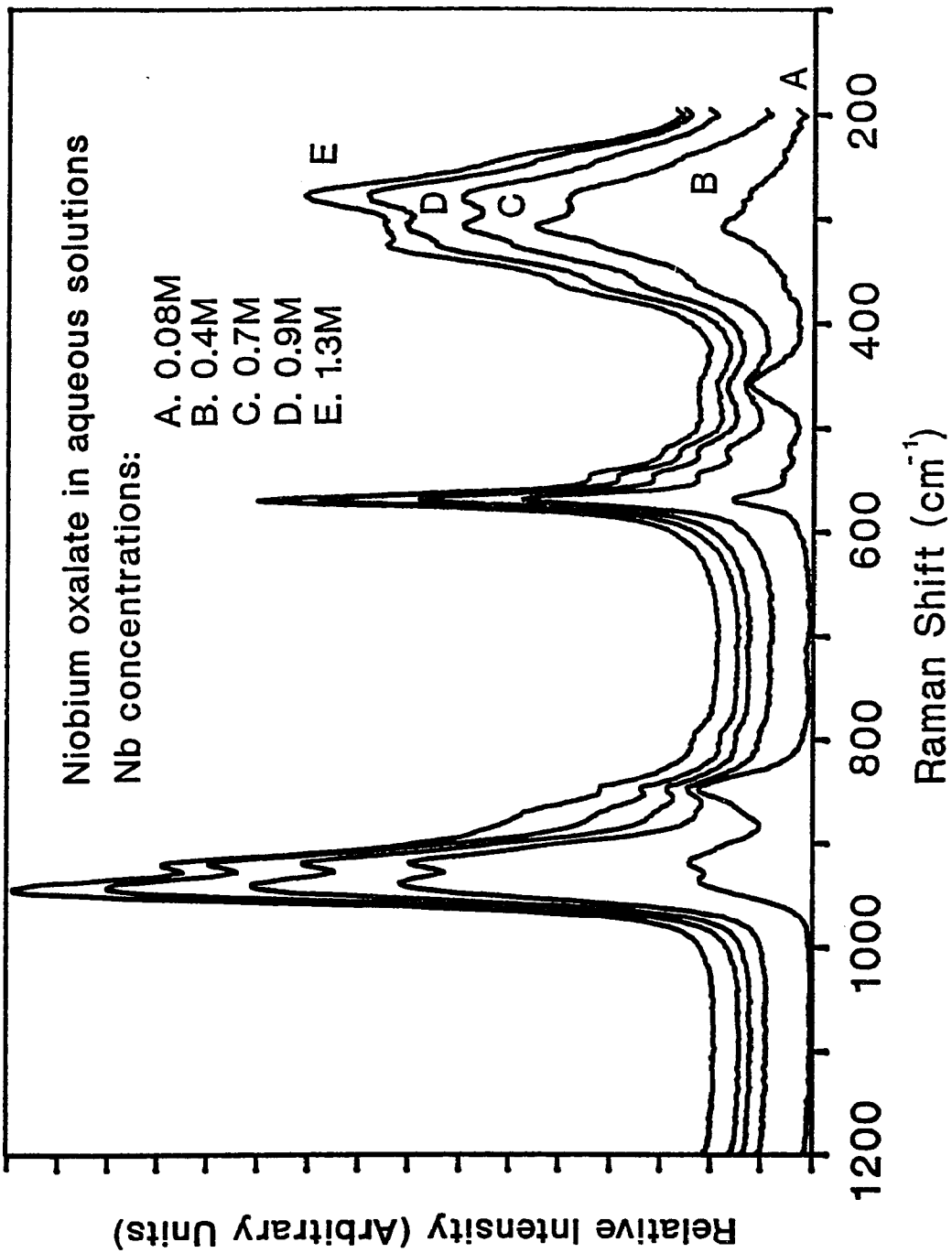


Fig. 3.5: Raman spectra of niobium oxalate in aqueous solutions as a function of the Nb concentration

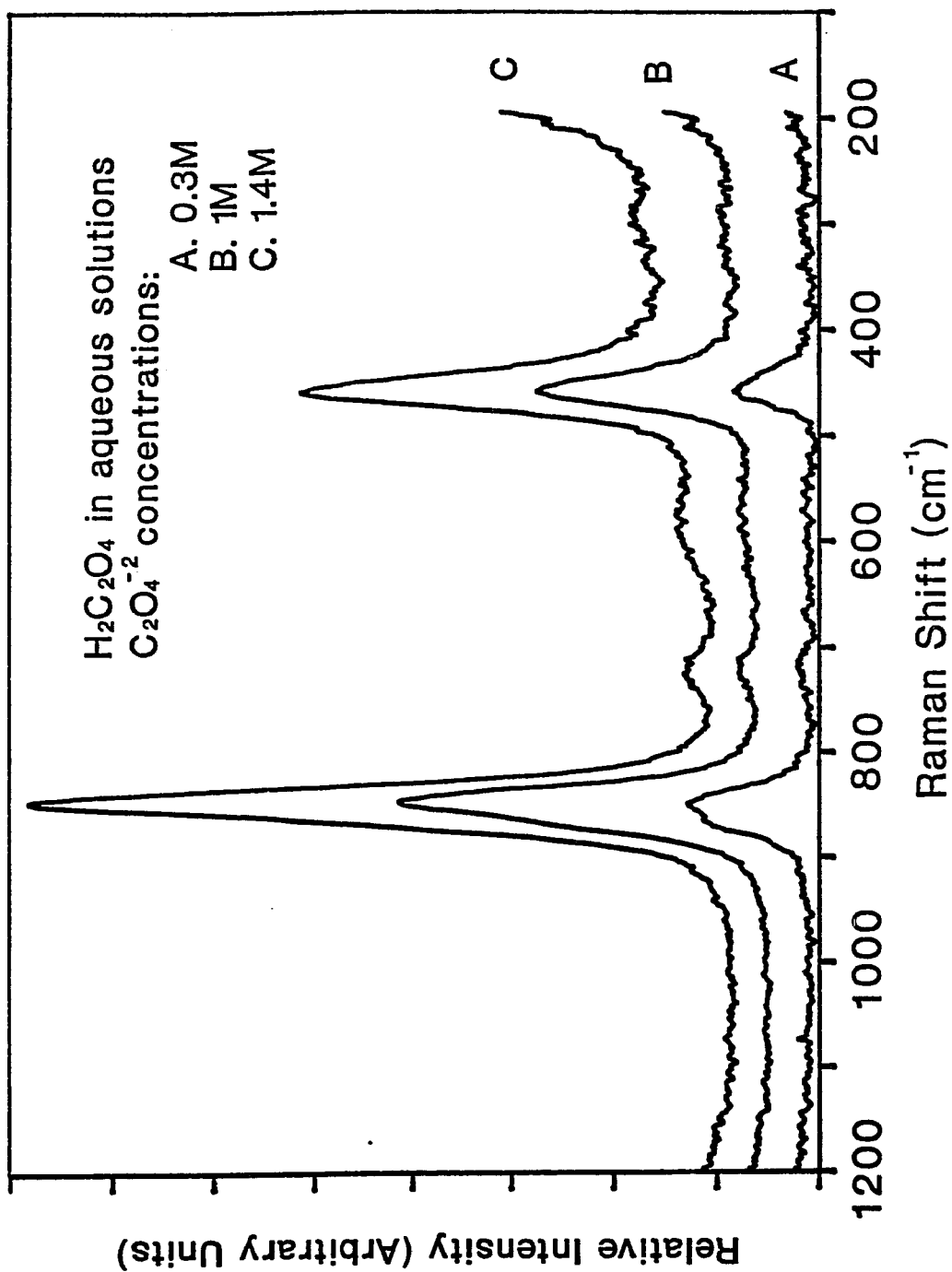


Fig. 3.6: Raman spectra of the aqueous oxalic acid solutions

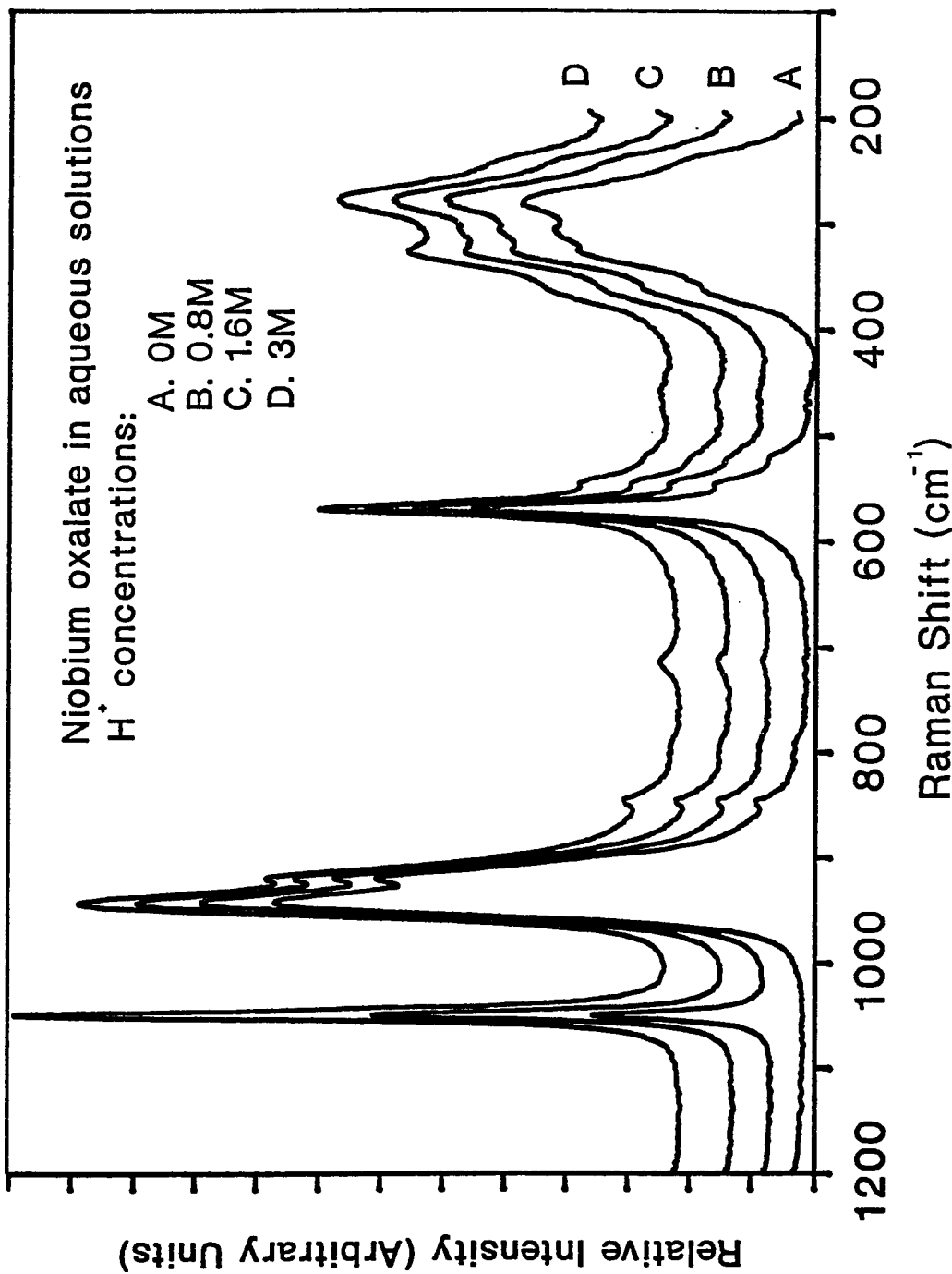


Fig. 3.7: Raman spectra of niobium oxalate in aqueous solutions as a function of the  $H^+$  concentration

## **CHAPTER 4**

# **MOLECULAR STRUCTURES OF SUPPORTED NIOBIUM OXIDE CATALYSTS UNDER AMBIENT CONDITIONS**

## SUMMARY

The supported niobium oxide catalysts were investigated by Raman spectroscopy and X-ray photoelectron spectroscopy in order to determine the molecular structure and monolayer coverage of the surface niobium oxide phase on oxide supports ( $\text{MgO}$ ,  $\text{Al}_2\text{O}_3$ ,  $\text{TiO}_2$ ,  $\text{ZrO}_2$ , and  $\text{SiO}_2$ ). The molecular structures of the surface niobium oxide phases present in the supported niobium oxide catalysts under ambient conditions, where adsorbed moisture is present, are controlled by the surface pH of the system. Basic surfaces result in the formation of highly distorted  $\text{NbO}_6$  groups and acidic surfaces result in the formation of slightly distorted  $\text{NbO}_6$ ,  $\text{NbO}_7$ , and  $\text{NbO}_8$  groups. The surface niobium oxide overlayer is stable to high calcination temperatures due to the strong surface niobium oxide-support interaction. The monolayer coverage of supported niobium oxide catalysts is reached at  $\sim 19$  wt%  $\text{Nb}_2\text{O}_5/\text{Al}_2\text{O}_3$ ,  $\sim 7$  wt%  $\text{Nb}_2\text{O}_5/\text{TiO}_2$ ,  $\sim 5$  wt%  $\text{Nb}_2\text{O}_5/\text{ZrO}_2$ , and  $\sim 2$  wt%  $\text{Nb}_2\text{O}_5/\text{SiO}_2$ , but not for the  $\text{Nb}_2\text{O}_5/\text{MgO}$  system due to the incorporation of  $\text{Nb}^{+5}$  into the  $\text{MgO}$  support.

#### 4.1. INTRODUCTION

Supported niobium oxide catalysts possess a surface niobium oxide overlayer on a high surface area oxide support. The surface niobium oxide phase is formed by the reaction of a suitable niobium precursor (i.e., oxalate [63], alkoxide [11], or chloride [106]) with the surface hydroxyls of the oxide support [107]. The physical and chemical properties of the surface niobium oxide can be quite different than those found in bulk  $\text{Nb}_2\text{O}_5$  phases, and can also dramatically influence the properties of the oxide supports [1]. For example, the surface niobium oxide phases impart thermal stability to oxide supports (i.e.,  $\text{Al}_2\text{O}_3$  and  $\text{TiO}_2$ ) at elevated temperatures [12,19], form strong acid centers on oxide supports [5,19-21], and are active for numerous catalytic reactions in the petrochemical (i.e., olefin metathesis, dimerization, trimerization, isomerization, as well as hydration and dehydration), petroleum (i.e., cracking, isomerization, and alkylation), and pollution control ( $\text{NO}_x$  reduction from stationary emissions) industries [1].

The molecular structures of the surface niobium oxide phases, however, have not received much attention and only preliminary Raman [12,63] and EXAFS [20,108] characterization studies have been reported. The multiple surface niobium oxide phases that simultaneously coexist in

the supported niobium oxide catalysts have generated confusion in the understanding of supported niobium oxide materials. This confusion results from the lack of the systematic studies on niobium oxide reference compounds and supported niobium oxide materials.

The niobium oxide structure-Raman spectra relationships and the niobium oxide solution chemistry have been previously reported [109]. In the present study, the molecular structures of the surface niobium oxide phases on  $\text{Al}_2\text{O}_3$ ,  $\text{TiO}_2$ ,  $\text{ZrO}_2$ ,  $\text{MgO}$ , and  $\text{SiO}_2$  supports will be investigated under ambient conditions with Raman spectroscopy as a function of  $\text{Nb}_2\text{O}_5$  loading and calcination temperature. The supported metal oxide catalysts contain adsorbed moisture under ambient conditions which influence the molecular structures of the surface metal oxide phases [78,93]. The molecular structures of the surface metal oxide phases under ambient conditions are directly related to the various aqueous metal oxide species [110]. Thus, the molecular structures of the surface niobium oxide phases under ambient conditions will be determined by the comparison of Raman spectra between the surface niobium oxide phases and the various niobium oxide species present in aqueous solutions at different solution pH.

The supported niobium oxide catalysts will be further

investigated by the BET surface area measurement and X-ray photoelectron spectroscopy (XPS) in order to determine the monolayer content of these catalysts. The formation of the surface niobium oxide overlayer can stabilize the high surface areas of the oxide supports at elevated calcination temperatures. XPS is a surface sensitive technique, and provide the information on composition, oxidation state, and dispersion of the surface niobium oxide phases [111,112]. Raman studies also indicate that a monolayer of surface niobium oxide phases is reached due to the detection of crystalline  $\text{Nb}_2\text{O}_5$ .

## 4.2. EXPERIMENTAL

### 4.2.1. Materials and Preparations

Niobium oxalate was supplied by Niobium Products Company (Pittsburgh, PA) with the following chemical analysis: 20.5%  $\text{Nb}_2\text{O}_5$ , 790 ppm Fe, 680 ppm Si, and 0.1% insolubles. Niobium ethoxide (99.999% purity) was purchased from Johnson Matthey (Ward Hill, MA). The oxide supports employed in the present investigation are:  $\text{MgO}$  (Fluka, ~80  $\text{m}^2/\text{g}$  after calcination at  $700^\circ\text{C}$  for 2 hrs),  $\text{Al}_2\text{O}_3$  (Harshaw, ~180  $\text{m}^2/\text{g}$  after calcination at  $500^\circ\text{C}$  for 16 hrs),  $\text{TiO}_2$  (Degussa, ~50  $\text{m}^2/\text{g}$  after calcination at  $450^\circ\text{C}$  for 2 hrs),  $\text{ZrO}_2$  (Degussa, ~39  $\text{m}^2/\text{g}$  after calcination at

450°C for 2 hrs), and SiO<sub>2</sub> (Cab-O-Sil, ~275 m<sup>2</sup>/g after calcination at 500°C for 16 hrs).

The TiO<sub>2</sub>, ZrO<sub>2</sub>, Al<sub>2</sub>O<sub>3</sub>, and SiO<sub>2</sub> supported niobium oxide catalysts were prepared by the incipient-wetness impregnation method using niobium oxalate/oxalic acid aqueous solutions (aqueous preparation) [63]. The water sensitive MgO support required the use of nonaqueous niobium ethoxide/propanol solutions under a nitrogen environment for the preparation of the Nb<sub>2</sub>O<sub>5</sub>/MgO catalysts. The supported niobium oxide on Al<sub>2</sub>O<sub>3</sub> catalysts were also prepared by the nonaqueous niobium ethoxide/propanol solution in order to compare the aqueous and nonaqueous preparation methods.

For the aqueous preparation method the samples were initially dried at room temperature for 16 hrs, further dried at 110-120°C for 16 hrs, and calcined at 450°C (Nb<sub>2</sub>O<sub>5</sub>/TiO<sub>2</sub> and Nb<sub>2</sub>O<sub>5</sub>/ZrO<sub>2</sub>, 2 hrs) or at 500°C (Nb<sub>2</sub>O<sub>5</sub>/Al<sub>2</sub>O<sub>3</sub> and Nb<sub>2</sub>O<sub>5</sub>/SiO<sub>2</sub>, 16 hrs) under flowing dry air. For the nonaqueous preparation method, the samples were initially dried at room temperature for 16 hrs, further dried at 110-120°C for 16 hrs under flowing N<sub>2</sub>, and calcined at 500°C for 1 hr under flowing N<sub>2</sub> then for 15 hrs (Nb<sub>2</sub>O<sub>5</sub>/Al<sub>2</sub>O<sub>3</sub>) or for 1 hr (Nb<sub>2</sub>O<sub>5</sub>/MgO) under flowing dry air.

#### 4.2.2. BET Surface Area Measurement

The BET surface areas of the supported niobium oxide catalysts were obtained with a Quantsorb surface area analyzer (Quantachrome corporation, Model OS-9) using a 3:7 ratio of N<sub>2</sub>/He mixture as a probe gas. Typically, 0.200-0.300 gram of sample was used for the measurement and the sample was outgassed at 250°C prior to N<sub>2</sub> adsorption.

#### 4.2.3. Raman Spectroscopy

Raman spectra were obtained with a Spex triplemate spectrometer (Model 1877) couple to an EG&G intensified photodiode array detector, cooled thermoelectrically to -35°C, and interfaced with an EG&G OMA III Optical Multichannel Analyzer (Model 1463). The samples were excited by the 514.5 nm line of the Ar<sup>+</sup> laser with 10-100 mw of power. The laser beam was focused on the sample illuminator, where the sample typically spins at about 2000 rpm to avoid local heating, and was reflected into the spectrometer by a 90° angle with the incident light. The scattered Raman light was collected by the spectrometer at room temperature, and analyzed with an OMA III software package. The overall spectral resolution of the spectra was determined to be about 2 cm<sup>-1</sup>. Additional details about the Raman spectrometer can be found elsewhere [65].

#### **4.2.4. X-Ray Photoelectron Spectroscopy (XPS)**

XPS experiments on the  $\text{Al}_2\text{O}_3$  supported niobium oxide catalysts were performed on a Physical Electronic Instruments ESCA/AUGER system. The samples were placed on the sample holder at a  $45^\circ$  angle to the entrance of analyzer and the system was evacuated to  $10^{-9}$  -  $10^{-10}$  Torr. The XPS spectra were calibrated against the  $\text{Au 4f}_{7/2}$  photoelectron line using the  $\text{Mg K}_\alpha$  exciting radiation from a dual anode operating at 10 kV, 40 mA.

XPS experiments on the  $\text{MgO}$ ,  $\text{TiO}_2$ ,  $\text{ZrO}_2$ , and  $\text{SiO}_2$  supported niobium oxide catalysts were performed on a VG ESCALAB I instrument with  $\text{Al K}_\alpha$  exciting radiation from a dual anode operating at 14 kV, 40 mA. The samples were placed on the sample holder at a  $90^\circ$  angle to the entrance of analyzer and the system was evacuated to  $10^{-9}$  -  $10^{-10}$  Torr. The XPS spectra were calibrated against the  $\text{C}_{1s}$  photoelectron line. Peak areas were determined from the background-subtracted spectra and corrected using instrument-dependent sensitivity factors.

### **4.3. RESULTS**

#### **4.3.1. BET Surface Area Measurements**

The BET surface areas of the supported niobium oxide catalysts are shown in Figure 4.1 as a function of  $\text{Nb}_2\text{O}_5$

loading. The results reveal that the high surface areas of the oxide supports (such as, MgO, Al<sub>2</sub>O<sub>3</sub>, TiO<sub>2</sub>, ZrO<sub>2</sub>, and SiO<sub>2</sub>) are maintained after the addition of niobium oxide. For the Nb<sub>2</sub>O<sub>5</sub>/Al<sub>2</sub>O<sub>3</sub> system, the aqueously prepared samples possess a slightly lower surface area at high niobium oxide loadings than the nonaqueously prepared samples.

The presence of the surface niobium oxide overlayer retards the loss in surface areas of the Al<sub>2</sub>O<sub>3</sub>, TiO<sub>2</sub>, ZrO<sub>2</sub>, and SiO<sub>2</sub> supports at elevated calcination temperatures, but not for the MgO support, as shown in Table 4.1. The addition of niobium oxide on the MgO support results in the dramatic decrease of surface area at high calcination temperatures.

#### 4.3.2. X-Ray Photoelectron Spectroscopy

The (Nb/M)<sub>surface</sub>, where M is Mg, Al, Ti, Zr, or Si, ratios of the supported niobium oxide catalysts were obtained by integrating the areas of the most intense photoelectron lines of Nb 3d<sub>3/2,5/2</sub> and M (Mg 2s, Al 2p, Ti 2p<sub>3/2</sub>, Zr 3d, and Si 2p), and the (Nb/M)<sub>surface</sub> vs. (Nb/M)<sub>bulk</sub> curves are shown in Figure 4.2. For the Nb<sub>2</sub>O<sub>5</sub>/MgO system, the (Nb/Mg)<sub>surface</sub> ratio linearly increases over the entire range of Nb<sub>2</sub>O<sub>5</sub> loading. For the Nb<sub>2</sub>O<sub>5</sub>/Al<sub>2</sub>O<sub>3</sub> system, the (Nb/Al)<sub>surface</sub> ratio linearly increases with increasing Nb<sub>2</sub>O<sub>5</sub> loading to ~19 wt%, and deviates from the linear curve at

high loadings due to the formation of bulk  $\text{Nb}_2\text{O}_5$  particles. Similarly, the  $\text{Nb}_2\text{O}_5/\text{TiO}_2$ ,  $\text{Nb}_2\text{O}_5/\text{ZrO}_2$ , and  $\text{Nb}_2\text{O}_5/\text{SiO}_2$  systems deviate from linearity at ~7 wt%, ~5 wt%, and ~2 wt%  $\text{Nb}_2\text{O}_5$ , respectively.

#### 4.3.3. Raman Spectroscopy

##### 4.3.3-1. $\text{Nb}_2\text{O}_5/\text{MgO}$

The Raman spectra of magnesium oxide supported niobium oxide are shown in Figure 4.3 as a function of  $\text{Nb}_2\text{O}_5$  loading. The Raman bands at ~875, ~450, ~380, and ~230  $\text{cm}^{-1}$  are associated with the surface niobium oxide phases since  $\text{MgO}$  is not Raman active and increase with  $\text{Nb}_2\text{O}_5$  loading. The Raman bands at ~1085 and ~280  $\text{cm}^{-1}$  are due to  $\text{CaCO}_3$  and decrease with  $\text{Nb}_2\text{O}_5$  loading. The Raman spectra of 5 wt%  $\text{Nb}_2\text{O}_5/\text{MgO}$  calcined at different temperatures are shown in Figure 4.4. The surface niobium oxide phase Raman bands (~875, ~450, ~380, and ~230  $\text{cm}^{-1}$ ) remain at the same positions after treatments at 500 and 700°C, while the  $\text{CaCO}_3$  Raman bands (~1085 and ~280  $\text{cm}^{-1}$ ) disappear after the 700°C calcination. For the 950°C calcined sample, multiple strong and sharp Raman bands appear in the 1000-200  $\text{cm}^{-1}$  region (suggest the formation of Mg-Nb-O solid solution).

#### 4.3.3-2. Nb<sub>2</sub>O<sub>5</sub>/Al<sub>2</sub>O<sub>3</sub>

The Raman spectra of the aqueously prepared alumina supported niobium oxide are shown in Figure 4.5. For Nb<sub>2</sub>O<sub>5</sub> loadings less than 5 wt%, broad and weak Raman bands due to the surface niobium oxide phase (since the Al<sub>2</sub>O<sub>3</sub> support is not Raman active) appear at ~900 and ~230 cm<sup>-1</sup>, and between 5 and 8 wt% Nb<sub>2</sub>O<sub>5</sub>/Al<sub>2</sub>O<sub>3</sub> the Raman band at ~900 cm<sup>-1</sup> shifts to ~930 cm<sup>-1</sup>. For Nb<sub>2</sub>O<sub>5</sub> loadings greater than 8 wt%, the Raman band at ~930 cm<sup>-1</sup> shifts to ~890 cm<sup>-1</sup>, an additional Raman band from the surface niobium oxide phase appears at ~645 cm<sup>-1</sup> and increases its intensity with Nb<sub>2</sub>O<sub>5</sub> loading. The intensity of the Raman band at ~230 cm<sup>-1</sup> also increases with Nb<sub>2</sub>O<sub>5</sub> loading. The Raman spectra of the nonaqueously prepared alumina supported niobium oxide catalysts are shown in Fig. 4.6, and reveal that the nonaqueously prepared catalysts possess the same Raman features as the aqueously prepared samples.

The influence of the calcination temperature upon the 5% Nb<sub>2</sub>O<sub>5</sub>/Al<sub>2</sub>O<sub>3</sub> sample is shown in Figure 4.7. The surface niobium oxide phase Raman bands at ~900 and ~230 cm<sup>-1</sup> are stable to elevated calcination temperature. However, the Raman band at ~900 cm<sup>-1</sup> shifts to ~930 cm<sup>-1</sup> in the 950°C calcined sample and the additional Raman bands appear at ~850, ~750, ~645, and ~250 cm<sup>-1</sup> due to the formation of  $\theta, \delta$ -Al<sub>2</sub>O<sub>3</sub> [113].

#### 4.3.3-3. Nb<sub>2</sub>O<sub>5</sub>/TiO<sub>2</sub>

The Raman data for titania supported niobium oxide catalysts was only collected in the 700-1200 cm<sup>-1</sup> region because of the strong scattering from the TiO<sub>2</sub> support below 700 cm<sup>-1</sup>. The Raman spectra of titania supported niobium oxide are shown in Figure 4.8 as a function of Nb<sub>2</sub>O<sub>5</sub> loading. The weak titania (anatase or rutile) Raman features in the 700-1200 cm<sup>-1</sup> region were subtracted from the spectrum in order to more clearly observe the Raman features of the surface niobium oxide phase. A weak and broad Raman band appears at ~895 cm<sup>-1</sup> from the surface niobium oxide phase which shifts from ~895 to ~930 cm<sup>-1</sup> upon increasing the Nb<sub>2</sub>O<sub>5</sub> loading to 5 wt%. For Nb<sub>2</sub>O<sub>5</sub> loadings greater than 5 wt%, an additional weak and broad Raman band appears at ~870 cm<sup>-1</sup> from the surface niobium oxide phase.

The Raman spectra of 5 wt% Nb<sub>2</sub>O<sub>5</sub>/TiO<sub>2</sub> after different calcination temperatures are shown in Figure 4.9. The surface niobium oxide phase Raman band at ~930 cm<sup>-1</sup> retains the same position after calcination between 300 to 700°C, but an additional weak and broad Raman band at ~870 cm<sup>-1</sup> appears after the 700°C calcination. For temperature treatments greater than 700°C, an additional weak and sharp Raman band appears at ~1000 cm<sup>-1</sup> and its intensity decreases slightly with further calcination at 950°C. The

Raman features of bulk  $TiO_2$ , in the  $700$ - $100$   $cm^{-1}$  region, are also changed after  $800^\circ C$  calcination indicating that the phase transformation from anatase ( $\sim 639$ ,  $\sim 517$ ,  $\sim 398$ , and  $\sim 144$   $cm^{-1}$ ) to rutile ( $\sim 614$ ,  $\sim 445$ , and  $\sim 240$   $cm^{-1}$ ) of  $TiO_2$  is detected at  $800^\circ C$  calcination.

#### 4.3.3-4. $Nb_2O_5/ZrO_2$

The Raman spectra of zirconia supported niobium oxide catalysts was also collected only in the  $750$ - $1200$   $cm^{-1}$  region because the strong scattering of  $ZrO_2$ . The  $ZrO_2$  support possesses a weak Raman band at  $\sim 755$   $cm^{-1}$  which arises from the first overtone of its strong Raman band at  $\sim 380$   $cm^{-1}$ . The Raman spectra were not corrected for the  $ZrO_2$  background because of the overlapping Raman band between the  $ZrO_2$  support and the surface niobium oxide phase. The Raman spectra of zirconia supported niobium oxide catalysts are shown in Figure 4.10 as a function of  $Nb_2O_5$  loading. The surface niobium oxide phase possesses a weak and broad Raman band at  $\sim 875$   $cm^{-1}$  which shifts from  $\sim 875$  to  $\sim 920$   $cm^{-1}$  with increasing  $Nb_2O_5$  loadings.

The influence of the calcination temperatures upon the 3 wt%  $Nb_2O_5/ZrO_2$  sample is shown in Figure 4.11. The surface niobium oxide phase Raman band appearing at  $\sim 900$   $cm^{-1}$  shifts to  $\sim 930$   $cm^{-1}$  upon increasing the calcination temperature from  $450$  to  $950^\circ C$  and an additional broad Raman

band at  $\sim 820$   $\text{cm}^{-1}$  appears after the  $950^\circ\text{C}$  calcination.

#### 4.3.3-5. $\text{Nb}_2\text{O}_5/\text{SiO}_2$

The Raman spectra of silica supported niobium oxide catalysts after calcination at  $500^\circ\text{C}$  are shown in Figure 4.12. For  $\text{Nb}_2\text{O}_5$  loadings less than 2 wt%, a weak and broad Raman band appears at  $\sim 960$   $\text{cm}^{-1}$ , and at higher loading additional Raman bands appear at  $\sim 650$  and  $\sim 240$   $\text{cm}^{-1}$ . Upon increasing the  $\text{Nb}_2\text{O}_5$  loading to 8 wt%, the surface niobium oxide phase has similar Raman features ( $\sim 900$ ,  $\sim 650$ , and  $\sim 240$   $\text{cm}^{-1}$ ) to bulk  $\text{Nb}_2\text{O}_5$  (amorphous) [93]. The silica supported niobium oxide catalysts were further calcined at  $600^\circ\text{C}$  in order to observe better Raman scattering of the surface niobium oxide phase as shown in Figure 4.13. At low  $\text{Nb}_2\text{O}_5$  loading (<2 wt%), the Raman intensity at  $\sim 960$   $\text{cm}^{-1}$  increases with increasing  $\text{Nb}_2\text{O}_5$  loading and remains constant with further increasing  $\text{Nb}_2\text{O}_5$  loading. At high  $\text{Nb}_2\text{O}_5$  loading (>2 wt%), the Raman band at  $\sim 900$   $\text{cm}^{-1}$  disappears and the Raman band at  $\sim 650$   $\text{cm}^{-1}$  shifts to  $\sim 680$   $\text{cm}^{-1}$  indicating the phase transformation of amorphous  $\text{Nb}_2\text{O}_5$  to TT- $\text{Nb}_2\text{O}_5$  [93].

The Raman spectra of the 4 wt%  $\text{Nb}_2\text{O}_5/\text{SiO}_2$  sample are shown in Figure 4.14 as a function of calcination temperature. The Raman band at  $\sim 960$   $\text{cm}^{-1}$  retains the same position, but becomes stronger with increasing temperature

treatment. Upon increasing calcination temperature to 950°C, bulk Nb<sub>2</sub>O<sub>5</sub> on silica support has a similar phase transformation order as Nb<sub>2</sub>O<sub>5</sub>.nH<sub>2</sub>O [93]: Amorphous Nb<sub>2</sub>O<sub>5</sub> (~900, ~650 and ~240 cm<sup>-1</sup>), TT-Nb<sub>2</sub>O<sub>5</sub> (~680 and ~240 cm<sup>-1</sup>), T-Nb<sub>2</sub>O<sub>5</sub> (~700 and ~240 cm<sup>-1</sup>), and H-Nb<sub>2</sub>O<sub>5</sub> (~993, ~670, ~625, and ~260 cm<sup>-1</sup>).

#### 4.4. DISCUSSIONS

The nature of the surface niobium oxide phase is determined from a comparison of the Raman spectra of the MgO, Al<sub>2</sub>O<sub>3</sub>, TiO<sub>2</sub>, ZrO<sub>2</sub>, and SiO<sub>2</sub> supported niobium oxide samples with those of niobium oxide reference compounds and solution chemistry [93,114]. The 1-15% Nb<sub>2</sub>O<sub>5</sub>/MgO, 1-19% Nb<sub>2</sub>O<sub>5</sub>/Al<sub>2</sub>O<sub>3</sub>, 1-5% Nb<sub>2</sub>O<sub>5</sub>/ZrO<sub>2</sub>, and 0.2-2% Nb<sub>2</sub>O<sub>5</sub>/SiO<sub>2</sub> samples after calcination at 450°C or 500°C do not contain the Raman features of crystalline Nb<sub>2</sub>O<sub>5</sub> phases (major band at ~690 cm<sup>-1</sup> due to slightly distorted NbO<sub>6</sub> octahedra), but possess weak and broad Raman bands in the 900-1000 cm<sup>-1</sup> region characteristic of a two-dimensional surface niobium oxide phase. The 1-10% Nb<sub>2</sub>O<sub>5</sub>/TiO<sub>2</sub> samples also possess weak and broad Raman bands in the 890-930 cm<sup>-1</sup> region which are characteristic of a two-dimensional surface niobium oxide phase. However, the very strong TiO<sub>2</sub> Raman scattering below 700 cm<sup>-1</sup> prevent the identification of

crystalline  $\text{Nb}_2\text{O}_5$  phases.

XPS studies reveal that a linear relation between the  $(\text{Nb}/\text{Al})_{\text{surface}}$  ratios and  $(\text{Nb}/\text{Al})_{\text{bulk}}$  ratios (see Figure 4.2) are observed due to the formation of two-dimensional niobium oxide overlayer [111,112]. The break in the linear curve corresponding to  $\sim 19$  wt%  $\text{Nb}_2\text{O}_5$  loading suggests that the transition from a two-dimensional overlayer to three-dimensional particles (monolayer coverage) occurs at this point [111,112]. This conclusion is supported by XRD measurements which only detect crystalline  $\text{Nb}_2\text{O}_5$  particles above  $\sim 19$  wt%  $\text{Nb}_2\text{O}_5/\text{Al}_2\text{O}_3$ , and  $\text{CO}_2$  chemisorption measurements [63] which indicate that the basic alumina hydroxyls have been removed by the niobium oxide overlayer at  $\sim 19$  wt%  $\text{Nb}_2\text{O}_5/\text{Al}_2\text{O}_3$  [115,116]. The XPS surface measurements of the  $\text{Nb}_2\text{O}_5/\text{TiO}_2$ ,  $\text{Nb}_2\text{O}_5/\text{ZrO}_2$ , and  $\text{Nb}_2\text{O}_5/\text{SiO}_2$  systems (see Figure 4.2) also suggest that the monolayer coverage of these three systems approaches  $\sim 7$ ,  $\sim 5$ , and  $\sim 2$  wt%  $\text{Nb}_2\text{O}_5$  loading, respectively. However, no break is observed in the curve of  $[\text{Nb}/\text{Mg}]_{\text{surface}}$  vs.  $[\text{Nb}/\text{Mg}]_{\text{bulk}}$ , and the linear increase of  $[\text{Nb}/\text{Mg}]_{\text{surface}}$  with increasing  $\text{Nb}_2\text{O}_5$  loading indicate that  $\text{Nb}^{+5}$  is incorporated into the  $\text{MgO}$  support surface.

Under ambient conditions surface metal oxide overlayers on oxide supports are hydrated due to the presence of adsorbed moisture, and the moisture influences

the molecular structures of these surface metal oxide phases [78,93]. The Raman frequencies of the supported niobium oxide catalysts under ambient conditions, after calcination at 450°C or 500°C, are tabulated in Table 4.2. Recent Raman characterization studies of supported vanadium oxide, molybdenum oxide, tungsten oxide, and chromium oxide catalysts under ambient conditions have demonstrated that the molecular structures of the hydrated surface metal oxide phases are directly related to the surface pH of the aqueous film which is determined by the combined pH of the oxide support and the metal oxide overlayer [110].

In aqueous environments the oxide support equilibrates at the pH which results in net zero surface charge (point zero surface charge or isoelectric point). The pH at the point zero surface charge of the metal oxide supports and niobium oxide are [35,117] :

<u>Support</u>	<u>The pH of the Point Zero Surface Charge</u>
MgO	12
Al <sub>2</sub> O <sub>3</sub>	9
TiO <sub>2</sub>	5-6
ZrO <sub>2</sub>	4-7
SiO <sub>2</sub>	~2
Nb <sub>2</sub> O <sub>5</sub>	~0.5

For supported metal oxide catalysts, the point zero surface charge of such composite materials is determined by the combined pH of the oxide support and the metal oxide overlayer. The influence of the metal oxide overlayer on the point zero surface charge of the composite system is directly related to the surface coverage of the surface metal oxide phases [118]. Thus, the addition of surface niobium oxide (pH ~0.5) to oxide supports (2<pH<12) will always decrease the pH of the point zero surface charge, and the decrease will be proportional to the surface niobium oxide coverage.

At low surface niobium oxide coverages of the supported niobium oxide catalysts, the surface pH under ambient conditions is dominated by the properties of the oxide support. The basic pH values of the MgO, pH=12, and Al<sub>2</sub>O<sub>3</sub>, pH=9, supports suggest that hexaniobate species (H<sub>x</sub>Nb<sub>6</sub>O<sub>19</sub><sup>-(8-x)</sup> where x= 1,2,3) should be present with corresponding Raman bands at ~880 cm<sup>-1</sup> [85,86,114]. Indeed, at low surface coverages for Nb<sub>2</sub>O<sub>5</sub>/MgO and Nb<sub>2</sub>O<sub>5</sub>/Al<sub>2</sub>O<sub>3</sub> only strong Raman bands are present at ~880 and ~900 cm<sup>-1</sup>, respectively (see Table 4.2). The somewhat acidic pH values of the TiO<sub>2</sub>, pH=5-6, and ZrO<sub>2</sub>, pH=4-7, supports suggest that the hexaniobate species should not be present in high concentrations [85,86,114] and that Nb<sub>2</sub>O<sub>5</sub>.nH<sub>2</sub>O type structures, containing slightly distorted

$\text{NbO}_6$  as well as  $\text{NbO}_7$  and  $\text{NbO}_8$  groups, should be present at  $\sim 650 \text{ cm}^{-1}$  for  $\text{Nb}_2\text{O}_5/\text{TiO}_2$  and  $\text{Nb}_2\text{O}_5/\text{ZrO}_2$  at low surface coverages. Unfortunately, the strong vibrations of the  $\text{TiO}_2$  and  $\text{ZrO}_2$  supports in this region do not allow direct confirmation of such niobium oxide species. However, the rather weak Raman bands for  $\text{Nb}_2\text{O}_5/\text{TiO}_2$  and  $\text{Nb}_2\text{O}_5/\text{ZrO}_2$  at  $\sim 895$  and  $\sim 875 \text{ cm}^{-1}$ , respectively, are consistent with this conclusion. For the acidic  $\text{SiO}_2$  support with a pH value of  $\sim 2$ ,  $\text{Nb}_2\text{O}_5 \cdot n\text{H}_2\text{O}$  type structures with Raman band at  $\sim 650 \text{ cm}^{-1}$  would be expected, but a weak and broad Raman band appearing at  $\sim 960 \text{ cm}^{-1}$  instead of  $\sim 650 \text{ cm}^{-1}$  is observed (see Figure 4.12 and 4.13). This indicates that the surface niobium oxide phase on silica after treated with  $500^\circ\text{C}$  or  $600^\circ\text{C}$  calcination contains a highly distorted  $\text{NbO}_6$  octahedra which is similar to the "capping" structure of layered niobium oxide reference compound [93]. The transformation of the structure of the surface niobium oxide phase, from a slightly distorted  $\text{NbO}_6$  octahedra to a highly distorted  $\text{NbO}_6$  octahedra, on  $\text{SiO}_2$  under high-temperature treatments is probably due to the weak interaction between the surface niobium oxide phase and the  $\text{SiO}_2$  support, and the presence of the surface niobium oxide phase, possessing a highly distorted  $\text{NbO}_6$  octahedra, on  $\text{SiO}_2$  under ambient conditions is probably due to the hydrophobicity of  $\text{SiO}_2$ .

At high surface niobium oxide coverages of the supported niobium oxide catalysts, the surface pH under ambient conditions is significantly influenced by the acidic niobium oxide overlayer. Under acidic aqueous conditions the  $\text{Nb}_2\text{O}_5 \cdot n\text{H}_2\text{O}$  type structures, containing slightly distorted  $\text{NbO}_6$  as well as  $\text{NbO}_7$  and  $\text{NbO}_8$  groups, should be present and give rise to a Raman band at  $\sim 650 \text{ cm}^{-1}$  [93]. Indeed, such Raman bands are observed at high loading for  $\text{Nb}_2\text{O}_5/\text{Al}_2\text{O}_3$  and  $\text{Nb}_2\text{O}_5/\text{SiO}_2$  catalysts. The thermal stability of these niobium oxide structures, however, are very different on the  $\text{SiO}_2$  and  $\text{Al}_2\text{O}_3$  structures. For  $\text{Nb}_2\text{O}_5/\text{SiO}_2$ , further calcination at  $700^\circ\text{C}$  shifts the Raman band from  $\sim 680$  to  $\sim 700 \text{ cm}^{-1}$  which is characteristic of crystalline T- $\text{Nb}_2\text{O}_5$  (see Figure 4.14). For  $\text{Nb}_2\text{O}_5/\text{Al}_2\text{O}_3$ , further calcination at  $700^\circ\text{C}$  does not shift the Raman band at  $\sim 650 \text{ cm}^{-1}$  [63]. Thus, it appears that on  $\text{SiO}_2$  the surface niobium oxide phase at high loading is present as a bulk  $\text{Nb}_2\text{O}_5$  phase which weakly interacts with the silica substrate, and that on  $\text{Al}_2\text{O}_3$  the supported niobium oxide phase at high loading is present as a two-dimensional overlayer anchored to the alumina support. The complete absence of Raman bands at  $\sim 650 \text{ cm}^{-1}$  for  $\text{Nb}_2\text{O}_5/\text{MgO}$  at high loading reveals that the extremely basic  $\text{MgO}$  support is dominating the surface pH. In addition, crystalline  $\text{Nb}_2\text{O}_5$  could not be formed at extremely high  $\text{Nb}_2\text{O}_5$  loading,  $\sim 15$  wt%  $\text{Nb}_2\text{O}_5/\text{MgO}$ , which corresponds to

approximately two monolayers of surface niobium oxide for this MgO support of  $\sim 80$   $\text{m}^2/\text{g}$ . The inability to form crystalline  $\text{Nb}_2\text{O}_5$  at high loadings and the very basic nature of the  $\text{Nb}_2\text{O}_5/\text{MgO}$  surface, absence of  $\sim 650$   $\text{cm}^{-1}$  Raman band at high loadings, is related to the strong acid-base interaction between  $\text{Nb}_2\text{O}_5$  and MgO, and leads to significant incorporation of  $\text{Nb}^{+5}$  into the MgO support surface. This is also consistent with the XPS surface measurements of the  $\text{Nb}_2\text{O}_5/\text{MgO}$  system that show a linear increase of  $[\text{Nb}/\text{Mg}]_{\text{surface}}$  ratio with increasing  $\text{Nb}_2\text{O}_5$  loading to  $\sim 15$  wt%. The strong vibrations of the  $\text{TiO}_2$  and  $\text{ZrO}_2$  supports in the  $\sim 650$   $\text{cm}^{-1}$  region prevented the direct detection of this species at high loadings of  $\text{Nb}_2\text{O}_5/\text{TiO}_2$  and  $\text{Nb}_2\text{O}_5/\text{ZrO}_2$ .

Niobium oxide reacts with the surface hydroxyl groups of the oxide supports ( $\text{MgO}$ ,  $\text{Al}_2\text{O}_3$ ,  $\text{TiO}_2$ ,  $\text{ZrO}_2$ , and  $\text{SiO}_2$ ) to form a surface niobium oxide overlayer. The interaction of the surface niobium oxide phase with the surface hydroxyl groups of the oxide support prevents the dehydroxylation of the oxide supports, and retards the loss in surface areas of the  $\text{Al}_2\text{O}_3$ ,  $\text{TiO}_2$ ,  $\text{ZrO}_2$ , and  $\text{SiO}_2$  supports at elevated calcination temperatures (see Table 4.1). However, the presence of niobium oxide does not stabilize the MgO surface area at  $950^\circ\text{C}$  calcination temperature due to the formation of Nb-Mg-O solid solution.

The different molecular states of niobium oxide

(crystalline  $\text{Nb}_2\text{O}_5$ , compounds, and surface niobium oxide phase) can be discriminated by Raman spectroscopy that monitor the structural transformations of supported niobium oxide systems with increasing temperature. The surface niobium oxide overlayer on the oxide supports ( $\text{Al}_2\text{O}_3$ ,  $\text{TiO}_2$ ,  $\text{ZrO}_2$ , and  $\text{SiO}_2$ ) is stable to high calcination temperatures (300-950°C) because of the strong surface niobium oxide phase-oxide support interaction. For the 5 wt%  $\text{Nb}_2\text{O}_5/\text{Al}_2\text{O}_3$  sample exhibit only the Raman bands of the surface niobium oxide phase and no evidence for the formation of crystalline  $\text{Nb}_2\text{O}_5$  and  $\text{AlNbO}_4$  phases (see Figure 4.7) [63,93]. For the 5 wt%  $\text{Nb}_2\text{O}_5/\text{TiO}_2$  sample, Raman studies reveal that the surface niobium oxide overlayer is partially transformed to crystalline  $\text{H-Nb}_2\text{O}_5$  (characteristic Raman band at  $\sim 1000 \text{ cm}^{-1}$ ) due to the loss surface area of  $\text{TiO}_2$  treated with a temperature greater than 800°C (see Figure 4.9). Upon increasing the temperature treatment from 800 to 950°C, the Raman band at  $\sim 1000 \text{ cm}^{-1}$  decreasing its intensity indicates that the crystalline  $\text{H-Nb}_2\text{O}_5$  reacts with  $\text{TiO}_2$  to form  $\text{Nb-Ti-O}$  phase at high calcination temperature [119]. For the 3 wt%  $\text{Nb}_2\text{O}_5/\text{ZrO}_2$  sample, the Raman band shifts from  $\sim 900$  to  $\sim 930 \text{ cm}^{-1}$  (see Figure 4.11) during thermal treatments and reflects the increase in surface density of the niobium oxide on the  $\text{ZrO}_2$  support surface as a result of the decrease in surface area [120]. For the 4 wt%  $\text{Nb}_2\text{O}_5/\text{SiO}_2$

sample, the surface niobium oxide phase and bulk  $\text{Nb}_2\text{O}_5$  coexist on the  $\text{SiO}_2$  support surface. Bulk  $\text{Nb}_2\text{O}_5$  is not stable at elevated calcination temperatures, and exhibits a phase transformation of amorphous  $\text{Nb}_2\text{O}_5$  to H- $\text{Nb}_2\text{O}_5$  due to the weak interaction with the  $\text{SiO}_2$  support. Thus, the surface niobium oxide phase-oxide support interaction controls the thermal stability of the surface niobium oxide phases.

Recent EXAFS/XANES studies on the  $\text{Al}_2\text{O}_3$ ,  $\text{TiO}_2$ , and  $\text{SiO}_2$  supported niobium oxide catalysts have been reported by Iwasawa et al. [7,9]. At low  $\text{Nb}_2\text{O}_5$  loadings (<3 wt%), they determine that the surface niobium oxide phases possess a dioxo  $\text{NbO}_4$  structure on the  $\text{Al}_2\text{O}_3$  as well as  $\text{SiO}_2$  supports and a mono-oxo  $\text{NbO}_5$  structure on the  $\text{TiO}_2$  support. A model for a monolayer of surface niobium oxide on silica,  $\sim 320 \text{ m}^2/\text{g}$ , corresponding to  $\sim 23.7 \text{ wt\% } \text{Nb}_2\text{O}_5/\text{SiO}_2$  was presented, and concluded that the Nb-O and Nb-Nb bond lengths of the surface niobium oxide monolayer are similar to those of T- $\text{Nb}_2\text{O}_5$  [121]. The  $\text{SiO}_2$  supported niobium oxide catalysts were also studied by Ko et al. [10], and determined that a monolayer of surface niobium oxide on silica,  $\sim 300 \text{ m}^2/\text{g}$ , corresponds to  $\sim 29.3 \text{ wt\% } \text{Nb}_2\text{O}_5/\text{SiO}_2$ . The surface niobium oxide monolayer contains no crystalline  $\text{Nb}_2\text{O}_5$  phase from X-ray diffraction [10].

The valence sum rule is a useful concept for

discussing the feasibility of a proposed surface niobium oxide structure [122]. The sum of the valencies or bond orders of the individual Nb-O bonds should equal to  $5\pm0.1$  valence units. A empirical expression relating Nb-O bond length to bond valence was developed by Brown and Wu [123]. The Nb valence units of the Iwasawa's proposed models for surface niobium oxide phases on the  $\text{Al}_2\text{O}_3$ ,  $\text{TiO}_2$ , and  $\text{SiO}_2$  supports are estimated to be 4.3, 3.6, and 5.7, respectively. These value are much less or higher than the  $\text{Nb}^{+5}$  valence state ( $5\pm0.1$  v.u.). In addition, the ratio of the  $\text{Nb}^{+5}$  ionic radius to the  $\text{O}^{2-}$  ionic radius, 0.5, is too large to fit into a  $\text{NbO}_4$  tetrahedral structure. Thus, the Iwasawa's models for the surface niobium oxide phases are less likely feasible. No crystalline  $\text{Nb}_2\text{O}_5$  phase was detected on the  $\text{Nb}_2\text{O}_5/\text{SiO}_2$  systems at high  $\text{Nb}_2\text{O}_5$  loadings from XRD. This suggests that the bulk  $\text{Nb}_2\text{O}_5$  phase on the  $\text{SiO}_2$  support possesses a particle size smaller than 40Å.

#### 4.5. CONCLUSIONS

Raman and XPS studies on the supported niobium oxide catalysts under ambient conditions reveal that the surface niobium oxide phase forms a two-dimensional overlayer on oxide supports ( $\text{MgO}$ ,  $\text{Al}_2\text{O}_3$ ,  $\text{TiO}_2$ ,  $\text{ZrO}_2$ , and  $\text{SiO}_2$ ). The available Raman data under ambient conditions on supported

niobium oxide catalysts are consistent with prior studies that the surface pH determines the molecular structures of the surface metal oxide phases. At low surface coverages on basic oxide supports ( $MgO$  and  $Al_2O_3$ ), hexaniobate-like surface species ( $H_xNb_6O_{19}^{-(8-x)}$  where  $x= 1,2,3$ ) appear to be present. The hexaniobate type surface species contain highly distorted  $NbO_6$  octahedra. At high surface coverages on basic ( $Al_2O_3$ ) and acidic ( $TiO_2$  and  $ZrO_2$ ) oxide supports, hydrated niobium oxide-type surface species ( $Nb_2O_5 \cdot nH_2O$ ) are also present. The hydrated niobium oxide-type surface species contain slightly distorted  $NbO_6$  octahedra as well as slightly distorted  $NbO_7$  and  $NbO_8$  structures. The hydrated niobium oxide-type surface species probably also predominate at low surface coverages on the acidic oxide supports ( $TiO_2$ ,  $ZrO_2$ , and  $SiO_2$ ), but can not be detected due to overlap with the strong vibrations from the oxide supports. In addition, bulk  $Nb_2O_5$  Raman bands at  $\sim 680$   $cm^{-1}$  could be observed above 19 wt%  $Nb_2O_5/Al_2O_3$ , 5 wt%  $Nb_2O_5/ZrO_2$ , and 2 wt%  $Nb_2O_5/SiO_2$  indicating that monolayer coverage, titration of reactive surface hydroxyls, had been achieved. These conclusions are also supported by the XPS measurements. Bulk  $Nb_2O_5$  was not formed on  $MgO$ , even at the equivalent of two monolayers loading, and could not be detected on  $TiO_2$  because of the very strong  $TiO_2$  vibrations. The XPS measurements of the surface niobium oxide on  $TiO_2$  suggest that the monolayer coverage is

reached at ~7 wt%  $\text{Nb}_2\text{O}_5/\text{TiO}_2$ . The surface niobium oxide phase on oxide supports (such as  $\text{Al}_2\text{O}_3$ ,  $\text{TiO}_2$ ,  $\text{ZrO}_2$ , and  $\text{SiO}_2$ ) is stable to high calcination temperatures. The high temperature stability of the surface niobium oxide overlayer is due to the strong interaction between the surface niobium oxide phase and these oxide supports.

Table 4.1: The influence of calcination temperature on the surface areas of supported niobium oxide catalysts

<u>Catalyst</u>	Calcination temperature (°C)			
	450	500	700	950
MgO	-	241	81	49
5 wt% Nb <sub>2</sub> O <sub>5</sub> /MgO	-	89	80	16
Al <sub>2</sub> O <sub>3</sub>	-	185	-	98
5 wt% Nb <sub>2</sub> O <sub>5</sub> /Al <sub>2</sub> O <sub>3</sub>	-	180	-	105
TiO <sub>2</sub>	50	-	24	6
5 wt% Nb <sub>2</sub> O <sub>5</sub> /TiO <sub>2</sub>	47	-	38	10
ZrO <sub>2</sub>	39	-	22	9
3 wt% Nb <sub>2</sub> O <sub>5</sub> /ZrO <sub>2</sub>	39	-	34	19
SiO <sub>2</sub>	-	275	-	127
1 wt% Nb <sub>2</sub> O <sub>5</sub> /SiO <sub>2</sub>	-	271	-	181

MgO, TiO<sub>2</sub>, and ZrO<sub>2</sub> samples calcined for 2 hrs

Al<sub>2</sub>O<sub>3</sub> and SiO<sub>2</sub> samples calcined for 16 hrs

Table 4.2: Raman bands of supported niobium oxide catalysts under ambient conditions

<u>Catalyst</u>	<u>BET Surface Area (m<sup>2</sup>/g)</u>	<u>Raman Bands (cm<sup>-1</sup>)</u>
5% Nb <sub>2</sub> O <sub>5</sub> /MgO	86	880(m), 450(w), 380(w), 230(w)
10% Nb <sub>2</sub> O <sub>5</sub> /MgO	75	880(s), 450(w), 380(w), 230(m)
5% Nb <sub>2</sub> O <sub>5</sub> /Al <sub>2</sub> O <sub>3</sub>	180	900(s), 230(m)
19% Nb <sub>2</sub> O <sub>5</sub> /Al <sub>2</sub> O <sub>3</sub>	151	890(s), 650(s), 230(s)
1% Nb <sub>2</sub> O <sub>5</sub> /TiO <sub>2</sub>	48	895(w)
7% Nb <sub>2</sub> O <sub>5</sub> /TiO <sub>2</sub>	45	930(w)
1% Nb <sub>2</sub> O <sub>5</sub> /ZrO <sub>2</sub>	39	875(w)
5% Nb <sub>2</sub> O <sub>5</sub> /ZrO <sub>2</sub>	40	920(w)
2% Nb <sub>2</sub> O <sub>5</sub> /SiO <sub>2</sub>	265	960(w)
4% Nb <sub>2</sub> O <sub>5</sub> /SiO <sub>2</sub>	262	960(w), 680(m), 230(w)

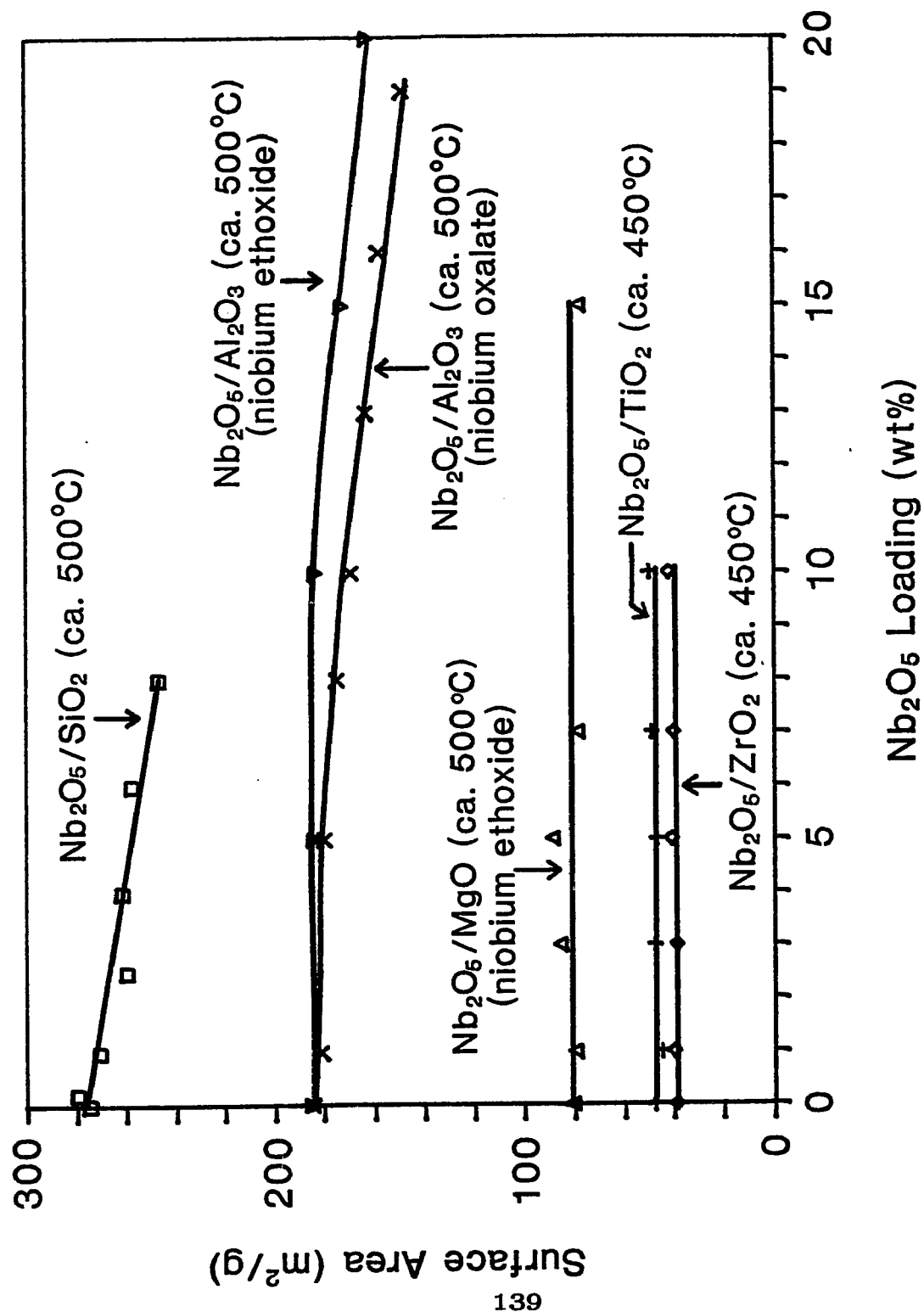


Figure 4.1: The surface areas of the supported niobium oxide catalysts as a function of  $\text{Nb}_2\text{O}_5$  loading

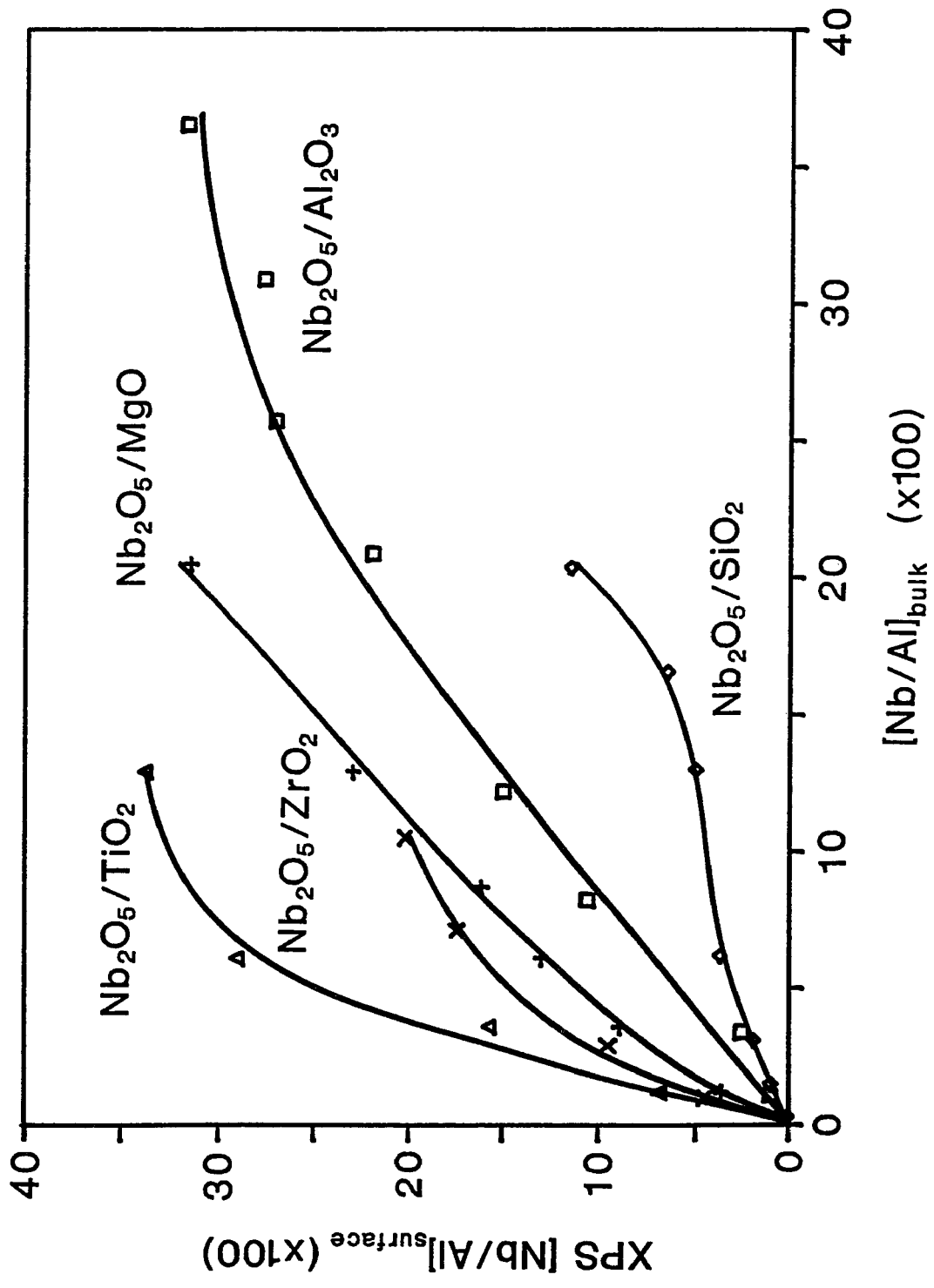


Figure 4.2: X-ray photoelectron spectroscopy analysis of supported niobium oxide catalysts

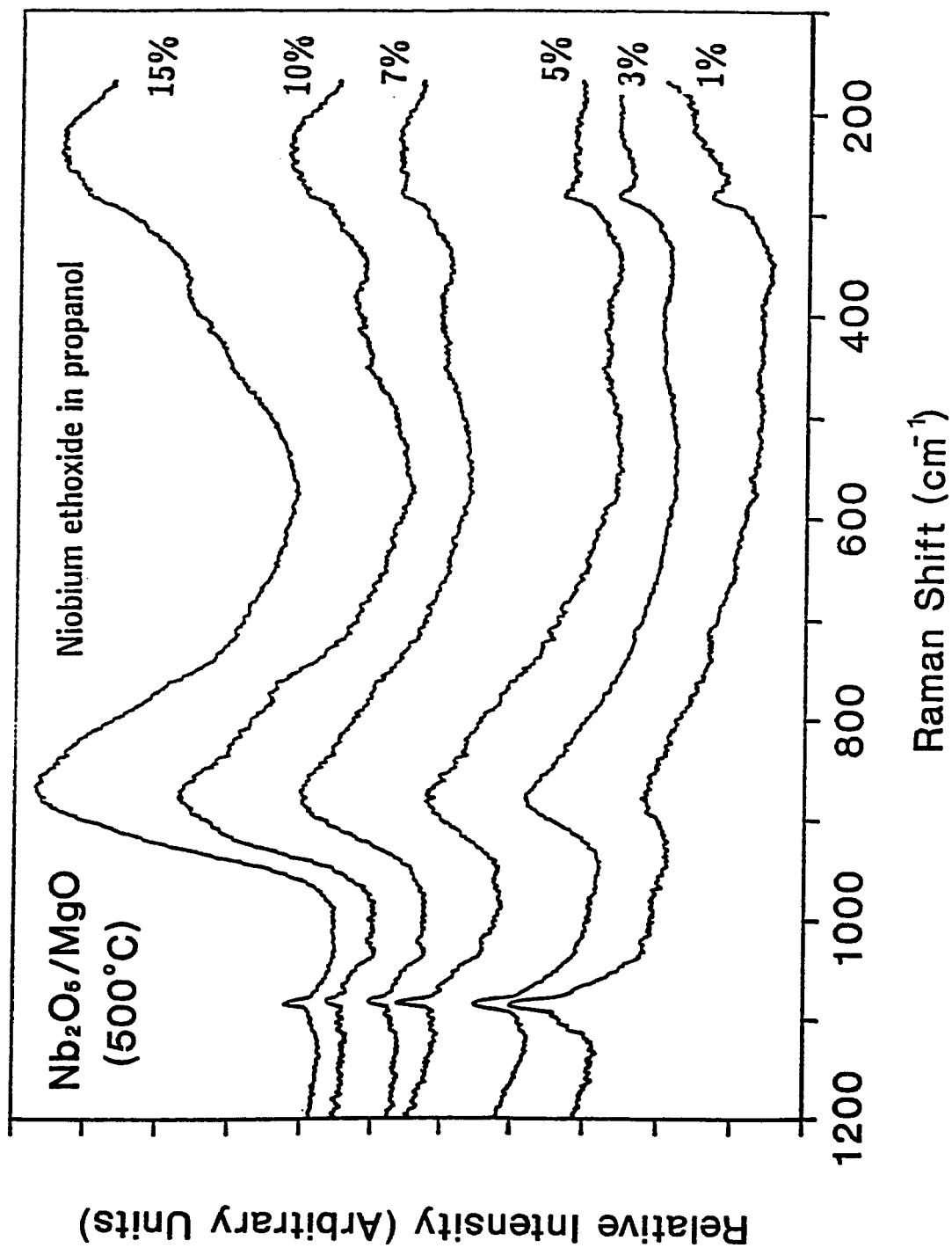


Figure 4.3: The Raman spectra of  $\text{MgO}$  supported niobium oxide (calcined at  $500^\circ\text{C}$ ) as a function of  $\text{Nb}_2\text{O}_5$  loading

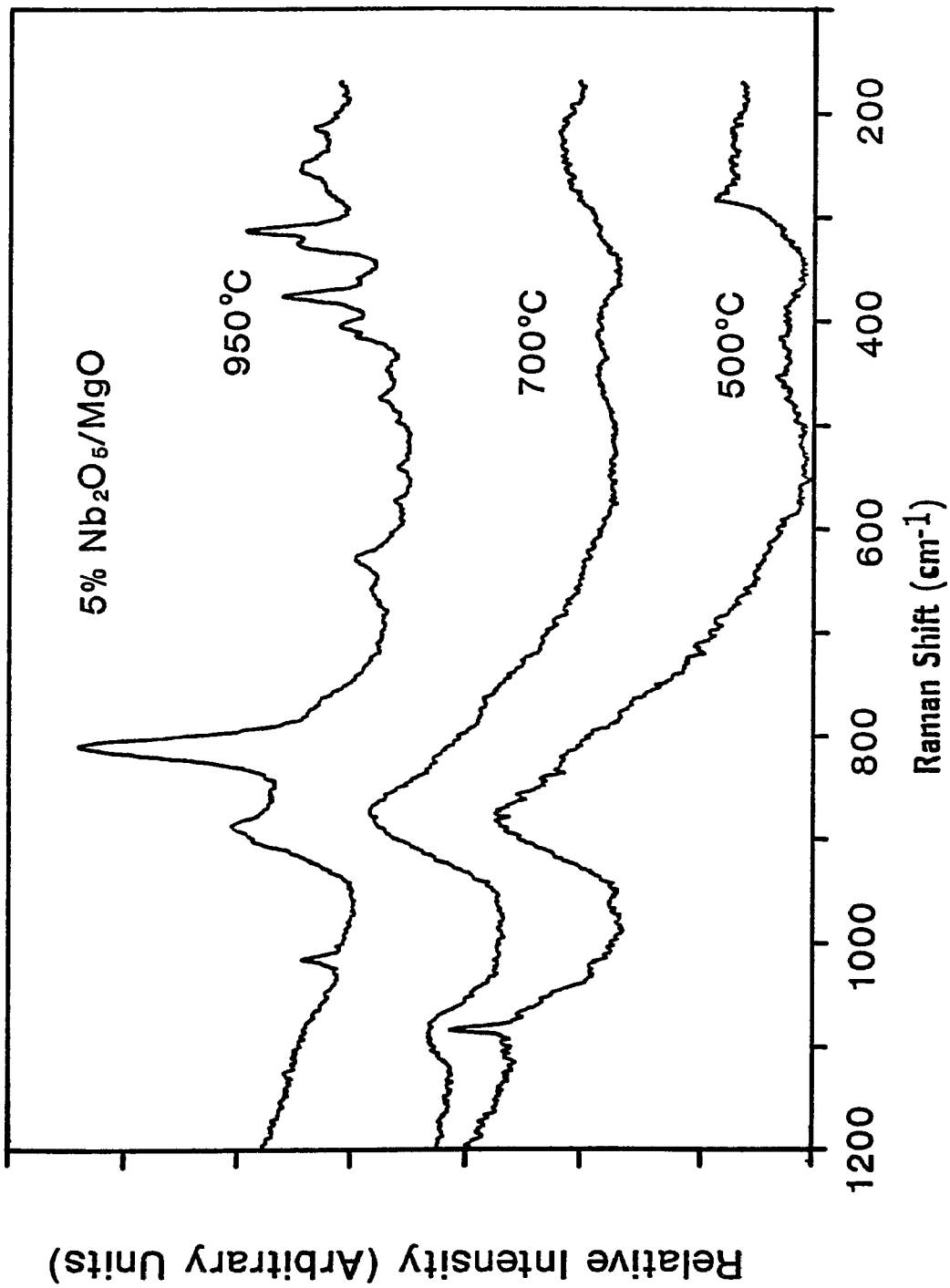


Figure 4.4: The Raman spectra of 5 wt%  $\text{Nb}_2\text{O}_5/\text{MgO}$  as a function of calcination temperature

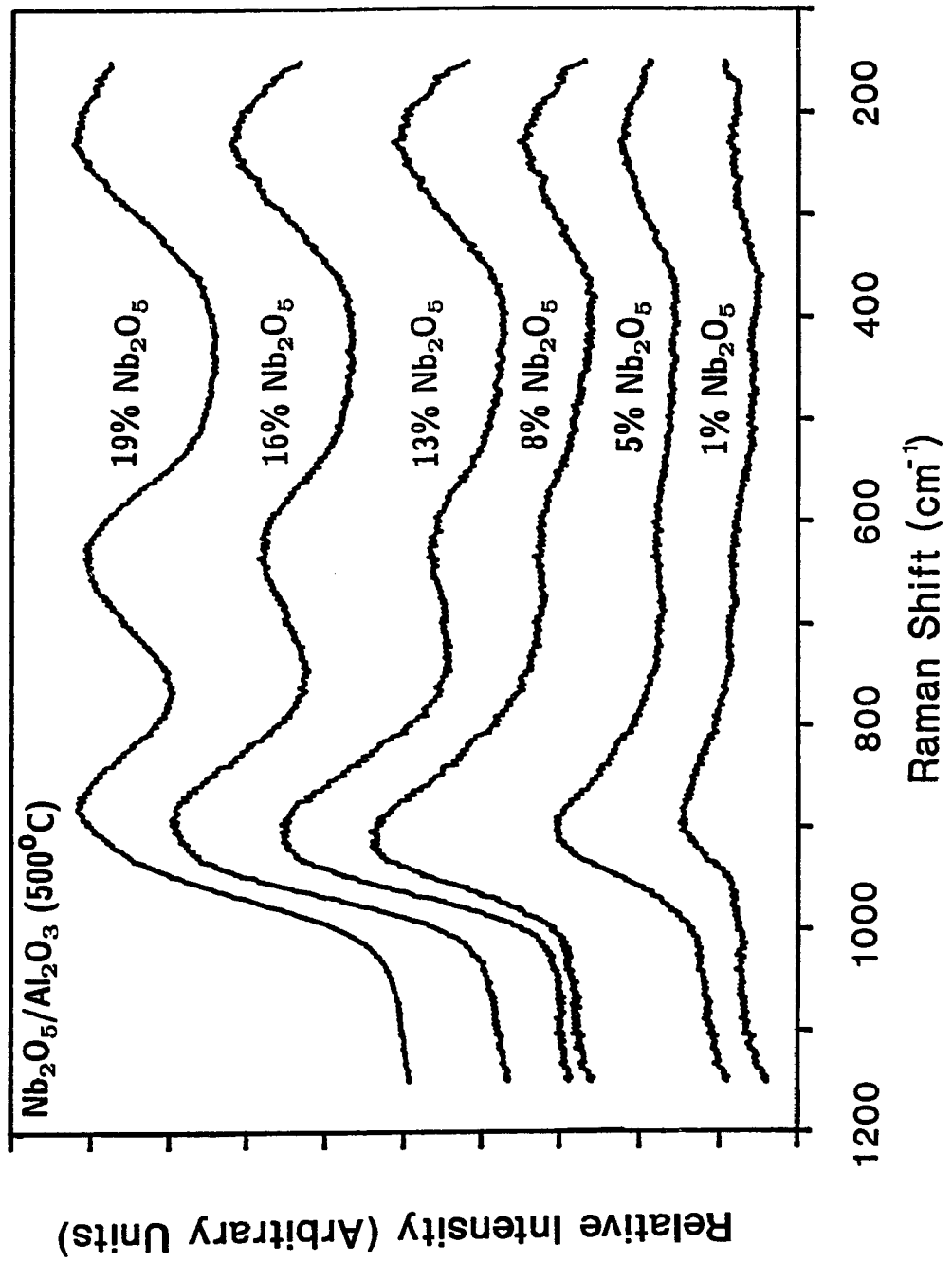


Figure 4.5: The Raman spectra of aqueously prepared  $\text{Al}_2\text{O}_3$  supported niobium oxide (calcined  $500^\circ\text{C}$ ) as a function of  $\text{Nb}_2\text{O}_5$  loading

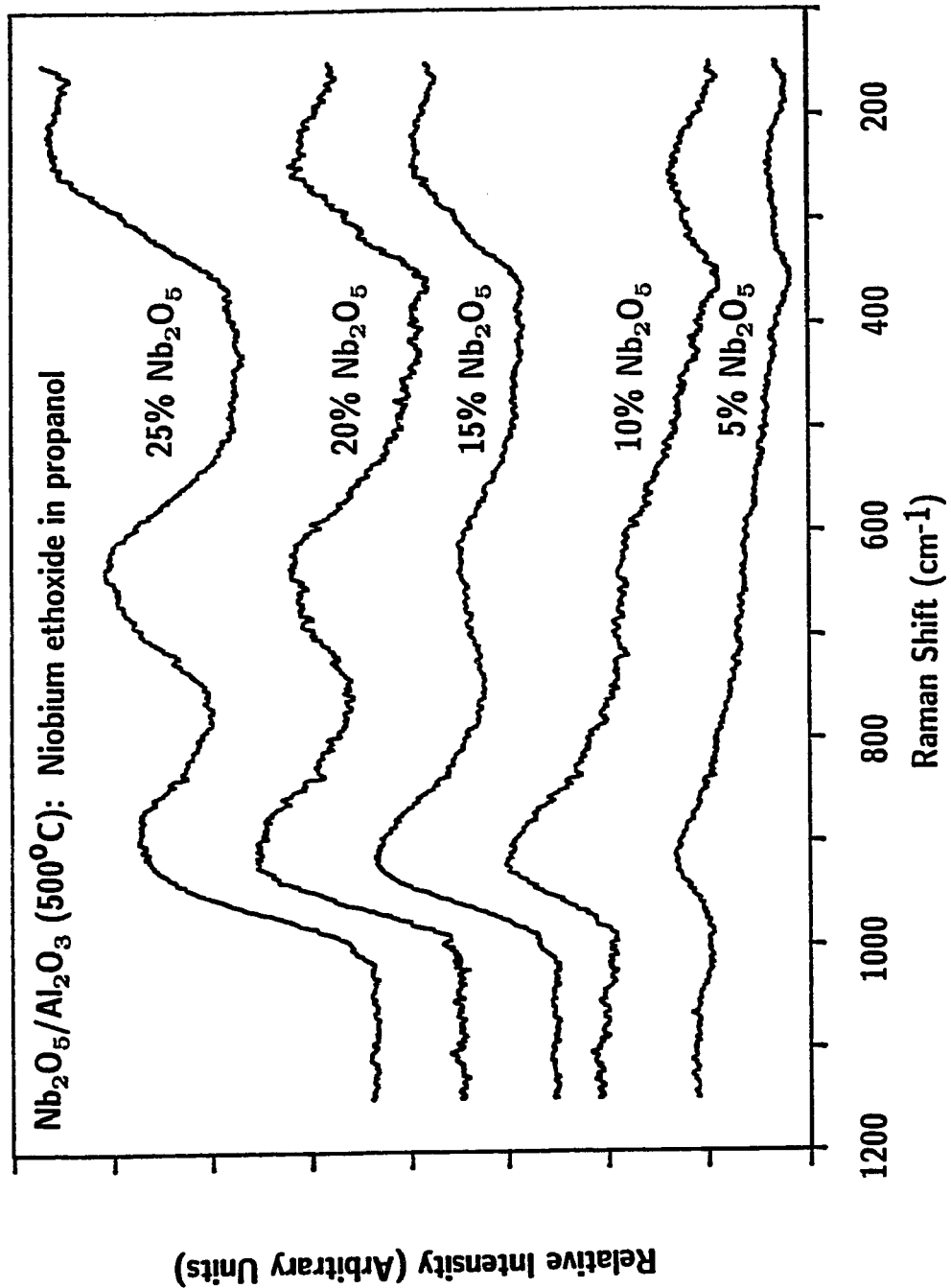
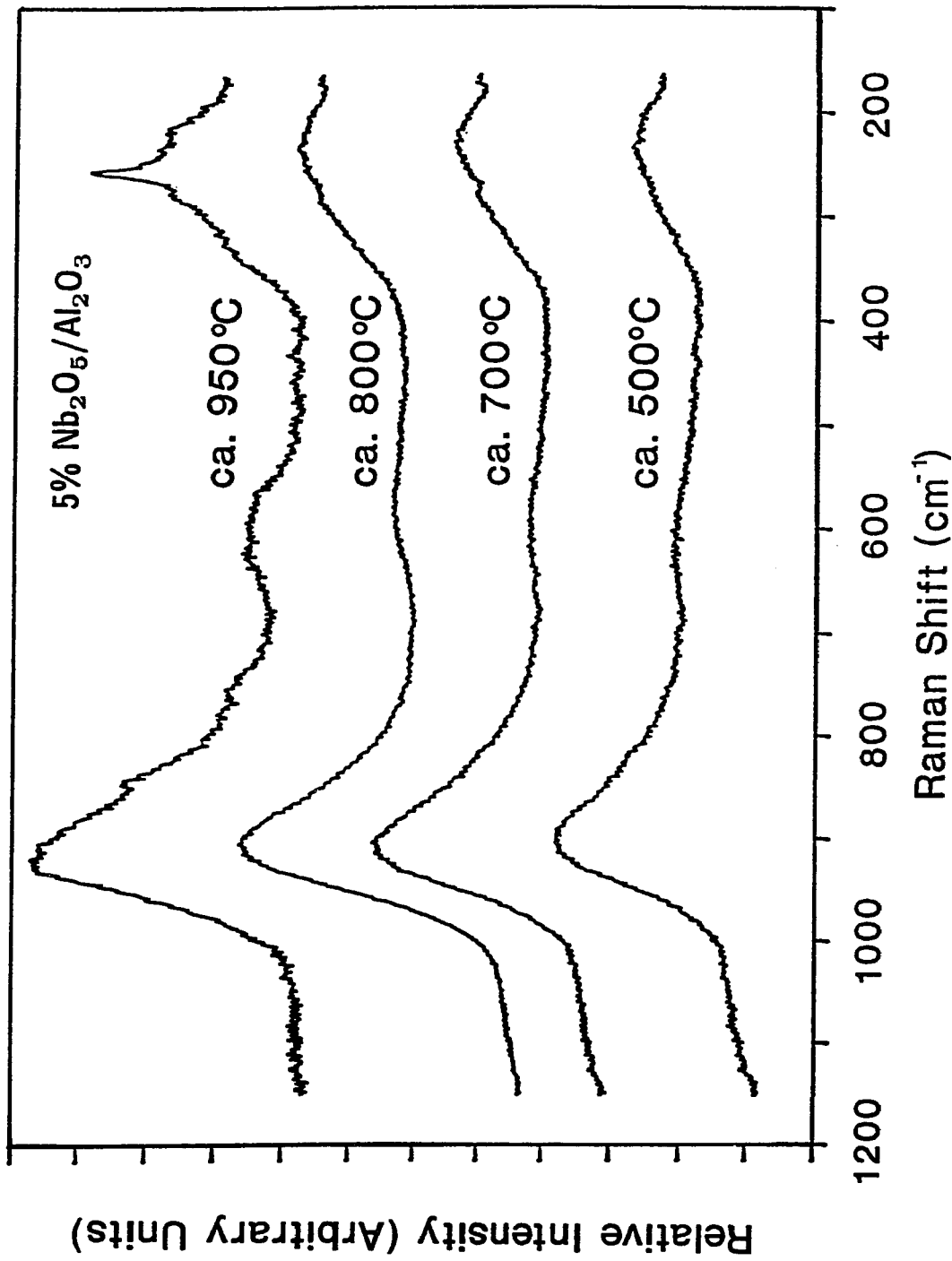
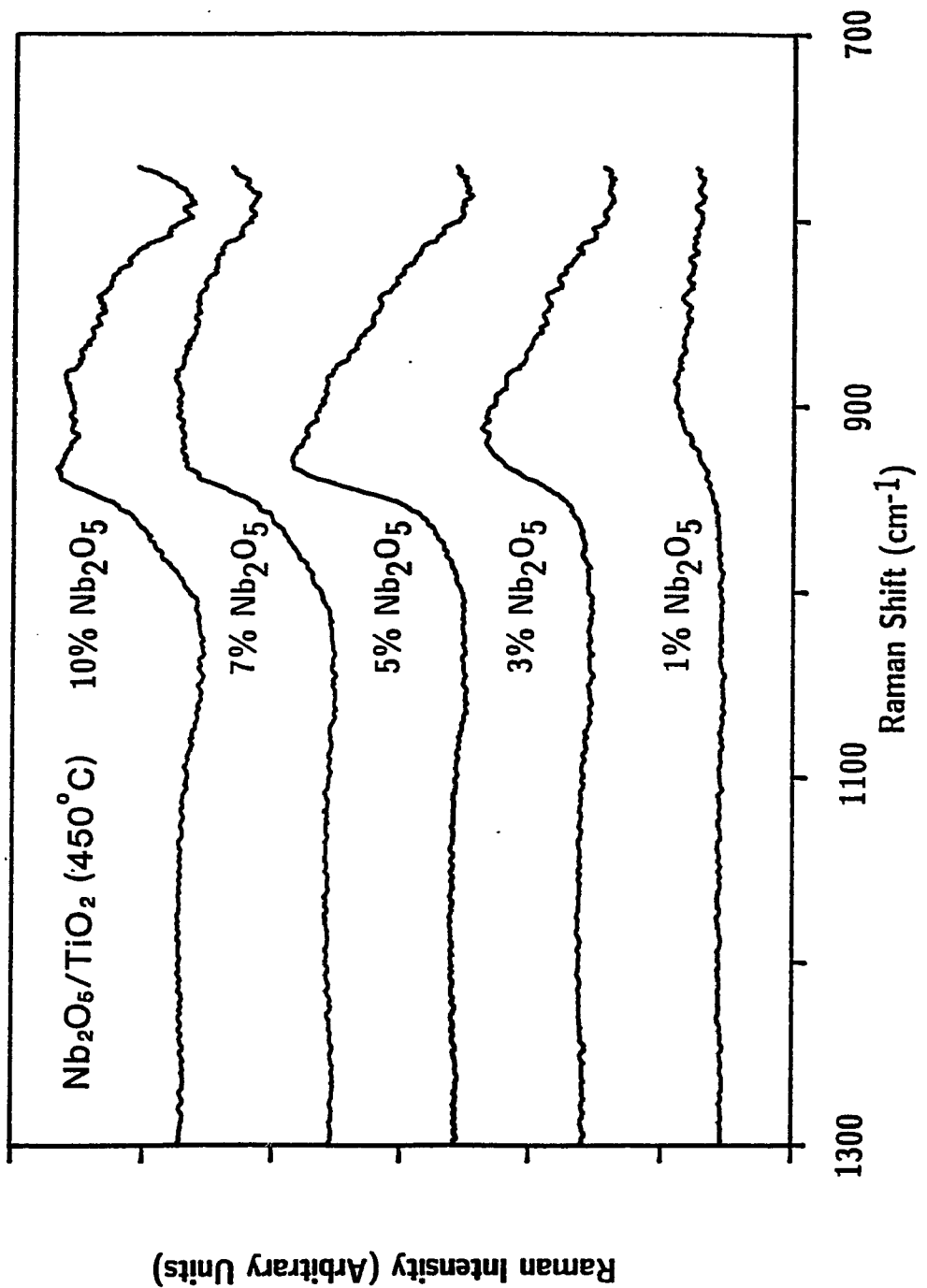


Figure 4.6: The Raman spectra of nonaqueously prepared  $\text{Al}_2\text{O}_3$  supported niobium oxide (calcined at 500°C) as a function of  $\text{Nb}_2\text{O}_5$  loading



**Figure 4.7:** The Raman spectra of 5 wt%  $\text{Nb}_2\text{O}_5/\text{Al}_2\text{O}_3$  as a function of calcination temperature



**Figure 4.8:** The Raman spectra of TiO<sub>2</sub> supported niobium oxide (calcined at 450°C) as a function of Nb<sub>2</sub>O<sub>6</sub> loading

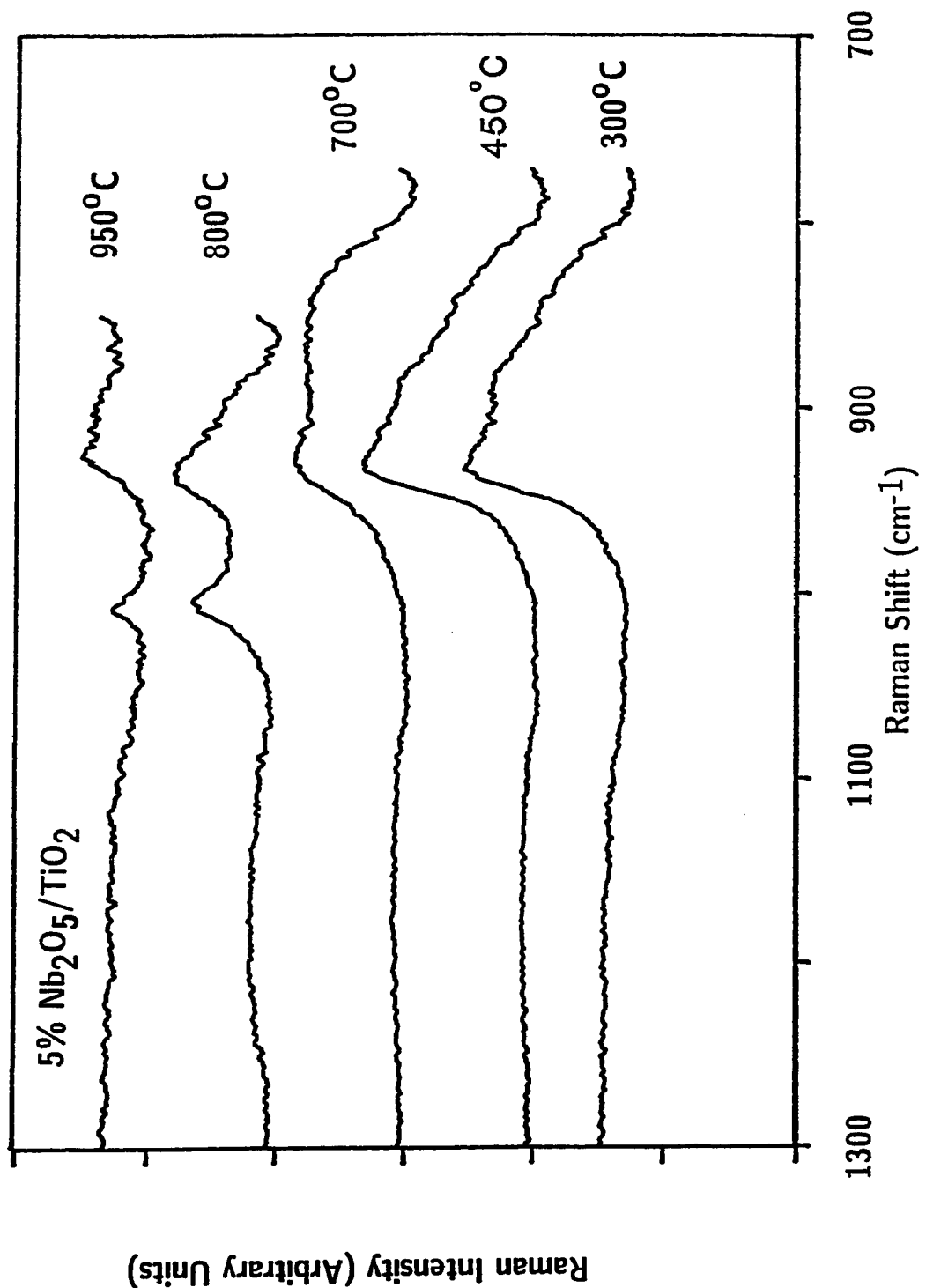
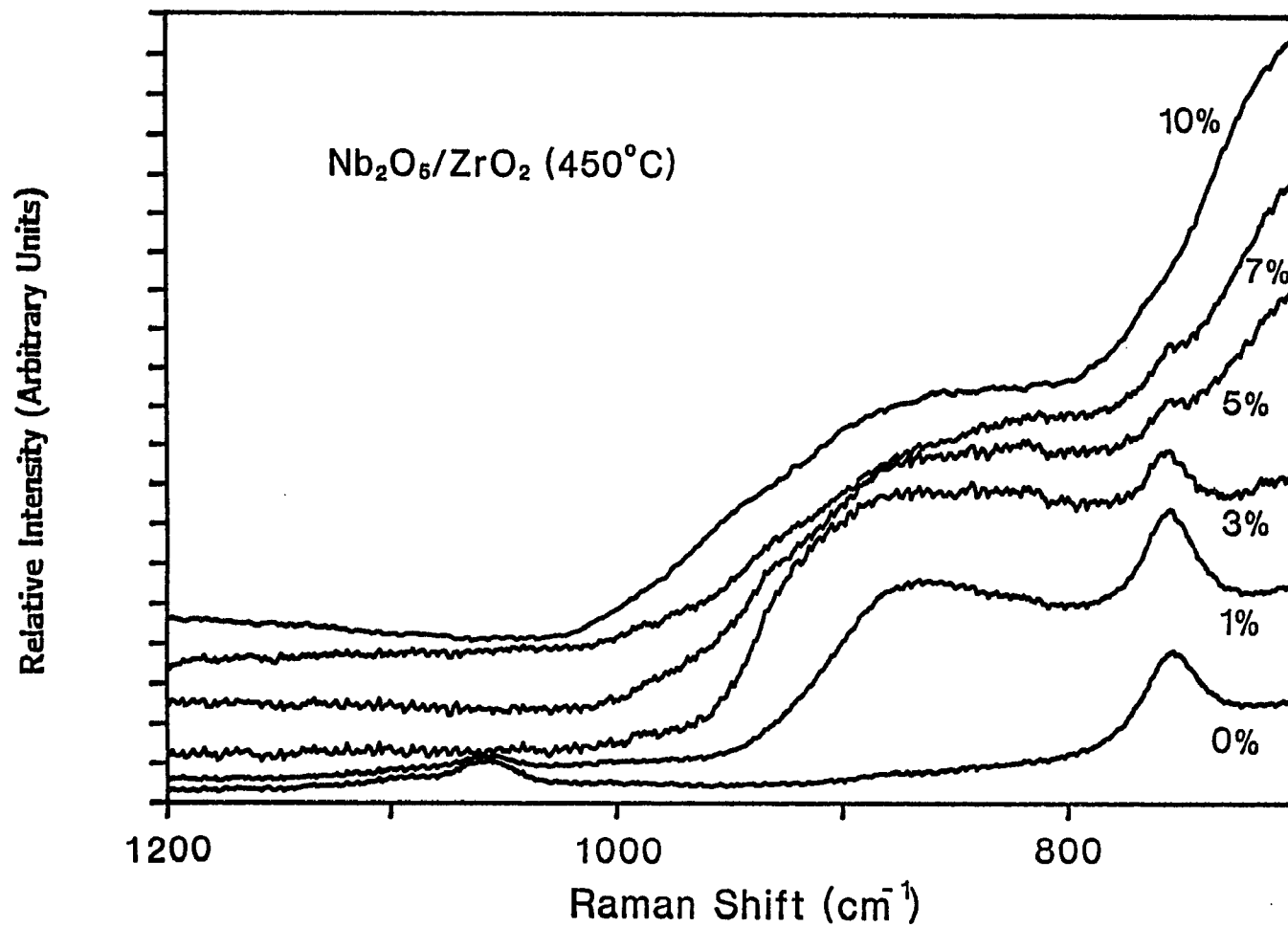
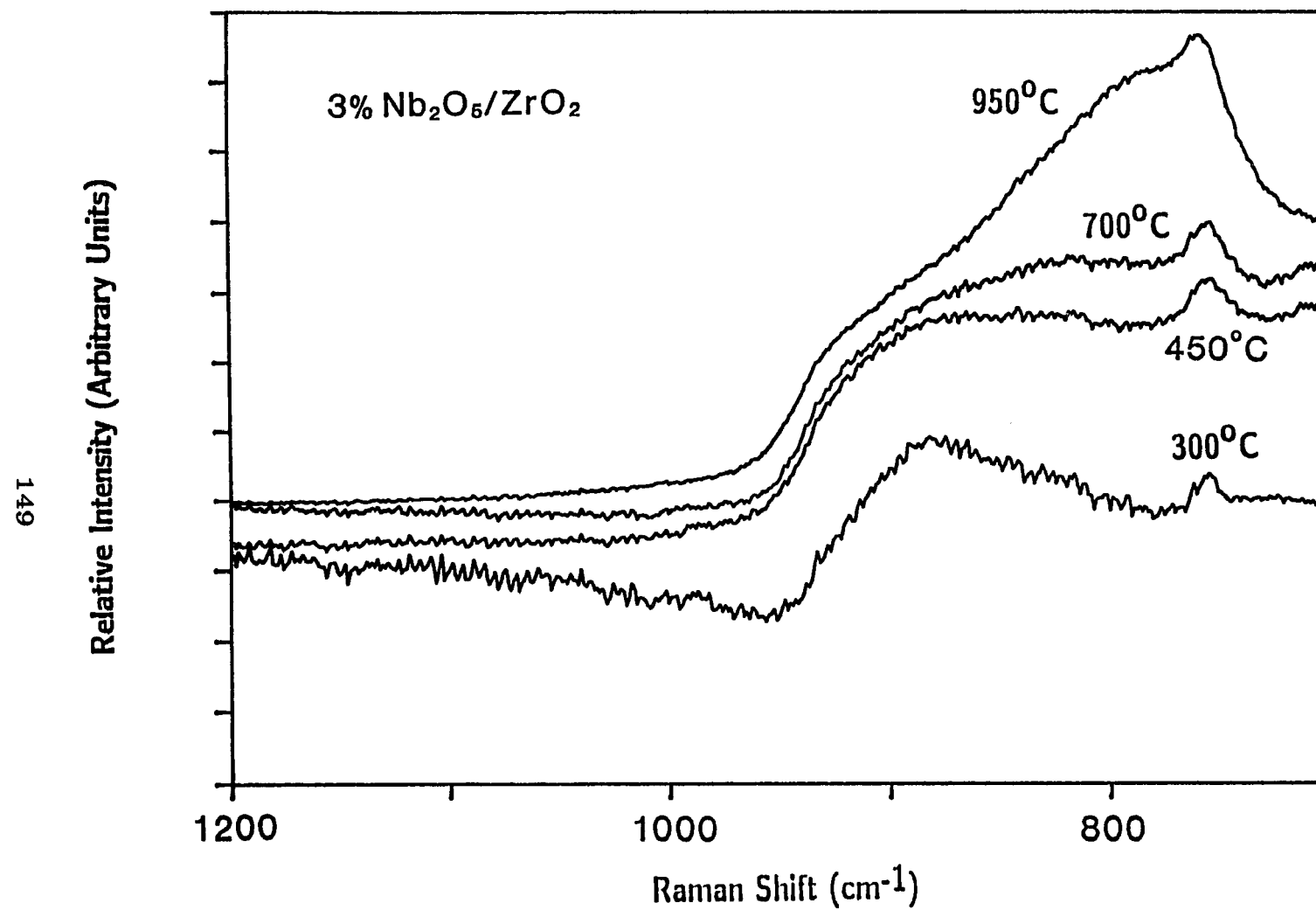


Figure 4.9: The Raman spectra of 5 wt%  $\text{Nb}_2\text{O}_5/\text{TiO}_2$  as a function of calcination temperature



**Figure 4.10:** The Raman spectra of  $\text{ZrO}_2$  supported niobium oxide (calcined at  $450^\circ\text{C}$ ) as a function of  $\text{Nb}_2\text{O}_5$  loading



**Figure 4.11:** The Raman spectra of 3 wt%  $\text{Nb}_2\text{O}_5/\text{ZrO}_2$  as a function of calcination temperature

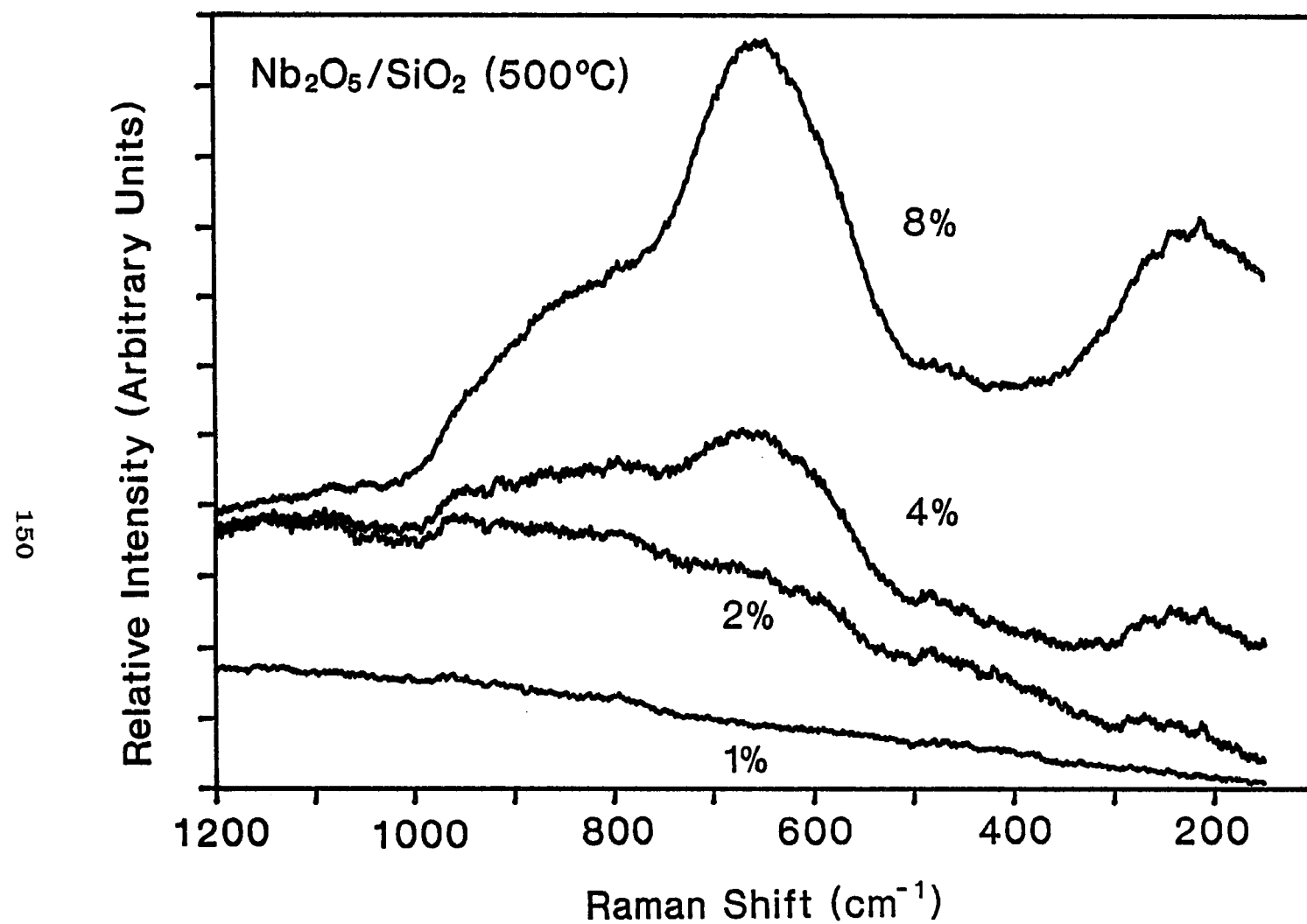


**Figure 4.12:** The Raman spectra of  $\text{SiO}_2$  supported niobium oxide (calcined at  $500^\circ\text{C}$ ) as a function of  $\text{Nb}_2\text{O}_5$  loading

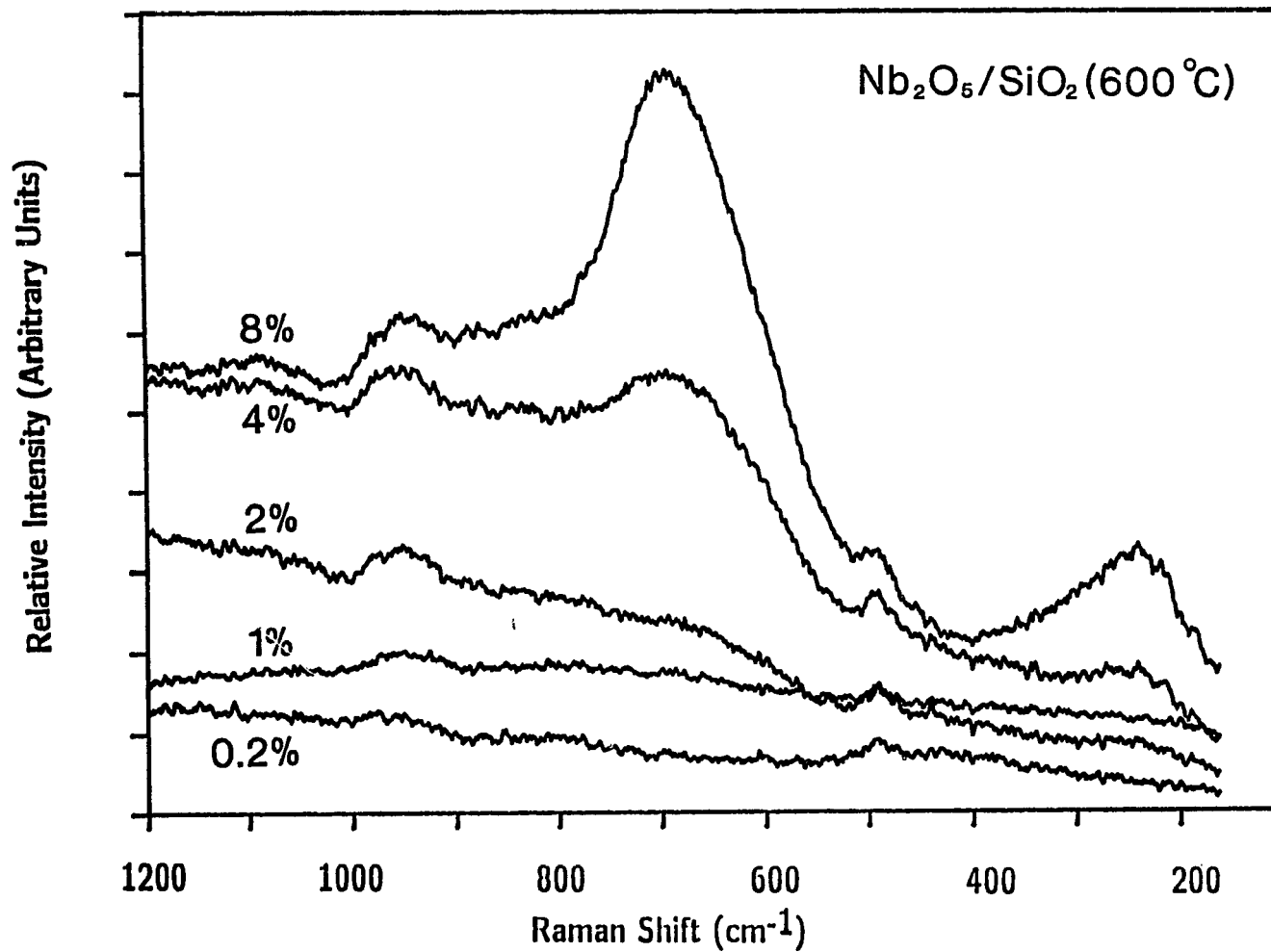


**Figure 4.13:** The Raman spectra of  $\text{SiO}_2$  supported niobium oxide (calcined at  $600^\circ\text{C}$ ) as a function of  $\text{Nb}_2\text{O}_5$  loading

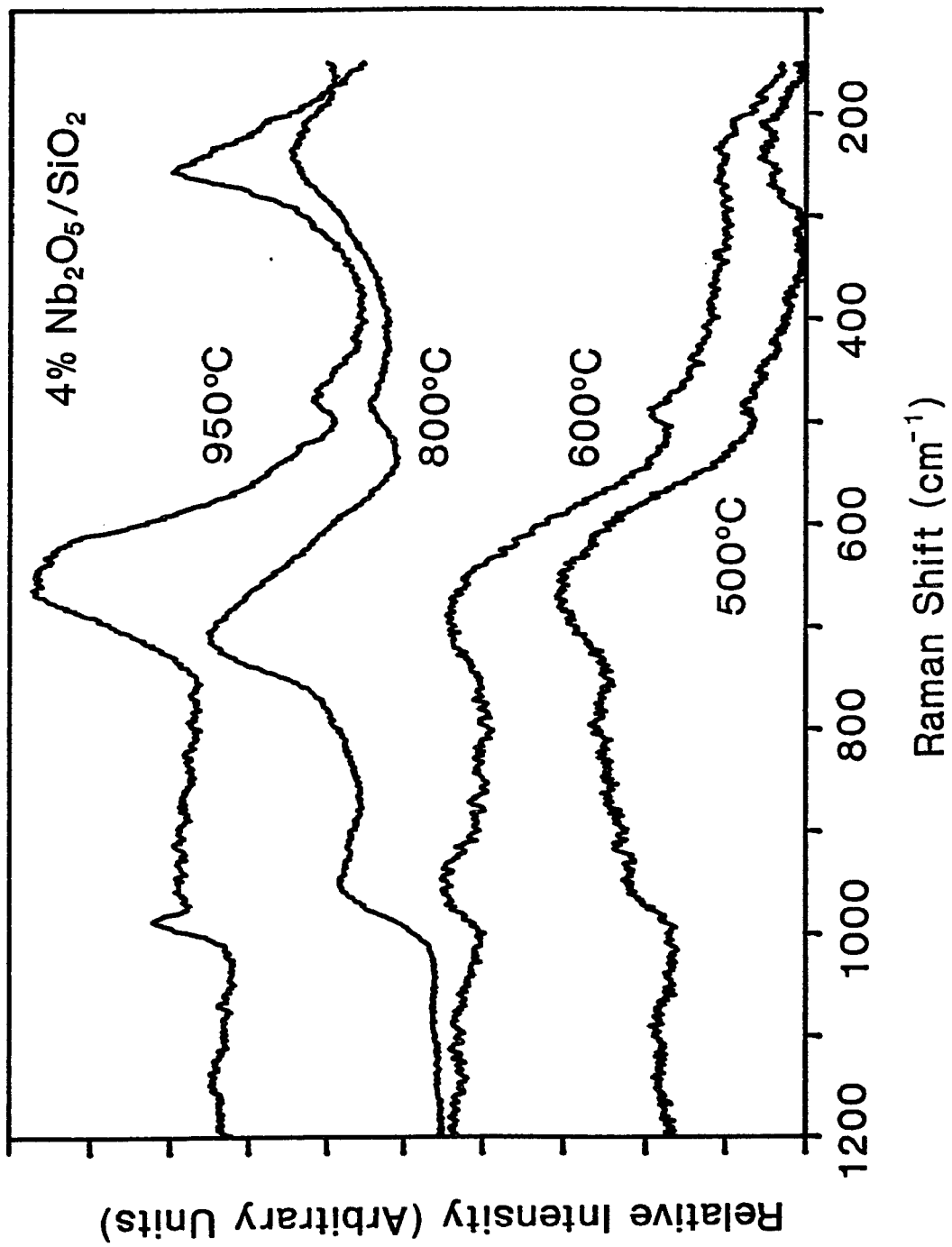


Figure 4.14: The Raman spectra of 4 wt%  $\text{Nb}_2\text{O}_5/\text{SiO}_2$  as a function of calcination temperature

## **CHAPTER 5**

# **MOLECULAR STRUCTURES OF SUPPORTED NIOBIUM OXIDE CATALYSTS UNDER IN SITU CONDITIONS**

## SUMMARY

Supported niobium oxide catalysts were investigated by in situ Raman spectroscopy as a function of  $\text{Nb}_2\text{O}_5$  loading and oxide support ( $\text{MgO}$ ,  $\text{Al}_2\text{O}_3$ ,  $\text{TiO}_2$ ,  $\text{ZrO}_2$ , and  $\text{SiO}_2$ ) in order to determine the molecular structures of the dehydrated surface niobium oxide species. On the  $\text{SiO}_2$  support, only one dehydrated surface niobium oxide species corresponding to the highly distorted  $\text{NbO}_6$  octahedral structure at  $\sim 980 \text{ cm}^{-1}$  is present. The highly distorted  $\text{NbO}_6$  octahedra responsible for Raman bands at  $\sim 985$  and  $\sim 935 \text{ cm}^{-1}$  are also observed on the  $\text{TiO}_2$  and  $\text{ZrO}_2$  supports at high surface coverages, however, the dehydrated surface niobium oxide phases possessing Raman bands in the  $600$ - $700 \text{ cm}^{-1}$  region can not be directly observed for  $\text{Nb}_2\text{O}_5/\text{TiO}_2$  and  $\text{Nb}_2\text{O}_5/\text{ZrO}_2$  because of the strong vibrations of the oxide supports in this region. Below half a monolayer coverage on the  $\text{Al}_2\text{O}_3$  support, two kinds of dehydrated surface niobium oxide species possessing highly and moderately distorted  $\text{NbO}_6$  octahedra with  $\text{Nb}=\text{O}$  Raman bands at  $\sim 980$  and  $\sim 883 \text{ cm}^{-1}$ , respectively, are present. Upon approaching monolayer coverage on the  $\text{Al}_2\text{O}_3$  support, additional Raman bands at  $\sim 935$  and  $\sim 647 \text{ cm}^{-1}$  characteristic of highly and slightly distorted  $\text{NbO}_6$  octahedra are present and are suggestive of a layered niobium oxide structure. Multiple niobium oxide species are present in the  $\text{Nb}_2\text{O}_5/\text{MgO}$  system and are due to the strong acid-base interactions between  $\text{Nb}_2\text{O}_5$  and  $\text{Mg}^{2+}$  as well as  $\text{Ca}^{2+}$  impurity cations present on the surface. The various dehydrated surface niobium oxide species present in the supported niobium oxide catalysts appear to be related to the oxide support surface hydroxyl chemistry.

### 5.1. INTRODUCTION

Recent studies of supported metal oxide catalysts have revealed that the supported metal oxide phase forms a two-dimensional metal oxide overlayer on oxide supports such as  $\text{Al}_2\text{O}_3$ ,  $\text{TiO}_2$ , and  $\text{SiO}_2$  [5,7,9,10,12,121,124]. These surface metal oxide phases possess different chemical states, which may simultaneously be present on the support surface, than their bulk metal oxide crystallites. The different chemical states of the surface metal oxide phases can be discriminated with Raman spectroscopy because each state possesses a unique vibrational spectrum corresponding to its structure [65,125]. Additional fundamental information about the supported metal oxide catalysts is provided by *in situ* Raman spectroscopy since this technique provides structural information about the surface metal oxide phases under a controlled environment (temperature and gas phase composition) [65,78,125,126].

The molecular structures of supported vanadium oxide on  $\text{Al}_2\text{O}_3$ ,  $\text{TiO}_2$ , and  $\text{SiO}_2$  supports have been extensively characterized under *in situ* conditions, where the surface metal oxide phases are dehydrated, with Raman spectroscopy [127-130], infrared spectroscopy [131],  $^{51}\text{V}$  NMR spectroscopy [132], as well as XANES [133]. Upon dehydration, the surface vanadium oxide Raman bands above

800  $\text{cm}^{-1}$ , which are characteristic of the V=O symmetric stretch, split into a sharp Raman band in the 1026-1038  $\text{cm}^{-1}$  region and a broad Raman band at  $\sim 900 \text{ cm}^{-1}$ . The relative intensity of these two Raman bands varies with surface vanadium oxide coverage on the oxide supports [78,127,128]. However, the  $\text{V}_2\text{O}_5/\text{SiO}_2$  system only possesses a single Raman band at  $\sim 1038 \text{ cm}^{-1}$  [127]. Raman and  $^{51}\text{V}$  NMR studies suggest that the dehydrated surface vanadium oxide phases are present as a monoxo tetrahedral vanadate species (Raman band in the 1026-1038  $\text{cm}^{-1}$  region) and a polymeric tetrahedral metavanadate species (Raman band at  $\sim 900 \text{ cm}^{-1}$ ) [18]. In situ IR studies also suggest that the dehydrated surface vanadium oxide species are present as an isolated vanadate species (IR band in the 1030-1050  $\text{cm}^{-1}$ ) and a polyvanadate species (expected IR band in the 600-800  $\text{cm}^{-1}$ ) [131]. In addition, in situ Raman studies on  $\text{Al}_2\text{O}_3$ ,  $\text{TiO}_2$ , and  $\text{SiO}_2$  supported molybdenum oxide and tungsten oxide catalysts also exhibit Raman shifts of the surface molybdenum oxide (from  $\sim 950$  to 985-1012  $\text{cm}^{-1}$ ) [78,135-137] and the surface tungsten oxide (from  $\sim 960$  to 1010-1027  $\text{cm}^{-1}$ ) [65,78,113,135,138,139] phases due to dehydration of the surface metal oxide phases. In situ XANES/EXAFS studies on  $\text{SiO}_2$  and  $\text{Al}_2\text{O}_3$  supported vanadium oxide catalysts reveal that the hydrated vanadium oxide species on  $\text{SiO}_2$  possess a polymeric octahedral structure which

transforms into a monoxo tetrahedral vanadate structure upon dehydration, and both hydrated and dehydrated vanadium oxide species on  $\text{Al}_2\text{O}_3$  possess an isolated tetrahedral structure at low surface coverages [133].

Raman and XPS studies on the supported niobium oxide catalysts under ambient conditions reveal that the surface niobium oxide phase forms a two-dimensional overlayer on oxide supports ( $\text{MgO}$ ,  $\text{Al}_2\text{O}_3$ ,  $\text{TiO}_2$ ,  $\text{ZrO}_2$ , and  $\text{SiO}_2$ ), and the monolayer coverage of supported niobium oxide catalysts is reached at  $\sim 19$  wt%  $\text{Nb}_2\text{O}_5/\text{Al}_2\text{O}_3$ ,  $\sim 7$  wt%  $\text{Nb}_2\text{O}_5/\text{TiO}_2$ ,  $\sim 5$  wt%  $\text{Nb}_2\text{O}_5/\text{ZrO}_2$ , and  $\sim 2$  wt%  $\text{Nb}_2\text{O}_5/\text{SiO}_2$ , but not for the  $\text{Nb}_2\text{O}_5/\text{MgO}$  system due to the incorporation of  $\text{Nb}^{+5}$  into the  $\text{MgO}$  support [124]. The molecular structures of the surface niobium oxide phases are controlled by the surface pH of the system. Basic hydrated surfaces result in the formation of highly distorted  $\text{NbO}_6$  groups and acidic hydrated surfaces result in the formation of slightly distorted  $\text{NbO}_6$ ,  $\text{NbO}_7$ , and  $\text{NbO}_8$  groups (with the exception of the  $\text{Nb}_2\text{O}_5/\text{SiO}_2$  system which forms bulk  $\text{Nb}_2\text{O}_5$ ). The molecular structures of the dehydrated surface niobium oxide phases, however, are still not understood and only preliminary *in situ* XANES studies for silica supported niobium oxide catalysts have been reported by Yoshida et al. [14]. In the present study, the  $\text{MgO}$ ,  $\text{Al}_2\text{O}_3$ ,  $\text{TiO}_2$ ,  $\text{ZrO}_2$ ,

and  $\text{SiO}_2$  supported niobium oxide catalysts will be investigated under in situ conditions with Raman spectroscopy in order to determine the molecular structures of the dehydrated surface niobium oxide phases as a function of  $\text{Nb}_2\text{O}_5$  loading and the specific oxide support.

## 5.2. EXPERIMENTAL

### 5.2.1. Materials and Preparations

Niobium oxalate was supplied by Niobium Products Company (Pittsburgh, PA) with the following chemical analysis: 20.5%  $\text{Nb}_2\text{O}_5$ , 790 ppm Fe, 680 ppm Si, and 0.1% insoluble. Niobium ethoxide (99.999% purity) was purchased from Johnson Matthey (Ward Hill, MA). The oxide supports employed in the present investigation are:  $\text{MgO}$  (Fluka,  $\sim 80 \text{ m}^2/\text{g}$  after calcination at  $700^\circ\text{C}$  for 2 hrs),  $\text{Al}_2\text{O}_3$  (Harshaw,  $\sim 180 \text{ m}^2/\text{g}$  after calcination at  $500^\circ\text{C}$  for 16 hrs),  $\text{TiO}_2$  (Degussa,  $\sim 50 \text{ m}^2/\text{g}$  after calcination at  $450^\circ\text{C}$  for 2 hrs),  $\text{ZrO}_2$  (Degussa,  $\sim 39 \text{ m}^2/\text{g}$  after calcination at  $450^\circ\text{C}$  for 2 hrs), and  $\text{SiO}_2$  (Cab-O-Sil,  $\sim 275 \text{ m}^2/\text{g}$  after calcination at  $500^\circ\text{C}$  for 16 hrs).

The  $\text{TiO}_2$ ,  $\text{ZrO}_2$ ,  $\text{Al}_2\text{O}_3$ , and  $\text{SiO}_2$  supported niobium oxide catalysts were prepared by the incipient-wetness impregnation method using niobium oxalate/oxalic acid aqueous solutions (aqueous preparation) [62]. The water

sensitive MgO support required the use of nonaqueous niobium ethoxide/propanol solutions under a nitrogen environment for the preparation of the Nb<sub>2</sub>O<sub>5</sub>/MgO catalysts.

For the aqueous preparation method the samples were initially dried at room temperature for 16 hrs, further dried at 110-120°C for 16 hrs, and subsequently calcined at 450°C (Nb<sub>2</sub>O<sub>5</sub>/TiO<sub>2</sub> and Nb<sub>2</sub>O<sub>5</sub>/ZrO<sub>2</sub>, 2 hrs) or at 500°C (Nb<sub>2</sub>O<sub>5</sub>/Al<sub>2</sub>O<sub>3</sub> and Nb<sub>2</sub>O<sub>5</sub>/SiO<sub>2</sub>, 16 hrs) under flowing dry air. For the nonaqueous preparation method, the samples were initially dried at room temperature for 16 hrs, further dried at 110-120°C for 16 hrs under flowing N<sub>2</sub>, and subsequently calcined at 500°C for 1 hr under flowing N<sub>2</sub> then for 1 hr under flowing dry air.

#### 5.2.2. In Situ Raman Spectroscopy

The in situ Raman spectrometer consists of a quartz cell and sample holder, a triple-grating spectrometer (SPEX, Model 1877), a photodiode array detector (EG&G, Princeton Applied Research, Model 1420), and an argon-ion laser (Spectra-Physics, Model 171). The sample holder is made from a quartz glass, and a 100-200 mg sample disc is held by a stationary slot in the sample holder. The sample is heated by a cylindrical heating coil surrounding the quartz cell, and the temperature is measured with an

internal thermocouple. The quartz cell is capable of operating up to 600°C, and dry oxygen gas (Linde Specialty Grade, 99.99% purity) is introduced into the cell at a rate of 50-500 cm<sup>3</sup>/min with a delivery pressure of 150-200 torr.

The Raman spectra are collected for the hydrated sample at room temperature, after heating the sample to 500°C in flowing dry air for 30 minutes, and again after cooling down to 50° to avoid the thermal broadening of Raman bands at high temperature. The laser beam 514.5 nm line of the Ar<sup>+</sup> laser with 10-100 mW of power is focused on the sample disc in a right-angle scattering geometry. An ellipsoid mirror collects and reflects the scattering light into the spectrometer's filter stage to reject the elastic scattering. The resulting filtered light, consisting primarily of the Raman component of the scattered light is collected with an EG&G intensified photodiode array detector which is coupled to the spectrometer and is thermoelectrically cooled to -35°C. The photodiode array detector is scanned with an EG&G OMA III Optical Multichannel Analyzer (Model 1463). The Raman spectrum is recorded only in the high wavenumber region (600-1100 cm<sup>-1</sup>) in the present experiments. The overall resolution of the spectra was determined to be better than 1 cm<sup>-1</sup>.

### 5.3. RESULTS

#### 5.3.1. Nb<sub>2</sub>O<sub>5</sub>/SiO<sub>2</sub>

The *in situ* Raman spectra of the silica supported niobium oxide were collected at 25°C (fresh from the oven) and 500°C in the closed cell because intense fluorescence occurred after the samples were cooled down to 50°C in the cell. The hydrated spectra were obtained after exposing the sample to ambient conditions for overnight. The SiO<sub>2</sub> support possesses Raman bands at ~979 and ~812 cm<sup>-1</sup> which are characteristic of the Si-OH stretch and Si-O-Si linkages [140]. The hydrated surface niobium oxide phase possessing a weak Raman band at ~960 cm<sup>-1</sup> shifts to ~980 cm<sup>-1</sup> upon dehydration as shown in Figures 5.1 and 5.2. Thus, the Raman spectrum collected at 25°C (fresh from the oven) possessing both a sharp Raman band at ~980 cm<sup>-1</sup> and a broad Raman band at ~960 cm<sup>-1</sup> indicates that the surface niobium oxide phase is partially dehydrated. For the 4 wt% Nb<sub>2</sub>O<sub>5</sub>/SiO<sub>2</sub> sample, an additional Raman band is present at ~680 cm<sup>-1</sup> and does not shift under the *in situ* conditions.

#### 5.3.2. Nb<sub>2</sub>O<sub>5</sub>/TiO<sub>2</sub>

The dehydration of the 1 wt% Nb<sub>2</sub>O<sub>5</sub>/TiO<sub>2</sub> sample reveals that the hydrated supported niobium oxide phase possessing a very weak and broad Raman band at ~895 cm<sup>-1</sup>

shifts to  $\sim 983$   $\text{cm}^{-1}$  as shown in Fig. 5.3 (also see Fig. 4.8). The disappearance of the weak Raman band at  $\sim 792$   $\text{cm}^{-1}$  at  $500^\circ\text{C}$ , the first overtone of the Raman band at  $\sim 394$   $\text{cm}^{-1}$  of  $\text{TiO}_2$ , is due to the thermal broadening of the crystalline  $\text{TiO}_2$  phase. Upon increasing the  $\text{Nb}_2\text{O}_5$  loading to 7 wt%, an additional weak and broad Raman band appears at  $\sim 935$   $\text{cm}^{-1}$  upon dehydrating the supported niobium oxide phase as shown in Fig. 5.4.

### 5.3.3. $\text{Nb}_2\text{O}_5/\text{ZrO}_2$

The in situ Raman spectra of the zirconia supported niobium oxide catalysts are presented in Figures 5.5 and 5.6 with different  $\text{Nb}_2\text{O}_5$  loadings. The  $\text{ZrO}_2$  support possesses a weak Raman band at  $\sim 756$   $\text{cm}^{-1}$  which arises from the first overtone of its strong Raman band at  $\sim 380$   $\text{cm}^{-1}$ . The thermal effect on the Raman scattering cross section of this band is similar to  $\text{TiO}_2$ . For the 1 wt%  $\text{Nb}_2\text{O}_5/\text{ZrO}_2$  sample, the hydrated supported niobium oxide phase possesses a weak and broad Raman band at  $\sim 875$   $\text{cm}^{-1}$  which shifts to  $\sim 958$  and  $\sim 823$   $\text{cm}^{-1}$  upon dehydration (see Fig. 5.8). For the 5 wt%  $\text{Nb}_2\text{O}_5/\text{ZrO}_2$  sample, the dehydrated surface niobium oxide Raman bands appear at  $\sim 988$ ,  $\sim 935$ , and  $\sim 823$   $\text{cm}^{-1}$ .

#### 5.3.4. Nb<sub>2</sub>O<sub>5</sub>/Al<sub>2</sub>O<sub>3</sub>

The in situ Raman spectra of the alumina supported niobium oxide containing 5 and 19 wt% Nb<sub>2</sub>O<sub>5</sub>, are shown in Figures 5.7 and 5.8, respectively. For the 5 wt% Nb<sub>2</sub>O<sub>5</sub> loading, a broad and weak Raman band due to the surface niobium oxide phase (since the Al<sub>2</sub>O<sub>3</sub> support is not Raman active) appears at ~905 cm<sup>-1</sup> under ambient conditions, and shifts to ~980 and ~883 cm<sup>-1</sup> upon surface dehydration. For the 19 wt% Nb<sub>2</sub>O<sub>5</sub> loading, the hydrated sample exhibits Raman bands at ~890 and ~645 cm<sup>-1</sup> due to the hydrated surface niobium oxide phases on the alumina support. Upon dehydration, the Raman band at ~890 cm<sup>-1</sup> shifts to ~988, ~935, and ~883 cm<sup>-1</sup> and the Raman band at ~645 cm<sup>-1</sup>, however, remains at the same position.

The Raman spectra of the dehydrated surface niobium oxide phases on alumina are also shown in Fig. 5.9 as a function of Nb<sub>2</sub>O<sub>5</sub> loading. For the loadings less than 5 wt% Nb<sub>2</sub>O<sub>5</sub>, only Raman bands at ~980 and ~883 cm<sup>-1</sup> are present and their intensity increases with Nb<sub>2</sub>O<sub>5</sub> loading. For the 8 wt% Nb<sub>2</sub>O<sub>5</sub> loading, the Raman band at ~980 cm<sup>-1</sup> shifts to ~988 cm<sup>-1</sup> and new Raman bands appear at ~950 and ~630 cm<sup>-1</sup>. Upon further increasing the Nb<sub>2</sub>O<sub>5</sub> loadings (> 8 wt%), the Raman bands originally occurring at ~950 and ~630 cm<sup>-1</sup> shift to ~935 and ~647 cm<sup>-1</sup>, respectively, and

their intensity increases with  $\text{Nb}_2\text{O}_5$  loading.

### 5.3.5. $\text{Nb}_2\text{O}_5/\text{MgO}$

The *in situ* Raman spectra of magnesia supported niobium oxide, with 5 and 10 wt%  $\text{Nb}_2\text{O}_5$ , are shown in Figures 5.10 and 5.11, respectively. The broad Raman band at  $\sim 870 \text{ cm}^{-1}$  is associated with the supported niobium oxide phase under ambient conditions since  $\text{MgO}$  is not Raman active and increases with  $\text{Nb}_2\text{O}_5$  loading. The Raman band at  $\sim 1085 \text{ cm}^{-1}$  is due to a  $\text{CaCO}_3$  impurity present in the  $\text{MgO}$  support. Under *in situ* conditions, the Raman band originally at  $\sim 870 \text{ cm}^{-1}$  splits into bands at  $\sim 935$ ,  $\sim 892$ , and  $\sim 833 \text{ cm}^{-1}$  for the 5 wt%  $\text{Nb}_2\text{O}_5/\text{MgO}$  sample and into bands at  $\sim 985$ ,  $\sim 898$ , and  $\sim 834 \text{ cm}^{-1}$  for the 10 wt%  $\text{Nb}_2\text{O}_5/\text{MgO}$  sample. After the sample was exposed to ambient conditions for overnight, the broad Raman band at  $\sim 870 \text{ cm}^{-1}$  reappeared due to the hydration of the surface niobium oxide phases by adsorbed moisture (see Fig. 5.2).

## 5.4. DISCUSSIONS

Raman studies on supported niobium oxide catalysts reveal that niobium oxide is present as a two-dimensional surface overlayer on oxide supports below monolayer coverage [124]. The two-dimensional surface niobium oxide

overlayer possesses the major Raman bands in the 800-1000  $\text{cm}^{-1}$  region which are different than bulk crystalline  $\text{Nb}_2\text{O}_5$  phases (major Raman band at  $\sim 690 \text{ cm}^{-1}$ ). Crystalline  $\text{Nb}_2\text{O}_5$  phases are present above monolayer coverage and at elevated temperatures. The molecular structures of the surface niobium oxide phases under ambient conditions, where adsorbed water is present, can be determined by directly comparing their Raman spectra with those of niobium oxide aqueous solutions and are controlled by the surface pH [124,141]. Under *in situ* conditions the adsorbed moisture desorbs upon heating and the surface metal oxide overlayers on the oxide supports become dehydrated [65,78,93,125]. The molecular structures of the surface metal oxide phases are generally altered upon dehydration because the surface pH can only exert its influence via an aqueous environment. Consequently, Raman shifts upon dehydration constitute direct proof of a two-dimensional surface metal oxide phase and the removal of coordinated water [65,78,93,125].

The Raman band positions of the supported niobium oxide catalysts under *in situ* conditions (spectra were taken at 50°C in a closed cell after being heated to 500°C in flowing oxygen with the exception of the  $\text{Nb}_2\text{O}_5/\text{SiO}_2$  spectra which were taken at 500°C) are presented in Table 5.1. The Raman positions of the surface niobium oxide

phases at 50°C usually occur at 2-3 cm<sup>-1</sup> higher than at 500°C due to the slight influence of temperature upon the Nb=O bond lengths. Upon dehydration, the surface niobium oxide Raman bands above 800 cm<sup>-1</sup> experience a shift and the surface niobium oxide Raman bands between 600-700 cm<sup>-1</sup> are not perturbed. Thus, the Raman bands appearing above 800 cm<sup>-1</sup> are associated with surface niobium oxide phases and Raman bands appearing between 600-700 cm<sup>-1</sup> are associated with either bulk niobium oxide phases or surface phases that still possess coordinated moisture as hydroxyl groups. Multiple dehydrated surface niobium oxide species with Raman bands in the 800-1000 cm<sup>-1</sup> region are present in the supported niobium oxide catalysts.

On the SiO<sub>2</sub> support, only one dehydrated surface niobium oxide species with a sharp Raman band at ~980 cm<sup>-1</sup> is observed, and no additional surface niobium oxide phases possessing Raman bands in the 880-950 cm<sup>-1</sup> region are present. A Raman band at ~980 cm<sup>-1</sup> is generally observed for highly distorted NbO<sub>6</sub> octahedra [93] and is also present at the interfaces of layered niobium oxide compounds [54,93]. Recent structural studies of the supported niobium oxide catalysts also suggest that the dehydrated surface niobium oxide species, which exhibits a sharp Raman band at ~980 cm<sup>-1</sup>, can only possess one

terminal  $\text{Nb}=\text{O}$  bond, because the  $\text{Nb}^{5+}$  atom can not accommodate two terminal  $\text{Nb}=\text{O}$  bonds, and should contain a highly distorted  $\text{NbO}_6$  octahedral structure [142]. Consequently, the dehydrated surface niobium oxide phase on  $\text{SiO}_2$  is present as the highly distorted  $\text{NbO}_6$  octahedron. Additional Raman band at  $\sim 680 \text{ cm}^{-1}$  is observed for 4 wt%  $\text{Nb}_2\text{O}_5/\text{SiO}_2$ , but this is assigned to a bulk  $\text{Nb}_2\text{O}_5$  phase because its band position is very close to T- $\text{Nb}_2\text{O}_5$  ( $\sim 690 \text{ cm}^{-1}$ ) and it readily crystallizes upon heating to elevated temperatures [124].

A Raman band at  $\sim 985 \text{ cm}^{-1}$  is also observed for the dehydrated titania and zirconia supported niobium oxide catalysts, and are also assigned to the highly distorted  $\text{NbO}_6$  octahedra. The somewhat lower Raman band positions of the dehydrated 1%  $\text{Nb}_2\text{O}_5/\text{ZrO}_2$  sample are attributed to the presence of surface Cl and F impurities which were detected with XPS only in this particular sample. Upon approaching monolayer coverage, an additional Raman band at  $\sim 935 \text{ cm}^{-1}$  is observed for the dehydrated titania and zirconia supported niobium oxide catalysts, and are also assigned to a highly distorted  $\text{NbO}_6$  octahedron with a slightly longer  $\text{Nb}=\text{O}$  bond.

On the dehydrated  $\text{Al}_2\text{O}_3$  support, Raman bands at  $\sim 980$  and  $\sim 883 \text{ cm}^{-1}$  are observed for the low  $\text{Nb}_2\text{O}_5$  loadings (see

Fig. 5.5) indicating the presence of two kinds of distorted  $\text{NbO}_6$  octahedral structure: one possesses a  $\text{Nb}=\text{O}$  bond length similar to layered niobium oxide compounds and the other possesses a  $\text{Nb}=\text{O}$  bond length similar to that found in hexaniobate,  $\text{Nb}_6\text{O}_{19}^{8-}$ , compounds [93]. At the surface coverage approaching half a monolayer (~8 wt%), the Raman band at  $\sim 980 \text{ cm}^{-1}$  shifts to  $\sim 988 \text{ cm}^{-1}$  and indicates that the nature of the dehydrated surface niobium oxide species changes with surface coverage. New *in situ* Raman bands are observed at  $\sim 950$  and  $\sim 630 \text{ cm}^{-1}$  and are characteristic of the dehydrated surface niobium oxide species containing both highly and slightly distorted  $\text{NbO}_6$  octahedral structures. These Raman bands are also observed for layered niobium oxide compounds which consist of both highly and slightly distorted  $\text{NbO}_6$  octahedral structure connected by sharing corners [54,93]. In addition, the shifts of Raman bands from  $\sim 950$  to  $\sim 935 \text{ cm}^{-1}$  and from  $\sim 630$  to  $\sim 647 \text{ cm}^{-1}$  upon approaching monolayer coverage also suggest that these two Raman bands arise from the same dehydrated surface niobium oxide species.

An *in situ* Raman band is present at  $\sim 890 \text{ cm}^{-1}$  on the  $\text{MgO}$  support which reflects the presence of another distorted  $\text{NbO}_6$  octahedron that possesses a  $\text{Nb}=\text{O}$  bond length similar to that found in the  $\text{MgNb}_2\text{O}_6$  compound [143,144].

The absence of crystalline  $\text{Nb}_2\text{O}_5$  formation for  $\text{Nb}_2\text{O}_5/\text{MgO}$  at very high niobium oxide loadings suggests that this species originates from  $\text{Nb}^{+5}$  incorporated into the  $\text{MgO}$  support surface due to the strong acid-base interaction between these two oxides. Recent Raman studies on the  $\text{MgO}$  supported molybdenum oxide catalysts have found that the  $\text{MgO}$  support contains  $\text{CaCO}_3$  on the surface, and the amount of  $\text{CaCO}_3$  decreases with increasing molybdenum oxide loading because of the formation of  $\text{CaMoO}_4$  [145]. The dehydrated  $\text{Nb}_2\text{O}_5/\text{MgO}$  sample also possesses additional Raman bands at  $\sim 833$  and  $\sim 770 \text{ cm}^{-1}$  which coincide with the Raman positions of a distorted  $\text{NbO}_6$  octahedral structure present in the  $\text{Ca}_2\text{Nb}_2\text{O}_7$  compound [146]. Similar to the  $\text{MoO}_3/\text{MgO}$  system, the formation of the  $\text{Ca}_2\text{Nb}_2\text{O}_7$  compound is due to the reaction of the surface niobium oxide phase with  $\text{CaCO}_3$  present on the  $\text{MgO}$  surface due to the acidic characteristics of niobium oxide. However, XRD does not detect the crystalline  $\text{MgNb}_2\text{O}_6$  and  $\text{Ca}_2\text{Nb}_2\text{O}_7$  phases present in the  $\text{Nb}_2\text{O}_5/\text{MgO}$  system suggest that the particle size of the crystalline phases are smaller than  $40\text{\AA}$ .

On the dehydrated  $\text{MgO}$  support, multiple niobium oxide species possessing Raman bands in the  $800\text{-}900 \text{ cm}^{-1}$  region are present due to the strong acid-base interactions of  $\text{Nb}_2\text{O}_5$  with the  $\text{Mg}^{2+}$  and the  $\text{Ca}^{2+}$  surface cations, and their

intensity increases with the  $\text{Nb}_2\text{O}_5$  loading. At high  $\text{Nb}_2\text{O}_5$  loadings (>10 wt%), the Raman band at  $\sim 985 \text{ cm}^{-1}$  is characteristic of a highly distorted  $\text{NbO}_6$  octahedral structure which coexists with the  $\text{MgNb}_2\text{O}_6$  and  $\text{Ca}_2\text{Nb}_2\text{O}_7$  compounds (see Fig. 5.11).

The molecular structures of the dehydrated surface niobium oxide species with their corresponding bond lengths are presented in Table 5.2. The predicted bond lengths of each structure are obtained from an empirical Nb-O bond distance/stretching frequency correlative equation which is derived by Hardcastle [142]. Below half monolayer coverage, the highly distorted  $\text{NbO}_6$  octahedra, with a Nb=O bond length of  $1.71\text{\AA}$ , are present on all the dehydrated oxide supports. On the  $\text{Al}_2\text{O}_3$  support, a second dehydrated surface niobium oxide species possessing a moderately distorted  $\text{NbO}_6$  octahedral structure, with a Nb=O bond length of  $1.76\text{\AA}$ , is also present. As monolayer coverage is approached, additional dehydrated surface niobium oxide species with structures similar to layered niobium oxide compounds, which contain both highly distorted  $\text{NbO}_6$  octahedra with a Nb=O bond length of  $1.73\text{\AA}$  and slightly distorted  $\text{NbO}_6$  octahedra with a Nb=O bond length of  $1.92\text{\AA}$ , are present on  $\text{Al}_2\text{O}_3$  but not on  $\text{SiO}_2$  and  $\text{MgO}$ . The dehydrated surface niobium oxide phases possessing Raman

bands in the 600-700  $\text{cm}^{-1}$  region may be present for  $\text{Nb}_2\text{O}_5/\text{TiO}_2$  and  $\text{Nb}_2\text{O}_5/\text{ZrO}_2$  but can not be determined by Raman spectroscopy because of the strong vibrations of the oxide supports in this region. Layered niobium oxide compounds react with the weak base, pyridine, which indicates that these compounds possess strong Brønsted acid sites due to the presence of  $\text{H}^+$  protons in the adjacent terminal oxygen layers [54]. Thus, surface acidic studies on  $\text{TiO}_2$  and  $\text{ZrO}_2$  supported niobium oxide catalysts with FTIR of pyridine adsorption can provide additional information for determining the molecular structures of the dehydrated surface niobium oxide species on these two systems.

In situ XANES/EXAFS studies on the silica supported niobium oxide catalysts containing different  $\text{Nb}_2\text{O}_5$  loadings have been reported by Yoshida et al. using  $\text{YbNbO}_4$  and  $\text{KNbO}_3$  as the reference compounds [14]. They suggest that the dehydrated surface niobium oxide phase possesses a highly distorted  $\text{NbO}_4$  tetrahedron at low  $\text{Nb}_2\text{O}_5$  loadings (< 1 wt%) and a square pyramidal structure at high  $\text{Nb}_2\text{O}_5$  loadings (> 7 wt%). The proposed dehydrated surface tetrahedral  $\text{NbO}_4$  structure consists of one terminal  $\text{Nb}=\text{O}$  bond, with a bond length of 1.77 Å, and three  $\text{Nb}-\text{O}$  bonds, with a bond length of 1.96 Å, coordinated to the  $\text{SiO}_2$  surface. At high  $\text{Nb}_2\text{O}_5$  loadings (> 7 wt%), the proposed dehydrated surface niobium

oxide structure consists of one terminal Nb=O bond, with a bond length of 1.79Å, and four Nb-O bonds, with a bond length of 1.96Å, coordinated to the SiO<sub>2</sub> surface. The XANES/EXAFS studies on the YbNbO<sub>4</sub> reference compound are in agreement with corresponding Raman studies that YbNbO<sub>4</sub> consists of a tetrahedral NbO<sub>4</sub> structure [93]. KNbO<sub>3</sub> is known as a perovskite structure containing a slightly distorted NbO<sub>6</sub> octahedral structure with Nb-O bond lengths between 1.87 and 2.17Å [93,142]. The Raman bands of KNbO<sub>3</sub> occur at ~840, ~601, ~540, and ~285 cm<sup>-1</sup> [93]. Thus, XANES/EXAFS studies on KNbO<sub>3</sub> are not representative of a dehydrated surface niobium oxide species which possess a highly distorted NbO<sub>6</sub> octahedral structure. Clearly, additional niobium oxide reference compound XANES/EXAFS studies are required.

The feasibility of Yoshida's model for the dehydrated surface niobium oxide structures is investigated by applying Brown & Wu's valence sum rule [123]. The sum of the valencies, or bond orders, of the individual metal-oxygen bonds should equal the formal oxidation state of the metal cation. The calculated valence state of the Nb<sup>5+</sup> atom for the NbO<sub>4</sub> tetrahedron proposed by Yoshida is 4.07 v.u. which is beyond the limit of the 3% relative error allowed for the Nb<sup>5+</sup> valence state (5.0±0.16 v.u.), and

that for the  $\text{NbO}_5$  square pyramidal also proposed by Yoshida is 4.86 v.u. which is under the limit of the 3% relative error. The Nb-O bond distance/stretching frequency correlation derived by Hardcastle [142] can also be used to predict the Raman band position of the dehydrated surface niobium oxide on the  $\text{SiO}_2$  support for the structure proposed by Yoshida. The predicted Nb-O stretching frequency, corresponding to the bond distances of 1.77, 1.79, and 1.96 Å proposed by Yoshida, would appear at  $\sim 870$ ,  $\sim 840$ , and  $\sim 605 \text{ cm}^{-1}$  ( $\pm 30 \text{ cm}^{-1}$  error). This predicted Raman band are not consistent with the present study in which the dehydrated surface niobium oxide on the  $\text{SiO}_2$  support is experimentally shown to possess a Raman band at  $\sim 980 \text{ cm}^{-1}$ . At high  $\text{Nb}_2\text{O}_5$  loading, the predicted Raman bands at  $\sim 840$  and  $\sim 605 \text{ cm}^{-1}$  for the structure proposed by Yoshida are consistent with the presence of bulk  $\text{Nb}_2\text{O}_5$  (see Fig. 5.2). In addition, the ratio of the  $\text{Nb}^{5+}$  ionic radius to the  $\text{O}^{2-}$  ionic radius is too large to fit into a  $\text{NbO}_4$  tetrahedral structure and a  $\text{NbO}_6$  octahedral structure is more plausible [147]. Thus, all the theories and experiments indicate that the dehydrated surface niobium oxide phases are not very likely to possess a  $\text{NbO}_4$  tetrahedral structure.

The various dehydrated surface niobium oxide

structures present in supported niobium oxide catalysts appear to be related to the oxide support surface hydroxyl chemistry [35]. The surface niobium oxide phases are formed by reaction of the niobium oxide precursor with the surface hydroxyl groups of the oxide supports which are directly observable with infrared spectroscopy [107,148]. The  $\text{SiO}_2$  surface possesses only one kind of surface hydroxyl group and only one dehydrated surface niobium oxide species (Raman band at  $\sim 980 \text{ cm}^{-1}$ ) is present. The  $\text{TiO}_2$  and  $\text{ZrO}_2$  surfaces possess two kinds of surface hydroxyl groups and two dehydrated surface niobium oxide species (Raman band at  $\sim 985$  and  $\sim 935 \text{ cm}^{-1}$ ) are present. The  $\text{Al}_2\text{O}_3$  surface possesses at least 4 different surface hydroxyl groups and three dehydrated surface niobium oxide species (Raman bands at  $\sim 985$ ,  $\sim 935$ ,  $\sim 880$ , and  $\sim 647 \text{ cm}^{-1}$ ) are present. The  $\text{MgO}$  surface possesses one kind of surface hydroxyl group, but three different niobium oxide species are observed (Raman bands at  $\sim 985$ ,  $\sim 890$ , and  $\sim 830 \text{ cm}^{-1}$ ) under in situ conditions. The multiple niobium oxide species present in the dehydrated  $\text{Nb}_2\text{O}_5/\text{MgO}$  system are due to the strong acid-base interaction between  $\text{Nb}_2\text{O}_5$  and  $\text{MgO}$  which results in the incorporation of niobium oxide into the  $\text{MgO}$  support surface and the reaction of  $\text{Nb}_2\text{O}_5$  with  $\text{CaCO}_3$  which is present on the  $\text{MgO}$  surface. The low surface hydroxyl concentration of the  $\text{SiO}_2$  support [35], relative

to the other oxide supports, is responsible for the low surface concentration of surface niobium oxide species and the formation of bulk  $\text{Nb}_2\text{O}_5$  at very low niobium oxide loadings.

### 5.5. CONCLUSIONS

The molecular structures of the dehydrated surface niobium oxide phases were determined with *in situ* Raman spectroscopy by comparing the Raman spectra of the supported niobium oxides with those of solid niobium oxide reference compounds. Under *in situ* conditions, the adsorbed moisture desorbs upon heating and the surface niobium oxide overlayers on oxide supports become dehydrated. The dehydration process further distorts the highly distorted  $\text{NbO}_6$  octahedra and shifts the surface niobium oxide Raman bands in the  $890\text{-}910\text{ cm}^{-1}$  region to  $930\text{-}990\text{ cm}^{-1}$  because of the removal of the coordinated water.

A dehydrated surface niobium oxide Raman band is observed at  $\sim 985\text{ cm}^{-1}$  on all the oxide supports and reveals that the same surface niobium oxide species possessing a highly distorted  $\text{NbO}_6$  octahedral structure is present for all the supported niobium oxide catalysts. Below half a monolayer coverage on the  $\text{Al}_2\text{O}_3$  support, a second

dehydrated surface niobium oxide species possessing a highly distorted  $\text{NbO}_6$  octahedral structure with a somewhat longer  $\text{Nb}=\text{O}$  bonds ( $\sim 883 \text{ cm}^{-1}$ ) is also present. Upon approaching monolayer coverage on the  $\text{Al}_2\text{O}_3$  support, additional Raman bands at  $\sim 935$  and  $\sim 647 \text{ cm}^{-1}$  are observed which are characteristic of highly and slightly distorted  $\text{NbO}_6$  octahedra similar to those present in layered niobium oxide compounds.

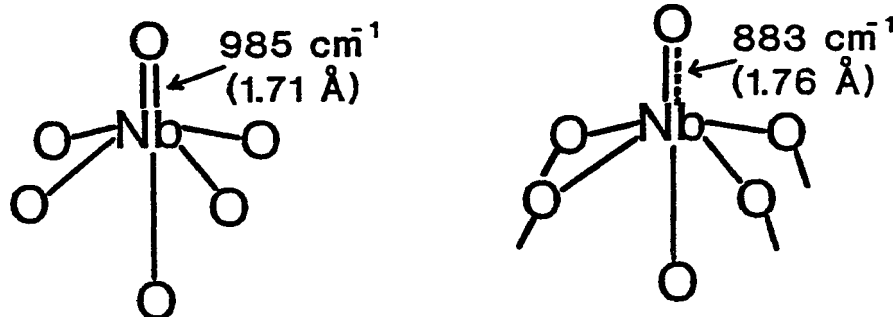
The highly distorted  $\text{NbO}_6$  octahedra exhibiting a Raman band at  $\sim 935 \text{ cm}^{-1}$  are also observed on the  $\text{TiO}_2$  and  $\text{ZrO}_2$  supports, however, surface niobium oxide phases possessing Raman bands in the  $600-700 \text{ cm}^{-1}$  region can not be determined for  $\text{Nb}_2\text{O}_5/\text{TiO}_2$  and  $\text{Nb}_2\text{O}_5/\text{ZrO}_2$  because of the strong vibrations of the oxide supports in this region. On the  $\text{SiO}_2$  support, only one dehydrated surface niobium oxide species possessing with the highly distorted  $\text{NbO}_6$  octahedral structure is found. The multiple niobium oxide species present in the  $\text{Nb}_2\text{O}_5/\text{MgO}$  system are due to the strong acid-base interaction of  $\text{Nb}_2\text{O}_5$  with the  $\text{Mg}^{2+}$  and the  $\text{Ca}^{2+}$  cations present on the surface to form  $\text{MgNb}_2\text{O}_6$  and  $\text{Ca}_2\text{Nb}_2\text{O}_7$ . The various dehydrated surface niobium oxide species present in the supported niobium oxide catalysts appear to be related to the oxide support surface hydroxyl chemistry.

**Table 5.1: Raman bands of supports of supported niobium oxide catalysts under in situ conditions (dehydrated state )**

	Raman Bands (cm <sup>-1</sup> )
5% Nb <sub>2</sub> O <sub>6</sub> /MgO	930(w), 892(m), 833(s)
10% Nb <sub>2</sub> O <sub>6</sub> /MgO	985(m), 898(s), 834(s)
5% Nb <sub>2</sub> O <sub>6</sub> /Al <sub>2</sub> O <sub>3</sub>	980(s), 883(m)
19% Nb <sub>2</sub> O <sub>6</sub> /Al <sub>2</sub> O <sub>3</sub>	988(m), 935(s), 883(w), 647(s)
1% Nb <sub>2</sub> O <sub>6</sub> /TiO <sub>2</sub>	983(m)
7% Nb <sub>2</sub> O <sub>6</sub> /TiO <sub>2</sub>	985(s), 935(m)
1% Nb <sub>2</sub> O <sub>6</sub> /ZrO <sub>2</sub>	956(s), 823(s)
5% Nb <sub>2</sub> O <sub>6</sub> /ZrO <sub>2</sub>	988(s), 935(m)
2% Nb <sub>2</sub> O <sub>6</sub> /SiO <sub>2</sub>	980(s)
4% Nb <sub>2</sub> O <sub>6</sub> /SiO <sub>2</sub>	980(s), 680(m)

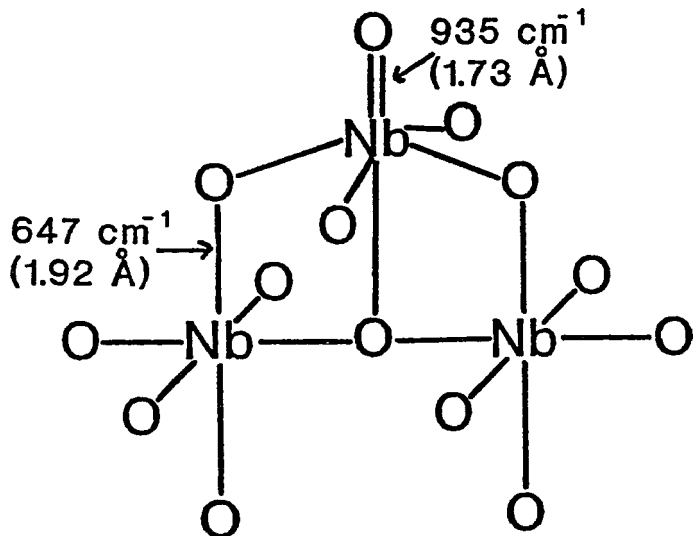
**Table 5.2: A molecular structure model for the dehydrated surface niobium oxide species**

- Below half a monolayer coverage:



Highly distorted  $\text{NbO}_6$  octahedra with different  $\text{Nb}=\text{O}$  bond distances

- Approaching monolayer coverage:



Highly and slightly distorted  $\text{NbO}_6$  octahedra coexist in the structure

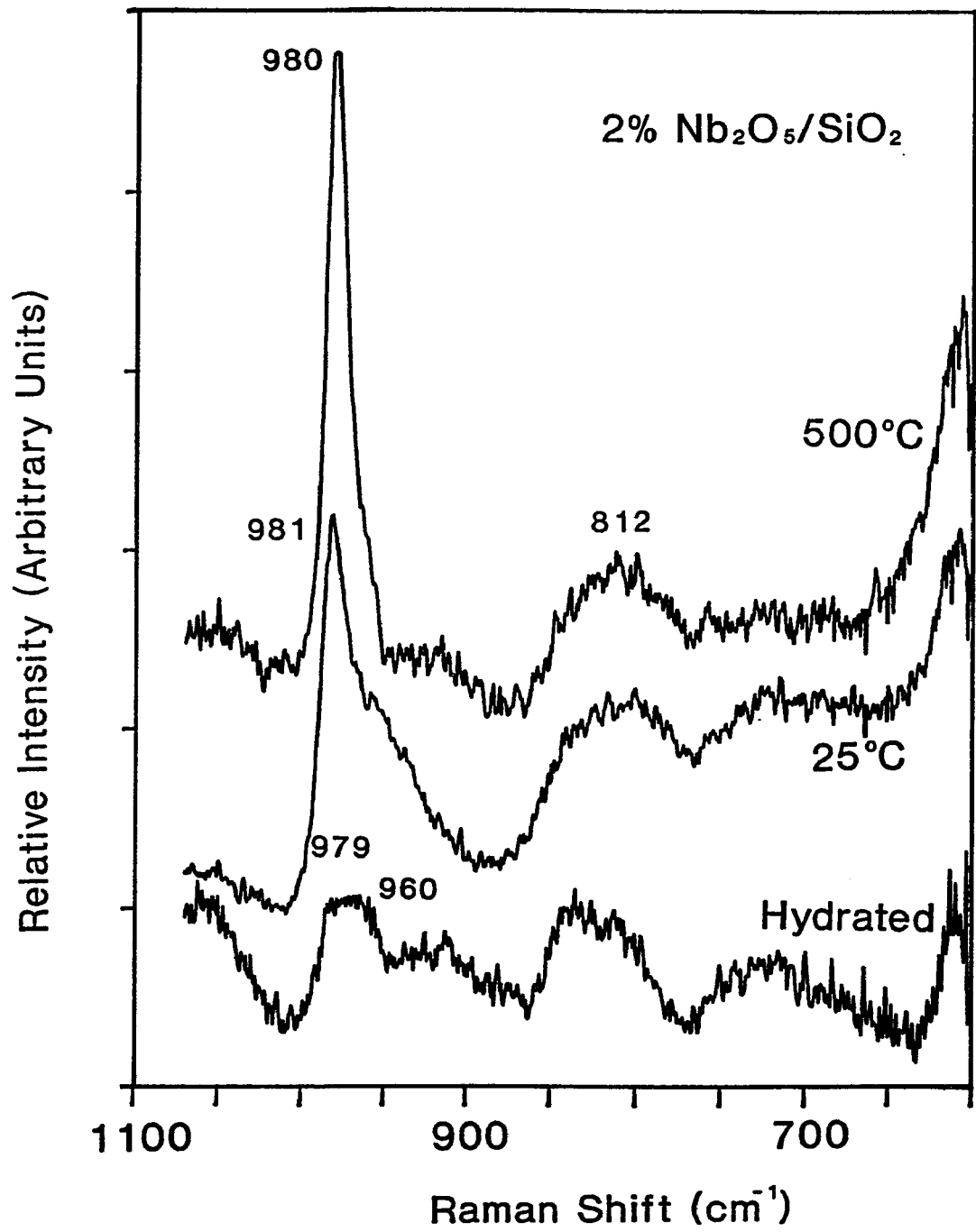
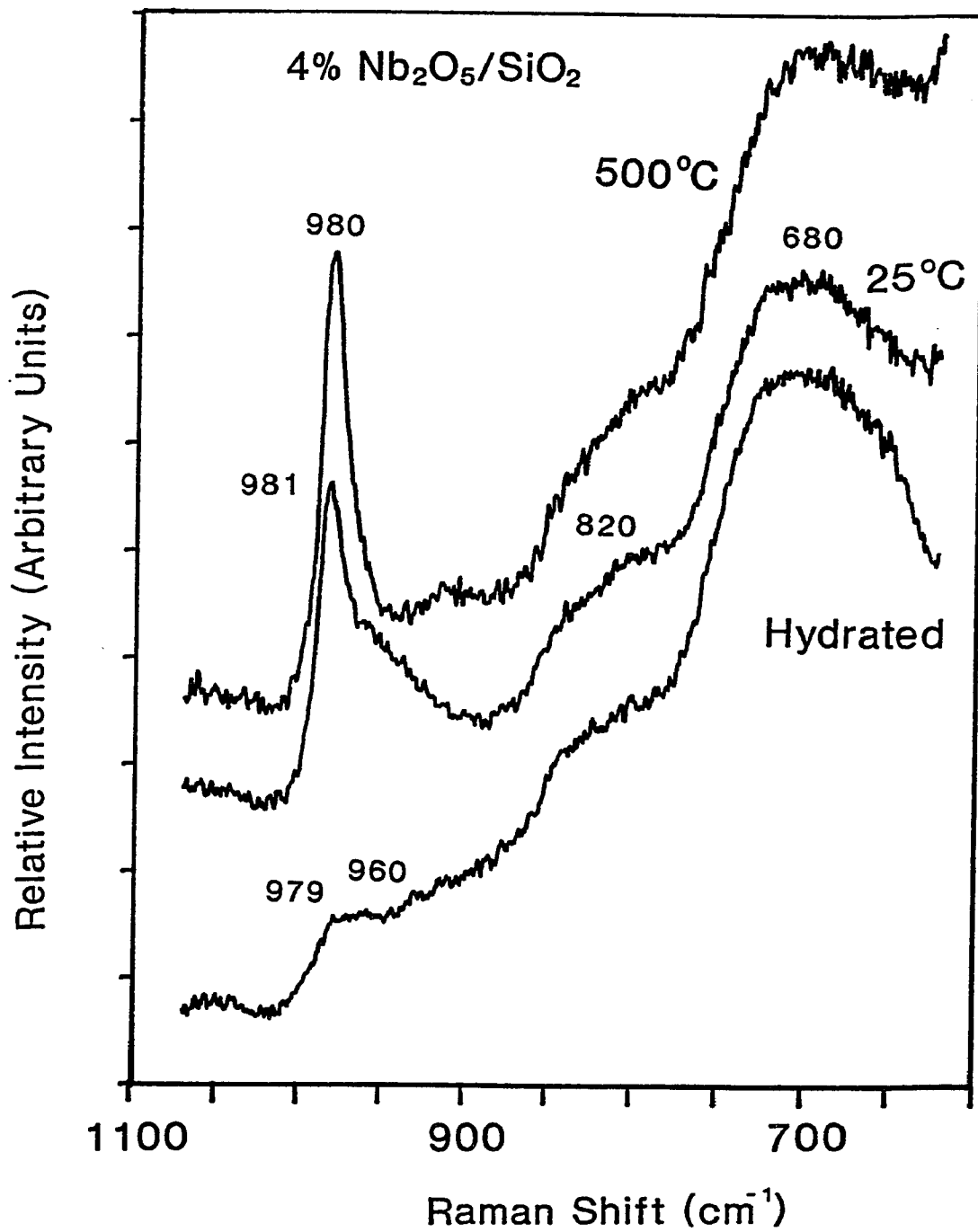


Figure 5.1: In situ Raman spectra of 2 wt%  $\text{Nb}_2\text{O}_5/\text{SiO}_2$



**Figure 5.2:** In situ Raman spectra of 4 wt%  $\text{Nb}_2\text{O}_5/\text{SiO}_2$

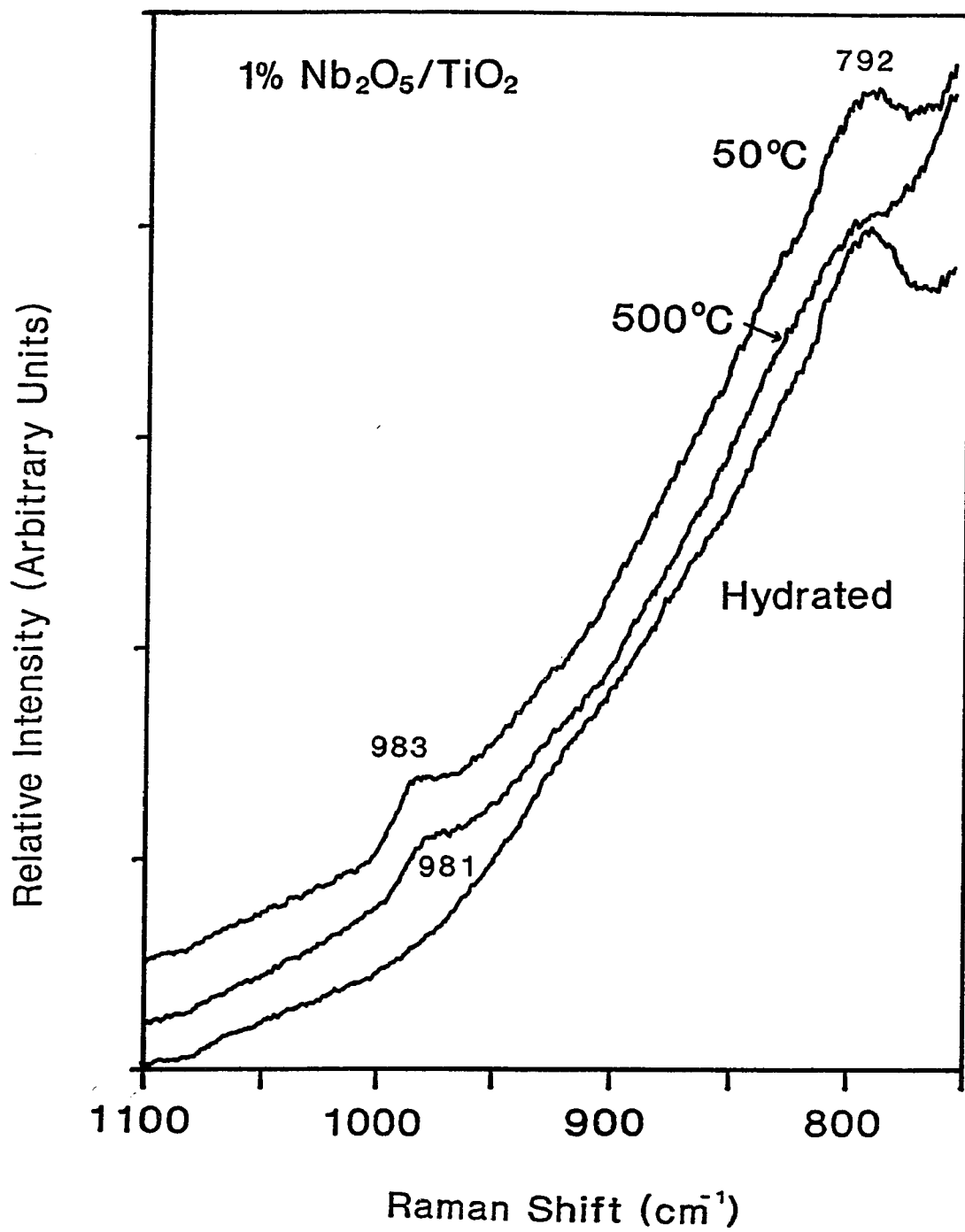


Figure 5.3: In situ Raman spectra of 1 wt%  $\text{Nb}_2\text{O}_5/\text{TiO}_2$

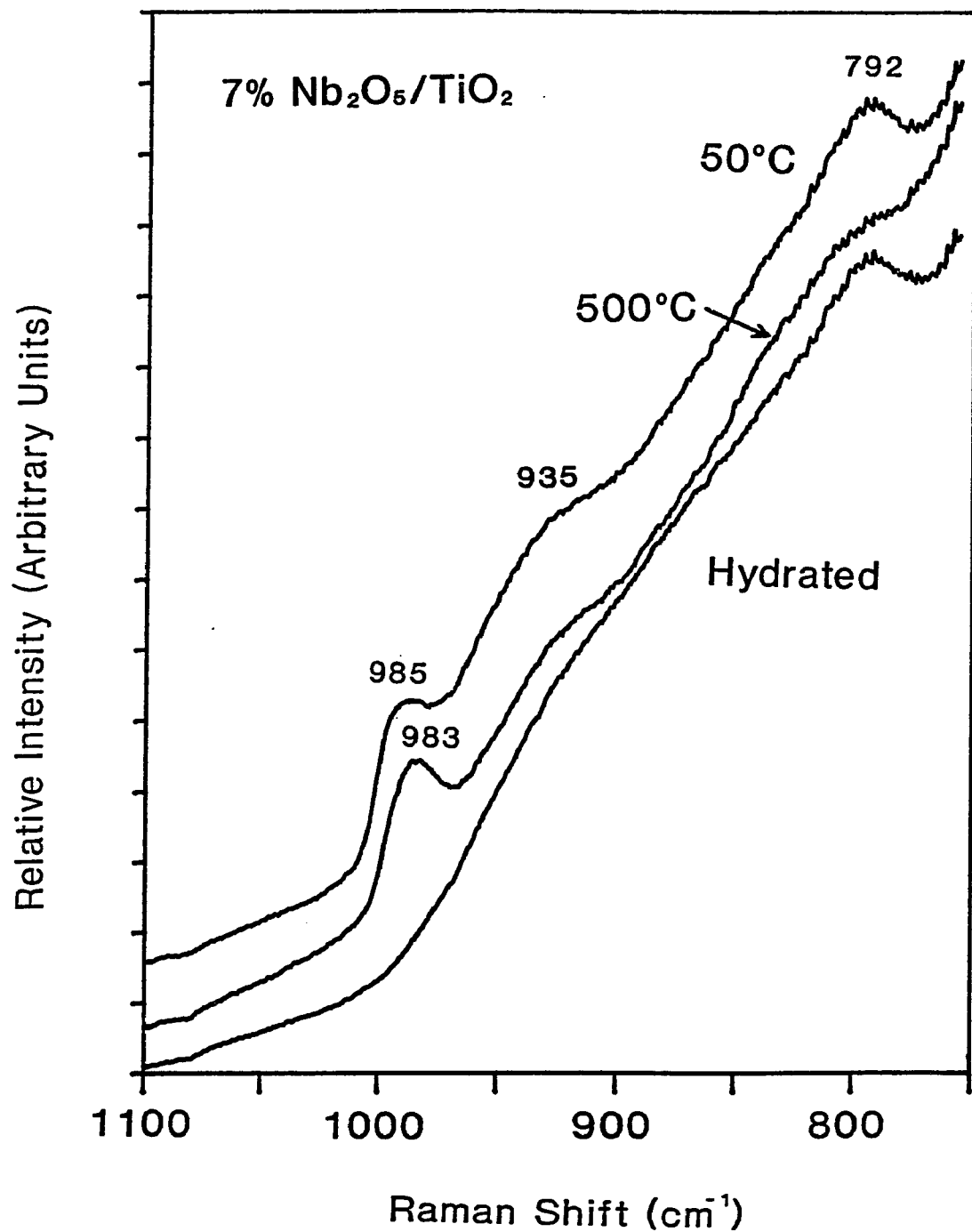
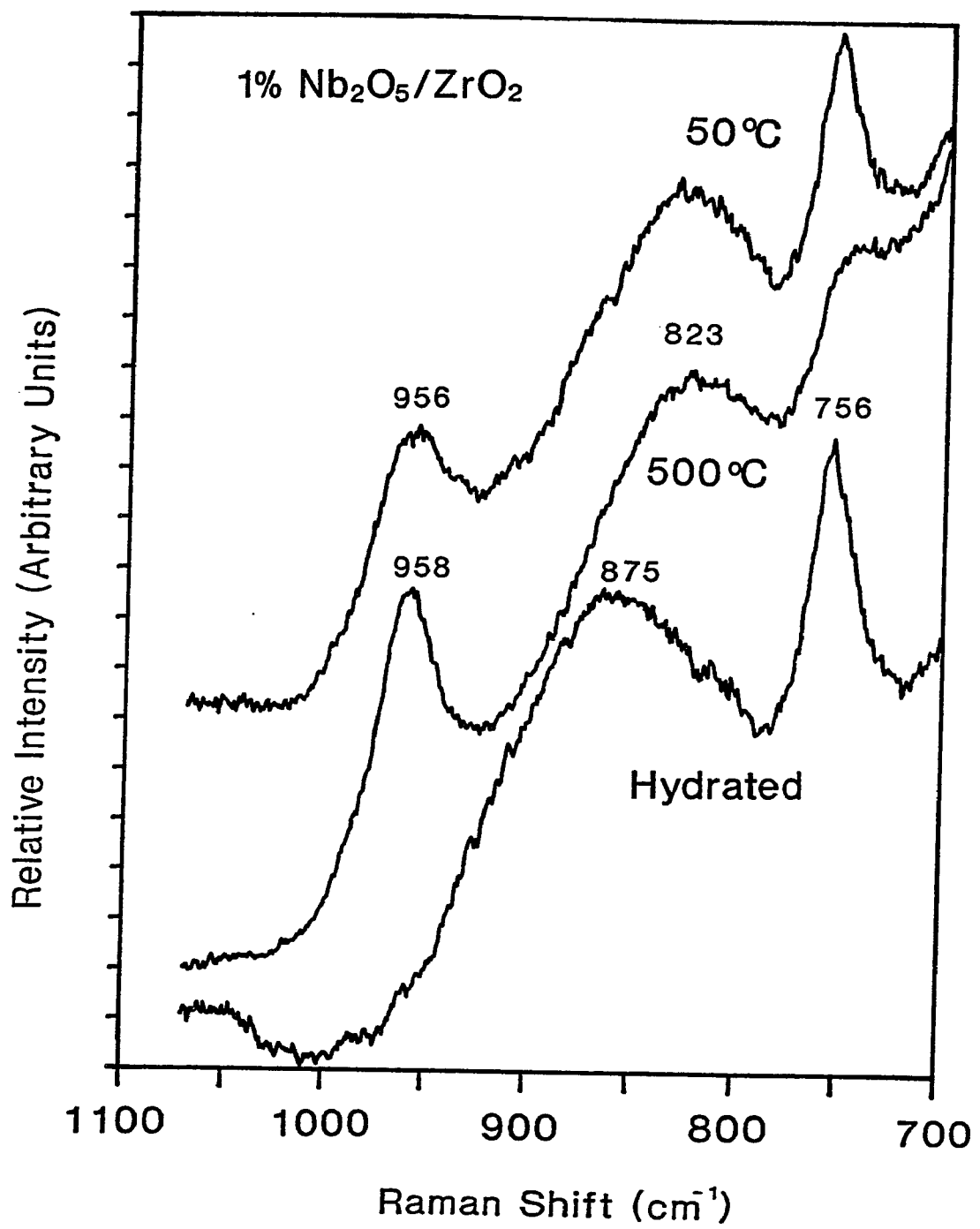


Figure 5.4: In situ Raman spectra of 7 wt%  $\text{Nb}_2\text{O}_5/\text{TiO}_2$



**Figure 5.5:** In situ Raman spectra of 1 wt%  $\text{Nb}_2\text{O}_5/\text{ZrO}_2$

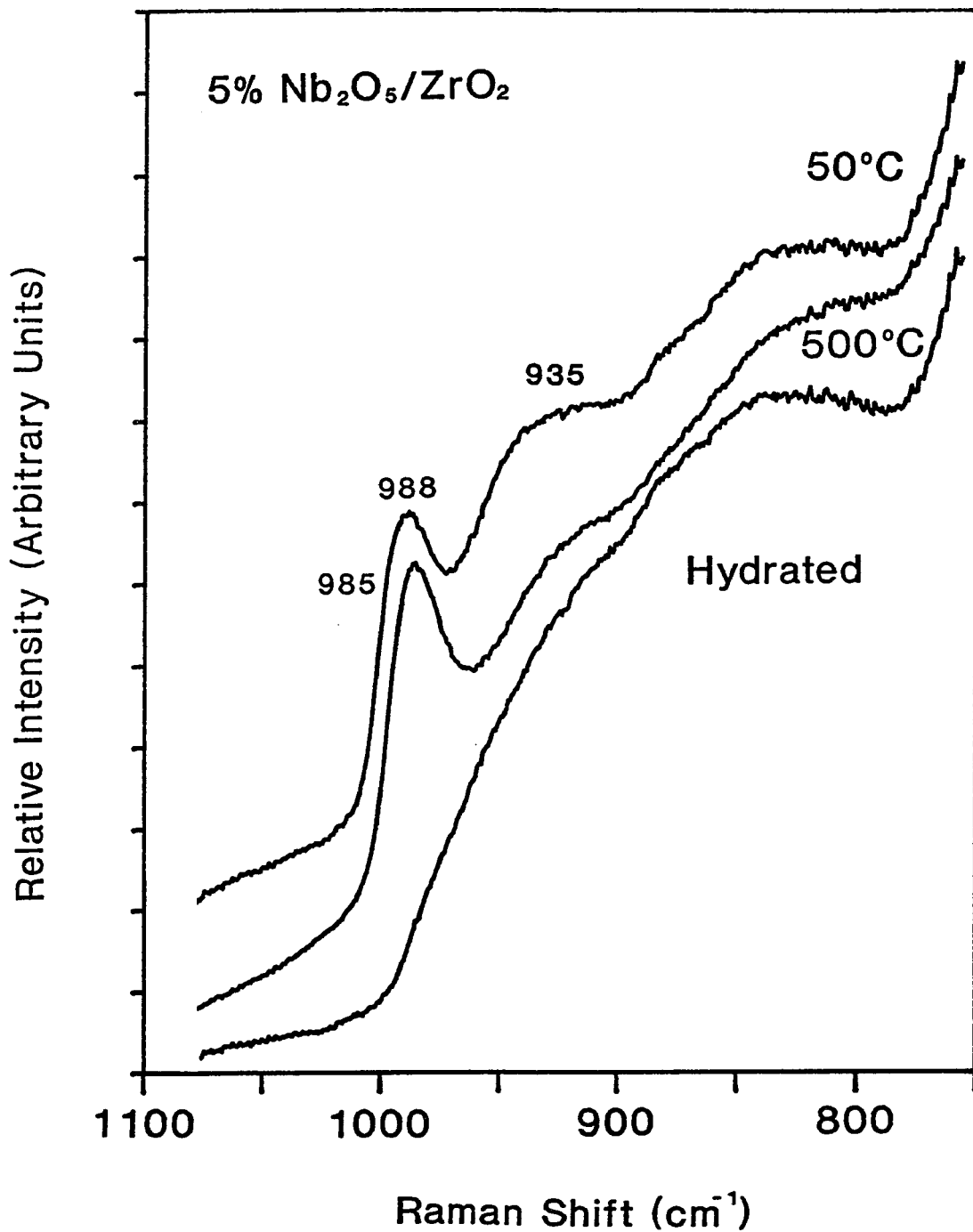


Figure 5.6: In situ Raman spectra of 5 wt%  $\text{Nb}_2\text{O}_5/\text{ZrO}_2$

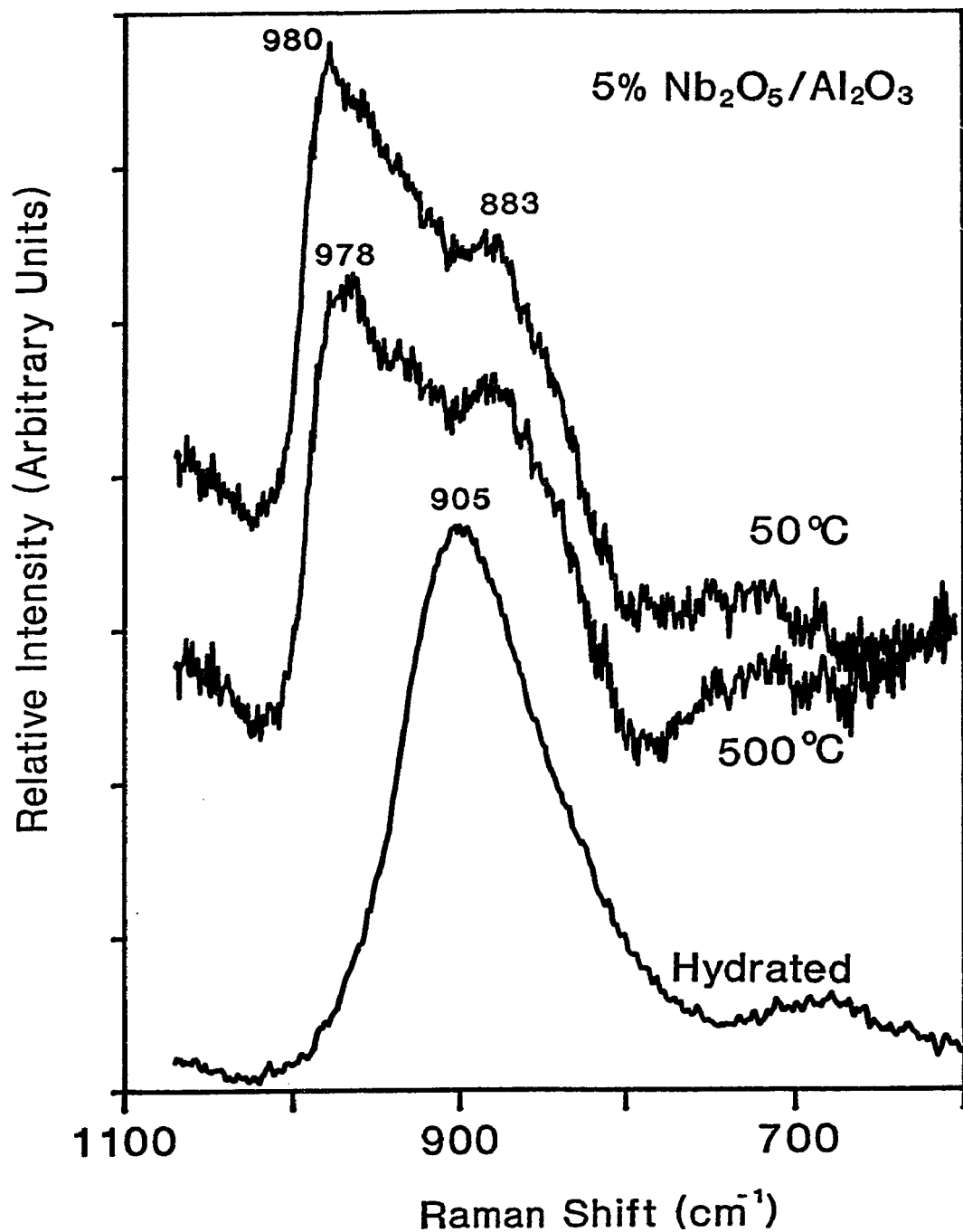


Figure 5.7: In situ Raman spectra of 5 wt%  $\text{Nb}_2\text{O}_5/\text{Al}_2\text{O}_3$

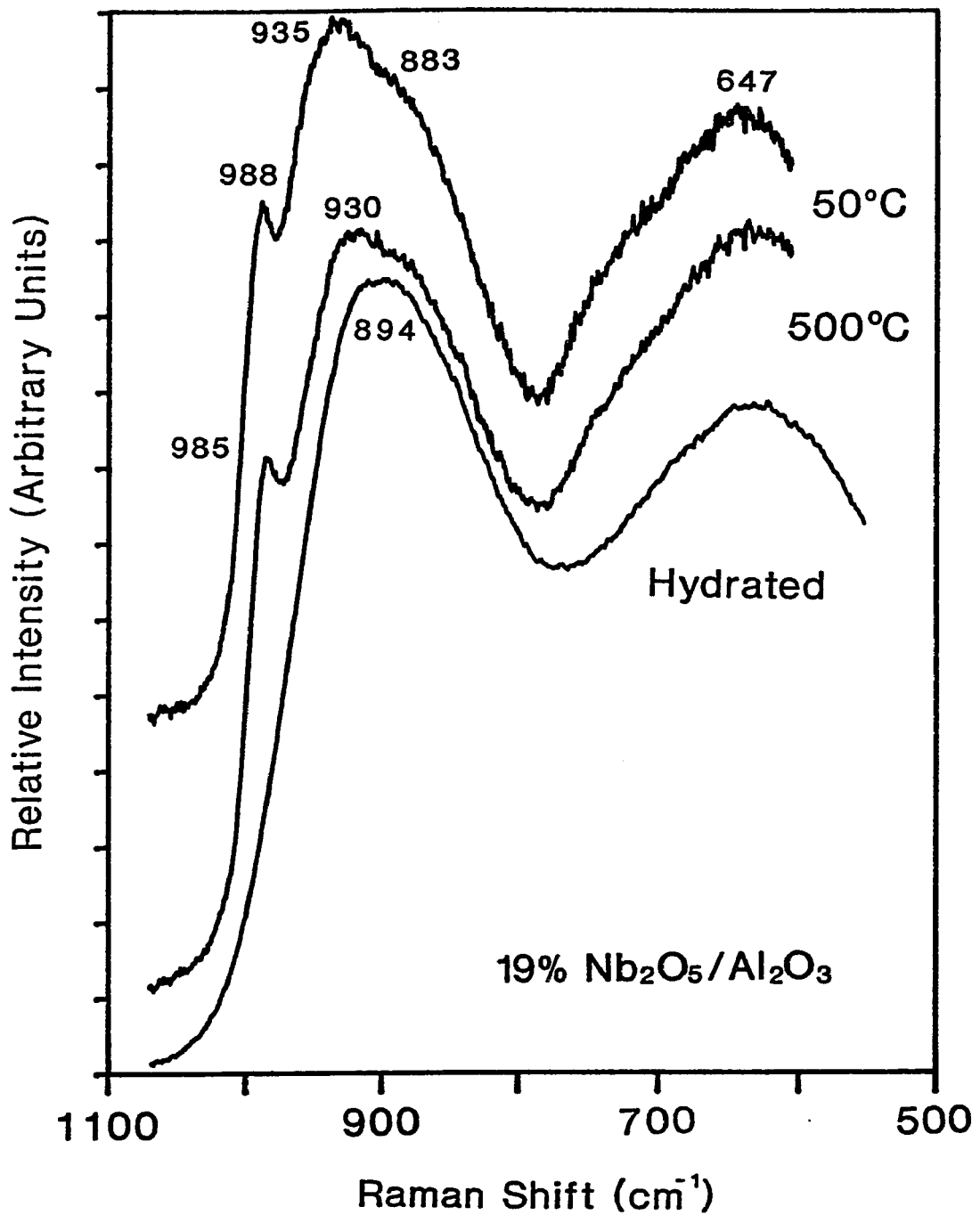
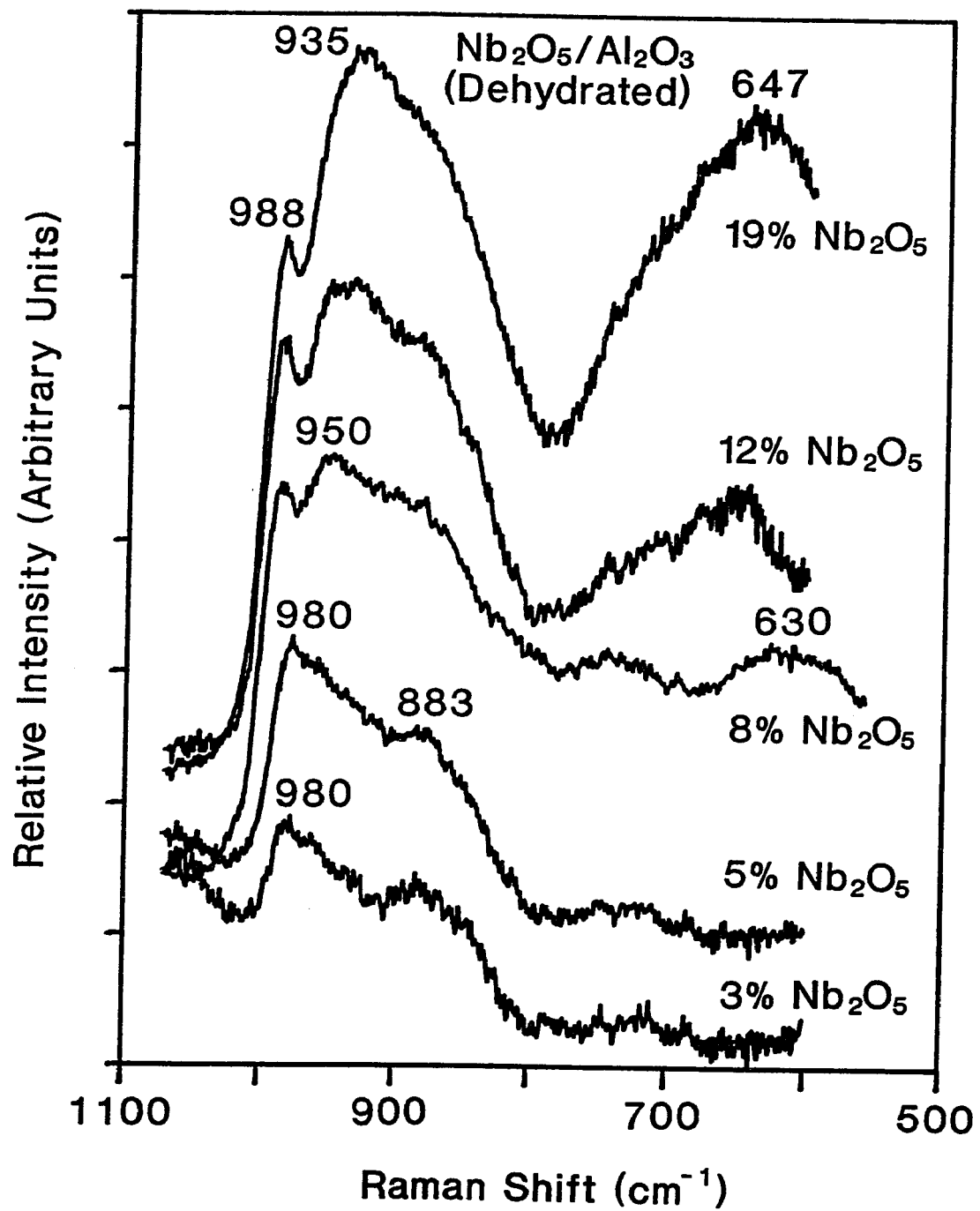


Figure 5.8: In situ Raman spectra of 19 wt%  $\text{Nb}_2\text{O}_5/\text{Al}_2\text{O}_3$



**Figure 5.9: In situ Raman spectra of the  $\text{Nb}_2\text{O}_5/\text{Al}_2\text{O}_3$  system as a function of  $\text{Nb}_2\text{O}_5$  loading**

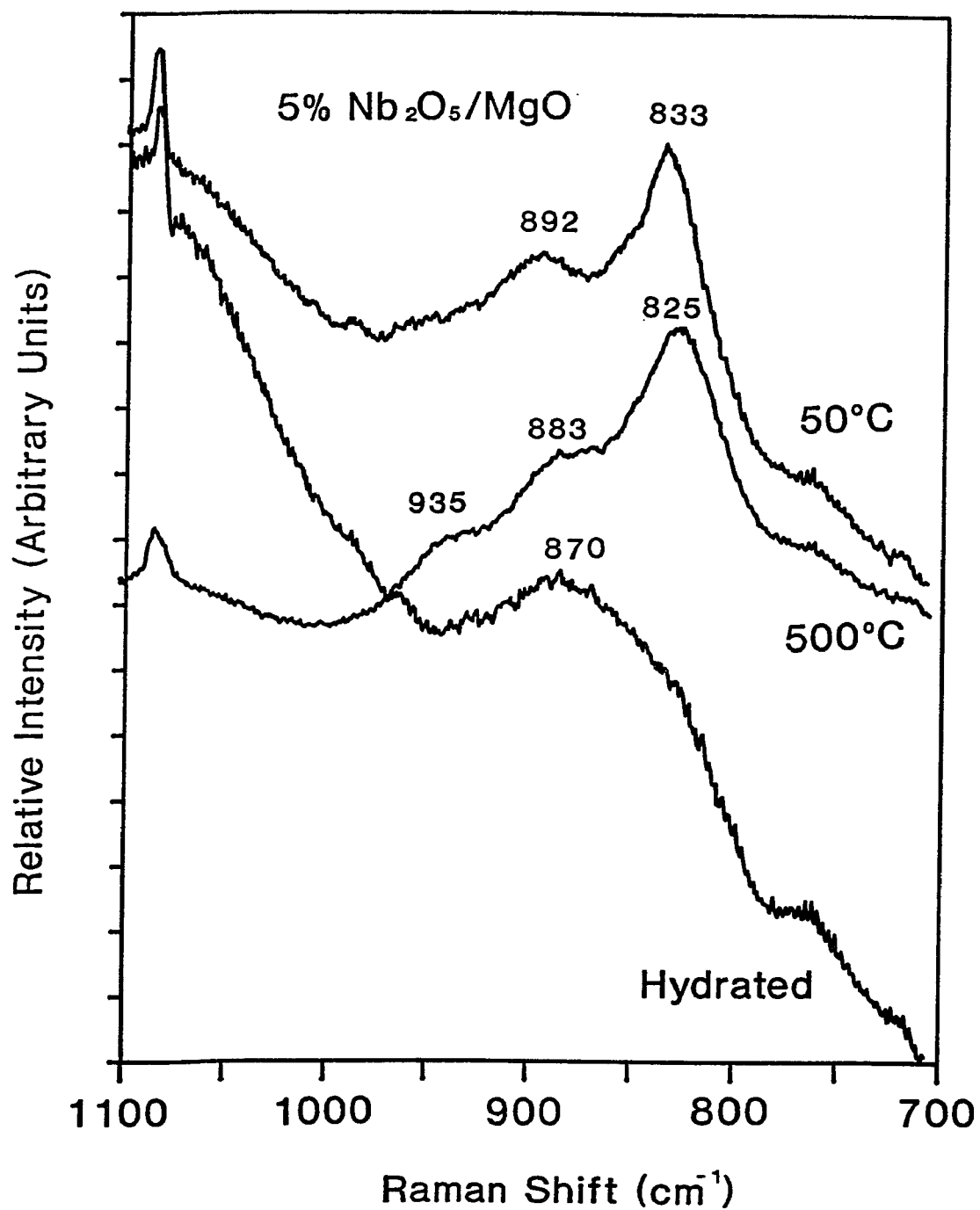
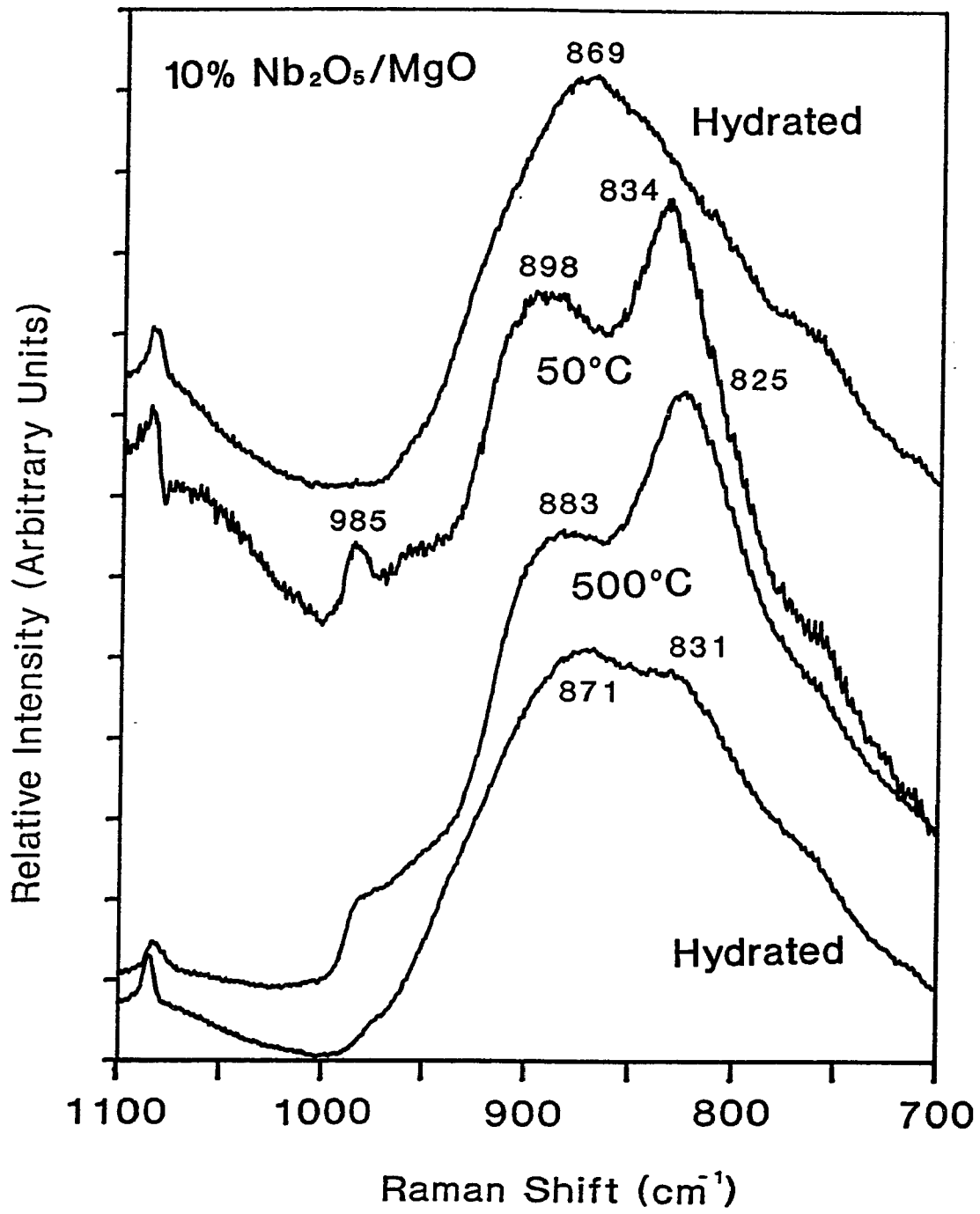


Figure 5.10: In situ Raman spectra of 5 wt%  $\text{Nb}_2\text{O}_5/\text{MgO}$



**Figure 5.11:** In situ Raman spectra of 10 wt%  $\text{Nb}_2\text{O}_5/\text{MgO}$

## **CHAPTER 6**

### **SURFACE ACIDITY AND REACTIVITY OF SUPPORTED NIOBIUM OXIDE CATALYSTS**

## SUMMARY

The surface chemistry of supported niobium oxide catalysts was investigated by pyridine adsorption infrared studies to probe the surface acidity and by methanol oxidation studies to probe the catalytic reactivity. In combination with structural characterization information of the surface niobium oxide overlayers, the molecular structure-reactivity relationships of the supported niobium oxide catalysts could be determined. The highly distorted  $\text{NbO}_6$  octahedra possess  $\text{Nb}=\text{O}$  bonds and are associated with Lewis acid sites. The Lewis acid surface sites are present on all the supported niobium oxide systems, but the Brønsted acid surface sites are limited to the  $\text{Nb}_2\text{O}_5/\text{Al}_2\text{O}_3$  and  $\text{Nb}_2\text{O}_5/\text{SiO}_2$  systems. The surface layered niobium oxide species possessing both highly and slightly distorted  $\text{NbO}_6$  octahedral structures are associated with Brønsted acid sites and are only found at high coverages on alumina. The Brønsted acid sites for the  $\text{Nb}_2\text{O}_5/\text{SiO}_2$  system are due to the formation of bulk  $\text{Nb}_2\text{O}_5$  particles. The surface niobium oxide Lewis acid sites are significantly more active when coordinated to the  $\text{Al}_2\text{O}_3$  surface than to the  $\text{TiO}_2$  and  $\text{ZrO}_2$  surfaces (surface oxide-support interaction). Furthermore, the surface niobium oxide sites on  $\text{SiO}_2$  and  $\text{MgO}$  behave as redox sites and the surface niobium oxide sites on  $\text{Al}_2\text{O}_3$ ,  $\text{TiO}_2$ , and  $\text{ZrO}_2$  are acid sites during partial oxidation reactions.

### 6.1. INTRODUCTION

In recent years supported metal oxides catalysts have been shown to possess higher activities and selectivities than unsupported metal oxide catalysts due to the formation of new surface metal oxide phases on the oxide supports [130,135,149-169]. The deposited metal oxides disperse on the oxide supports by reacting with the surface hydroxyl groups of the support to form new surface metal oxide phases. These surface metal oxide phases have been found to enhance the chemical and physical properties of the resultant catalysts. The supported  $\text{MoO}_3$  and  $\text{V}_2\text{O}_5$  systems (on oxide supports such as  $\text{TiO}_2$ ,  $\text{SiO}_2$ , and  $\text{Al}_2\text{O}_3$ ) have been found to be effective catalysts for selective oxidation of hydrocarbons in the petrochemical, chemical, and pollution control industries. The interaction between the surface metal oxide and the oxide support strongly affects the surface metal oxide structure, and the different surface metal oxide states result in different catalytic properties. The overall catalytic activity and selectivity of supported metal oxide catalysts are also dependent on the concentration of these surface metal oxide species. In comparison to the supported  $\text{MoO}_3$  and  $\text{V}_2\text{O}_5$  systems very little fundamental information is currently available about supported  $\text{Nb}_2\text{O}_5$  catalytic systems

The  $\text{Nb}^{5+}$  atom is located in the same group VB family

as the  $V^{5+}$  atom in the periodic table, and is expected to possess somewhat similar properties as the  $V^{+5}$  atom. Indeed, supported niobium oxide catalysts have been found to form two-dimensional surface niobium oxide overlayers on high surface area oxide supports such as  $Al_2O_3$ ,  $TiO_2$ , and  $SiO_2$  [5-7,9-12,19,21,124,170]. The surface niobium oxide phases have a pronounced effect on the physical and chemical properties of the oxide supports. The thermal stability of the  $Al_2O_3$  and  $TiO_2$  supports is increased by the presence of the surface niobium oxide overlayers [12], and the surface niobium oxide phase on the  $Al_2O_3$  support also possesses strong Brønsted acidity which results in a high hydrocarbon cracking activity at elevated temperatures [5,19,21]. No information currently exists between the molecular structures of the surface niobium oxide species and their catalytic properties.

Previous Raman and XPS studies on supported niobium oxide catalysts under ambient conditions have shown that the surface niobium oxide species form a two-dimensional overlayer on oxide supports ( $MgO$ ,  $Al_2O_3$ ,  $TiO_2$ ,  $ZrO_2$ , and  $SiO_2$ ). The monolayer coverage of these systems is reached at ~19 wt%  $Nb_2O_5/Al_2O_3$ , ~7 wt%  $Nb_2O_5/TiO_2$ , ~5 wt%  $Nb_2O_5/ZrO_2$ , and ~2 wt%  $Nb_2O_5/SiO_2$ , but not for the  $Nb_2O_5/MgO$  system due to the incorporation of  $Nb^{+5}$  into the  $MgO$  support. Under in situ conditions the adsorbed moisture

desorbs upon heating and the surface niobium oxide overlayer on oxide supports become dehydrated. On the  $\text{SiO}_2$  support, only one dehydrated surface niobium oxide species corresponding to the highly distorted  $\text{NbO}_6$  octahedral structure at  $\sim 980 \text{ cm}^{-1}$  is present. Highly distorted  $\text{NbO}_6$  octahedra responsible for Raman bands at  $\sim 985$  and  $\sim 935 \text{ cm}^{-1}$  are also observed on the  $\text{TiO}_2$  and  $\text{ZrO}_2$  supports at monolayer coverages ( $\sim 7$  and  $\sim 5 \text{ wt\% } \text{Nb}_2\text{O}_5$ , respectively). Upon approaching monolayer coverage on the  $\text{Al}_2\text{O}_3$  support ( $\sim 19 \text{ wt\% } \text{Nb}_2\text{O}_5$ ), the dehydrated surface niobium oxide species are present as the highly distorted  $\text{NbO}_6$  octahedra (Raman band at  $\sim 988 \text{ cm}^{-1}$ ), the moderately distorted  $\text{NbO}_6$  octahedra (Raman band at  $\sim 883 \text{ cm}^{-1}$ ), and the layered niobium oxide species containing both highly and slightly distorted  $\text{NbO}_6$  octahedral structure (Raman bands at  $\sim 935$  and  $\sim 647 \text{ cm}^{-1}$ ). Multiple niobium oxide species are present in the  $\text{Nb}_2\text{O}_5/\text{MgO}$  system due to the strong acid-base interactions of  $\text{Nb}_2\text{O}_5$  with the  $\text{Mg}^{2+}$  and the  $\text{Ca}^{2+}$  impurity cations present on the surface.

In the present study, the surface acidity and reactivity of the supported niobium oxide catalysts on  $\text{MgO}$ ,  $\text{Al}_2\text{O}_3$ ,  $\text{TiO}_2$ ,  $\text{ZrO}_2$ , and  $\text{SiO}_2$  supports will be probed by FTIR pyridine adsorption studies and the sensitive methanol oxidation reaction. Comparison of the surface acidity and the reactivity data with the corresponding molecular

characterization information previously determined will allow the establishment of molecular structure-reactivity relationships for supported niobium oxide catalysts. Knowledge of the molecular structure-reactivity relationships will further assist in the molecular design of supported niobium oxide catalysts for specific applications.

## 6.2. EXPERIMENTAL

### 6.2.1. Materials

The supported niobium oxide catalysts on  $\text{Al}_2\text{O}_3$ ,  $\text{TiO}_2$ ,  $\text{ZrO}_2$ , and  $\text{SiO}_2$  supports were prepared by the incipient-wetness impregnation method using niobium oxalate/oxalic acid aqueous solutions [62]. The water sensitive  $\text{MgO}$  support required the use of niobium ethoxide/propanol solutions under a nitrogen environment for the preparation of the  $\text{Nb}_2\text{O}_5/\text{MgO}$  catalysts. All samples were dried at 110-120°C and calcined at 450-500°C. Niobium oxalate was supplied by Niobium Products Company (Pittsburgh, PA) with the following chemical analysis: 20.5%  $\text{Nb}_2\text{O}_5$ , 790 ppm Fe, 680 ppm Si, and 0.1% insolubles. Niobium ethoxide (99.999% purity) was purchased from Johnson Matthey (Ward Hill, MA). The oxide supports employed in the present investigation are:  $\text{MgO}$  (Fluka, ~80  $\text{m}^2/\text{g}$ ),  $\text{Al}_2\text{O}_3$  (Harshaw, ~180  $\text{m}^2/\text{g}$ ),

$TiO_2$  (Degussa,  $\sim 50$   $m^2/g$ ),  $ZrO_2$  (Degussa,  $\sim 39$   $m^2/g$ ), and  $SiO_2$  (Cab-O-Sil,  $\sim 275$   $m^2/g$ ). The  $MgO$  support was calcined at  $700^\circ C$  for 2 hrs to convert the magnesium hydroxide to magnesium oxide.

Methanol (99.9% purity) was obtained from Aldrich Chemical Company, Inc. (Milwaukee, WI). The He and  $O_2$  carrier gases were purchased from Linde Specialty Gases (Union Carbide) with 99.995% and 99.9% purity, respectively.

#### 6.2.2. Acidity Studies

The surface acidity of the supported niobium oxide catalysts was measured with an Analect FX-6160 FTIR spectrometer using pyridine as the probe molecule [148]. Pyridine adsorbs on Brønsted acid surface sites to form pyridinium ion ( $PyH^+$ ) which possesses IR bands in the  $1440$ - $1460$   $cm^{-1}$  region and at  $\sim 1640$   $cm^{-1}$ , and adsorbs on Lewis acid surface sites to form coordinatively bonded complex ( $PyL$ ) which possesses IR bands in the  $1440$ - $1460$  and  $1600$ - $1635$   $cm^{-1}$  region [171]. The samples were pressed into thin wafers ( $10$ - $30$   $mg/cm^2$ ) and evacuated in the IR cell at  $350^\circ C$  for 1 hour. Upon cooling the cell to  $200^\circ C$ , the IR spectrum (A) was recorded. Pyridine vapor with a pressure of 5 Torr was then introduced into the cell which is maintained at  $200^\circ C$  for about 30 seconds. Subsequently,

physically adsorbed pyridine was desorbed by evacuating the sample for 15 minutes, and the pyridine adsorption IR spectrum (B) was recorded. The concentration of Brønsted and Lewis acid sites were calculated from the intensities of  $\text{PyH}^+$  ( $\sim 1540 \text{ cm}^{-1}$ ) and  $\text{PyL}$  ( $\sim 1450 \text{ cm}^{-1}$ ) bands and calibration of their corresponding extinction coefficients after subtraction of spectrum A from B.

The integrated extinction coefficient of the  $\text{PyL}$  band at  $\sim 1450 \text{ cm}^{-1}$  was determined by the adsorption of pyridine on  $\text{Al}_2\text{O}_3$  which contains only Lewis acid sites (no  $\text{PyH}^+$  bands were observed). The integrated intensity of the  $\text{PyL}$  band at  $\sim 1450 \text{ cm}^{-1}$  linearly increased with increasing adsorbed pyridine, and the slope was measured as the extinction coefficient of the  $\text{PyL}$  band at  $\sim 1450 \text{ cm}^{-1}$  with a value of  $1.11 \text{ cm} \mu\text{mol}^{-1}$ . The extinction coefficient of the  $\text{PyH}^+$  band at  $\sim 1540 \text{ cm}^{-1}$  was similarly determined by adsorption of pyridine on HY zeolite,  $\text{Si/Al}=2.6$ , which was activated at  $450^\circ\text{C}$  to prevent dehydroxylation ( $\text{PyL}$  bands were absent). The extinction coefficient of the  $\text{PyH}^+$  band at  $\sim 1540 \text{ cm}^{-1}$  was calculated to be  $0.73 \text{ cm} \mu\text{mol}^{-1}$ .

#### 6.2.3. Catalysis Studies

Catalysis studies on the supported niobium oxide catalysts were performed with the sensitive methanol oxidation reaction in order to study the reactivity of

these catalysts. The reactor consisted of a digital flow rate controller (Brooks), a tube furnace (Lindberg), a condenser and methanol reservoir, and a gas chromatograph (HP 5840).

A portion of the methanol in the bottom flask was constantly evaporated under a controlled temperature and pressure. The evaporated methanol was mixed with the He and O<sub>2</sub> gases whose flow rates were adjusted by the mass flow rate controller. This mixed gas flowed through the condenser at a temperature of 9.6°C. The methanol content was obtained by calculating the partial pressure of methanol at this temperature. The 6.9:11.0:82.1 ratio of the CH<sub>3</sub>OH/O<sub>2</sub>/He gaseous mixture then flowed to the reactor. The catalysts were placed in the center of a 6mm OD Pyrex microreactor supported by glass wool. The reactor was heated up by a programmable tube furnace to a constant reaction temperature that varied from 230°C to 280°C. The effluent gases were analyzed online by the gas chromatograph. The gas chromatograph was modified to operate with two thermal conductivity detectors (TCD) and one flame ionization detector (FID), and programmed to perform automatic data acquisition and analysis. The catalytic activity and selectivity were obtained by integrating the peak areas of products with respect to the reference peak area of methanol. The methanol conversion

was kept below 5% to avoid complication due to heat and mass transfer limitations.

The temperature gradient from the inlet and the outlet of the catalyst bed was predicted to be 0.5K by assuming an adiabatic fixed-bed reactor [172]. The adiabatic temperature gradient is so small that the reactor is considered to be isothermal. The  $\text{SiO}_2$  support was used to test the pore diffusion limitation by calculating the Thiele modulus,  $\phi$ , from the Weisz-Prater criterion. The effective diffusion coefficient of the  $\text{SiO}_2$  support was determined to be  $6.0 \times 10^{-3}$   $\text{cm}^2/\text{sec}$  from the Knudsen diffusion model [172]. The calculated Thiele modulus,  $\phi$ , was determined to be  $\sim 5.0 \times 10^{-2}$  which indicates no pore diffusion limitations.

### 6.3. RESULTS

#### 6.3.1. Surface Acidity of Bulk Niobium Oxide and Supported Niobium Oxide Catalysts

##### Bulk Niobium Oxide

The nature of Lewis acid and Brønsted acid surface sites present for bulk  $\text{Nb}_2\text{O}_5$  is dependent on the calcination temperature as shown in Table 6.1. Acidity measurements indicate that considerable Lewis and Brønsted acid surface sites are present on hydrated niobium oxide when it is treated at 120°C. The surface acidic sites,

however, are eliminated at high temperature treatment (500°C) due to loss in surface area, removal of water, and crystallization of the hydrated niobium oxide structure. These results are consistent with Tanabe's acidity studies on hydrated niobium oxide [25].

### Supported Niobium Oxide Catalysts

Pyridine adsorption IR studies on supported niobium oxide catalysts are presented in Figures 6.1 and 6.2 as a function of  $\text{Nb}_2\text{O}_5$  loading. The  $\text{MgO}$  and  $\text{SiO}_2$  supports do not possess Lewis acid surface sites, but the addition of niobium oxide moderately increases the surface concentration of Lewis acid sites. The  $\text{TiO}_2$  and  $\text{ZrO}_2$  supports contain an intermediate amount of Lewis acid surface sites and the addition of niobium oxide moderately decreases the surface concentration of Lewis acid sites. The  $\text{Al}_2\text{O}_3$  support contains a high concentration of Lewis acid surface sites which is modulated by the niobium oxide loading. None of the oxide supports possess Brønsted acid sites, but the addition of niobium oxide generates a fair amount of Brønsted acid surface sites for the  $\text{Nb}_2\text{O}_5/\text{Al}_2\text{O}_3$  and  $\text{Nb}_2\text{O}_5/\text{SiO}_2$  systems and a very small concentration of Brønsted acid surface sites for  $\text{Nb}_2\text{O}_5/\text{TiO}_2$ ,  $\text{Nb}_2\text{O}_5/\text{ZrO}_2$ , and  $\text{Nb}_2\text{O}_5/\text{MgO}$  at high  $\text{Nb}_2\text{O}_5$  loadings.

### **6.3.2. Reactivity of Bulk Niobium Oxide and Supported Niobium Oxide Catalysts**

The reactivity of bulk  $\text{Nb}_2\text{O}_5$  and the supported niobium oxide catalysts was probed by the sensitive methanol oxidation reaction. The methanol oxidation reaction has two different pathways which depend on the nature of the active sites present on the catalyst surface as shown in Scheme 1 [156,167,173,174]. Surface redox sites produce  $\text{HCHO}$  and  $\text{HCOOCH}_3$ , and surface acid sites produce only  $\text{CH}_3\text{OCH}_3$ .

#### **Bulk Niobium Oxide**

The catalytic activity and selectivity data of the methanol oxidation reaction over bulk  $\text{Nb}_2\text{O}_5$  are shown in Table 6.2 as a function of calcination temperature. The activity dramatically decreases with increasing calcination temperature due to the formation of large particles of crystalline  $\text{Nb}_2\text{O}_5$  and the loss of surface area under thermal treatments. Dimethyl ether ( $\text{CH}_3\text{OCH}_3$ ) is the only product for bulk  $\text{Nb}_2\text{O}_5$  treated at  $120^\circ\text{C}$ . At high calcination temperatures ( $>500^\circ\text{C}$ ), small amounts of formaldehyde ( $\text{HCHO}$ ) are detected at reaction temperatures below  $260^\circ\text{C}$ . The thermal treatment affects the surface active sites on bulk  $\text{Nb}_2\text{O}_5$ .

The activities for bulk  $\text{Nb}_2\text{O}_5$  can be converted to turnover number (TON) which is defined as the molecules of

methanol converted per Nb atom per sec. The TON of bulk  $\text{Nb}_2\text{O}_5$  depends on the temperature treatment and has a 6-fold decrease with increasing temperature treatment from 120 to 700°C. The TON is also proportional to the rate constant,  $k_0 e^{(-E_A/RT)}$ , and a plot of the  $\ln(\text{TON})$  vs.  $(1/T)$  exhibits a linear relation. The activation energy,  $E_A$ , of methanol oxidation over bulk  $\text{Nb}_2\text{O}_5$  can be determined from the slope of the Arrhenius plot as shown in Figure 6.3. The activation energies of bulk  $\text{Nb}_2\text{O}_5$  at different temperature treatments are found to be 20.6, 22.7, and 26.0 kcal/mole, respectively. The increase in the  $E_A$  of bulk  $\text{Nb}_2\text{O}_5$  with increasing temperature treatments indicates that the activation energy somewhat depends on the size of  $\text{Nb}_2\text{O}_5$  crystallites.

### Supported Niobium Oxide Catalysts

The influence of the surface niobium oxide overlayer on the methanol oxidation catalytic activity over a series of supported niobium oxide catalysts is presented in Table 6.3. The surface niobium oxide overlayer has almost no influence on the reactivity of the  $\text{TiO}_2$ ,  $\text{ZrO}_2$ , and  $\text{MgO}$  supported systems. In contrast, the surface niobium oxide overlayer significantly enhances the reactivity of the  $\text{Al}_2\text{O}_3$  and  $\text{SiO}_2$  supported systems. The selectivity of the methanol oxidation reaction over the series of supported

niobium oxide catalysts is presented in Table 6.4 as a function of  $\text{Nb}_2\text{O}_5$  loading. Monolayer coverage of supported niobium oxide catalysts was previously determined to be ~19%  $\text{Nb}_2\text{O}_5/\text{Al}_2\text{O}_3$ , ~7%  $\text{Nb}_2\text{O}_5/\text{TiO}_2$ , ~5%  $\text{Nb}_2\text{O}_5/\text{ZrO}_2$ , and ~2%  $\text{Nb}_2\text{O}_5/\text{SiO}_2$ , but not for the  $\text{Nb}_2\text{O}_5/\text{MgO}$  system due to the incorporation of  $\text{Nb}^{+5}$  into the  $\text{MgO}$  support [124]. The surface niobium oxide overlayer on  $\text{Al}_2\text{O}_3$  produces only  $\text{CH}_3\text{OCH}_3$ . On the  $\text{TiO}_2$  and  $\text{ZrO}_2$  supports, the surface niobium oxide overlayer exhibits high  $\text{CH}_3\text{OCH}_3$  selectivity as well as a small amount of  $\text{HCHO}$ , and the  $\text{CH}_3\text{OCH}_3$  selectivity increases with increasing  $\text{Nb}_2\text{O}_5$  loading. The surface niobium oxide overlayer on  $\text{MgO}$  produces mainly  $\text{HCHO}$  and  $\text{CO}_2$  up to 5%  $\text{Nb}_2\text{O}_5/\text{MgO}$ . The presence of niobium oxide on the  $\text{SiO}_2$  surface with loadings less than 2%  $\text{Nb}_2\text{O}_5$ , exhibits a high selectivity for  $\text{HCHO}$  and  $\text{HCOOCH}_3$ . The selectivity of  $\text{CH}_3\text{OCH}_3$  increases with further addition of niobium oxide due to the formation of bulk  $\text{Nb}_2\text{O}_5$  phase above 2%  $\text{Nb}_2\text{O}_5/\text{SiO}_2$  [141]. Thus, the surface niobium oxide overlayers on the  $\text{SiO}_2$  and  $\text{MgO}$  supports possess mainly redox sites due to high selectivity of  $\text{HCHO}$ ,  $\text{HCOOCH}_3$ , as well as  $\text{CO}_2$ , and the surface niobium oxide overlayers on the  $\text{Al}_2\text{O}_3$ ,  $\text{TiO}_2$ , and  $\text{ZrO}_2$  supports possess mainly acid sites due to high selectivity of  $\text{CH}_3\text{OCH}_3$ .

The Arrhenius plots of the surface niobium oxide overlayers on the different oxide supports are shown in

Figure 6.4. The calculated activation energies have the following values: 8%  $\text{Nb}_2\text{O}_5/\text{Al}_2\text{O}_3$  (26.9 kcal/mole) > 7%  $\text{Nb}_2\text{O}_5/\text{TiO}_2$  (21.1 kcal/mole) > 5%  $\text{Nb}_2\text{O}_5/\text{ZrO}_2$  (19.2 kcal/mole) > 2%  $\text{Nb}_2\text{O}_5/\text{SiO}_2$  (15.7 kcal/mole) > 10%  $\text{Nb}_2\text{O}_5/\text{MgO}$  (15.1 kcal/mole). In addition, the influence of the surface niobium oxide coverage on the activation energies for methanol oxidation over the surface niobium oxide overlayers on these oxide supports are tabulated in Table 6.5. For low  $\text{Nb}_2\text{O}_5$  loadings (1%), the  $\text{MgO}$  supported niobium oxide catalyst exhibits the highest activation energy among these catalysts. Upon increasing the  $\text{Nb}_2\text{O}_5$  loadings, the activation energy of the  $\text{MgO}$  supported niobium oxide catalyst decreases from 35.9 to 15.1 kcal/mole which is close to that of the silica supported niobium oxide, and the activation energy of the  $\text{Al}_2\text{O}_3$  supported niobium oxide catalyst decreases from 33.5 to 26.9 kcal/mole. An increase in surface niobium oxide coverage does not have a pronounced effect on the activation energy of the  $\text{SiO}_2$ ,  $\text{TiO}_2$ , and  $\text{ZrO}_2$  supported niobium oxide catalysts.

#### 6.4. DISCUSSIONS

##### Molecular Structures of Supported Niobium Oxide Catalysts

The molecular structures of the  $\text{MgO}$ ,  $\text{Al}_2\text{O}_3$ ,  $\text{TiO}_2$ ,  $\text{ZrO}_2$ ,

and  $\text{SiO}_2$  supported niobium oxide catalysts were investigated with *in situ* Raman spectroscopy, and the various dehydrated surface niobium oxide species present in the supported niobium oxide catalysts appear to be related to the nature of the oxide supports [175].

On the  $\text{SiO}_2$  support up to a loading of 2%  $\text{Nb}_2\text{O}_5$ , only one dehydrated surface niobium oxide species corresponding to the highly distorted  $\text{NbO}_6$  octahedral structure at  $\sim 980 \text{ cm}^{-1}$  is present. Upon increasing the  $\text{Nb}_2\text{O}_5$  loading above 2%  $\text{Nb}_2\text{O}_5/\text{SiO}_2$ , an additional Raman band appears at  $\sim 680 \text{ cm}^{-1}$  which is characteristic of bulk  $\text{Nb}_2\text{O}_5$  and possesses a slightly distorted  $\text{NbO}_6$  octahedral structure.

The dehydrated  $\text{TiO}_2$  and  $\text{ZrO}_2$  supported niobium oxide catalysts also exhibit a Raman band at  $\sim 985 \text{ cm}^{-1}$  at low  $\text{Nb}_2\text{O}_5$  loading which is also assigned to the highly distorted  $\text{NbO}_6$  octahedra. The somewhat lower Raman band positions of the dehydrated 1%  $\text{Nb}_2\text{O}_5/\text{ZrO}_2$  sample are attributed to the presence of surface Cl and F impurities which were detected with XPS only in this particular sample. The highly distorted  $\text{NbO}_6$  octahedra responsible for Raman bands at  $\sim 985$  and  $\sim 935 \text{ cm}^{-1}$  are observed on the  $\text{TiO}_2$  and  $\text{ZrO}_2$  supports with loadings of 7 and 5%  $\text{Nb}_2\text{O}_5$ , respectively. The dehydrated surface niobium oxide phases possessing Raman bands in the  $600\text{-}700 \text{ cm}^{-1}$  region, however, can not be directly observed for  $\text{Nb}_2\text{O}_5/\text{TiO}_2$  and  $\text{Nb}_2\text{O}_5/\text{ZrO}_2$

because of the strong vibrations of the oxide supports in this region.

Below half monolayer coverage on the  $\text{Al}_2\text{O}_3$  support, two kinds of dehydrated surface niobium oxide species which possess highly and moderately distorted  $\text{NbO}_6$  octahedra with  $\text{Nb}=\text{O}$  Raman bands at  $\sim 980$  and  $\sim 883 \text{ cm}^{-1}$ , respectively, are present. Upon approaching monolayer coverage on the  $\text{Al}_2\text{O}_3$  support, additional Raman bands at  $\sim 935$  and  $\sim 647 \text{ cm}^{-1}$  which are characteristic of highly and slightly distorted  $\text{NbO}_6$  octahedra similar to a layered niobium oxide structure are present.

Multiple niobium oxide species are present in the  $\text{Nb}_2\text{O}_5/\text{MgO}$  system and are due to the strong acid-base interactions of  $\text{Nb}_2\text{O}_5$  with  $\text{Mg}^{2+}$  and  $\text{Ca}^{2+}$  impurity cations present on the surface to form  $\text{MgNb}_2\text{O}_6$  and  $\text{Ca}_2\text{Nb}_2\text{O}_7$ , which possess major Raman bands in the  $800\text{-}900 \text{ cm}^{-1}$  region. Consequently, the dehydrated surface niobium oxide species, which give rise to the  $\sim 985 \text{ cm}^{-1}$  band and contain a highly distorted  $\text{NbO}_6$  octahedral structure, coexist with the  $\text{MgNb}_2\text{O}_6$  and  $\text{Ca}_2\text{Nb}_2\text{O}_7$  compounds at high  $\text{Nb}_2\text{O}_5$  loadings. The low relative intensity of the Raman band at  $\sim 985 \text{ cm}^{-1}$  for the 10%  $\text{Nb}_2\text{O}_5/\text{MgO}$  system indicates that only small concentration of the dehydrated surface niobium oxide species which possesses a highly distorted  $\text{NbO}_6$  octahedron are present on the  $\text{MgO}$  surface [175].

### Molecular Structures-Acidity Relationships

Comparison of the surface acidity measurements, Figures 6.1 and 6.2, with the previous *in situ* Raman studies [175], provides insight into the origin of the Lewis acid and Brønsted acid surface sites for supported niobium oxide catalysts.

For the  $\text{Nb}_2\text{O}_5/\text{SiO}_2$  system, the dehydrated surface niobium oxide Raman band at  $\sim 980 \text{ cm}^{-1}$  is observed at low loadings (< 2%) and corresponds to the presence of Lewis acid surface sites (see Fig. 6.1). The dehydrated surface niobium oxide species consist of highly distorted  $\text{NbO}_6$  octahedra that possess  $\text{Nb}=\text{O}$  bonds which appear to be coordinatively unsaturated surface acid sites. At loadings greater than 2%  $\text{Nb}_2\text{O}_5$ , the presence of Brønsted acidity for the  $\text{Nb}_2\text{O}_5/\text{SiO}_2$  system corresponds to the formation of bulk  $\text{Nb}_2\text{O}_5$ , and the maximum with niobium oxide loading suggest that there is an effect of  $\text{Nb}_2\text{O}_5$  particle size on the concentration of Brønsted and Lewis acid surface sites. Hydrated niobium oxide ( $\text{Nb}_2\text{O}_5 \cdot n\text{H}_2\text{O}$ ) is well known to possess both Lewis and Brønsted acid surface sites [28]. The decrease of Brønsted acid surface sites and the maximum intensity of Lewis acid surface sites with increasing temperature treatment from 100 to  $500^\circ\text{C}$  indicate that a phase transformation of amorphous  $\text{Nb}_2\text{O}_5 \cdot n\text{H}_2\text{O}$  to TT- $\text{Nb}_2\text{O}_5$  occurs [28]. In other words, the concentration of Brønsted

and Lewis acid surface sites present on bulk  $\text{Nb}_2\text{O}_5$  is affected by its particle size.

On the  $\text{TiO}_2$  and  $\text{ZrO}_2$  supports, an intermediate amount of Lewis acid sites are present, and the addition of niobium oxide, below monolayer coverage, moderately decreases the surface concentration of Lewis acid sites due to the decrease of coordinatively unsaturated surface sites. These surface sites are replaced by the dehydrated surface niobium oxide species with a Raman band at  $\sim 985 \text{ cm}^{-1}$  which is characteristic of the highly distorted  $\text{NbO}_6$  octahedral structure. For the  $\text{Nb}_2\text{O}_5/\text{TiO}_2$  and  $\text{Nb}_2\text{O}_5/\text{ZrO}_2$  systems, a second dehydrated surface niobium oxide species possessing a Raman band at  $\sim 935 \text{ cm}^{-1}$  is observed when monolayer coverages ( $\sim 7\% \text{ Nb}_2\text{O}_5/\text{TiO}_2$  and  $\sim 5\% \text{ Nb}_2\text{O}_5/\text{ZrO}_2$ ) are reached. The presence of the new highly distorted  $\text{NbO}_6$  octahedral surface species with a longer  $\text{Nb}=\text{O}$  bond does not further decrease the concentration of Lewis acid surface sites which indicates that the surface niobium oxide species with a Raman band at  $\sim 935 \text{ cm}^{-1}$  occupies different surface sites on the  $\text{TiO}_2$  and  $\text{ZrO}_2$  supports than those sites responsible for the Raman band at  $\sim 985 \text{ cm}^{-1}$ . The small amount of Brønsted acid surface sites for 10%  $\text{Nb}_2\text{O}_5/\text{TiO}_2$  and 10%  $\text{Nb}_2\text{O}_5/\text{ZrO}_2$  are attributed to the presence of bulk  $\text{Nb}_2\text{O}_5$  since monolayer coverage of surface niobium oxide was exceeded for these samples.

The  $\text{Al}_2\text{O}_3$  support contains a high concentration of Lewis acid surface sites which is modulated by the niobium oxide loading. Below half monolayer coverage, the increase of Lewis acid surface sites suggests that the highly distorted surface  $\text{NbO}_6$  with Raman bands at  $\sim 980$  and  $\sim 883 \text{ cm}^{-1}$  serve as coordinatively unsaturated surface acid sites. The appearance of the  $\sim 935$  and  $\sim 647 \text{ cm}^{-1}$  Raman bands correspond to the formation of Brønsted acid surface sites at high loading on the  $\text{Al}_2\text{O}_3$  support. The Brønsted acid surface sites increase upon approaching monolayer coverage ( $\sim 19\% \text{ Nb}_2\text{O}_5/\text{Al}_2\text{O}_3$ ) while the Lewis acid surface sites simultaneously decrease which suggests that the conversion of Lewis acid sites to Brønsted acid sites may occur with increasing  $\text{Nb}_2\text{O}_5$  loadings. The exact location of these protons are not known from the IR and Raman characterization studies. However, the layered niobium oxide compounds are found to react with the weak base, pyridine, and indicate that these compounds possess strong Brønsted acid sites due to the presence of  $\text{H}^+$  protons in the adjacent terminal layers to form  $\text{Nb}=\text{OH}^+$  sites [54]. Thus, the dehydrated surface niobium oxide species possessing both highly and slightly distorted  $\text{NbO}_6$  octahedra, similar to layered niobium oxide compounds [93], are associated with protons that form Brønsted acid surface sites. Furthermore, the absence of Brønsted acid surface sites for  $\text{Nb}_2\text{O}_5/\text{TiO}_2$  and  $\text{Nb}_2\text{O}_5/\text{ZrO}_2$  indicates that the

slightly distorted surface niobium oxide species responsible for the  $\sim 650$   $\text{cm}^{-1}$  Raman band is not present in these systems (recall that this region was overshadowed by the strong vibrations of the  $\text{TiO}_2$  and  $\text{ZrO}_2$  supports).

For the  $\text{Nb}_2\text{O}_5/\text{MgO}$  system, the  $\sim 890$ , and  $\sim 823$   $\text{cm}^{-1}$  Raman bands are probably not related to the Lewis acid surface sites since they appear to be incorporated into the  $\text{MgO}$  support surface to form the  $\text{MgNb}_2\text{O}_6$  as well as  $\text{Ca}_2\text{Nb}_2\text{O}_7$  compounds and would not be expected to be exposed. The increase of Lewis acid surface sites with increasing  $\text{Nb}_2\text{O}_5$  loading corresponds to the presence of coordinatively unsaturated surface sites on the highly distorted  $\text{NbO}_6$  octahedral species at  $\sim 935$  and  $\sim 985$   $\text{cm}^{-1}$ . The origin of the small amount of Brønsted acid surface sites at 15%  $\text{Nb}_2\text{O}_5/\text{MgO}$  is not known since bulk  $\text{Nb}_2\text{O}_5$  at  $\sim 680$   $\text{cm}^{-1}$  and the surface layered niobium oxide species at  $\sim 935$  and  $\sim 650$   $\text{cm}^{-1}$  are not present in this sample.

In summary, the highly distorted surface  $\text{NbO}_6$  octahedra sites correspond to the Lewis acid sites and the surface layered niobium oxide species containing both highly as well as slightly distorted surface  $\text{NbO}_6$  sites are associated with the Brønsted acid sites of supported niobium oxide catalysts. In addition, a microcrystalline bulk  $\text{Nb}_2\text{O}_5$  particles present in these systems will also give rise to Brønsted acid surface sites (see Table 6.1).

### Molecular Structures-Reactivity Relationships

The catalytic properties of the supported niobium oxide catalysts were probed with the methanol oxidation reaction because of its ability to discriminate between surface acid sites, formation of dimethyl ether ( $\text{CH}_3\text{OCH}_3$ ), and surface redox sites, formation of formaldehyde ( $\text{HCHO}$ ) and methyl formate ( $\text{HCOOCH}_3$ ).

The  $\text{SiO}_2$  supported niobium oxide catalysts at low  $\text{Nb}_2\text{O}_5$  loadings (< 2%) were surprisingly found to possess surface redox sites of high reactivity and selectivity towards  $\text{HCHO}$  and  $\text{HCOOCH}_3$  (see Figures 6.3 and 6.4). Comparison of these catalytic data with the earlier structure-acidity studies reveals that the Lewis acid surface sites, consisting of highly distorted  $\text{NbO}_6$  octahedra, result in these superior catalytic properties. The decrease in methanol oxidation reactivity above 2%  $\text{Nb}_2\text{O}_5/\text{SiO}_2$  is due to the formation of bulk  $\text{Nb}_2\text{O}_5$  particles which block the surface  $\text{Nb}=\text{O}$  sites (see Fig. 6.3). The decrease in  $\text{HCHO}$  and  $\text{HCOOCH}_3$  selectivity, and the simultaneous increase in  $\text{CH}_3\text{OCH}_3$  selectivity above 2%  $\text{Nb}_2\text{O}_5/\text{SiO}_2$  is due to the Brønsted and Lewis acid surface sites on the bulk  $\text{Nb}_2\text{O}_5$  particles present at these loadings (see Fig. 6.4).

The highly distorted  $\text{NbO}_6$  Lewis acid sites are significantly more reactive when coordinated to the  $\text{Al}_2\text{O}_3$

surfaces than the  $TiO_2$  and  $ZrO_2$  surfaces (see Table 6.3) due to the increase in coordinatively unsaturated surface sites on the  $Nb_2O_5/Al_2O_3$  system at loadings less than 5%  $Nb_2O_5$  (see Fig. 6.1). The reactivity of Brønsted acid surface sites, consisting of highly and slightly distorted  $NbO_6$  octahedra, appears to be very close to the reactivity of the Lewis acid surface sites for methanol oxidation over  $Nb_2O_5/Al_2O_3$  at the loadings greater than 5%  $Nb_2O_5$ . This is demonstrated by the comparison TON of 5%  $Nb_2O_5/Al_2O_3$ , possessing only Lewis acid surface sites, which is equal to 0.177 with that of 12%  $Nb_2O_5/Al_2O_3$ , possessing both Lewis and Brønsted surface acid sites, which is equal to 0.184. The dramatic decrease in reactivity for 19%  $Nb_2O_5/Al_2O_3$  is attributed to self-poisoning of the extremely reactive catalyst (i.e. carbon deposition). The high selectivity towards  $CH_3OCH_3$  of the surface niobium oxide overlayers on  $TiO_2$ ,  $ZrO_2$ , and  $Al_2O_3$  reveals that predominantly only acid sites, and essentially no redox sites, are present on these niobium oxide overlayers. Thus, the reactivity of these surface acid sites appear to be markedly influenced by the specific oxide support, and the coordinated niobium oxide on the alumina surface enhances the reactivity of these sites.

Furthermore, the acid sites on the  $TiO_2$ ,  $ZrO_2$ , and  $Al_2O_3$  supported niobium oxide catalysts are similar to

those present on the bulk  $\text{Nb}_2\text{O}_5$  surface because of the similar activation energies (see Table 6.5 and Fig. 6.5). In contrast, the surface niobium oxide overlayer on  $\text{SiO}_2$ , less than 2%  $\text{Nb}_2\text{O}_5/\text{SiO}_2$ , behaves predominantly as a redox site and exhibits a high selectivity towards  $\text{HCHO}$  and  $\text{HCOOCH}_3$ . The low activation energy, 15.7 kcal/mole, of 2%  $\text{Nb}_2\text{O}_5/\text{SiO}_2$  also suggests that the  $\text{Nb}_2\text{O}_5/\text{SiO}_2$  system has different reaction mechanisms than the  $\text{Nb}_2\text{O}_5/\text{TiO}_2$ ,  $\text{Nb}_2\text{O}_5/\text{ZrO}_2$ , and  $\text{Nb}_2\text{O}_5/\text{Al}_2\text{O}_3$  systems. The addition of niobium oxide on the  $\text{MgO}$  support exhibits low reactivity due to the acid-base interaction to form  $\text{MgNb}_2\text{O}_6$  and  $\text{Ca}_2\text{Nb}_2\text{O}_7$ . Upon increasing the  $\text{Nb}_2\text{O}_5$  loading, the activation energy of  $\text{Nb}_2\text{O}_5/\text{MgO}$  changes from 35.9 to 15.1 kcal/mole which indicates the presence of surface niobium oxide species that possess a highly distorted  $\text{NbO}_6$  octahedral structure that is similar to the  $\text{Nb}_2\text{O}_5/\text{SiO}_2$  system ( $E_A=15.7$  kcal/mole). The selectivity pattern of the  $\text{Nb}_2\text{O}_5/\text{MgO}$  system is more complex because of the reaction products from the Lewis acid surface sites as well as the exposed  $\text{MgO}$  surface sites which possess high selectivity towards  $\text{CO}_2$  and  $\text{HCHO}$ . Thus, the same Lewis acid surface site, consisting of a highly distorted  $\text{NbO}_6$  octahedra, can behave as either an acid site or redox site depending on the specific oxide support to which it is coordinated.

The  $\text{SiO}_2$ ,  $\text{TiO}_2$ , and  $\text{Al}_2\text{O}_3$  supported niobium oxide

catalysts containing low  $\text{Nb}_2\text{O}_5$  loadings were recently investigated by Iwasawa et al. for the ethanol dehydrogenation reaction [7,9]. It was determined that the  $\text{Nb}_2\text{O}_5/\text{SiO}_2$  system exhibits a high reactivity and selectivity for acetaldehyde ( $\text{C}_2\text{H}_5\text{CHO}$ ) and that the  $\text{Nb}_2\text{O}_5/\text{Al}_2\text{O}_3$  system exhibits a high reactivity and selectivity for diethylether ( $\text{C}_2\text{H}_5\text{OC}_2\text{H}_5$ ) and ethene ( $\text{C}_2\text{H}_4$ ). The  $\text{Nb}_2\text{O}_5/\text{TiO}_2$  system has a low reactivity for ethanol dehydrogenation but it shows high selectivity for acetaldehyde. These findings are consistent with the present study which shows that surface active sites can behave as either an acid site or redox site depending on the specific oxide support to which it is coordinated. The surface niobium oxide overlayer on the  $\text{Al}_2\text{O}_3$  support was also investigated by Murrell et al. [5,22] as acid cracking catalysts, and determined that the  $\text{Nb}_2\text{O}_5/\text{Al}_2\text{O}_3$  system possesses strong Brønsted acid surface sites at one-third monolayer coverage and the support has a dramatic effect on the Brønsted acidity due to the lower proton removal energies of the supported metal oxides.

## 6.5. CONCLUSIONS

The molecular structure-reactivity relationships for supported niobium oxide catalysts were achieved by

combining Raman spectroscopy structural studies with chemical probes that measured the acidity and reactivity of the surface niobium oxide sites. The highly distorted  $\text{NbO}_6$  octahedra possess  $\text{Nb}=\text{O}$  bonds and are associated with Lewis acid sites. The slightly distorted  $\text{NbO}_6$  octahedra as well as the highly distorted  $\text{NbO}_6$  octahedra, which are similar to layered niobium oxide compounds, are associated with Brønsted acid sites. The Lewis acid surface sites are present on all the supported niobium oxide systems, but the Brønsted acid surface sites are limited to the  $\text{Nb}_2\text{O}_5/\text{Al}_2\text{O}_3$  and  $\text{Nb}_2\text{O}_5/\text{SiO}_2$  systems. The surface niobium oxide Lewis acid sites are significantly more active when coordinated to the  $\text{Al}_2\text{O}_3$  surface than to the  $\text{TiO}_2$ ,  $\text{ZrO}_2$ , and  $\text{MgO}$  surfaces (surface oxide-support interaction). Furthermore, the surface niobium oxide sites on  $\text{SiO}_2$  with an activation energy,  $E_A$ , of 15.7 kcal/mole behave as redox sites and the surface niobium oxide sites on  $\text{Al}_2\text{O}_3$  with an activation energy,  $E_A$ , of 26.9 kcal/mole, which are similar to bulk  $\text{Nb}_2\text{O}_5$ , are acid sites during partial oxidation reactions. These different activation energies are a direct consequence of the different methanol reaction pathways.

Table 6.1: Surface acid sites present in bulk niobium oxide as a function of temperature treatment

<u>Catalyst</u>	<u>Lewis Acid Sites (<math>\mu</math>mole/g)</u>	<u>Bronsted Acid Sites (<math>\mu</math>mole/g)</u>
$\text{Nb}_2\text{O}_5$ (120°C)	152	57
$\text{Nb}_2\text{O}_5$ (500°C)	0	0

Scheme 1  
Two Reaction Pathways for Methanol Oxidation

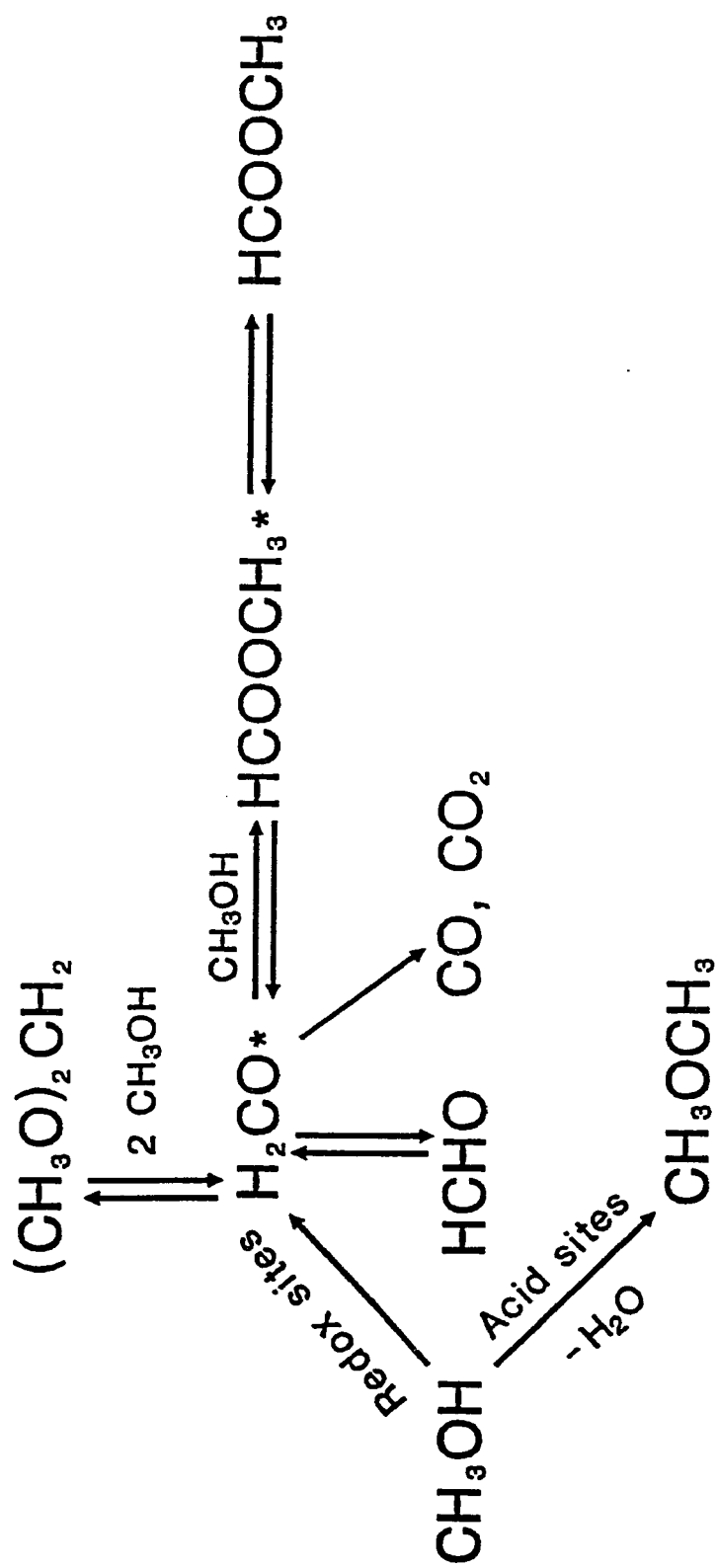


Table 6.2: The reactivity and selectivity of methanol oxidation reaction over bulk  $\text{Nb}_2\text{O}_5$

Catalyst	Reaction Temperatures (°C)					
	230		260		280	
	A	$S_{\text{DME}}$	A	$S_{\text{DME}}$	A	$S_{\text{DME}}$
$\text{Nb}_2\text{O}_5$ (120 °C, 16 hrs)	39.5	100	129.4	100	250.8	100
$\text{Nb}_2\text{O}_5$ (500 °C, 2 hrs)	5.84	95	20.1	98	45.2	100
$\text{Nb}_2\text{O}_5$ (700 °C, 2 hrs)	0.57	94	2.53	99	5.84	100

A: Activity (mmole/g·h)

$S_{\text{DME}}$ :  $\text{CH}_3\text{OCH}_3$  selectivity (%)  
 $\text{HCHO} = 100 - S_{\text{DME}}$

**Table 6.3: The reactivity of methanol oxidation reaction over supported niobium oxide catalysts**

$\text{Nb}_2\text{O}_5$ Loading (wt%)	Initial Rate [mmole/(g)(h)]				
	$\text{MgO}$	$\text{Al}_2\text{O}_3$	$\text{TiO}_2$	$\text{ZrO}_2$	$\text{SiO}_2$
0	8.4	64	2.1	7.3	0.7
0.2					21.4
1.0	2.8	69	2.5	7.1	26.5
2.0					38.4
2.5					26.2
3.0	6.8	323	3.9	5.3	
4.0					24.9
5.0	3.9	240	5.8	6.3	
6.0					15.4
7.0			6.2		
8.0		320			
10.0	2.0				
12.0		600			
19.0		75			

**Table 6.4: The selectivity of methanol oxidation reaction over supported niobium oxide catalysts**

<u>Nb<sub>2</sub>O<sub>5</sub></u> Loading (wt %)	<u>MgO</u>		<u>Al<sub>2</sub>O<sub>3</sub></u>		<u>TiO<sub>2</sub></u>		<u>ZrO<sub>2</sub></u>		<u>SiO<sub>2</sub></u>	
	<u>Redox</u>	<u>Acid</u>	<u>Redox</u>	<u>Acid</u>	<u>Redox</u>	<u>Acid</u>	<u>Redox</u>	<u>Acid</u>	<u>Redox</u>	<u>Acid</u>
0	32.8	-	100		9.5	90.5	58.4	5.2	-	-
0.2									91.5	1.1
1	50.3	0.5	100		10.5	89.5	31.2	50.7	86.6	7.3
2									87.2	5.2
2.5									79.6	17.6
3	61.5	0.5	100		8.6	91.4	-	96.0	66.9	28.5
4										
5	71.4	2.1	100		3.7	96.3	-	98.0		
6									52.8	45.4
7					2.5	96.5				
10	56.5	27.9	100		1.4	97.2				

Redox: HCHO and HCOOCH<sub>3</sub>  
CO/CO<sub>2</sub>: 100-(Redox+Acid)

Acid: CH<sub>3</sub>OCH<sub>3</sub>

**Table 6.5: The activation energy of methanol oxidation over supported niobium oxide catalysts as a function of  $\text{Nb}_2\text{O}_5$  loading**

<u>Catalyst</u>	<u><math>E_A</math> (kcal/mole)</u>	
	<u>Low Coverage</u>	<u>High Coverage</u>
$\text{Nb}_2\text{O}_5/\text{MgO}$	35.9 (1% $\text{Nb}_2\text{O}_6$ )	15.1 (10% $\text{Nb}_2\text{O}_6$ )
$\text{Nb}_2\text{O}_5/\text{Al}_2\text{O}_3$	33.5 (1% $\text{Nb}_2\text{O}_6$ )	26.9 (8% $\text{Nb}_2\text{O}_6$ )
$\text{Nb}_2\text{O}_5/\text{TiO}_2$	20.2 (1% $\text{Nb}_2\text{O}_6$ )	20.9 (7% $\text{Nb}_2\text{O}_6$ )
$\text{Nb}_2\text{O}_5/\text{ZrO}_2$	19.2 (1% $\text{Nb}_2\text{O}_6$ )	19.2 (5% $\text{Nb}_2\text{O}_6$ )
$\text{Nb}_2\text{O}_5/\text{SiO}_2$	16.7 (1% $\text{Nb}_2\text{O}_6$ )	15.7 (2% $\text{Nb}_2\text{O}_6$ )

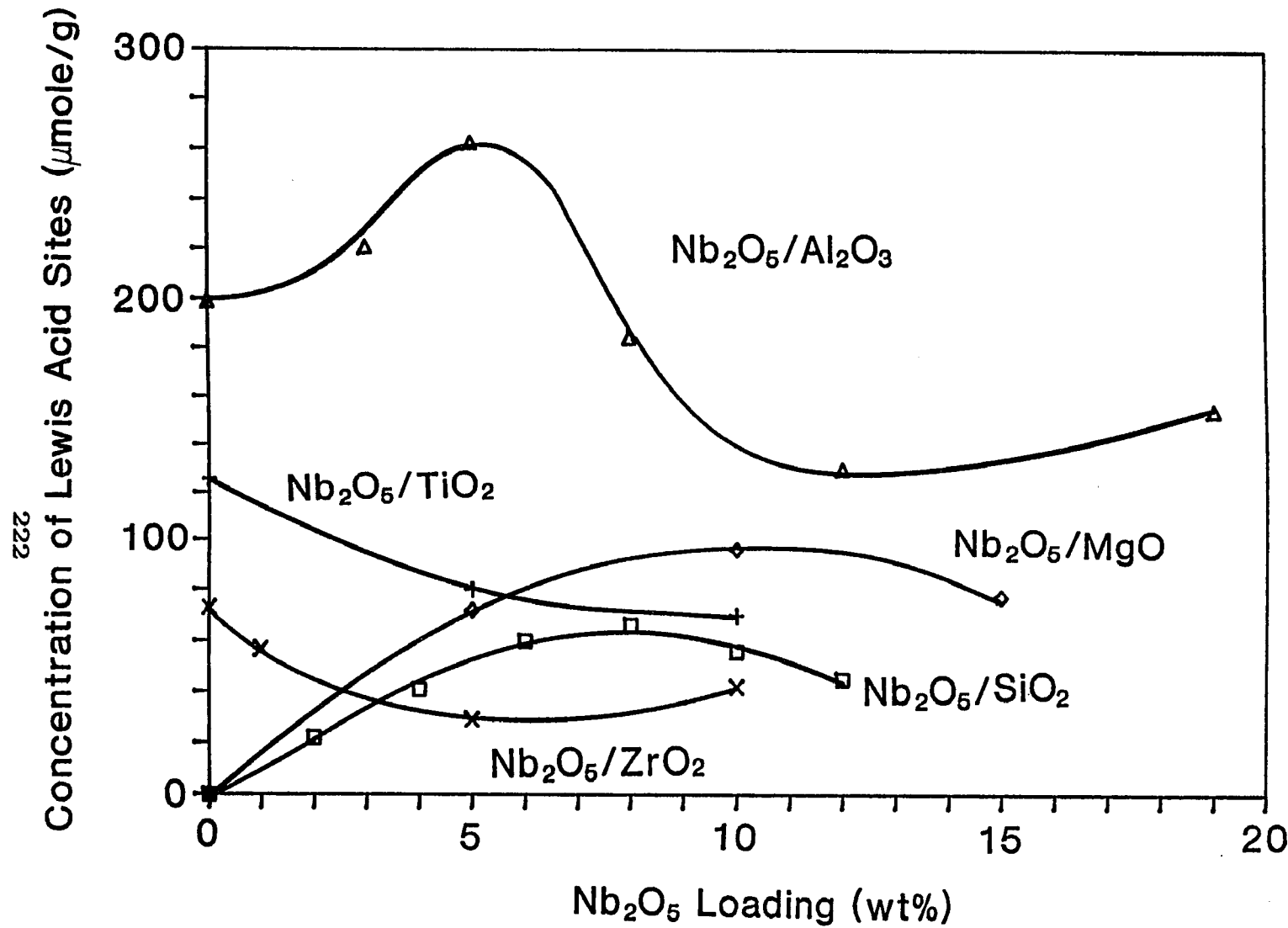


Figure 6.1: The Lewis acid surface sites present in the supported niobium oxide catalysts

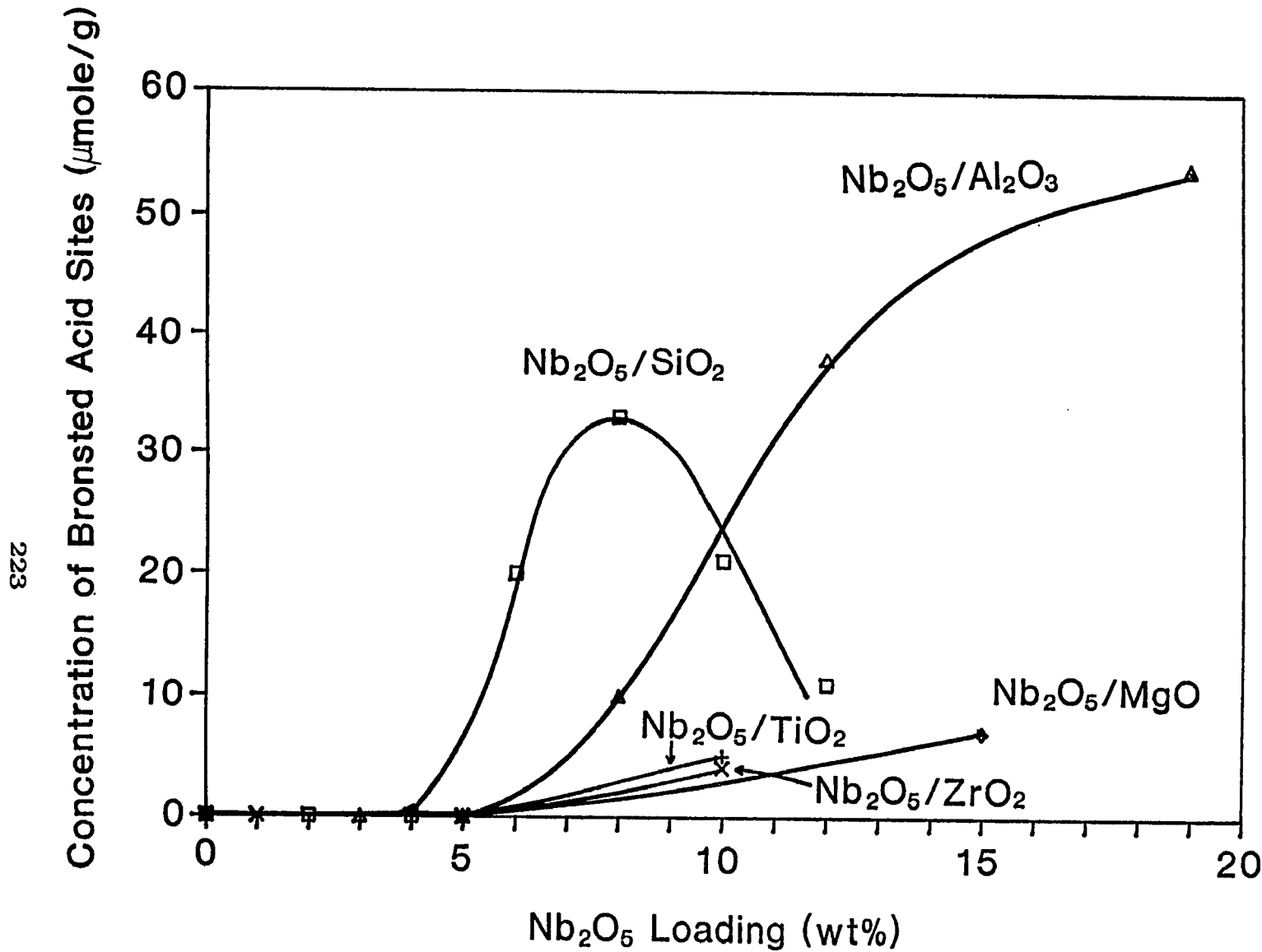
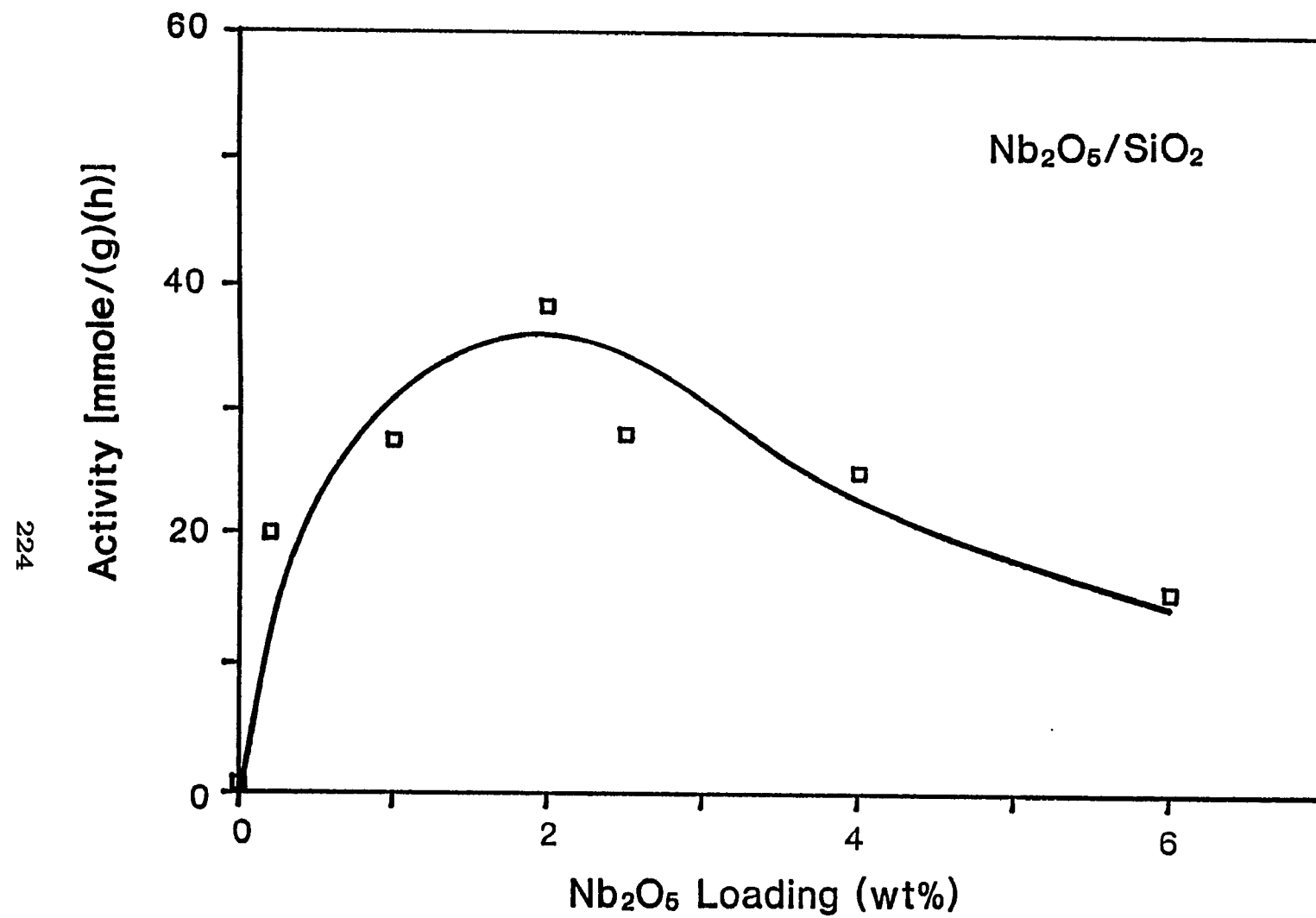


Figure 6.2: The Brønsted acid surface sites present in the supported niobium oxide catalysts



**Figure 6.3:** The reactivity of the  $\text{SiO}_2$  supported niobium oxide catalysts as a function of  $\text{Nb}_2\text{O}_5$  loading

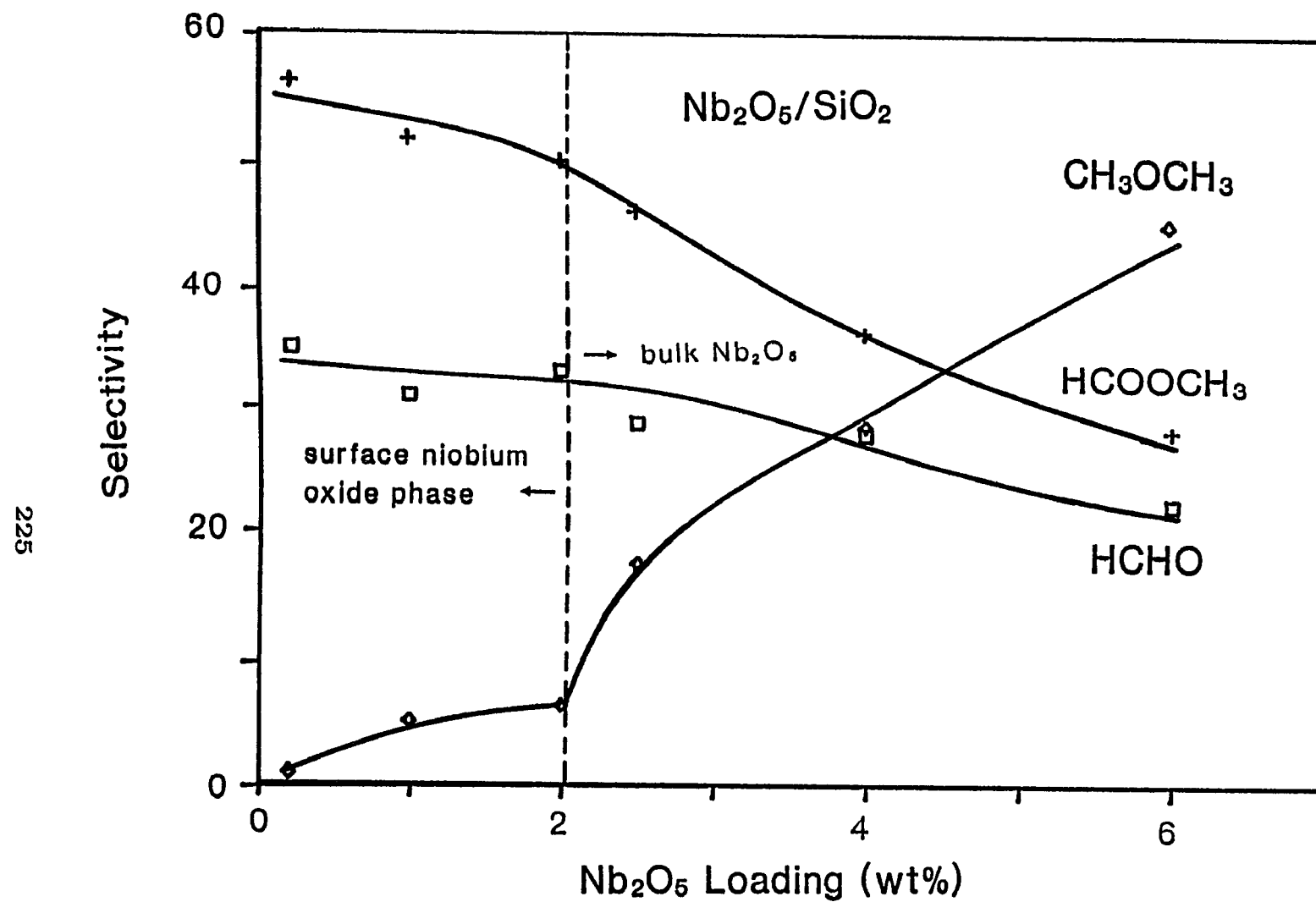


Figure 6.4: The selectivity of the  $\text{SiO}_2$  supported niobium oxide catalysts as a function of  $\text{Nb}_2\text{O}_5$  loading

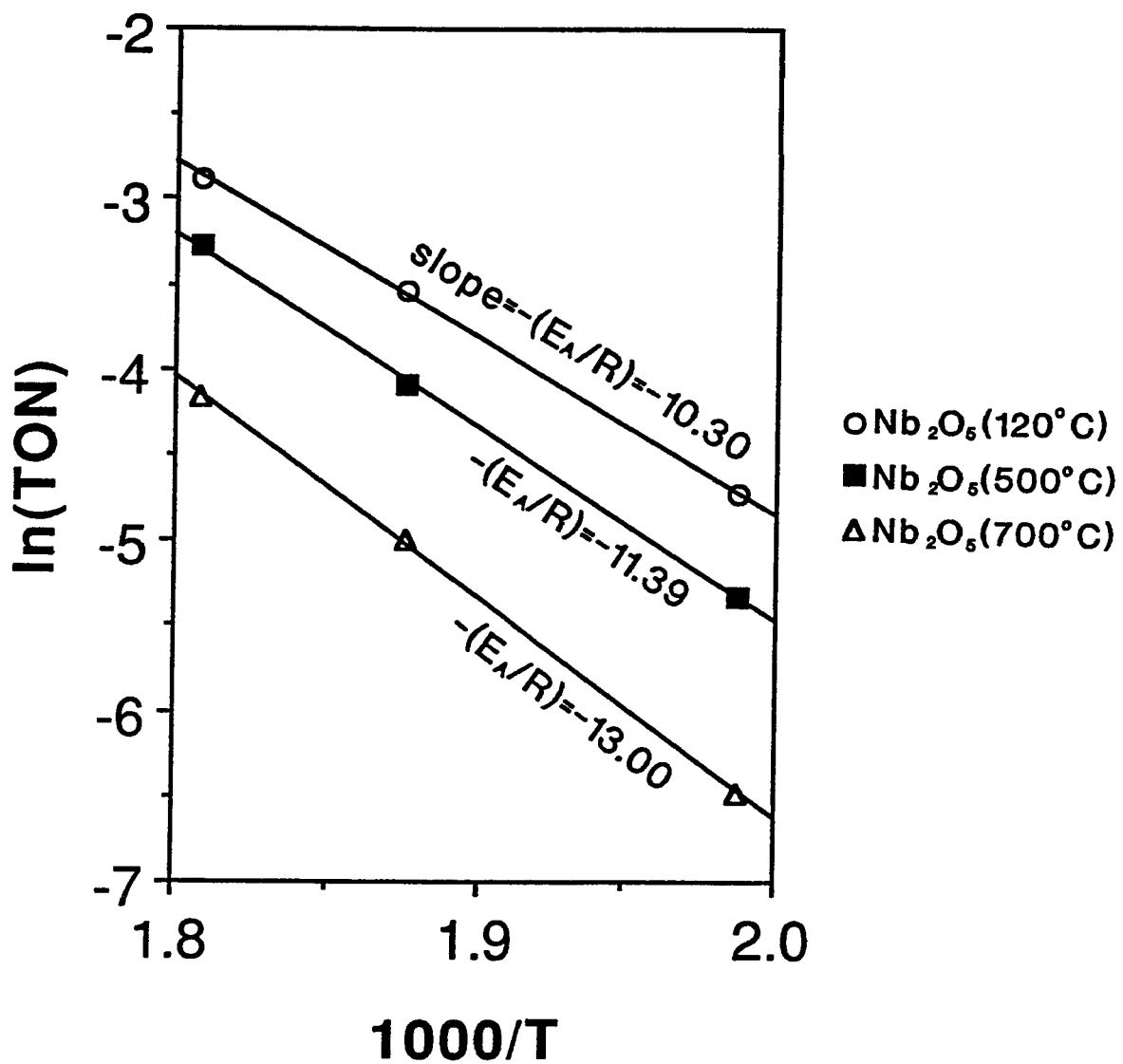
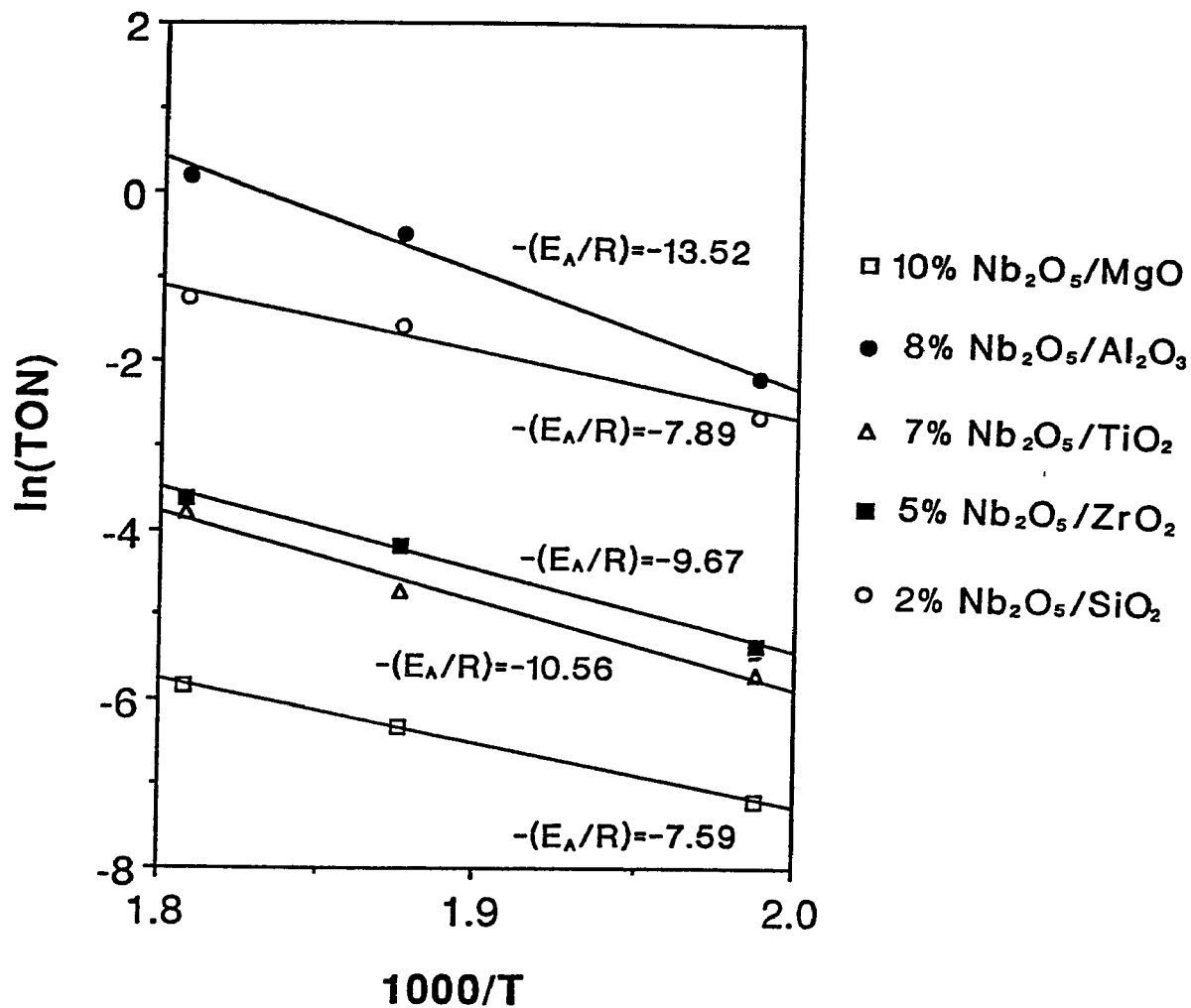


Figure: 6.5: Arrhenius plot of bulk Nb<sub>2</sub>O<sub>5</sub> for methanol oxidation



**Figure 6.6: Arrhenius plot of supported niobium oxide catalysts for methanol oxidation**

## CHAPTER 7 CONCLUSIONS

This work has demonstrated that the understanding of surface niobium oxide-support interactions influence the molecular structure and surface chemistry of the surface niobium oxide overlayer. Knowledge of the nature of surface active sites, combined with information on the structure of surface niobium oxide species, can lead to improve niobium-based catalysts for achieving high reactivity and selectivity.

The molecular structure-reactivity relationships for supported niobium oxide catalysts were achieved by combining Raman spectroscopy structural studies with chemical probes that measured the acidity and reactivity of the surface niobium oxide sites. Supported niobium oxide catalysts under ambient conditions form a two-dimensional overlayer on oxide supports, and the monolayer coverage of these systems is reached at ~19 wt%  $\text{Nb}_2\text{O}_5/\text{Al}_2\text{O}_3$ , ~7 wt%  $\text{Nb}_2\text{O}_5/\text{TiO}_2$ , ~5 wt%  $\text{Nb}_2\text{O}_5/\text{ZrO}_2$ , and ~2 wt%  $\text{Nb}_2\text{O}_5/\text{SiO}_2$ , but not for the  $\text{Nb}_2\text{O}_5/\text{MgO}$  system due to the incorporation of  $\text{Nb}^{+5}$  into the  $\text{MgO}$  support. The molecular structures of the surface niobium oxide species under ambient conditions,

where adsorbed moisture is present, are controlled by the surface pH of the system. Under *in situ* conditions the adsorbed moisture desorbs upon heating and the surface niobium oxide overlayer on oxide supports become dehydrated. On the  $\text{SiO}_2$  support, only one dehydrated surface niobium oxide species corresponding to the highly distorted  $\text{NbO}_6$  octahedral structure at  $\sim 980 \text{ cm}^{-1}$  is present. The highly distorted  $\text{NbO}_6$  octahedra responsible for Raman bands at  $\sim 985$  and  $\sim 935 \text{ cm}^{-1}$  are also observed on the  $\text{TiO}_2$  and  $\text{ZrO}_2$  supports at monolayer coverage. Below half a monolayer coverage on the  $\text{Al}_2\text{O}_3$  support, two kinds of dehydrated surface niobium oxide species possessing highly and moderately distorted  $\text{NbO}_6$  octahedra with  $\text{Nb}=\text{O}$  Raman bands at  $\sim 980$  and  $\sim 883 \text{ cm}^{-1}$ , respectively, are present. Upon approaching monolayer coverage on the  $\text{Al}_2\text{O}_3$  support, additional Raman bands at  $\sim 935$  and  $\sim 647 \text{ cm}^{-1}$  characteristic of highly and slightly distorted  $\text{NbO}_6$  octahedra are present and are suggestive of a layered niobium oxide structure. Multiple niobium oxide species are present in the  $\text{Nb}_2\text{O}_5/\text{MgO}$  system due to the strong acid-base interactions of  $\text{Nb}_2\text{O}_5$  with the  $\text{Mg}^{2+}$  and the  $\text{Ca}^{2+}$  impurity cations present on the surface. The highly distorted  $\text{NbO}_6$  octahedra possess  $\text{Nb}=\text{O}$  bonds and are associated with Lewis acid sites. The surface layered niobium oxide species possessing both  $\text{Nb}=\text{O}$  and  $\text{Nb}-\text{O}$  bonds

are associated with Brønsted acid sites. The Lewis acid surface sites are present on all the supported niobium oxide systems, but the Brønsted acid surface sites are limited to the  $\text{Nb}_2\text{O}_5/\text{Al}_2\text{O}_3$  and  $\text{Nb}_2\text{O}_5/\text{SiO}_2$  systems. The surface niobium oxide Lewis acid sites are significantly more active when coordinated to the  $\text{Al}_2\text{O}_3$  surface than to the  $\text{TiO}_2$ ,  $\text{ZrO}_2$ , and  $\text{MgO}$  surfaces (surface oxide-support interaction). Furthermore, the surface niobium oxide sites on  $\text{SiO}_2$  and  $\text{MgO}$  behave as redox sites and the surface niobium oxide sites on  $\text{Al}_2\text{O}_3$ ,  $\text{TiO}_2$ , and  $\text{ZrO}_2$  are acid sites during partial oxidation reactions. Thus, the same Lewis acid surface site, consisting of a highly distorted  $\text{NbO}_6$  octahedra, can behave as either an acid site or redox site depending on the specific oxide support to which it is coordinated.

The nature of the oxide support has a pronounced effect on the chemical and physical properties of the surface niobium oxide overlayer. The various dehydrated surface niobium oxide structures present in supported niobium oxide catalysts appear to be related to the oxide support surface hydroxyl chemistry because the surface niobium oxide phases are formed by reaction of the niobium oxide precursor with the surface hydroxyl groups of the oxide supports. The  $\text{SiO}_2$  surface possesses only one kind

of surface hydroxyl group and only one dehydrated surface niobium oxide species (Raman band at  $\sim 980 \text{ cm}^{-1}$ ) is present. The  $\text{TiO}_2$  and  $\text{ZrO}_2$  surfaces possess two kinds of surface hydroxyl groups and two dehydrated surface niobium oxide species (Raman band at  $\sim 985$  and  $\sim 935 \text{ cm}^{-1}$ ) are present. The  $\text{Al}_2\text{O}_3$  surface possesses at least 4 different surface hydroxyl groups and three dehydrated surface niobium oxide species (Raman bands at  $\sim 985$ ,  $\sim 935$ ,  $\sim 880$ , and  $\sim 647 \text{ cm}^{-1}$ ) are present. The  $\text{MgO}$  surface possesses one kind of surface hydroxyl group, but three different niobium oxide species are observed (Raman bands at  $\sim 985$ ,  $\sim 890$ , and  $\sim 830 \text{ cm}^{-1}$ ) due to the acid-base interactions.

## REFERENCES

1. I. E. Wachs,  
"Proc. Intern. Conf. on Niobium and Tantalum," 679  
(1989).
2. K. Domen, A. Kudo, M. Shibata, A. Tanaka, K. Maruya,  
and T. Onishi,  
J. Chem. Soc. Chem. Commun., 1706 (1986).
3. K. Domen, J. Yoshimuta, A. Tanaka, and K. Maruya,  
PACIFICHEM'89, "Catalytic Conversion with Niobium  
Materials," Honolulu, Dec. 17-22, 1989.
4. A. J. Jacobson, J. W. Johnson, and J. T. Lewandowski,  
Mat. Res. Bull. 22, 45 (1987).
5. L. L. Murrell, D. C. Grenoble, C. J. Kim, and  
N. C. dispenziere, Jr.,  
J. Catal. 107, 463 (1987).
6. M. Nishimura, K. Asakura, and Y. Iwasawa,  
Chem. Lett., 1457 (1986).
7. M. Nishimura, K. Asakura, and Y. Iwasawa,  
J. Chem. Soc. Chem. Commun., 1660 (1986).
8. H. Kobagashi, M. Yamaguchi, T. Tanaka, Y. Nishimura,  
H. Kawakami, and S. Yoshida,  
J. Phys. Chem. 92, 2316 (1988).

9. M. Nishimura, K. Asakura, and Y. Iwasawa,  
"Proc. 9th Intern. Congr. Catal." 4, 1842 (1988).
10. J. G. Weissman, E. I. Ko, and P. Wynblatt,  
J. Catal. 108, 383 (1987).
11. E. I. Ko, R. Bafrali, N. T. Nuhfer, and N. J. Wagner,  
J. Catal. 95, 260 (1985).
12. J. M. Jehng, F. D. Hardcastle, and I. E. Wachs,  
Solid State Ionics 32/33, 904 (1989).
13. S. Okazaki and T. Okuyama,  
Bull. Chem. Soc. Jpn. 56, 2159 (1983)
14. Y. Nishimura, T. Tanaka, H. Kanai, T. Funabiki,  
and S. Yoshida,  
PACIFICHEM'89, "Catalytic Conversion with Niobium  
Materials," Honolulu, Dec. 17-22, 1989.
15. G. Albanesi and P. Moggi,  
Applied Catalysis 6, 293 (1983).
16. P. Moggi and G. Albanesi,  
React. Kinet. Catal. Lett. 22, 247 (1983).
17. Y. Wada and A. Morikawa,  
Bull. Chem. Soc. Jpn. 60, 3509 (1987)
18. A. Morikawa, T. Nakajima, I. Nishiyama, and K. Otsuka,  
Nippon Kagaku Kaishi, 239 (1984).
19. L. L. Murrell and D. C. Grenoble,  
US Patent 4,415,480 (1983).

20. S. Okazaki and T. Okayama,  
Bull. Chem. Soc. Jpn. 56, 2159 (1983).

21. L. L. Murrell, D. C. Grenoble, and C. J. Kim,  
US Patent 4,233,139 (1980).

22. J. Bernholc, J. A. Horsley, L. L. Murrell,  
L. G. Sherman, and S. Soled,  
J. Phys. Chem. 91, 1526 (1987).

23. H. Yoshida, S. Morikawa, K. Takahashi, and M. Kurita,  
Japan Patent 57-48342 (1982).

24. K. Tanabe,  
"Heterogeneous Catalysis,"  
Texas A & M Univ. Press, p. 71 (1984).

25. K. Tanabe,  
Mat. Chem. and Phys. 17, 217 (1987).

26. Z. Chen, T. Iizuka, and K. Tanabe,  
Chem. Lett., 1085 (1984).

27. K. Ogasawara, T. Iizuka, and K. Tanabe,  
Chem. Lett., 645 (1984).

28. T. Iizuka, K. Ogasawara, and K. Tanabe,  
Bull. Chem. Soc. Jpn. 56, 2927 (1983)

29. T. Matsuzaki, Y. Sugi, T. Hanaoka, K. Takeuchi,  
H. Arakawa, and T. Tokoro,  
PACIFICHEM'89, "Catalytic Conversion with Niobium  
Materials," Honolulu, Dec. 17-22, 1989.

30. S. Okazaki and A. Kurosaki,  
PACIFICHEM'89, "Catalytic Conversion with Niobium  
Materials," Honolulu, Dec. 17-22, 1989.

31. T. Hanaoka, Y. Sugi, K. Takeuchi, H. Arakawa,  
and T. Matsuzaki,  
PACIFICHEM'89, "Catalytic Conversion with Niobium  
Materials," Honolulu, Dec. 17-22, 1989.

32. T. Iizuka, T. Tanaka, and K. Tanabe,  
J. Mol. Catal. 17, 381 (1982).

33. M. A. Vannice and S. J. Tauster,  
U. K. Patent 2,006,261 (1978).

34. E. I. Ko, J. M. Hupp, and N. J. Wagner,  
J. Catal. 86, 315 (1984).

35. Y. S. Jin, A. Ouqour, A. Auroux, and J. C. Vedrine,  
Study in Surf. Sci. Catal. Vol. 48, 525 (1989).

36. Y. Kera and T. Kawashima,  
Bull. Chem. Soc. Jpn 61, 1491 (1988).

37. R. Parthasara and F. G. Ciapetta,  
U. S. Patent 3557199 (1971).

38. Y. Oda, K. Uchida, M. Suhara, and T. Morimoto,  
U. K. Patent 1,377,325 (1974).

39. E. M. Thorsteinson, J. P. Wilson, F. G. Young,  
and P. H. Kasai,  
J. Catal. 52, 116 (1978).

40. A. A. Sobdeva, E. I. Andreikov, V. L. Volkov,  
and N. D. Rusyanova,  
Russ. J. Phys. Chem. 50, 763 (1976).

41. S. Okazaki, H. Kuroha, and T. Okuyama,  
Chem. Lett. 45 (1985).

42. T. Ikeya and M. Senna,  
J. of Non-Cryst. Solids 105, 243 (1988).

43. F. Izumi and H. Kodama,  
Z. Anorg. Allg. Chem. 440, 155 (1978).

44. A. Ann McConnell, J. S. Anderson, and C. N. R. Rao,  
Spectrochimica Acta Vol 32A, 1067 (1976).

45. J. G. Weissman, E. I. Ko, P. Wynblatt, and J. M. Howe,  
Chemistry of Materials, Vol. 1, No. 2, 187 (1989).

46. L. A. Aleshina, V. P. Malnenko, A. D. Phouphanov, and  
N. M. Jakovleva,  
J. of Non-Cryst. Solids 87, 350 (1986).

47. K. Kato and S. Tamura,  
Acta Cryst. B31, 673 (1975).

48. B. M. Gatehouse and A. Wadsley,  
Acta Cryst. 17, 1545 (1964).

49. H. D. Megaw,  
Acta Cryst. A24, 589 (1968).

50. A. C. Sakowski-Cowley, K. Lukaszwickz, and H. D. Megaw,  
*Acta Cryst.* B25, 851 (1969).

51. L. Katz and H. D. Megaw,  
*Acta Cryst.* 22, 269 (1967).

52. M. Dion, M. Ganne, and M. Tournoux,  
*Mat. Res. Bull.* Vol. 16, 1429 (1981).

53. A. J. Jacobson, J. W. Johnson, and J. T. Lewandowski,  
*Inorg. Chem.* 24, 3727 (1985).

54. A. J. Jacobson, J. T. Lewandowski, and J. W. Johnson,  
*J. of Less-Common Metals* 116, 137 (1986).

55. F. J. Farrell, V. A. Maroni, and T. G. Spiro,  
*Inorg. Chem.* 8(12), 2638 (1969).

56. R. S. Tobias,  
*Can. J. Chem.* 43, 1222 (1965).

57. C. Rocchiccioli-Deltcheff, R. Thouvenot, and  
M. Dabbabi,  
*Spectrochimica Acta* 33A, 143 (1977).

58. A. M. Glass, K. Nassau, and J. T. Negran,  
*J. Appl. Phys.* 49, 1075 (1978).

59. A. El Jazouli, J. C. Viala, C. Parent, and  
P. Hagenmuller,  
*J. of Solid State Chemistry* 73, 433 (1988).

60. S. J. Jang, K. Uchino, S. Nomura, and L. E. Cross,  
*Ferroelectrics* 27, 31 (1980).

61. S. L. Swartz and T. R. Shrout,  
Mat. Res. Bull. 17, 1245 (1982).

62. J. M. Jehng and I. E. Wachs,  
ACS Div. Petrol. Chem. preprints, 34(3), 546 (1989).

63. G. Blasse,  
J. of Solid State Chem. 7, 169 (1973).

64. H. P. Rooksby and E. A. D. White,  
Acta. Cryst. 16, 888 (1963).

65. I. E. Wachs, F. D. Hardcastle, and S. S. Chan,  
Spectroscopy 1(8), 30 (1986).

66. M. Muller and J. Dehand,  
Bull. Soc. Chim. France No. 8, 2837 (1971).

67. L. E. Orgel,  
"An Introduction to Transition Metal Chemistry,"  
John Wiley, New York, 174 (1960).

68. L. Pauling,  
"The Nature of the Chemical Bond,"  
Oxford University Press (1952).

69. B. Kojic-Prodic, R. Limingu, and S. Scavnicar,  
Acta Cryst. B29, 864 (1973).

70. N. Galesic, B. Matkovic, M. Herceg, and M. Sljukic,  
J. of Less-Common Metals 25, 234 (1971).

71. N. Brnicevic and C. Djordjevic,  
J. of Less-Common Metals 23, 107 (1971).

72. Par G. Mathern and R. Weiss,  
Acta Cryst. B27, 1610 (1971).

73. B. F. Pedersen,  
Acta Chemica Scand. 16, 421 (1962).

74. G. Brauer,  
Z. Anorg. Allgen. Chem. 248, 1 (1941).

75. H. Schafer and G. Breil,  
Z. Anorg. Allgem. Chem. 267, 265 (1952).

76. H. Schafer, R. Gruehn, and F. Schulte,  
Angew. Chem. 78, 28 (1966).

77. V. Bhide and E. Husson,  
Mat. Res. Bull. 15, 1339 (1980).

78. S. S. Chan, I. E. Wachs, L. L. Murrell, L. Wang, and  
W. K. Hall,  
J. Phys. Chem. 88, 5831 (1984).

79. L. A. Kinzhibalo, V. K. Trunov, A. A. Evdokimov, and  
V. G. Krongauz,  
Kristallografiya 27, 43 (1982).

80. V. K. Trunov, V. A. Efremov, Yu. A. Velikopodny, and  
I. M. Averina,  
Kristallografiya 26, 67 (1981).

81. M. T. Pope,  
"Heteropoly and Isopoly Oxometalates,"  
Springer-Verlag, Heidelberg (1983).

82. V. W. Day and W. G. Klemperer,  
Science, Vol. 228, 533 (1985).

83. C. F. Baes, Jr., R. E. Mesmer,  
"The Hydrolysis of Cations,"  
Wiley-Interscience, New York (1976).

84. M. Filowitz, R. K. C. Ho, W. G. Klemperer, and W. Shum,  
Inorg. Chem. 18, 93 (1979).

85. A. Goiffon and B. Spinner,  
Bull. Soc. Chimi. France, No. 11-12, 2435 (1975).

86. A. Goiffon, R. Granger, C. Bockel, and B. Spinner,  
Rev. Chim. Minerale 10, 487 (1973).

87. H. A. Flaschka and A. J. Barnard, Jr.,  
"Chelates in Analytical Chemistry," Vol. 2, 213 (1969).

88. M. Muller and J. Dehand,  
Bull. Soc. Chimi. France, No. 8, 2837 (1971).

89. M. Muller and J. Dehand,  
Bull. Soc. Chimi. France, No. 8, 2843 (1971).

90. G. Schwarzenbach,  
Angew. Chem. 70, 451 (1958).

91. H. Schafer,  
Angew. Chem. 71, 153 (1959).

92. F. T. Sisco and E. Epremian,  
"Niobium and Tantalum," Wiley, New York (1963).

93. J. M. Jehng and I. E. Wachs,  
"Structural chemistry and Raman spectra of niobium  
oxides," submitted to Chemistry of Materials.

94. D. P. Strommen and K. Nakamoto,  
"Laboratory Raman Spectroscopy,"  
Wiley-Interscience (1984).

95. W. H. Nelson and R. S. Tobia,  
Can. J. Chem. 42, 731 (1964).

96. W. H. Nelson and R. S. Tobia,  
Inorg. Chem. 3, 653 (1964).

97. J. Aveston and J. S. Johnson,  
Inorg. Chem. 3, 1051 (1964).

98. G. Neumann,  
Acta Chem. Scand. 18, 278 (1964).

99. A. Goiffon and B. Spinner,  
Rev. Chim. Minerale 11, 262 (1974).

100. W. P. Griffith and A. Lesniak,  
J. Chem. Soc. A, 1066 (1969).

101. E. M. Zhurenkov and N. Pobezhimovskaya,  
Radiokhimiya 12(1), 105 (1970).

102. C. Djordjevic, H. Gorican, and S. L. Tan,  
J. Less-Common Metals II, 342 (1966).

103. F. Basolo and R. G. Pearson,  
"Mechanisms of Inorganic Reactions,"  
John Wiley and Sons, New York (1967).

104. F. A. Cotton and G. Wilkinson,  
"Advanced Inorganic Chemistry,"  
Interscience, London (1966).

105. F. P. Dwyer and D. P. Mellor,  
"Chelating Agents and Metal Chelates,"  
Academic Press, New York (1964).

106. Y. Wada, M. Inaida, Y. Murakami, and A. Morikawa,  
Bull. Chem. Soc. Jpn. 61, 3839 (1988).

107. E. DeCanio, J. M. Jehng, and I. E. Wachs,  
to be published.

108. K. Asakura and Y. Iwasawa,  
Chem. Lett., 511 (1986).

109. K. Asakura and Y. Iwasawa,  
Chem. Lett., 633 (1988).

110. G. Deo and I. E. Wachs,  
submitted to J. Phys. Chem..

111. F. P. J. M. Kerkhof and J. A. Moulijn,  
J. Phys. Chem. 83, 1612 (1979).

112. Z. X. Liu, Z. D. Lin, H. Fan, and F. H. Li,  
Appl. Phys. A45, 160 (1988).

113. S. S. Chan, I. E. Wachs, L. L. Murrell,  
and C. C. Dispenziere, Jr.,  
J. Catal. 92, 1 (1985).

114. J. M. Jehng and I. E. Wachs,  
"Solution Chemistry of Niobium Oxide,"  
submitted to J. Raman spectroscopy.

115. W. S. Millman, K. I. Segawa, D. Smrz, and W. K. Hall,  
Polyhedron 5, 169 (1986).

116. C. L. O'Young, C. H. Yang, S. J. DeCanio, M. S. Patel,  
and D. A. Storm,  
J. Catal. 113, 307 (1988).

117. G. A. Park,  
Chem. Rev. 65, 177 (1965);  
Adv. Chem. Series 61, 121 (1967).

118. F. J. Gil-Llamblas, A. M. Escudey, J. C. G. Fierro,  
and A. C. Agudo,  
J. Catal. 95, 520 (1985).

119. A. F. Wells,  
"Structural Inorganic Chemistry," Oxford, London  
(1984).

120. F. Roozeboom, J. Medema, and P. J. Gellings,  
Z. Phys. Chem. 111, 215 (1978).

121. M. Shirai, A. Asakura, and Y. Iwasawa,  
PACIFICHEM'89, "Catalytic Conversion with Niobium  
Materials," Honolulu, Dec. 17-22 (1989).

122. I. D. Brown,

Chem. Soc. Rev. 7, 359 (1978).

123. I. D. Brown and K. K. Wu,

Acta Cryst. B32, 1957 (1976).

124. J. M. Jehng and I. E. Wachs,

"Molecular Structures of Supported Niobium Oxide Catalysts Under Ambient Conditions,"

to be submitted to J. Molecular Catalysis.

125. J. M. Stencel,

"Raman Spectroscopy for Catalysis,"

Van Nostrand Reinhold, New York (1990).

126. L. Wang, Dissertation, University of Wisconsin-Milwaukee (1982).

127. G. Deo, H. Eckert, and I. E. Wachs,

Prep. Amer. Chem. Soc. Div. Petrol. Chem. 35(1), 16 (1990).

128. M. Vuurman and I. E. Wachs,

to be published.

129. G. T. Went, S. T. Oyama, and A. T. Bell,

J. Phys. Chem. 94, 4240 (1990).

130. S. T. Oyama, G. T. Went, K. B. Lewis, A. T. Bell,  
and G. Somarjai,

J. Phys. Chem. 93, 6786 (1989).

131. G. Busca,  
Mat. Chem. and Phys. 19, 157 (1988);  
C. Cristinai, P. Forzatti, and G. Busca,  
J. Catal. 116, 586 (1989).

132. H. Eckert and I. E. Wachs,  
J. Phys. Chem. 93, 6796 (1989).

133. S. Yoshida, T. Tanaka, Y. Nishimura, H. Mizutani,  
and T. Funabiki,  
Proc. 9th Inter. Cong. Catal. Vol 3, 1473 (1988).

134. I. E. Wachs,  
J. Catal. 104, (1990).

135. T. Machej, J. Haber, A. M. Turek, and I. E. Wachs,  
to be published.

136. J. M. Stencel, L. E. Makovsky, T. A. Sarkus,  
J. de Vries, R. Thomas, and J. Moulijn,  
J. Catal. 90, 314 (1984).

137. J. M. Stencel, J. R. Diehl, J. R. D'Este,  
L. E. Makovsky, L. Rodrigo, K. Marcinkowska, A. Adnot,  
P. C. Roberge, and S. Kaliaguine,  
J. Phys. Chem. 90, 4739 (1986).

138. S. S. Chan, I. E. Wachs, and L. L. Murrell,  
J. Catal. 90, 150 (1984).

139. J. M. Stencel, L. E. Makovsky, J. R. Diehl,  
and T. A. Sarkus,  
J. Raman Spectrsc. 15, 282 (1984).

140. D. R. Tallant, B. C. Bunker, C. J. Brinker,  
and C. A. Balfe,  
"Better Ceramics Through Chemistry II,"  
eds C. J. Brinker, D. E. Clark, and D. R. Ulrich,  
Materials Research Society, pp. 261, 1986.

141. J. M. Jehng and I. E. Wachs,  
"The Molecular structures and Reactivity of Supported  
Niobium Oxide Catalysts,"  
submitted to *Catalysis Today*.

142. F. D. Hardcastle, Dissertation, Lehigh University;  
University Microfilms International: Ann Arbor, MI  
(1990).

143. E. Husson, Y Repelin, N. Q. Dao, and H. Brusset,  
*Mat. Res. Bull.*, Vol. 12, 1199 (1977).

144. E. Husson, Y Repelin, N. Q. Dao, H. Brusset,  
and E. Fardouet,  
*Spectrochimica Acta*. 33A, 995 (1977).

145. C. C. Williams, J. G. Ekerdt, J. M. Jehng,  
F. D. Hardcastle, and I. E. Wachs,  
to be submitted to *J. Phys. Chem.*.

146. J. M. Jehng and I. E. Wachs,  
unpublished work.

147. L. Pauling, "General Chemistry,"  
Dover Publications, Inc., New York (1988).

148. J. Datka, A. Turek, J. M. Jehng, and I. E. Wachs,  
"Acidic Properties of Supported Niobium Oxide  
Catalysts: An Infrared Spectroscopy Investigation  
to be submitted to J. Catal..

149. D. van Hove, M. Blanchard,  
Bull. Soc. Chim. Fr., 329 (1971).

150. R. Grabowski, B. Grzybowska, J. Haber,  
and J. Sloczynski,  
React. Kinet. Catal. Lett. 2, 81 (1975).

151. G. C. Bond, and P. J. Konig,  
J. Catal. 77, 309 (1978).

152. I. Gasior, M. Gasior, B. Grzybowska, R. Kozlowski,  
and J. Sloczynski,  
Bull. Acad. Pol. Sci., Ser. Sci. Chim. 27, 829 (1979).

153. G. C. Bond, J. Sarkany, and G. D. Parfitt,  
J. Catal. 5, 476 (1979).

154. F. Roozeboom, T. Fransen, P. Mars, and P. J. Gellings,  
Z. anorg. allg. Chem. 25, 449 (1979);  
F. Roozeboom, M. C. Mittelmeijer-Hazeleger,  
J. A. Moulijn, J. Medema, V. H. J. de Beer,  
and P. J. Gellings,  
J. Phys. Chem. 84, 2783 (1980).

155. Y. Murakami, M. Inomata, A. Miyamoto, and K. Mou,  
"Proc. 7th Intern. Cong. on Catal.," p.1344 (1980).

156. F. Roozeboom, P. D. Cordingley, and P. J. Gellings,  
J. Catal. 68, 464 (1981).

157. A. J. van Hungsteun, J. G. van Ommen, H. Bosch,  
and P. J. Gellings,  
Appl. Catal. 8, 369 (1983).

158. Y. Iwasawa, and M. Yamagishi,  
J. Catal. 82, 373 (1983).

159. M. Gasior, I. Gasior, B. Grzybowska,  
Appl. Catal. 10, 87 (1984).

160. N. K. Nag, K. V. R. Chary, B. M. Reddy, B. Ramaro,  
and V. S. Subrahmanyam,  
Appl. Catal. 9, 225 (1984).

161. I. E. Wachs, R. Y. Saleh, S. S. Chan,  
and C. C. Chersich,  
Appl. Catal. 15, 339 (1985).

162. I. E. Wachs, S. S. Chan, and R. Y. Saleh,  
J. Catal. 91, 366 (1985).

163. R. Y. Saleh, I. E. Wachs, S. S. Chan,  
and C. C. Chersich,  
J. Catal. 98, 102 (1986).

164. M. Gasior, J. Haber, and T. Machej,  
Appl. Catal. 33, 1 (1987).

165. T. J. Yang, and J. H. Lunsford,  
J. Catal. 103, 55 (1987).

166. D. S. Kim, Y. Kurusu, I. E. Wachs, F. D. Hardcastle,  
and K. Segawa,  
J. Catal. 120, 325 (1989).

167. C. Louis, J. M. Tatibouet, and M. Che,  
J. Catal. 109, 354 (1988).

168. T. Ono, H. Kamisuki, H. Hisashi, and H. Miyata,  
J. Catal. 116, 303 (1989).

169. G. Deo and I. E. Wachs,  
"Predicting the Molecular Structures of Surface Metal  
Oxide Species on Oxide Supports Under Ambient  
Conditions," to be submitted to J. Phys. Chem..

170. H. Kobagashi, M. Yamaguchi, T. Tanaka, Y. Nishimura,  
H. Kawakami, and S. Yoshida,  
J. Phys. Chem. 92, 2316 (1988).

171. H. Knozinger,  
Adv. Catal. 25, 184 (1976).

172. C. N. Satterfield,  
"Mass Transfer in Heterogeneous Catalysis,"  
The Colonial Press Inc., Clinton, Massachusetts, 1970.

173. Y. C. Liu, G. L. Griffin, S. S. Chan, and I. E. Wachs,  
J. Catal. 94, 108 (1985).

174. J. M. Tatibouet, J. E. Germain, and J. C. Volta,  
J. Catal. 82, 240 (1983).

175. J. M. Jehng and I. E. Wachs,  
"Molecular structures of Supported Niobium Oxide  
Catalysts Under In Situ Conditions," to be submitted  
to J. Phys. Chem..

## CURRICULUM VIATE

Name: Jih-Mirn Jehng

Place of Birth: Taipei, Taiwan, Republic of China

Date of Birth: August 29, 1956

Parents: Chi-Yuan and Mei-Yu Jehng

### Education:

PhD, Lehigh University, Bethlehem, PA, 10/1990.

Dissertation: Niobium Oxide Catalysts: Synthesis,  
Characterization, and Catalysis

MSChE, Lehigh University, Bethlehem, PA, 1985

Thesis: An Experimental and Correlative Study of  
the Vapor-Liquid Equilibria of the Carbon  
Dioxide/Isobutane System.

BSChE, Tung-Hai University, Taichung, Taiwan, 1979

### Professional Experience:

Research and Development Engineer, National Bureau  
of Standards, Taiwan, 1981-1983

- Established standards for chemical industries
- Tested the physical properties of tires
- Inspected the physical and chemical properties  
of Portland white cement

### Activities:

- Member of American Institute of Chemical Engineers
- Member of American Chemical Society

### Publications:

1. "The Interaction of  $V_2O_5$  and  $Nb_2O_5$  with Oxide Surfaces,"  
(coauthors: F. D. Hardcastle, and I. E. Wachs,  
Solid State Ionics, 904-910, 1989)
2. "Supported Molybdenum Oxide Monomers and Dimers:  
Characterization and Methanol Oxidation Studies,"  
in preparation, (coauthors: C. C. Williams,  
J. G. Ekerdt, F. D. Hardcastle, and I. E. Wachs)

3. "Niobium Oxalate: A New Precursor for the Preparation of Supported Niobium Oxide Catalysts,"  
(coauthor: I. E. Wachs, Div. Petrol. Chem., ACS, 34(3), 546, 1989)
4. "A Laser Raman and UV Diffuse Reflectance Spectroscopic Investigation of Silica Supported Molybdenum Oxide,"  
submitted to J. Catal. (coauthors: C. C. Williams, J. G. Ekerdt, I. E. Wachs, and F. D. Hardcastle)
5. "A Laser Raman and UV Diffuse Reflectance Spectroscopic Investigation of Alumina Supported Molybdenum Oxide,"  
submitted to J. Catal. (coauthors: C. C. Williams, J. G. Ekerdt, I. E. Wachs, and F. D. Hardcastle)
6. "Synthesis, Characterization, and Catalysis of Surface Modified Niobic Acid," in preparation  
(coauthor: I. E. Wachs)
7. "Structural Chemistry and Raman Spectra of Niobium Oxides," submitted to Chemistry of Materials,  
(coauthor: I. E. Wachs)
8. "Solution Chemistry and Raman Spectra of Niobium Oxides," submitted to J. Raman Spectroscopy,  
coauthor: I. E. Wachs)
9. "Acidic Properties of Supported Niobium Oxide Catalysts: An Infrared Spectroscopy Investigation," submitted to J. Catal., (coauthors: J. Datka, A. M. Turek, and I. E. Wachs)
10. "The Molecular Structures and Reactivity of Supported Niobium Oxide Catalysts," submitted to Catalysis Today,  
(coauthor: I. E. Wachs)
11. "Molecular Structures of Supported Niobium Oxide Catalysts Under Ambient Conditions," submitted to J. Molecular Catalysis (coauthor: I. E. Wachs)
12. "Molecular Structures of Supported Niobium Oxide Catalysts Under In Situ Conditions," submitted to J. Phys. Chem.,  
(coauthor: I. E. Wachs)
13. "Surface Acidity and Reactivity of Supported Niobium Oxide Catalysts" submitted to J. Catal..  
(coauthor: I. E. Wachs)